Energy Storage and Conversion Applications of Conductive Metal-Organic Frameworks

by

Elise Marie Miner

B.S., Northeastern University (2014)

Submitted to the Department of Chemistry
in Partial Fulfillment of the Requirements for the Degree of

Doctor of Philosophy

at the

MASSACHUSETTS INSTITUTE OF TECHNOLOGY

February 2019

Signature redacted

Signature of Author..... .....
Department of Chemistry
December 17th, 2018

Signature redacted

Certified by..... .....
Mircea Dincă
Associate Professor of Chemistry
Thesis Supervisor

Signature redacted

Accepted by..... .....
Robert Field
Haslam and Dewey Professor of Chemistry; Chair, Department Committee on Graduate Students

This doctoral thesis has been examined by a committee of the
Department of Chemistry as follows:

Professor Yogesh Surendranath..... Signature redacted

Thesis Committee Chair
Paul M Cook Career Dev Associate Professor of Chemistry

Professor Mircea Dincă..... Signature redacted .....

Thesis Supervisor
Associate Professor of Chemistry

Professor Yang Shao-Horn..... Signature redacted .....

Thesis Committee Member
W.M. Keck Professor of Energy, Department of Mechanical Engineering

Energy Storage and Conversion Applications of Conductive Metal-Organic Frameworks

by

Elise Marie Miner

Submitted to the Department of Chemistry
on December 17th, 2018 in Partial Fulfillment of the
Requirements for the Degree of Doctor of Philosophy in
Chemistry

ABSTRACT

Establishing catalytic structure-function relationships enables optimization of the catalyst structure for enhanced activity, selectivity, and durability against reaction conditions and prolonged catalysis. One class of catalysts that could benefit from systematic optimization is non-platinum group metal (non-PGM) electrocatalysts for the O_2 reduction reaction (ORR) to water ($4e^-$ reduction) and / or hydrogen peroxide ($2e^-$ reduction). The electrically conductive metal-organic frameworks (MOFs) $M_3(HXTP)_2$ (HXTP = 2,3,6,7,10,11-hexaimino or hexahydroxytriphenylene (HITP or HHTP, respectively)) feature a crystalline structure that contains homogeneously distributed, square planar transition metal sites reminiscent of those doped into carbonaceous media for ORR catalysis. $Ni_3(HITP)_2$ functions as an active and stable ORR electrocatalyst in alkaline medium. Experimental and computational techniques enabled elucidation of the kinetics, mechanism, and active site for ORR with $Ni_3(HITP)_2$, as well as understanding the essential nature of the extended MOF structure in providing catalytic activity. Varying the metal and ligand combinations within this class of MOFs afforded two distinct phases. Probing the stability, catalytic activity, product distribution, and electronic properties of the two phases of MOFs identified phase-dependent catalytic activity, regardless of the metal or chelating atom identity.

Since the birth of the first rechargeable battery in 1860, emerging battery technologies have both provided answers to energy demands as well as additional obstacles to navigate. Recent works have explored using MOFs as ionically conductive solid-state electrolytes which would eliminate the need for volatile organic liquids and potentially offer a wider electrolyte potential window and means of controlling the plating of alkali metals during charging. This work has taken advantage of the modular charge found in a Cu-azolate MOF, wherein guest Cl^- ions coordinated to Cu_4-lined clusters can be washed out of the structure, and stoichiometric loadings of anions varying in size can be reconstituted into the MOF when soaking the MOF in solutions containing alkali or alkaline earth metal salts. The anions are held in place through coordination to the Cu^{2+} centers, thus enabling the charge-balancing metal cations to achieve high transference numbers within this solid electrolyte. Further, the versatility regarding the identity of the guest metal salt provides a handle for modulating the cation transport activation energy and ionic conductivity.

Thesis Supervisor: Mircea Dincă
Title: Associate Professor of Chemistry

Contents

Part I. Heterogeneous Electrocatalysis of the O_2 Reduction Reaction Using Electrically Conductive Triphenylene-Based MOFs

List of Figures

List of Tables

List of Schemes

Part I

◊

Heterogeneous Electrocatalysis of the O_2 Reduction Reaction Using Electrically Conductive Triphenylene-Based MOFs

Chapter 1

Oxygen Electroreduction

1.1 Introduction

Perhaps one of the greatest displays of human ingenuity has been the diverse and resourceful development of energy conversion and storage technologies. Born from the necessity to meet society's increasing demands for energy, the harnessing and housing thereof has manifested in a multi-pronged approach to answering these demands. In addition to energy technologies targeting high energy density and operating efficiency, portability, long lifetime, and low cost, increased greenhouse gas emissions and the environmental impacts stemming from this have also made apparent the need for low carbon or carbon-free energy sources.[1,2] One such energy source, the fuel cell, has received increased attention since the manifestation of the original design in 1839.[3] Evolving design principles have introduced varietals beyond the original sulfuric acid cell, such as solid oxide fuel cells,[4] polymer electrolyte membrane fuel cells,[5] and alkaline fuel cells.[6] Although each of these models feature operational nuances, all categories are unified by their overall circuitry, potential as renewable energy devices, and challenges hindering widespread commercialization. Broadly speaking, all fuel cells are comprised of an anode and a cathode separated by an electrolyte, and in some cases, a membrane or separator (**Figure 1-1**). At the anode, H_2 gas is electrooxidized, forming protons and electrons. The electrons shuttle through an external circuit, generating

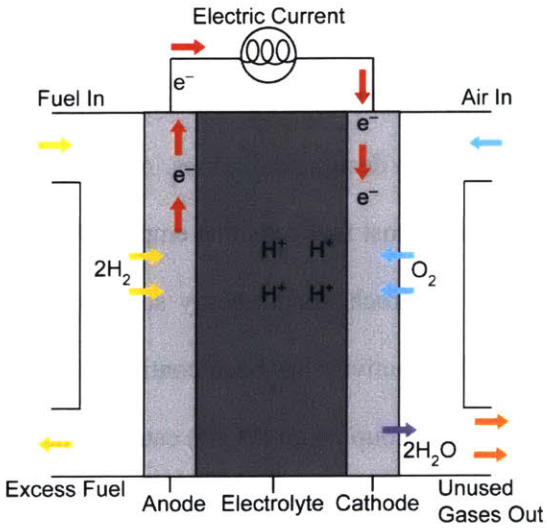

Figure 1-1. Diagram of a fuel cell.

electrical energy in the form of current. Protons migrate through the electrolyte to the cathode, where O_2 is reduced by a maximum of $4e^-$ and combined with the protons (unless this has already occurred by proton-coupled electron transfer (PCET)) to form H_2O. A proton-conductive membrane or separator may be employed to prevent fuel crossover between the anode and cathode. In the case of polymer electrolyte membrane fuel cells, this membrane also serves as the electrolyte.[5] The attraction of fuel cells as alternative energy technologies is several-fold. Firstly, the electrochemical reactions in fuel cells enable the efficiency to exceed the 20% ceiling associated with Carnot-limited processes. If both the anodic and cathodic reactions proceed with minimal overpotential, fuel cell efficiency (ζ) can approach 100%, as described by **Equation 1-1**, where η_{anode} = the overpotential of the anodic reaction, $\eta_{cathode}$ = the overpotential of the

$$\zeta = 1 - \frac{\eta_{anode} + \eta_{cathode}}{\Delta E^o} \cdot 100 \qquad \text{Eq. 1–1}$$

cathodic reaction, and ΔE^o = the difference between the formal potentials at the anode and cathode.[7] Further, fuel cells also exhibit up to two orders of magnitude higher gravimetric energy density than other portable power technologies.[6,8] The ability to stack multiple cells in series allows for a modular setup that can accommodate a plethora of applications, such as propulsion systems, light traction vehicles, auxiliary power units, portable devices, and emergency backup power sources.[6] Perhaps one of the most notable draws of fuel cell technology, and one of the major drivers for the development thereof, is the carbon-free emission benefit associated with an idealized hydrogen economy. Available fuel cells share these benefits, along with various drawbacks that also stem from design similarities. Although the nature of the electrolyte may differ greatly among fuel cell categories, most fuel cells that employ the H_2 oxidation reaction (HOR) and O_2 reduction reaction (ORR) as the electrochemical energy sources use the same electrode materials. Specifically, unparalleled electrocatalytic activity has been continuously shown with Pt or other precious metal-based materials; as such, platinum group metal (PGM) catalysts have been employed as both anode and cathode materials. The high efficiency of the HOR allows significantly lower loadings of PGM catalysts on the anode,[7] thus minimizing costs associated with the oxidizing side of the cell. Conversely, the slow

reaction kinetics suffered by the ORR necessitate high PGM loadings at the cathode. This profusion of PGMs on the cathode is a principal contributor to the economically inaccessible cost of fuel cells, and one major factor hindering the widespread commercialization thereof.[9] In addition to the high cost of PGM catalysts, such metals are plagued by instability to certain electrolyte ions, fuels such as methanol and associated crossover products, and trace impurities such as CO.[10,11] The propensity for catalyst poisoning by exogenous species threatens the lifetime of the cell. As such, efforts spanning decades have targeted development of highly active and durable ORR catalysts featuring more abundant and thus less costly elements. These efforts have involved intensive studying of ORR pathways on both Pt and non-Pt electrocatalysts, with the goal of directing catalyst design.

1.2 ORR pathways

The ORR can proceed via either $2e^-$ reduction forming H_2O_2 or HO_2^-, or $4e^-$ reduction forming H_2O or OH^-, depending on the electrolyte pH.[12,13] In the case of molecular catalysts, both inner and outer sphere electron transfer (ET) mechanisms for ORR have been proposed, with outer-sphere ET being promoted by tethering molecular catalysts to the electrode surface using thiols or other functional groups.[14,15] Metal electrodes can have adsorbed OH^- species that serve as "bridges" between the electrode and O_2, facilitating the first ET without O_2 adsorbing directly onto the metal surface. In this case, solvated O_2 would interact with the electrode through hydrogen bonding interactions among the OH^-, H_2O, and O_2 species, and the reduced hydroperoxide would coordinate to the metal surface after the first ET and participate in further reduction.[16] Hydroxide-mediated electron transfer may be operative if a sharp ring current peak during rotating ring disk electrode (RRDE) studies is observed. This peak has been ascribed to OH^- adsorption onto the metal sites, which could facilitate ET to proximal O_2.[17] Beyond this hydroxide bridge-mediated ET to O_2, other mechanisms for heterogeneous electrocatalytic ORR proceed through inner-sphere ET directly to bound O_2. Given that electrically conductive electrocatalysts possess a continuum of orbitals that give rise to an extended band structure representing charge delocalization rather

than charge being localized on one given catalytic site, electron transfer to O_2 must be preceded by surface bond formation.[18] As such, if no bridging OH^- species between the electrode and O_2 is present in the aqueous electrolyte, O_2 adsorption onto the electrode enables electron transfer.

Within the realm of inner-sphere ORR, several pathways can yield the aforementioned products, the prevalence of which are dictated by adsorption energetics of oxygenated intermediates and reaction barriers on the catalyst surface. Specifically, the dissociative pathway, wherein the O—O bond is cleaved upon adsorption of O_2 onto the catalyst, may be favored when the catalytic site interacts sufficiently strongly to retain atomic O as opposed to molecular oxygen remaining intact. This pathway can be promoted by having two catalytic sites in close (several angstroms) proximity, so molecular oxygen can bind in a side-on fashion, with both O atoms interacting with the catalyst surface. One caveat associated with targeting strong catalyst—O interactions is that sufficiently strong interactions may reduce the reactivity of the activated O and in turn slow catalyst turnover. This phenomenon can be likened to the undesirable poisoning of Pt catalysts by CO due to the strong adsorption of CO onto the Pt sites. The associative pathway, wherein the O—O bond is retained during reduction, may dominate when a single catalytic site is available for O_2 interaction, thus promoting end-on coordination. The latter may still enable $4e^-$ ORR, but a 2 x $2e^-$ mechanism that further reduces bound OOH to H_2O is necessary (**Table 1-1**).[12,19] Stepwise reduction of O_2 can result in lower faradaic efficiency; as such, the dissociative mechanism is targeted for fuel cell applications.

1.3 Metrics for evaluating ORR electrocatalytic performance

Previous work and theory has established methods for evaluating ORR catalyst performance and probing ORR mechanisms. As shown previously in **Equation 1-1**, fuel cell efficiency is dictated by the overpotentials of the anodic and cathodic reactions. Consequently, a primary goal of ORR electrocatalyst development is minimizing the overpotential associated with catalyzing the reduction. Pt, the industrial standard, reduces O_2 with an onset potential of 1.00 V vs RHE, or an overpotential of 0.23 V given the

thermodynamic $4e^-$ ORR potential of 1.23 V vs RHE.[13] Many non-PGM electrocatalysts typically exhibit ORR overpotentials several hundred mV higher than that of Pt. Another metric for benchmarking

Table 1-1. ORR pathways in alkaline conditions. * denotes the catalytic site.

Pathway	Reactions
Dissociative ($4e^-$)	$O_2 + 2^* \rightarrow 2O^*$
	$2O^* + 2e^- + 2H_2O \rightarrow 2OH^* + 2OH^-$
	$2OH^* + 2e^- \rightarrow 2OH^- + 2^*$
Associative ($4e^-$)	$O_2 + ^* \rightarrow O_2^*$
	$O_2^* + H_2O + e^- \rightarrow OOH^* + OH^-$
	$OOH^* + e^- \rightarrow O^* + OH^-$
	$O^* + H_2O + e^- \rightarrow OH^* + OH^-$
	$OH^* + e^- \rightarrow OH^- + ^*$
Associative ($2e^-$)	$O_2 + ^* \rightarrow O_2^*$
	$O_2^* + H_2O + e^- \rightarrow OOH^* + OH^-$
	$OOH^* + e^- \rightarrow OOH^- + ^*$

electrocatalysts is Tafel analysis. Tafel plots and the associated equation (**Equation 1-2**) express the relationship between applied overpotential (driving force) and measured current, and thus reflect the electrokinetics of the electrochemical reaction.[20,21] In the Tafel equation, i = measured current, i_o = exchange

$$i = i_o \exp\left(\frac{\beta \eta F}{RT}\right) \qquad \text{Eq. 1-2}$$

current, β = the dimensionless symmetry factor of the reaction, η = applied overpotential, F = Faraday's constant, R = the universal gas constant, and T = temperature in K. More current passed at lower overpotential is indicative of faster electrokinetics. In this vein, the exchange current (i_o), or the current at zero overpotential (x-intercept of the Tafel plot), is also reflective of the electrochemical activity at the

electrode as it represents the electrokinetics of the equilibrium reaction.[20] Electrodes capable of fast electron transfer will exhibit high exchange current values. Exchange current density values observed for ORR with precious metal electrocatalysts typically fall between 10^{-8} and 10^{-6} $A \cdot cm^{-2}$.[12] Given that current passed is dependent on the electrode area and / or catalyst loading on the electrode, current values are often normalized by these parameters and expressed as current densities (j).

In logarithmic form, the slope of the line represented by the Tafel equation, the Tafel slope (b), as represented in **Equation 1-3**, can shed light on the reaction mechanism occurring at the electrode.

$$b = \frac{2.3RT}{\beta F} \qquad \text{Eq. 1-3}$$

Specifically, given that β represents the ratio between the effect of the electrode potential on the electrochemical free energy of activation and the effect of the electrode potential on the electrochemical free energy of the reaction, the value of β (and by association, the Tafel slope) indicates whether rate-limiting ET is operative. Likening β to an efficiency factor of sorts, an efficient electrochemical reaction would have $\beta = 1.0$. A value of $\beta = 1.0$ gives a Tafel slope of 59 $mV \cdot dec^{-1}$ under standard conditions, and a value of $\beta = 0.5$ gives a Tafel slope of 118 $mV \cdot dec^{-1}$ under standard conditions. When $\beta = 1.0$ and the Tafel slope ~ 59 $mV \cdot dec^{-1}$, efficient electrokinetics are at play so the reaction is rate-limited by a chemical step. When $\beta < 1.0$, and the Tafel slope > 59 $mV \cdot dec^{-1}$, this can be indicative of rate-limiting ET as the free energy of the overall reaction is in this case more sensitive to changes in applied potential than is the free energy of the activated complex, formation of which is treated as a chemical reaction. Since β is a theoretical parameter that is used to describe a single-step reaction, multi-step reactions observed experimentally must be expressed instead by the experimental transfer coefficient, α. This parameter is functionally the reciprocal Tafel slope in dimensionless form. Importantly, obtaining insightful electrokinetic data necessitates elimination of diffusion limitations in the system. As such, Tafel plots should be generated from Koutecky-Levich data, which represents the current-potential relationship purely under activation

control.[21] The importance of the current-potential relationship, as defined by the Tafel equation, is complemented by the importance of the absolute current density passed at a given potential. Although current density may be passed with low overpotential, achieving sufficient power density with a given overpotential is necessary for commercial applications. This is achieved in catalysts with both high-turnover active sites and a high density of electroactive sites in a geometric area.[8]

In addition to favorable electrokinetics, electrocatalysts are evaluated based on their faradaic efficiency (FE). As described in **Equation 1-4**, faradaic efficiency reflects product selectivity of the catalyst.[19] The faradaic efficiency of the ORR is determined using rotating ring-disk electrode (RRDE) studies, wherein H_2O_2 produced at the disk electrode from $2e^-$ ORR will be re-oxidized at the ring electrode. The anodic current passed at the ring electrode is divided by the experimentally determined collection efficiency of the ring, and this value is divided by the total current passed at the disk to get the faradaic efficiency for H_2O_2.

$$FE = \frac{I_{ring}}{I_{disk} \cdot \text{ring collection efficiency}} \cdot 100 \qquad \text{Eq. 1-4}$$

Minimal current passed at the ring is indicative of high faradaic efficiency for $4e^-$ ORR, ideal for fuel cell applications. Pt-based ORR catalysts exhibit high faradaic efficiency for $4e^-$ ORR.[16] In addition to predominantly producing water during ORR, the catalyst would ideally be stable to O_2, ORR products, fuel crossover products from the anode, the electrolyte, and to prolonged application of an electrochemical bias so that the cell lifetime can be maximized.

1.4 Metal-free ORR electrocatalysts

In addition to lowering Pt content by alloying Pt with non-noble metals such as Fe, Co, and Ni,[22–27] several avenues have been explored for developing non-PGM electrocatalysts for the ORR. For example, metal-free carbon-based catalysts have been identified as promising alternatives to Pt due to their enhanced lower cost, sp^2 hybridization which promotes electron mobility, high surface area that minimizes mass transport limitations, and stability to fuels and related crossover products.[28] One common tactic for

producing active carbon-based ORR catalysts is doping the carbon matrix with heteroatoms such as N.[29] It is thought that the more electronegative nitrogenous dopants can enhance the adsorption strength of O_2 on the carbon-based catalyst surfaces by activating neighboring carbon sites. Such additives can be introduced with physical blending, chemical vapor deposition, solvothermal synthesis, or post-synthetic treatment with N-containing gases.[28] It is noted that B-doped carbons investigated for ORR catalysis have also demonstrated activity. Given the electronegativity differences between B and N, the mechanism by which B dopants modulates ORR activity with doped carbons is thought to differ from that of N dopants.[30,31] Most carbon hosts are a variety of graphene, graphite, carbon nanotubes, or mesoporous carbons. One challenge with doping carbons is achieving homogeneous dispersion of the dopant that would enable reproducible results. Additionally, leaching of N-based active sites can cause problems with catalyst longevity. Recent works have cleverly addressed these issues by appending the catalytic N-doped-C moieties directly onto glassy carbon electrodes. *Ortho*-quinone sites located on the edge planes of the graphite served as docking sites for *ortho*-phenylenediamine derivatives used to catalyze ORR.[32] Facile condensation of the aminated compounds with the *ortho*-quinone groups afforded a library of graphite conjugated pyrazines (GCPs). The ability to utilize organic synthetic methods for altering the substituents on the parent phenylenediamine molecules provided a handle for systematically tuning the electronic properties and thereby the catalytic activity of the resulting GCPs. Under alkaline aqueous conditions, an onset potential of 0.75 V vs RHE was observed. Owing to the synthetic tunability of the materials, the ORR overpotential could be modulated as a function of electronegativity of the pyrazine-appended functional group. Electron-donating methyl substituents raised the ORR overpotential whereas electron-withdrawing pyridinium groups shifted the ORR activity to lower overpotential. Theoretical studies revealed the preferred O_2 adsorption site as being α-C with respect to the pyridinium moiety, highlighting the role of electrophilic groups in activating O_2 adsorption sites. One caveat of increasing the electrophilicity of an O_2 adsorption site to increase ORR

activity is this also increased the propensity for OH adsorption.[33] Understanding the interplay of adsorption energetics of these species can inform catalyst design.

Another interesting metal-free material explored for ORR catalysis has been conductive polymers. Chloride-doped conductive polymers have been shown not only to serve as hosts for metal-containing ORR catalysts,[34] but they also can exhibit some ORR activity themselves. In a 1.0 M HCl electrolyte, polyaniline emulsified with polytetrafluoroethylene (PTFE) and coated onto a graphite current collector exhibited an increase in cathodic current with a peak potential of 0.28 V versus NHE under O_2 versus Ar atmosphere.[35] Electrodes formulated in the same fashion but containing 5 wt% of polythiophene, poly(3-methyl)thiophene, and polypyrrole all exhibited the same cathodic current in the presence of O_2. In particular, in O_2-saturated electrolyte the polypyrrole-modified electrode passed 300% more cathodic current than that which had been observed under argon, with a cathodic current onset at ca. 0.5 V vs NHE. Poly(3,4-ethylenedioxythiophene) prepared in the same manner showed no activity for ORR. Although the overpotentials and current density values associated with such materials would likely not be competitive in commercial applications, these provide interesting examples as metal-free ORR electrocatlaysts.

1.5 Transition metal chalcogenide-based ORR electrocatalysts

Another example of non-Pt ORR catalysts includes transition metal chalcogenides, which gained attention in the 1970s due to their stability to acidic pH and tolerance to methanol.[36–40] Within the oxides, combinations of Ni and Co have been widely investigated as ORR electrocatalysts.[41] Early reports included exploration of Co_2NiO_4 / NiO for ORR activity as a function of the varying contents of the respective oxides. Increasing the temperature of the heat treatment from 300-600 °C resulted in amorphization of the Co_2NiO_4 spinel structure and increased the content of NiO in the sample starting above 400 °C. It was found that the sample heated at 400 °C, just below the temperature associated with formation of the NiO phase, exhibited the highest ORR activity in 5 M KOH.[42] The analogue treated at 400 °C exhibited an ORR onset potential of 0.9 V vs RHE, nearing that of Pt. Although active, lack of structural definition made probing

the nature of the active material difficult. ORR with Co_2NiO_4 was studied further by Singh, Chartier, and coworkers.[43] Thin films of Co_2NiO_4 and Co_3O_4 were deposited on CdO coated glass electrodes using a chemical spray pyrolysis technique at 400 °C with air as the carrier gas. ORR activity with the metal oxides showed a dependence on $[O_2]$ as well as the supporting electrolyte (KOH) concentration, supporting the assertion that electrocatalysis on these surfaces was influenced by the surface coverage of adsorbed OH species or other oxygenated moieties that would block O_2 adsorption. In addition to combining Co with later transition metals in an oxide structure, Co and Mn have also been partnered in metal oxide-based ORR materials. Cheng, Chen, and coworkers reported a method for synthesizing Co-Mn-oxide spinel structures, $Co_xMn_{3-x}O_4$, under ambient conditions, eliminating the need for energy-intensive heat treatment processes.[44] This was achieved via reduction of amorphous MnO_2 in aqueous Co^{2+} solutions, affording either tetragonal or cubic phases of the spinel structures depending on the reductant used. It was found that the cubic phase exhibited enhanced ORR activity compared to the tetragonal phase, with an ORR onset potential of approximately −0.1 V vs Ag/AgCl under alkaline conditions. Koutecky-Levich slope analysis suggested the $4e^-$ reduction product to dominate. More exotic metals have also been incorporated into metal-oxide based ORR catalyst structures. In particular, La has shown promising ORR activity in oxide structures along with Mn. A $LaMnO_3$ perovskite structure was combined with electrically conductive carbon black and subjected to a pyrolysis treatment at 650 °C in the presence of N_2.[45] The resulting catalyst showed notable onset potentials of ~ 0 V vs Hg/HgO in 8 M KOH. The operating overpotential of the catalyst was enhanced as a function of increased $LaMnO_3$ loading, with optimal performance achieved with 30 wt% perovskite loading.

Application of transition metal chalcogenides beyond oxides has expanded down the group. An early report examined the effect of metal identity on ORR activity in bimetallic metal sulfides[38] Ti, V, Cr, Fe, Co, or Ni (Me^a) were incorporated into a structure with Mn, Fe, Co, Ni, Cu, or Zn (Me^b) to form the sulfides $Me_z^aMe_{(3-z)}^bS_4$, where $0 \leq z \leq 1$. The effect of replacing a percentage of the sulfur atoms with O,

Se, or Te on ORR activity was also explored. The conductivity of these materials eliminated the need for conductive additives. It was found that $FeCo_2S_4$ exhibited the highest ORR activity, with an onset potential of ~800 mV vs RHE in 1 M H_2SO_4. Further, utilizing exclusively S as the chalcogenide showed enhanced activity over doped compounds, and incorporation of Co improved ORR activity compared to non-Co-containing chalcogenides. This study catalyzed the interest of Co-S containing materials for ORR electrocatalysis.[46,47]

Expanding the utility of such materials involved application of transition metal selenides as ORR electrocatalysts. $Mo_{4.2}Ru_{1.8}Se_8$ was the first reported Chevrel phase to exhibit high ORR activity. This material contained octahedral metal clusters which contributed to the electrical conductivity and ability to engage in electron transfer with other species.[48] This material exhibited current density approximately 30-40% less than that passed by Pt during ORR at an overpotential of 0.7 V. Further, the slopes of the Koutecky-Levich plots indicated that the $4e^-$ transfer product dominated. As it was shown that the stoichiometry of the metals significantly influenced the catalytic activity, this work was later expanded upon by other groups. For example, MoRuS and MoRuSe were probed for ORR activity in a 2.5 M H_2SO_4 medium. These materials showed stability to the corrosive electrolyte as well as to methanol, highlighting potential utility in acid electrolyte fuel cells and direct methanol fuel cells.[37] It is noted that these materials were still formulated by blending a 35 wt% mixture of the chalcogenide with carbon black; the ORR activity of the parent chalcogenides was not reported. The carbon-supported MoRuS catalysts showed the most promising ORR activity, with cathodic current onsetting at approximately 0.7 V vs RHE, and minimal diffusion limitations as evidenced by the mass transport region of the CV. Although MoRuSe exhibited similar onset potential, slower mass transport was observed.

In addition to ORR activity of metal chalcogenides being explored in acid electrolyte, electrocatalysis under neutral pH has also been probed. Falkowski, Surendranath, and coworkers applied the heazlewoodite phase of Ni_3S_2 as a robust ORR catalyst in pH 7 phosphate buffer.[10] This material

exhibited an ORR onset potential of 0.80 V vs RHE, as well as high stability to phosphate ions as well as durability against protolytic corrosion under reducing conditions. The increased covalency found in the transition metal sulfide bonds within this structure compared to that in metal oxides contributed this stability to corrosion. Use of a substitutionally labile first row transition metal prevented deactivation from phosphate binding. Excitingly, this material exhibited ~90% faradaic efficiency for O_2 reduction to water, selectivity which proved useful in a membrane-free formate fuel cell.[49] Detailed studies of this material revealed that the heazelwoodite Ni_3S_2 underwent a self-limiting oxidative phase conversion upon electrochemical polarization, such that the Ni stoichiometry was reduced.[50] Specifically, ~2 nm thick amorphous *a*-NiS layers formed on the catalyst surfaces and this layer was found to contribute the high ORR activity. This study showcased the effect of the metal coordination environment on catalytic activity, and how this environment can be tuned to modulate the adsorption energy of ORR-relevant species such as OH.

1.6 M-N_x ORR electrocatalysts

In the development of non-PGM ORR electrocatalysts, one structural motif that has been identified as a promising substitute for Pt is late first-row transition metal macrocycles, or MN_x centers. These structures were popularized after the 1964 report by Jasinski that detailed the high ORR activity of cobalt phthalocyanine complexes blended with electrically conductive acetylene black (**Figure 1-2**).[51] The ability

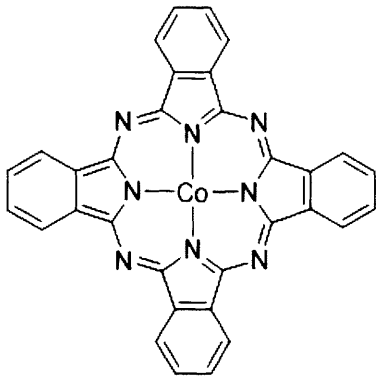

Figure 1-2. Co(II) phthalocyanine, the first transition metal macrocycle explored for ORR electrocatalysis.

for O_2 to chemisorb onto these M-N_x sites without degrading the material fueled extensive investigations of ORR on M-N_x-containing catalysts.[52–58] Such studies have revealed that ORR with transition metal macrocycles can proceed via both a $2e^-$ and $4e^-$ ORR pathway.[59] In these cases, whether the O—O bond is cleaved may depend on the interaction mode of O_2 on the metal site(s).[60–65] **Figure 1-3** shows the various proposed / observed configurations of O_2 on square planar metal sites. Although O_2 activation is typically proposed to occur directly on the metal centers, the electronic structure of the surrounding ligand, e.g.

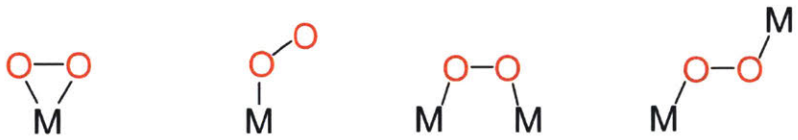

Figure 1-3. Possible configurations during O_2 activation by metal complexes (M = metal center): **a)** side-on, **b)** end-on, **c)** side-on bridging, and **d)** trans bridging.

substitution patterns on the porphyrin or phthalocyanine ring, can influence catalytic activity as well. Additionally, the chelating atom identity plays a role in the activity of such macrocycles, in that substituting N for other atoms such as S or O tends to diminish ORR activity.[59] Studies of transition metal phthalocyanines revealed that altering the ligand electronics can alter the ORR activity on certain metal centers due to changes in the energy of the metal orbitals that interact with O_2.[66,67] Of course, the energy of the metal-based orbitals also depends on the identity of the metal itself. Regardless of the mode of interaction between O_2 and the metal centers, the metal-centered d_{z^2} orbital typically participates in this interaction. Thus, metals that have appropriate energetic orbital overlap with O_2 and can accommodate electron donation into the d_{z^2} orbital by O_2 to form the metal—O_2 interaction are well suited to activating O_2. Additionally, metals that can facilitate back-donation into the O_2 π^* orbitals will lower the O_2 bond order and facilitate cleavage of the O—O bond, thereby promoting H_2O production over H_2O_2 production.[66]

Unsurprisingly, given the similarities with heme-based systems, it has been found that Fe-based phthalocyanines exhibit the highest ORR activity, an observation which has been the focus of many studies.[52,59,68–72] Although active for ORR, transition metal macrocyclic catalysts must typically be blended with an electrically conductive host such as carbon to facilitate electron transfer. Another route for introducing electrical conductivity into such complexes as well as enhancing stability towards electrolytes has involved high-temperature treatment of the materials.[54,56,58] Thermal treatment indeed increased the conductivity and stability of the materials, but introduced new challenges in maintaining synthetic control over structure formation, identifying the catalytic active sites, and establishing structure–function relationships useful for catalyst optimization and mechanistic understanding. Thus, pursuit of active, intrinsically conductive, and chemically and electrochemically stable ORR electrocatalysts possessing well-defined and tunable active sites has continued.

1.7 Metal-organic framework-based ORR electrocatalysts

One class of materials that could answer these challenges is metal-organic frameworks (MOFs). These materials are compelling choices for electrocatalytic applications because their high surface area maximizes active site density, and their tunable chemical structure affords tailor-made microenvironments for controllable reaction conditions within the pores. Despite their promising features, MOFs have rarely been used for electrocatalytic applications because they are typically electrical insulators due to their paucity of low energy charge transport pathways and / or mobile charge carriers.[73] Several avenues have been pursued to overcome the issue of insulation within MOFs, including pyrolysis and doping with conductive additives such as graphene oxide or metal oxides.[7,59,74–84] Although such approaches can afford highly active and robust catalysts, incorporation of additives may block access to active sites, counteracting the benefits of having a high surface area material that can provide high active site density. Pyrolysis of MOFs is commonly in excess of 600 °C, an energy-intensive process that destroys the crystallinity of the MOFs, affording amorphous carbon hosts. These relatively poorly defined materials do not lend themselves

to facile mechanistic studies; the inhomogeneous dispersion and irregular orientation of the heteroatoms throughout the MOF matrix engenders structural ambiguity that makes identification, experimental probing, and computational modeling of active sites difficult.

Recently, synthetic advances have given rise to conductive MOFs, some of which exhibit encouraging properties as electrocatalysts for other reactions including CO_2 reduction, hydrogen evolution, oxygen evolution, and ethanol oxidation.[19,74,85–88] In addition to promising reports of electrically conductive MOFs facilitating other energy conversion reactions, several works have reported successful ORR catalysis with neat MOFs. An early report of MOF-catalyzed ORR utilized a non-conductive MOF, copper(II)-2,2′-bipyridine-benzene-1,3,5-tricarboxylate (Cu-bipy-BTC).[89] The instability of the related structure, Cu-BTC, to water prompted exploration of this modified, water-stable analogue in which 2-2′-bypiridine acted as an auxiliary ligand with stabilizing binding affinity to the Cu^{2+} centers. When dropcast onto a glassy carbon electrode, Cu-bipy-BTC showed cathodic current in the presence of O_2 between 0 and −0.2 V vs Ag/AgCl in pH 6.0 phosphate buffer. In the cyclic voltammograms, diffusion-limiting current reached a maximum of ca. −35 μA, possibly due to slow electron transfer kinetics rising from low conductivity of the MOF. Mechanistic studies on Cu-bipy-BTC may reveal interesting similarities with multicopper oxidases that are known to reduce O_2.[7]

In addition to Cu-based enzymes inspiring the exploration of ORR with structurally similar MOFs, heme-like motifs have also been targeted in MOFs for ORR electrocatalysis. The MOF PCN-223-Fe ($Zr_6O_4(OH)_4$(Fe(III)-(TCPP)$_3$ which features Zr_6 oxo clusters linked with ferric porphyrin centers, electrochemically reduced O_2 with a maximum of 94% faradaic efficiency for H_2O production when acetic acid was used as the proton source.[90] Although these results showcased the potential for heme-like structures to be installed in MOFs and used for electrocatalysis, the applicability of this specific example is unclear. A nonaqueous electrolyte, $LiClO_4$ in DMF and acetic or tricholoroacetic acid, was utilized so the ORR activity of the MOF in an industrial setup wherein the protons would have different activities is

uncertain. Additionally, the free-base version of this MOF also showed nearly identical ORR activity compared to the Fe-MOF, so the source of the ORR activity and the specific role of Fe(III) in this system remains unclear.

Another example of a MOF featuring a porphyrinic metalloligand targeted at reducing O_2 was reported by Lions, Fateeva, and coworkers.[91] The MOF Al-$(OH)_2$-(H_2TCPP) (H_2TCPP = tetrakis(4-carboxyphenyl)porphyrin) was reacted with Co(II) acetate to produce a Co-porphyrin MOF (Co-Al-PMOF). Within the structure, the porphyrins were aligned in a face-on fashion, with Co—Co distances of 6.6 Å. This MOF exhibited ORR activity with an onset of ca. 0.7 V vs RHE in 0.1 M H_2SO_4 electrolyte, concomitant with the $Co^{III/II}$ redox. However, the metalloligand CoTCPP alone passed more cathodic current than the porphyrinic MOF, indicating that incorporation of the porphyrin into the framework can hinder the catalytic competence of the active site. Another Co-MOF, [{$Co_3(\mu_3$-OH)$(BTB)_2(BPE)_2$}{$Co_{0.5}$N-(C_5H_5)}] (BTB = 1,3,5-tris(4-carboxyphenyl)benzene and BPE = 1,2-bis(4-pyridyl)ethane), which featured monomeric and trimeric Co clusters, was shown to have semiconducting properties with $\sigma = 5 \cdot 10^{-4}$ S·cm^{-1}, and catalytic activity for ORR in 0.1 M KOH.[92] ORR with the Co-MOF occurred at a notable onset potential of 0.81 V vs RHE, and retention of 80% of the cathodic current density over 25 h. It was observed that when the working electrode was not rotated, the signature catalytic wave was not present in the cyclic voltammograms under O_2, but rather only capacitive current remained at higher overpotentials. This could be indicative of slow diffusion, or reactivity of the reduced species.[93] Additionally, although the MOF did indeed show ORR electrocatalytic activity at higher electrode rotation rates, quantification of the reduction products remained uncertain due to the fact that the Pt ring during rotating ring disk electrode studies was only polarized at 0.45 V vs RHE, 0.25 V more cathodic than the thermodynamic oxidation potential of H_2O_2 and therefore insufficient to electrochemically detect H_2O_2 under these conditions.[13] Nevertheless, the semiconducting behavior combined with the crystallographically well-defined sites of this Co-MOF contributed promising electrical properties that could be applied to electrocatalysis. Additionally, the highly

ordered system can enable probing and modeling structure-function relationships and in turn allow a deeper understanding of the catalytic pathways and direct optimization thereof.

1.8 Outlook

The above examples showcase the diverse range of MOF structures and how the many components comprising these structures may be capitalized upon for energy conversion applications. In reviewing heterogeneous catalysts reported for ORR thus far, the benefits and challenges thereof have been highlighted. Specifically, heterogenization of such materials enhances catalyst stability, minimizes mass transport issues, and introduces the opportunity to either intimately interface the active sites with the conductive substrate or directly impose electrical conductivity in active species themselves. Despite these advantages, current heterogeneous catalysts suffer from lack of structural definition. This challenge makes identification of active sites, elucidation of catalytic mechanisms, and subsequent directed catalyst optimization difficult when equipped with analytical methods typically suited for homogeneous molecular species. The crystallographic definition inherent to MOFs in the context of heterogeneous catalysis is highlighted here as an advantage; a full arsenal of analytical tools that are typically restricted to homogenous systems can be used in ordered MOF structures, which in turn can provide insight into structure-catalytic function relationships. The work herein aims to enhance the depth of understanding in one particular system used for heterogeneous electrocatalysis of the ORR. In doing so, a roadmap is presented for fully taking advantage of the tools that can be used to probe the mechanisms of electrocatalysis with MOFs, which are typically limited to homogeneous molecular systems. The breadth of applicability of MOFs in the energy field will subsequently be explored by applying MOFs as solid electrolytes for battery applications.

Chapter 2

Electrochemical Oxygen Reduction Catalyzed by Ni_3(hexaiminotriphenylene)$_2$

Portions of this chapter previously appeared in Miner, E. M.; Fukushima, T.; Sheberla, D.; Sun, L.; Surendranath, Y.; Dincă, M. *Nature Commun.* **2016**, *7*, 10942–10948 and are reproduced here with permission from Springer Nature.

2.1 Introduction

The development of heterogeneous oxygen reduction reaction (ORR) electrocatalysts for implementation into fuel cell and electrolyzer cathodes is a major research thrust in the arena of renewable fuel development. Achieving desired architectural and electronic properties of such catalysts remains difficult, however, because several variables must be optimized simultaneously, requiring synthetic tunability that is rarely available in the solid state. Desirable characteristics of an ORR electrocatalyst include: high active site density, reproducible synthesis and catalytic activity, stability in the electrolyte and in oxygen and peroxide, and low overpotential relative to the thermodynamic $4e^-$ oxygen-to-water reduction potential of 1.23 V (versus the reversible hydrogen electrode, RHE). One structural motif that has proven successful in catalyzing ORR with high activity and physical robustness is the M-N_x unit, where M = a non-platinum group metal (e.g. Fe, Co, Ni, Cu) chelated in a nitrogenous environment. These structures were popularized after the 1964 report by Jasinski which detailed the high ORR activity of cobalt phthalocyanine complexes blended with electrically conductive acetylene black.[51] The ability for oxygen to chemisorb onto these M-N_x sites without degrading the material fueled extensive investigations of ORR on M-N_x containing catalysts.[53–56] Though active towards ORR, M-N_x complexes have shown inconsistent stability in various electrolytes, motivating high-temperature treatment of the materials to enhance catalyst longevity and electrical conductivity.[54,56] Thermal treatment indeed increased the stability of the materials, but introduced new challenges in maintaining synthetic control over structure formation, identifying the catalytic active sites, and establishing structure-function relationships useful for catalyst optimization and mechanistic understanding. Thus, the search for active, intrinsically conductive, and chemically and electrochemically stable ORR electrocatalysts possessing well-defined and tunable active sites has continued.

One class of materials that could answer these challenges is metal-organic frameworks (MOFs). These materials are compelling choices for electrocatalytic applications because their high surface area maximizes active site density, and their tunable chemical structure affords tailor-made microenvironments

for controllable reaction conditions within the pores. Despite their promising features, MOFs have rarely been used for electrocatalytic applications because they are typically electrical insulators.[79–81,94–96] Recently, synthetic advances have given rise to conductive MOFs, some of which exhibit encouraging properties as electrocatalysts.[97–101]

Here we introduce $Ni_3(HITP)_2$, a conductive two-dimensionally layered material structurally reminiscent of the long-studied M-N_x ORR electrocatalysts (**Figure 2-1**),[102] as a representative of a new class of highly ordered ORR electrocatalysts exhibiting ORR activity and electrical conductivity (σ = 40 $S \cdot cm^{-1}$)[102] with no post-synthetic treatment or modification. In addition to possessing ORR activity

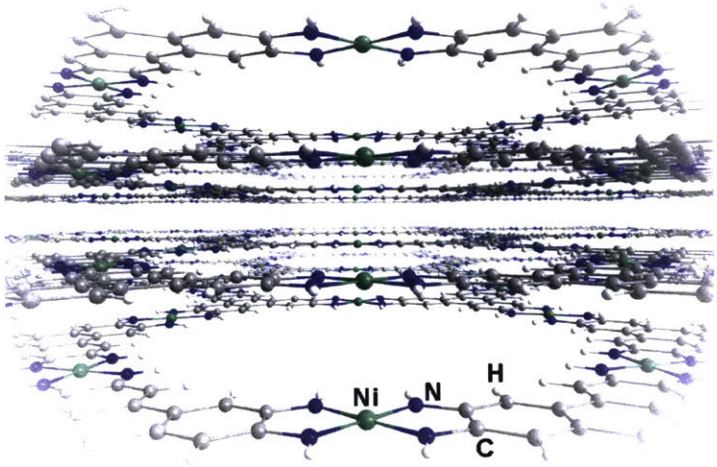

Figure 2-1. Perspective view of the two-dimensional layered structure of $Ni_3(HITP)_2$.

competitive with the most active non-Pt group metal (non-PGM) electrocatalysts to date, $Ni_3(HITP)_2$ retained 88% of its current density and underwent no visible morphological degradation during prolonged electrocatalysis. This study highlights conductive MOFs as a powerful platform for the development of tunable, designer electrocatalysts. It is noted that MOFs have been used as scaffolds for ORR electrocatalysts formed from high temperature (> 600 °C) pyrolysis[103–122] as well as incorporated into composites containing graphene oxide and porphyrin additives.[77,96] Whereas such materials indeed

exhibited competitive ORR activity, the pyrolysis involved in their preparation eliminated the crystallinity and synthetic control inherent to MOFs. Our aim herein is to introduce a multi-faceted handle on imposing in a controlled manner structural, chemical, and electronic properties upon such materials for reaction-targeted, MOF-based electrocatalyst design.

2.2 Results and discussion

$Ni_3(HITP)_2$ can be grown solvothermally as a thin film on a variety of electrode surfaces using synthetic conditions mimicking those employed for the synthesis of bulk material.[102] Glassy carbon (GC) disk electrodes (5 mm diameter) served as the working electrodes for all investigations described herein unless otherwise noted, and all potentials were referenced to the reversible hydrogen electrode (RHE). Deposition of $Ni_3(HITP)_2$ onto the GC electrodes typically afforded loadings of approximately 5 μg of MOF. The loadings were determined precisely in each case by atomic absorption spectroscopy (AAS) and verified by inductively coupled plasma-mass spectrometric (ICP-MS) measurements. The thickness of the film was analyzed by atomic force microscopy (AFM), conducted by L. Sun. $Ni_3(HITP)_2$ films grown on GC electrodes had a thickness of approximately 120 nm, whereas films grown on indium tin oxide (ITO) exhibited a similar morphology with a thickness of approximately 300 nm (**Figure 2-2**). Direct adhesion of the $Ni_3(HITP)_2$ film onto the electrode surface eliminated the need for binders or conductive additives that may block access to active sites by pore filling. This direct contact between the parent material and the electrode allowed for investigation of the inherent electrocatalytic behavior of pure $Ni_3(HITP)_2$.

Cyclic voltammograms of $Ni_3(HITP)_2$ thin films on glassy carbon rotating disk electrodes (RDEs) recorded in the absence of O_2 revealed a significant double layer capacitance that increased with increasing scan rate (**Figure 2-3**), reflecting the high surface area of the modified electrodes.[20] Indeed, $Ni_3(HITP)_2$ exhibited a Brunauer-Emmett-Teller (BET) specific surface area (SSA) of 629.9±0.7 $m^2 \cdot g^{-1}$, as calculated from its nitrogen adsorption isotherm measured by D. Sheberla (**Figure 2-4, Table 2-1**).

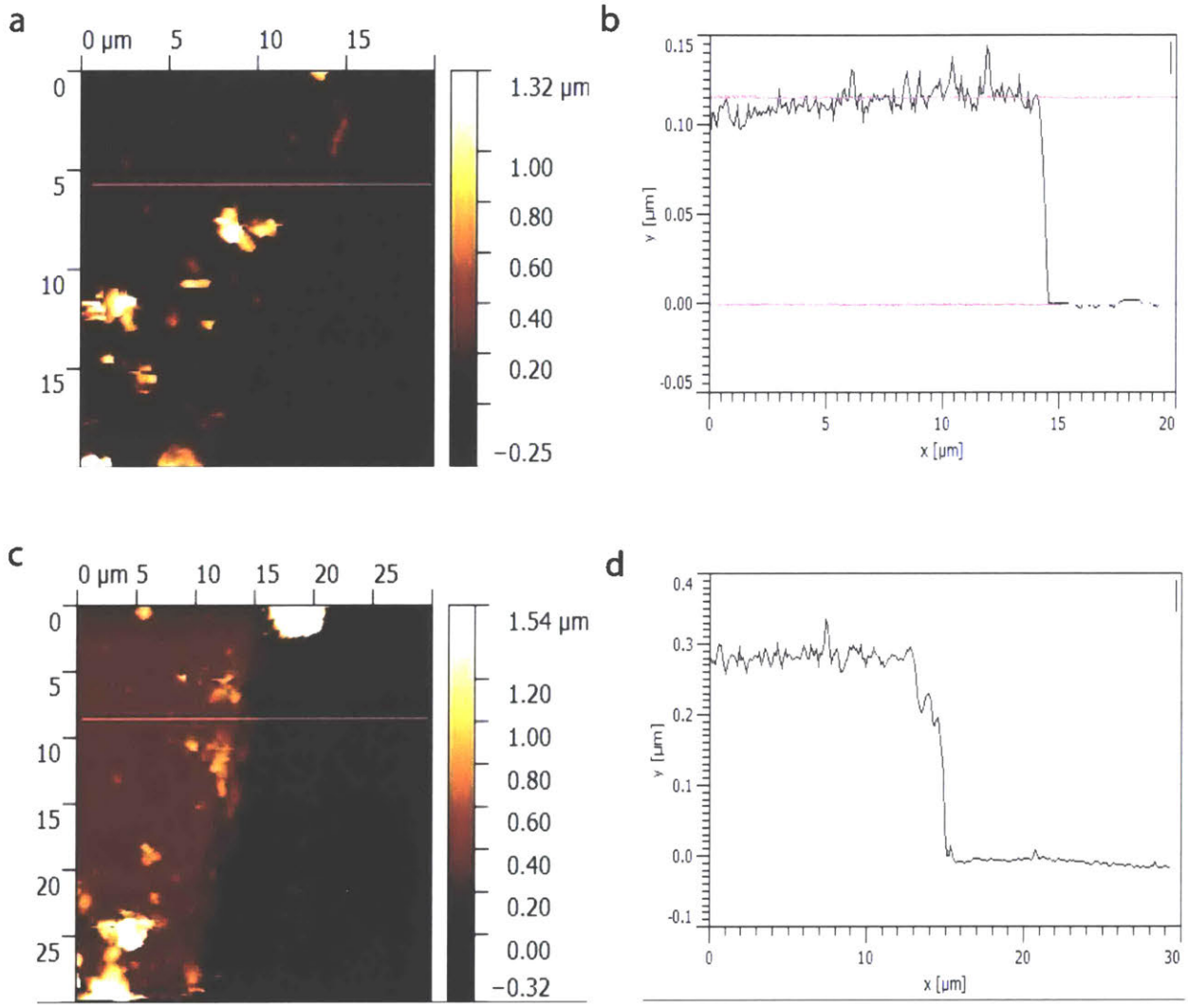

Figure 2-2. a) Thickness / roughness and **b)** height profile of $Ni_3(HITP)_2$ film on a GC electrode, and **c)** thickness / roughness and **d)** height profile of $Ni_3(HITP)_2$ film on an ITO electrode as measured by atomic force microscopy.

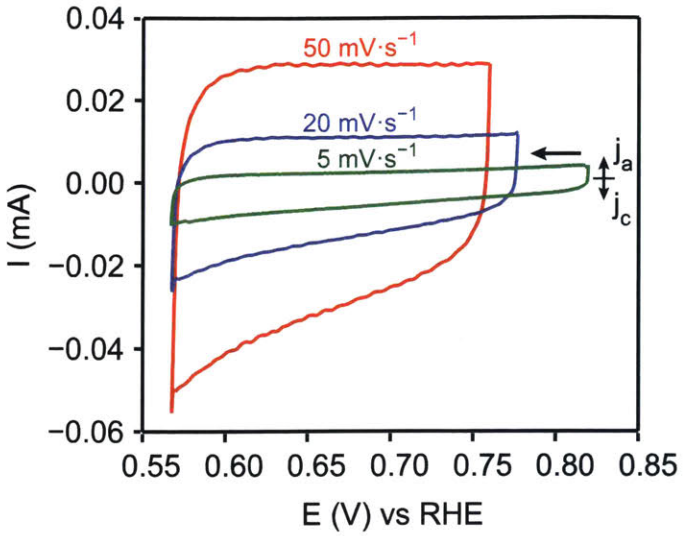

Figure 2-3. Double layer capacitance polarization curves of $Ni_3(HITP)_2$ under N_2 atmosphere with varying CV scan rates. The initial potential shift among the three scans is a result of the working electrode open circuit potential shifting during electrolysis.

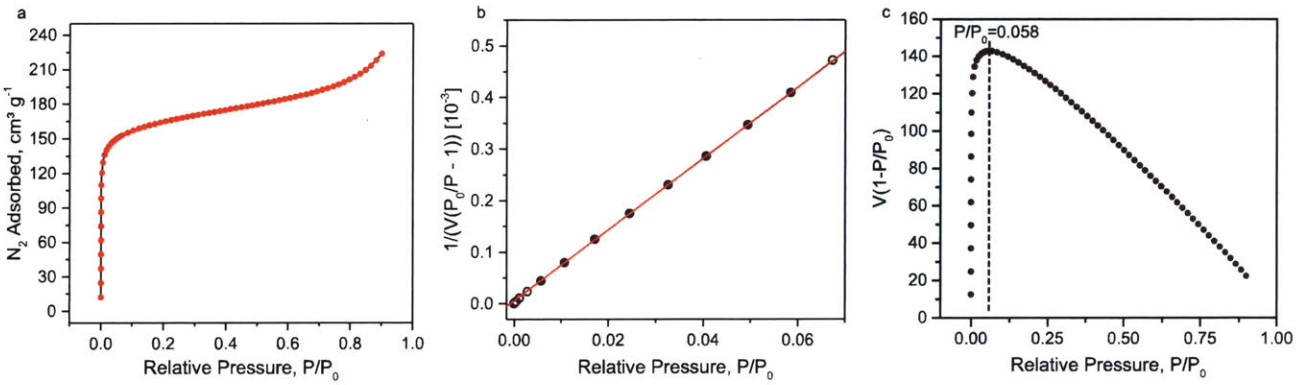

Figure 2-4. Nitrogen adsorption isotherm for $Ni_3(HITP)_2$ powder at 77 K. **a**) adsorption isotherm, **b**) BET linear fit, **c**) $V(1\text{-}P/P_0)$ vs. P/P_0 plot used to select upper limit for BET linear fit. Range selection and consistency checks for BET fit were done as suggested by Rouquerol et al.[1]

Table 2-1. Relevant data for BET fit of the N_2 adsorption isotherm.

BET Surface Area	629.9 ± 0.7 m^2 g^{-1}
C	1253
Correlation Coefficient	0.9999962
Fit range (P/P_0)	0.0057-0.0585 (8 points)
V_m	144.7 cm^3 g^{-1} STP
P/P_0 @ V_m	0.0282
$1/(\sqrt{C}+1)$	0.0275

Under O_2 atmosphere, the material reduced oxygen with an onset potential ($j = -50$ μA·cm^{-2}) of 0.82 V in a 0.10 M aqueous solution of KOH (pH = 13.0, **Figure 2-5**), as observed in collaboration with T. Fukushima. The measured ORR onset potential was competitive with the most active non-PGM ORR electrocatalysts reported thus far[123] and sat at an overpotential of 0.18 V relative to Pt (E_{onset} = 1.00 V).

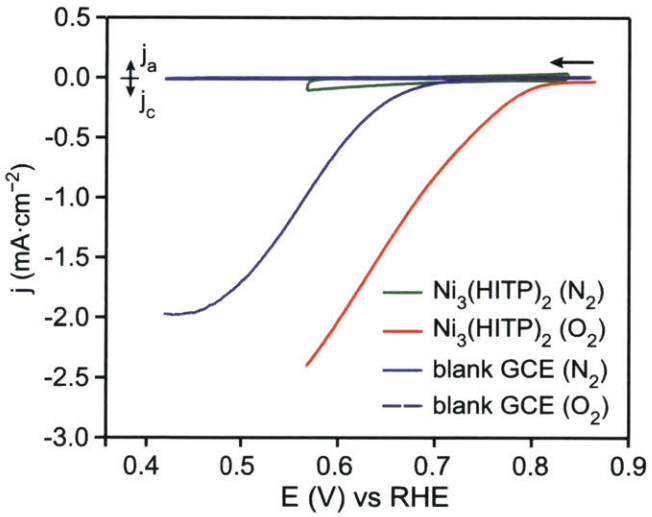

Figure 2-5. Polarization curves of $Ni_3(HITP)_2$ under N_2 (green) versus O_2 atmosphere (red) as well as of the blank GC electrode under N_2 versus O_2 atmosphere (blue and purple respectively). Scan rate = 5 mV·s^{-1}, rotation rate = 2000 rpm, electrolyte = 0.10 M aqueous KOH, counter electrode = Pt mesh, reference electrode = Hg/HgO (1.00 M KOH).

Notably, cyclic voltammetry of the film on indium tin oxide (ITO) electrodes showed the same ORR activity as the films on the glassy carbon electrodes (**Figure 2-6**), verifying that the MOF did not simply enhance the ORR activity of the glassy carbon electrode but rather acted as a stand-alone ORR electrocatalyst regardless of the substrate. The high surface area and porosity inherent to $Ni_3(HITP)_2$ may

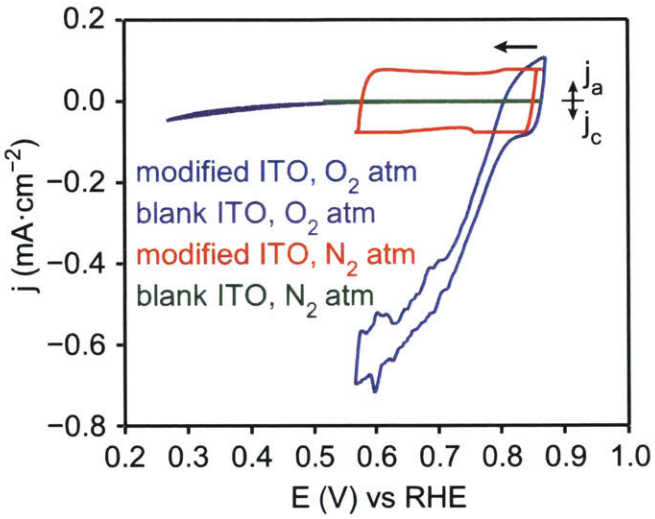

Figure 2-6. Cyclic voltammograms of $Ni_3(HITP)_2$-modified and blank indium tin oxide (ITO) electrodes under N_2 and O_2 atmosphere. Fluctuations in the polarization curve of the $Ni_3(HITP)_2$-modified ITO (blue trace) are due to interference from sparging O_2 gas during data collection. The hysteresis observed in the $Ni_3(HITP)_2$ polarization curve under O_2 atmosphere is ascribed to pseudocapacitance.

increase the density of and facilitate easy access to the catalytic active sites on $Ni_3(HITP)_2$, contributing to the notable ORR activity. Given that this high ORR activity was observed after the film purification procedure which involved heating the modified electrode in methanol at 65 °C for 20 hours, $Ni_3(HITP)_2$ and related materials may be strong candidates for implementation into direct methanol fuel cells (DMFCs) where methanol tolerance of the anodic and cathodic catalysts is a necessity.[124] High stability in the presence

of methanol / related fuel crossover products is not observed for Pt-based electrocatalysts, a major hurdle currently slowing DMFC development.[125]

Steady state potentiostatic measurements at E = 0.77 V showed that 88% of the initial current density was retained over 8 hours (**Figure 2-7**), in-line with other non-PGM ORR catalysts.[56,126–130] Cyclic voltammetry of the modified electrode after the durability study showed no shift in the diffusion-limited region of the polarization curve, indicating that any alterations to the material during electrocatalysis were not significant enough to decrease the mass transport properties of the $Ni_3(HITP)_2$ film (**Figure 2-8**). Moreover, cyclic voltammetry of the electrolyte after these 8 hours, using a fresh unmodified GC electrode, indicated no leaching from the $Ni_3(HITP)_2$ films, evidencing the heterogeneous nature of the catalyst. Additionally, ICP-MS and AAS analyses of films prior to and post-electrolysis indicated the same quantity of Ni, suggesting that no part of the catalyst, homogeneous or heterogeneous, was lost from the films during catalysis (**Tables 2-2 and 2-3**).

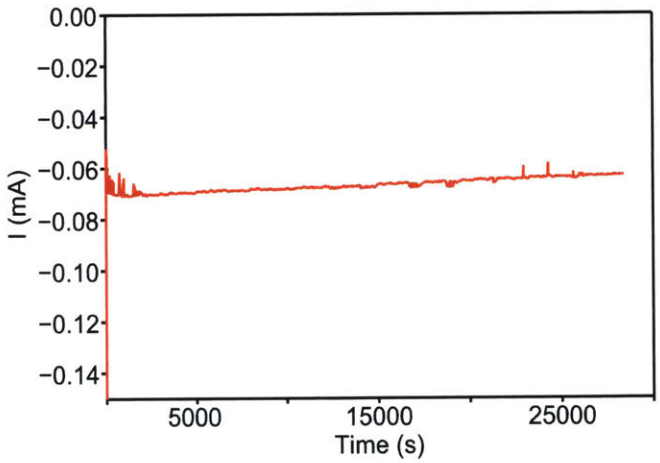

Figure 2-7. Potentiostatic stability test of $Ni_3(HITP)_2$ electrocatalyzing ORR at E = 0.767 V versus RHE over 8 hours. It is noted that the periodic current spikes were concomitant with spikes in the potential applied to the disk, presumably due to some disturbance in the contact of the rotator to the electrode shaft. The slight fluctuations in potential never exceeded the potential range in which $Ni_3(HITP)_2$ is stable, so potential changes likely did not influence the catalyst stability in this experiment.

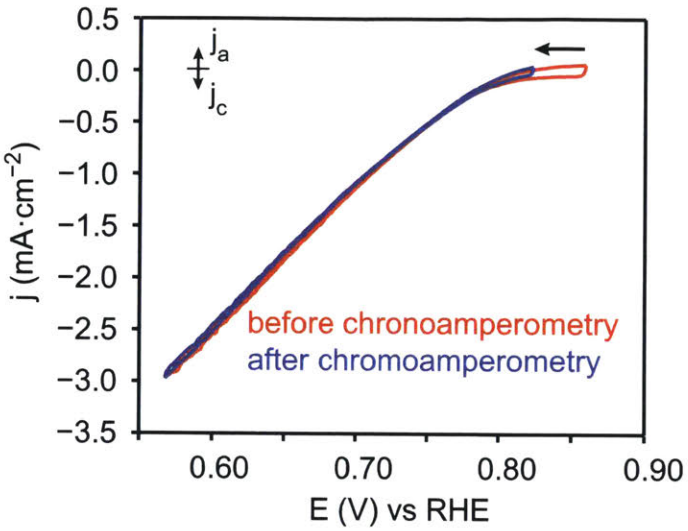

Figure 2-8. Cyclic voltammograms of $Ni_3(HITP)_2$ before and after the potentiostatic stability test shown in Supplementary Figure 5, under O_2 atmosphere.

Table 2-2. Calculated number of nickel sites from ICP-MS quantification of nickel sites on glassy carbon electrodes.

Sample	**$[Ni]_{avg}$ (ppb)**	**SD**	**# Ni sites on electrode**	**Catalyst loading (μg $Ni_3(HITP)_2$)**	**mol $Ni_3(HITP)_2$**
RRDE	58.393	3.562	$1.198 \cdot 10^{16}$	5.311	$6.633 \cdot 10^{-9}$
unused	47.147	3.006	$9.675 \cdot 10^{15}$	4.288	$5.355 \cdot 10^{-9}$
unused	55.053	5.043	$1.130 \cdot 10^{15}$	5.008	$6.253 \cdot 10^{-9}$

Table 2-3. AAS quantification of nickel sites on glassy carbon electrodes

Sample	**$[Ni]_{avg}$ (ppb)**	**SD**	**%RSD**	**# Ni sites on electrode**	**Catalyst loading (μg $Ni_3(HITP)_2$)**	**mol $Ni_3(HITP)_2$**
RRDE	61.92	0.570	0.921	$1.26199 \cdot 10^{16}$	5.6321	$7.03316 \cdot 10^{-9}$
unused	51.73	0.414	0.801	$1.06151 \cdot 10^{16}$	4.70523	$5.8757 \cdot 10^{-9}$
unused	59.47	0.831	1.397	$1.22034 \cdot 10^{16}$	5.40924	$6.75488 \cdot 10^{-9}$

Spectroscopic, microscopic and diffractometric techniques enabled analysis of the film before and after ORR catalysis. X-ray photoelectron spectroscopy (XPS) of catalyst films before and after catalysis revealed an increase in binding energy of the Ni_{2p} envelope region (850-885 eV) by +1.0 eV (**Figure 2-9**). Also visible by XPS was a shoulder peak that was present in the N_{1s} region prior to ORR (399 eV) which disappeared after catalysis (**Figure 2-10**). The +1 eV shift in the Ni_{2p} XPS after ORR catalysis could be indicative of a Ni—O interaction,[131,132] or alternatively a strengthening of the ligand field as electron density

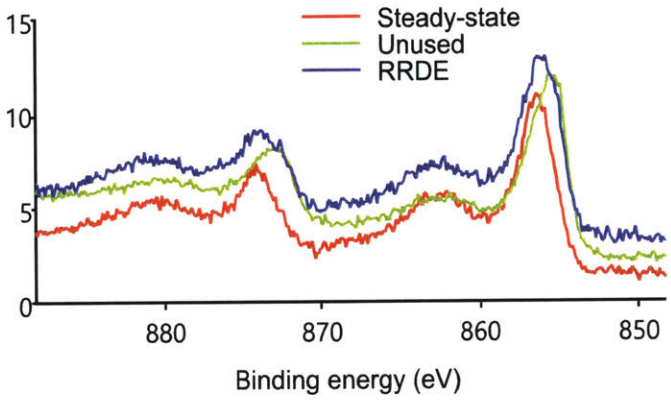

Figure 2-9. X-ray photoelectron spectrum of $Ni_3(HITP)_2$ film on GCE Ni_{2p} envelope region. Both unused (before ORR) and used (after ORR, labeled 'RRDE' and 'steady-state') samples are shown here.

around the imine decreases. The loss of asymmetry in the N_{1s} region of the XPS after catalysis was consistent with an alteration of the ligand field during ORR. Importantly, though the catalyst may undergo minor structural rearrangement during ORR, the high activity was largely retained over extended steady state measurements, i.e. neither access to the active sites nor the integrity of the active sites themselves was severely compromised during prolonged electrocatalysis. The structural robustness was supported by Raman spectroscopy conducted on the unused film, the film after submersion in the 0.10 M KOH

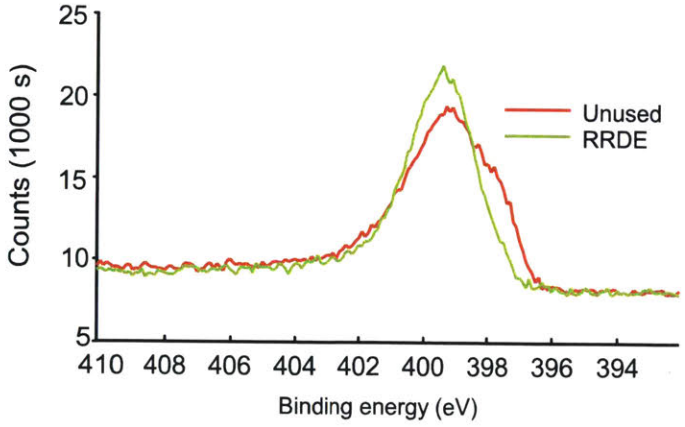

Figure 2-10. X-ray photoelectron spectrum of $Ni_3(HITP)_2$ film on GCE N_{1s} envelope region. Both unused (before ORR) and used (after ORR, labeled 'RRDE') samples are shown here.

electrolyte, and the film after electrochemical cycling under either N_2 or O_2. There were no missing or additional Raman bands for any of the altered films compared to the spectrum of the unused film (**Figure 2-11**), indicating that the polarizability of the $Ni_3(HITP)_2$ bonds was unaffected by catalysis. Additional evidence supporting the stability of the film was observed in scanning electron micrographs (SEMs) of the film taken before and after ORR catalysis (**Figure 2-12**). No perturbations in the morphology of the film were observed upon electrochemical cycling under O_2. Grazing incidence X-ray diffraction of the $Ni_3(HITP)_2$ film before and after ORR catalysis showed retention of the long-range order in the *ab* plane of $Ni_3(HITP)_2$ during ORR, further highlighting the structural stability of this catalyst during electrochemical cycling under O_2 (**Figure 2-13**). The stability of the catalyst in aqueous media is industrially advantageous given the lower cost of water-based electrolytes.

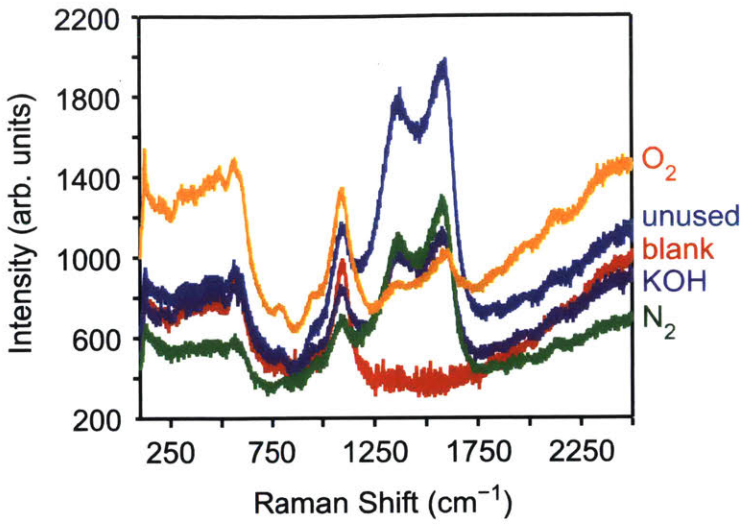

Figure 2-11. Raman spectra of $Ni_3(HITP)_2$ on ITO electrodes. The blank ITO electrode (blank, red), the unused $Ni_3(HITP)_2$-modified electrode (unused, blue), the $Ni_3(HITP)_2$-modified electrode submerged in the 0.10 M KOH electrolyte for 1 hour (KOH, purple), the $Ni_3(HITP)_2$-modified electrode cycled exclusively under N_2 atmosphere (N_2, green), and the $Ni_3(HITP)_2$-modified electrode cycled exclusively under O_2 atmosphere (O_2, orange) are shown.

Using standard rotating ring-disk electrode experiments (**Figure 2-14**) and assuming that catalytically competent sites within $Ni_3(HITP)_2$ were distributed homogeneously throughout the film and not just on the surface, lower-limit turnover frequencies (TOFs), determined by AAS, were found to be 0.042 electrons·$[Ni_3(HITP)_2]^{-1}$·s^{-1} and 0.052 electrons·$[Ni_3(HITP)_2]^{-1}$·s^{-1} for H_2O_2 and H_2O production,respectively, at E = 0.79 V. Quantifying the Ni content in the same films by ICP-MS gave lower-limit TOF values of 0.046 electrons·$[Ni_3(HITP)_2]^{-1}$·s^{-1} and 0.056 electrons·$[Ni_3(HITP)_2]^{-1}$·s^{-1} for H_2O_2 and H_2O production, respectively, also at E = 0.79 V (**Tables 2-4 to 2-7**). The TOF values for H_2O_2 and H_2O production increased by one order of magnitude to 0.491 electrons·$[Ni_3(HITP)_2]^{-1}$·s^{-1} and 0.466 electrons·$[Ni_3(HITP)_2]^{-1}$·s^{-1}, respectively, at 0.67 V. Notably, the intrinsic ORR turnover frequencies for $Ni_3(HITP)_2$ could exceed the values reported here because the Ni quantification methods do not distinguish

exclusively electroactive Ni sites; if some percent of the potentially active sites are not catalytically competent because of mass transport limitations within the films, the ORR current-to-active-site ratio would increase, consequently increasing the TOF.

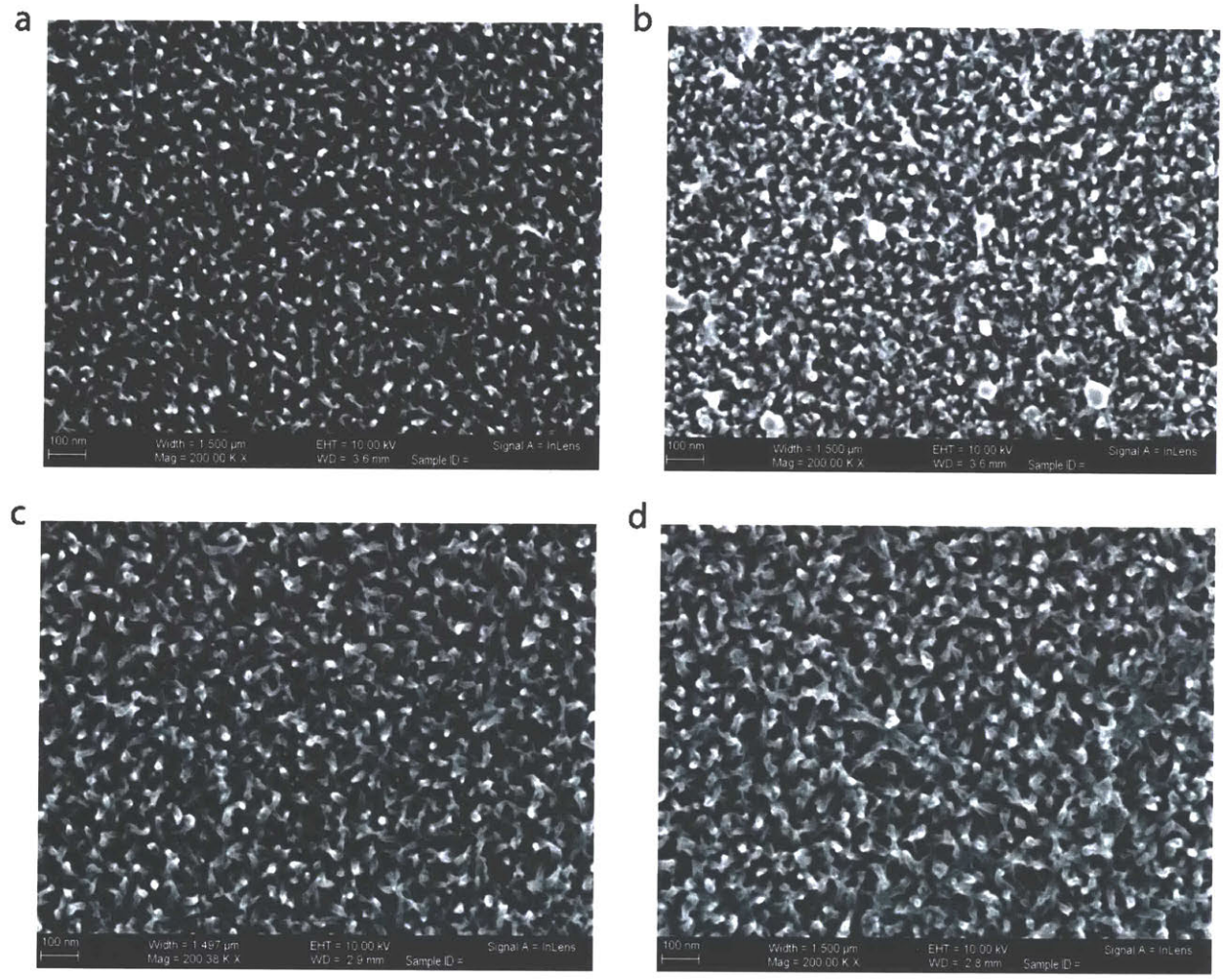

Figure 2-12. Scanning electron micrographs of $Ni_3(HITP)_2$ **a-b)** on GC electrodes and **c-d)** on ITO electrodes **a, c)** before ORR catalysis versus **b, d)** after ORR catalysis.

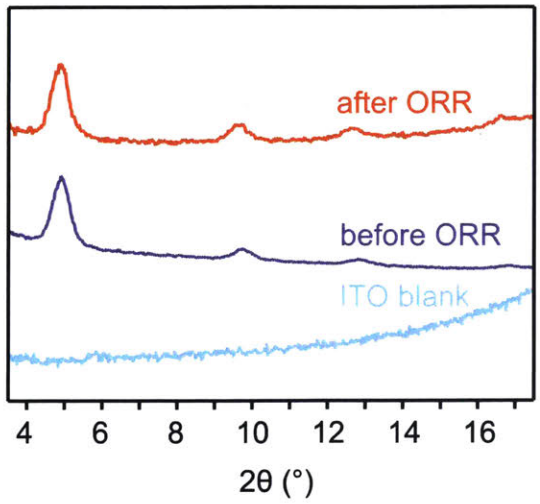

Figure 2-13. Grazing incidence X-ray diffraction patterns of unmodified ITO (teal), $Ni_3(HITP)_2$ film on ITO before ORR (purple), and $Ni_3(HITP)_2$ film on ITO after ORR (orange).

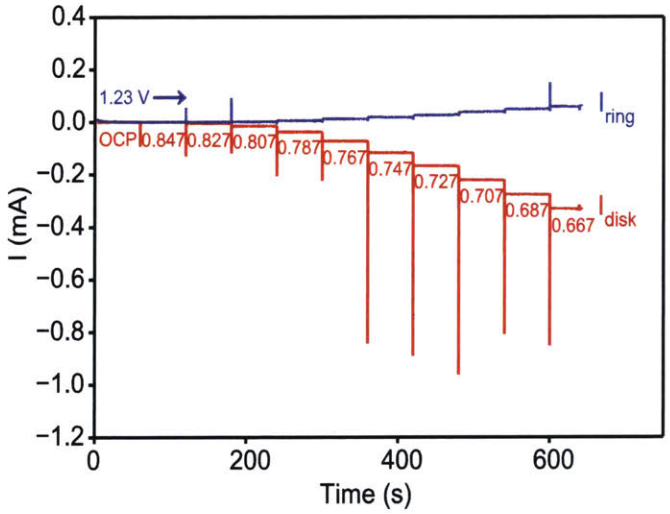

Figure 2-14. Potentiostatic rotating ring disk electrode measurement for determination of $2e^-$ and $4e^-$ ORR TOF as catalyzed by $Ni_3(HITP)_2$. Disk potentials (red) are referenced to RHE. A constant potential of 1.23 V versus RHE was applied to the platinum ring (blue).

Table 2-4. $2e^-$ ORR TOF calculations using nickel loading determined by ICP-MS.

E (V) vs RHE	background and collection efficiency corrected I_{ring} (A)	$2e^-$ ORR TOF (electrons·s^{-1})	$2e^-$ ORR TOF (electrons·$[Ni_3(HITP)_2]^{-1}\cdot s^{-1}$)
0.807	$3.496\cdot10^{-6}$	$2.182\cdot10^{13}$	0.00596
0.787	$2.674\cdot10^{-5}$	$1.669\cdot10^{14}$	0.0456
0.767	$5.456\cdot10^{-5}$	$3.405\cdot10^{14}$	0.0930
0.747	$8.367\cdot10^{-5}$	$5.222\cdot10^{14}$	0.143
0.727	0.000136	$8.498\cdot10^{14}$	0.232
0.707	0.000192	$1.198\cdot10^{14}$	0.327
0.687	0.000242	$1.508\cdot10^{14}$	0.412
0.667	0.000288	$1.798\cdot10^{14}$	0.491

Table 2-5. $4e^-$ ORR TOF calculations using nickel loading determined by ICP-MS.

E (V) vs RHE	I_{disk} – corrected I_{ring} (A)	$4e^-$ ORR TOF (electrons·s^{-1})	$4e^-$ ORR TOF (electrons·$[Ni_3(HITP)_2]^{-1}\cdot s^{-1}$)
0.807	$1.539\cdot10^{-5}$	$9.608\cdot10^{13}$	0.0262
0.787	$3.309\cdot10^{-5}$	$2.066\cdot10^{14}$	0.0564
0.767	$6.288\cdot10^{-5}$	$3.924\cdot10^{14}$	0.107
0.747	0.000101	$6.329\cdot10^{14}$	0.173
0.727	0.000141	$8.800\cdot10^{14}$	0.240
0.707	0.000184	$1.148\cdot10^{15}$	0.313
0.687	0.000229	$1.430\cdot10^{15}$	0.390
0.667	0.000273	$1.706\cdot10^{15}$	0.466

Table 2-6. $2e^-$ ORR TOF calculations using nickel loading determined by AAS.

E (V) vs RHE	background and collection efficiency corrected I_{ring} (A)	$2e^-$ ORR TOF (electrons·s^{-1})	$2e^-$ ORR TOF (electrons·$[Ni_3(HITP)_2]^{-1}\cdot s^{-1}$)
0.807	$3.496\cdot10^{-6}$	$2.182\cdot10^{13}$	0.0554
0.787	$2.674\cdot10^{-5}$	$1.669\cdot10^{14}$	0.0424
0.767	$5.456\cdot10^{-5}$	$3.405\cdot10^{14}$	0.0865
0.747	$8.367\cdot10^{-5}$	$5.222\cdot10^{14}$	0.133
0.727	0.000136	$8.498\cdot10^{14}$	0.216
0.707	0.000192	$1.198\cdot10^{15}$	0.304
0.687	0.000242	$1.508\cdot10^{15}$	0.383
0.667	0.000288	$1.798\cdot10^{15}$	0.457

Table 2-7. $4e^-$ ORR TOF calculations using nickel loading determined by AAS

E (V) vs RHE	I_{disk} – corrected I_{ring} (A)	$4e^-$ ORR TOF (electrons·s^{-1})	$4e^-$ ORR TOF electrons·$[Ni_3(HITP)_2]^{-1}\cdot s^{-1}$)
0.807	$1.539\cdot10^{-5}$	$9.608\cdot10^{13}$	0.0244
0.787	$3.310\cdot10^{-5}$	$2.066\cdot10^{14}$	0.0525
0.767	$6.288\cdot10^{-5}$	$3.924\cdot10^{14}$	0.0997
0.747	0.000101	$6.329\cdot10^{14}$	0.161
0.727	0.000141	$8.780\cdot10^{14}$	0.223
0.707	0.000184	$1.148\cdot10^{14}$	0.291
0.687	0.000229	$1.430\cdot10^{15}$	0.363
0.667	0.000273	$1.706\cdot10^{15}$	0.433

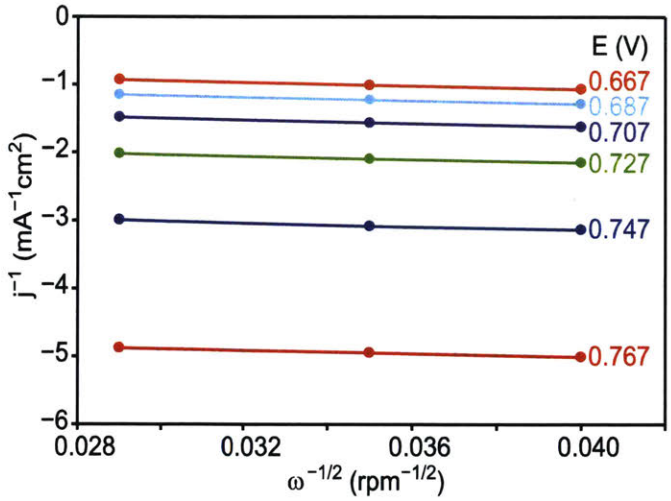

Figure 2-15. Koutecky-Levich plots from $Ni_3(HITP)_2$-electrocatalyzed ORR. See below for electron transfer numbers derived from K-L B factors.

The activation-controlled Tafel plot generated from Koutecky-Levich (K-L) data (**Figure 2-15**) revealed a Tafel slope of −128 mV·dec^{-1} (**Figure 2-16**). This Tafel slope corresponds to an irreversible one-electron pre-equilibrium process, likely indicating the formation of the superoxide anion as the rate-limiting step (theoretical Tafel slope = −120 mV·dec^{-1}). The total number of electrons transferred during ORR was determined using the inverse of the slope of the K-L plots, termed the B factor (**Equation 2-1**):

$$B = 0.62nFD_{O_2}{}^{2/3}v^{-1/6}c_{O_2}(\frac{2\pi}{60})^{1/2} \qquad \textbf{Eq. 2-1}$$

where n = number of electrons transferred, F = Faraday's constant, D_{O_2} = O_2 diffusion coefficient in the electrolyte, v = kinematic viscosity of the electrolyte, and c_{O_2} = the saturation concentration of O_2 in the electrolyte at 1 atm O_2 pressure. Assuming the typical values in 0.10 M KOH: D_{O_2} = 1.9·10^{-5} cm·s^{-1}, v = 0.1 m^2·s^{-1},[95] and c_{O_2} = 1.26·10^{-6} mol·cm^{-3}, and using B = 0.0831 mA·cm^{-2}·rpm$^{-1/2}$ from the K-L plot at E = 0.767 V, the number of transferred electrons in our system was calculated to be n = 2.25 (**Table 2-8**). This electron transfer number was consistent with predominant (87.5%) production of H_2O_2 (more

accurately, production of HO_2^- in 0.10 M KOH given the pK_a of H_2O_2 = 11.63),[133] with the remaining activity ascribed to $4e^-$ reduction to H_2O.

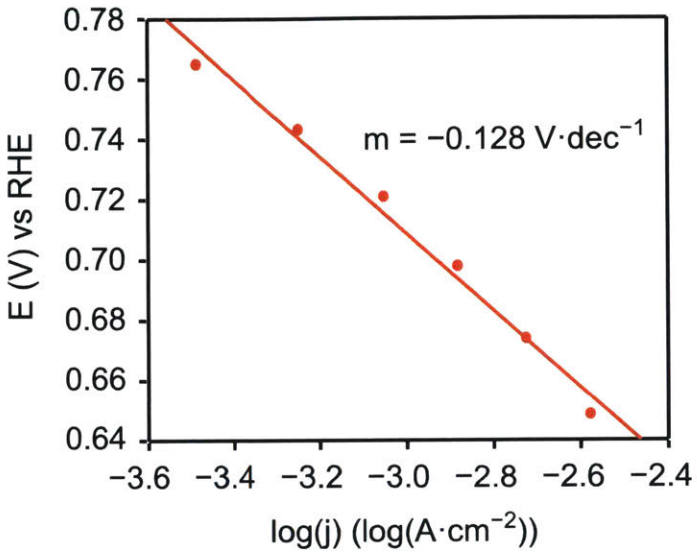

Figure 2-16. Activation-controlled Tafel plot for $Ni_3(HITP)_2$- electrocatalyzed ORR, derived from the Koutecky-Levich plots (**Figure 2-15**).

Table 2-8. Electron transfer calculations from K-L plots at varying potentials

***E* (V) vs RHE**	***B* ($A \cdot cm^{-2} \cdot rpm^{-0.5}$)**	***n* (electrons)**
0.767	$-8.391 \cdot 10^{-5}$	2.25
0.747	$-7.590 \cdot 10^{-5}$	2.04
0.727	$-7.669 \cdot 10^{-5}$	2.06
0.707	$-7.625 \cdot 10^{-5}$	2.05
0.687	$-7.920 \cdot 10^{-5}$	2.12
0.667	$-8.315 \cdot 10^{-5}$	2.23

The Faradaic efficiency for H_2O_2 production was determined by measuring the ratio of the ring current to the disk current in rotating ring-disk electrochemical experiments (see Methods section). In the 0.82 V – 0.54 V potential range, the Faradaic efficiency for H_2O_2 production decreased from 100% to 63% as formation of H_2O increased with increasing overpotential before reaching a plateau at approximately 0.75 V **(Figure 2-17)**.

The H^+ order for ORR catalysis was probed galvanostatically at I = −5.0 μA in a 0.1 M $NaClO_4$/0.1 M NaOH aqueous electrolyte titrated from pH 12.89 to pH 11.54 with 1.0 M $HClO_4$. These studies revealed a slope of zero for δE/δpH above pH 12.80, suggesting a zeroth order dependence on $[H^+]$ for the kinetic rate law (**Figure 2-18**). However, a non-zero slope was observed below pH 12.80, indicating a change in mechanism that involved proton-coupled electron transfer (PCET) or proton-dependent chemical steps before or during the rate-limiting step. The observed potential dependence on $[H^+]$ was unlikely related to the relative ionic strengths of the titrated electrolytes, which could influence the rate of O_2 uptake in the pores as well as the electron mobility; the system was sparged with O_2 for 10 minutes prior to electrolysis. Detailed mechanistic investigations of ORR with $Ni_3(HITP)_2$ are discussed in the following chapter.

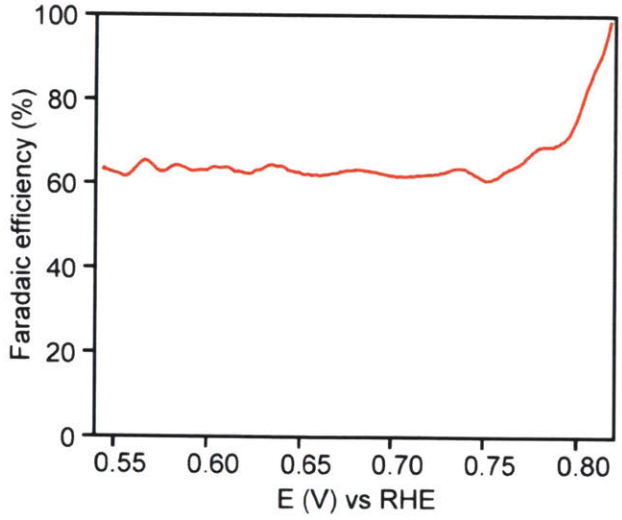

Figure 2-17. Potential-dependent faradaic efficiency for H_2O_2 production during ORR catalyzed by $Ni_3(HITP)_2$ at pH 13.

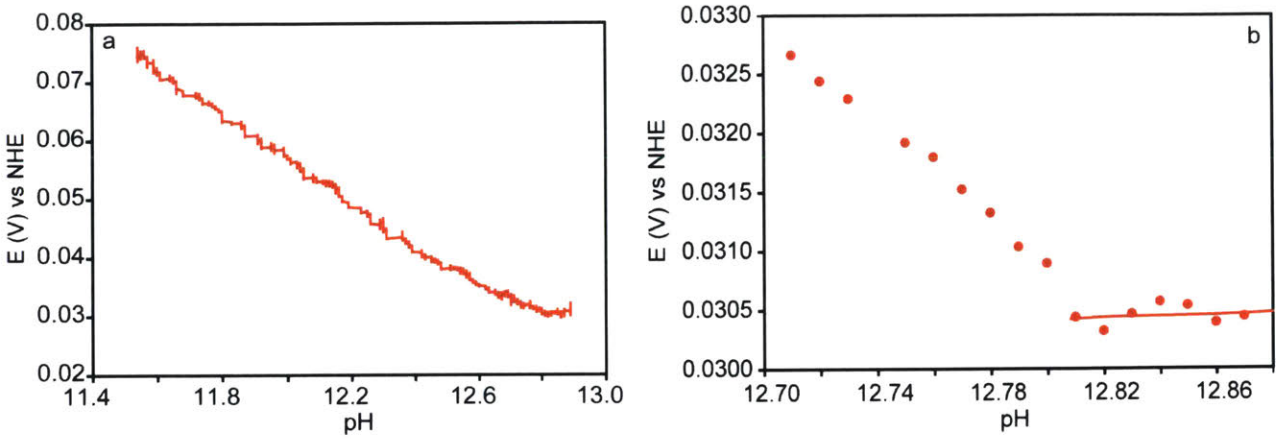

Figure 2-18. a) Galvanostatic ORR proton order study at $I = -5$ μA, pH 11.54-12.89. **b)** Magnified portion of the plot for the galvanostatic ORR proton order experiment highlighting the inflection point at pH 12.80, which indicated a deviation from a zeroth order in $[H^+]$ dependence.

2.3 Conclusions and outlook

The foregoing results demonstrated for the first time electrocatalytic ORR activity in a well-defined, intrinsically conductive MOF. Clearly, the faradaic efficiency for water production should be increased for maximizing energy density in industrial settings, but such a goal may be more tractable with MOFs, whose well-defined structures provide the ability to systematically investigate a number of variables including the metal center identity, valency, and coordination environment. Structure-function and mechanistic studies could facilitate understanding, development, and diversification of such materials into platform structures primed for the targeted design of other ORR electrocatalysts.

2.4 Methods

Characterization of the $Ni_3(HITP)_2$ film. Samples were prepared for inductively coupled plasma-mass spectrometric (ICP-MS) and atomic absorption spectroscopic (AAS) analysis by sonication of the modified

electrode buttons in concentrated ICP (Omnitrace purity, 67-70% w/w) (EMD) grade HNO_3 for 4 hours. The electrode buttons were removed from the acid, and the acid was diluted to 2% v/v with Milli-Q water.

ICP-MS was conducted on an Agilent 7900 at the MIT Center for Environmental and Health Science (Cambridge, MA). An external calibration curve was generated with a Ni standard (1000 ppm in 2% HNO_3) (Ultra Scientific) diluted to 0, 15, 30, 60, and 120 ppb in 2% ICP grade HNO_3. Argon flowing at 1.06 $L \cdot min^{-1}$ was used as the carrier gas. The ICP-MS data was analyzed by MassHunter 4.1 software.

Graphite furnace AAS was conducted on a Perkin Elmer AAnalyst 600 GFAAS (property of the Lippard Group, MIT, Cambridge, MA). An ICP-grade Ni standard (1000 ppm in 2% HNO_3) (Ultra Scientific) was diluted to 100 ppb in 2% HNO_3 in Milli-Q water. The AAS performed a serial dilution to generate a Ni calibration curve with 0, 25, 50, 75, and 100 ppb Ni calibration points. The Ni content was probed by monitoring the optical absorption at $\lambda = 232.0$ nm. The graphite furnace temperature was ramped from 110 °C to 2500 °C during AAS analysis. The AAS results were analyzed by WinLab32 for AA, version 6.5.0.0266.

Atomic force microscopy was conducted at the MIT Institute for Soldier Nanotechnologies (Cambridge, MA) using a Veeco Dimension 3100 scanning probe microscope (Veeco Digital Instruments by Bruker) equipped with a Nanoscope V controller. Images were recorded in tapping mode in the air at room temperature (23-25 °C) using an Al reflex coated silicon micro cantilever (AC240TS-R3, Asylum Research). The scan rate was set at 1.0 Hz. The atomic force microscopy results were analyzed by Gwyddion 2.43 software.

X-ray photoelectron spectroscopy (XPS) was conducted at the Harvard Center for Nanoscale Systems (Cambridge, MA) on a Thermo Scientific K-Alpha XPS. A survey scan was taken and C, N, O, and Ni were probed with a pass energy = 50 eV, beam width = 400 μm. Data analysis was executed with the Advantage 5.938 software program.

Raman spectroscopy was conducted on a Horiba Raman spectrophotometer (property of the Myerson Group, MIT, Cambridge, MA) operated at 457 nm with a hole diameter of 500 μm, a slit size of 100 μm, a range of 100-3000 cm^{-1}, a 100x magnification lens, a laser intensity of 39 A, and 2 second runs with three accumulations per sample.

Scanning electron microscopy was conducted at the Harvard Center for Nanoscale Systems (Cambridge, MA) on a Zeiss Ultra Plus FE-SEM with an InLens detector, a voltage of 10 kV, and 200 kX magnification. Data analysis was executed with SmartSEM V05.04.02.00 software.

Grazing incidence X-ray diffraction was conducted at the MIT Center for Materials Science and Engineering (Cambridge, MA) on a Bruker D8 Discover Diffractometer with a Vantec 2000 2D detector, a Cu K_α X-ray source (1.5409 Å), and a tube voltage and current of 40 kV and 40 mA, respectively. The diffraction patterns were collected in a grazing incidence geometry with a grazing incidence angle of 3.6°. The blank ITO slide and the ITO slides modified with the $Ni_3(HITP)_2$ film were secured onto the diffractometer stage with double-sided tape during data collection. The data for each sample was collected in a single exposure with an exposure time of 10 minutes per sample. The 2D data was reduced by azimuth averaging over 180° of the Debye Scherrer ring. It is noted that the remaining 180° of the Debye Scherrer ring was blocked by the sample due to the grazing incidence geometry.

Electrochemistry with the $Ni_3(HITP)_2$ film. KOH (99.99% trace metals) was purchased from Sigma Aldrich. Oxygen gas was purchased from Airgas (99.8% purity). Reference and glassy carbon working electrodes were purchased from CH Instruments. Pt gauze (100 mesh, 99.9% metal basis) and wires (ϕ = 0.404 mm, annealed, 99.9% metal basis, and ϕ = 0.5 mm dia., hard, 99.95% metal basis) comprising the auxiliary electrode were purchased from Alfa Aesar. The auxiliary electrode was cleaned by submersion in concentrated HCl followed by sonication for 5 minutes, washing with Milli-Q water, and drying under a stream of air before each experiment. Working electrodes were cleaned by submersion in concentrated HCl

followed by sonication for 5 minutes, washing with Milli-Q water, and drying under a stream of air. The working electrodes were then sequentially polished with 100 μm, 30 μm, and 5 μm diameter alumina powder from BASI. All electrochemical experiments were executed with a BioLogic SP200 potentiostat in a custom 2-compartment electrochemical cell. Rotating disk electrode and rotating ring disk electrode studies were conducted with a Pine Research Instrumentation Modulated Speed Rotator. Unless otherwise specified, internal resistance of the electrolyte was measured with the BioLogic SP200 potentiostat, and iR drop correction was applied. Generally, the resistance of 0.10 M KOH was measured to be approximately 40 Ω.

Synthesis of the $Ni_3(HITP)_2$ film on glassy carbon electrode. 2,3,6,7,10,11-hexaaminotriphenylene hexahydrochloric acid (HATP•6HCl) salt (10.4 mg) was dissolved in Milli-Q water (6 mL) and heated to 65°C with stirring in a 20 mL capped glass vial (Vial A). In a second glass reaction vial (Vial B), nickel(II) chloride hexahydrate (4.6 mg) was dissolved in Milli-Q water (4 mL) and to this was added concentrated aqueous ammonium hydroxide (0.4 mL, 25% aqueous solution). The heated HATP solution in Vial A was added to the $NiCl_2/NH_4OH$ solution (Vial B) and two alumina micropolished glassy carbon electrodes (5 mm diameter) were placed in the reaction so that the polished faces of the GC buttons were parallel to the bottom of the reaction vial. Each button was inserted into an NMR tube cap so that only the polished face of the glassy carbon was exposed for modification. The vial was capped and the reaction was heated without stirring at 65 °C for 15 hours. The next day, the reaction afforded a translucent film on the glassy carbon electrode buttons. Additionally, a translucent black film was visible on the reaction vial walls and a black flaky solid had settled at the bottom of the reaction vial. The electrode film and the reaction mixture solid were purified separately.

The electrode was removed from the reaction mixture and heated in Milli-Q water (20 mL) at 65 °C for 4 hours in a capped vial, rinsed with Milli-Q water, then heated again in water 65 °C for 15 hours in

a capped vial. The electrode was rinsed with CH_3OH and then heated in fresh CH_3OH in a capped vial at 65 °C for 5 hours. The CH_3OH was removed and the electrode was heated at 65 °C for 15 hours in fresh CH_3OH. The next day after drying under dynamic vacuum, a black translucent film coating the polished side of the glassy carbon button was visible. The electrode button was stored under dynamic vacuum.

For purification of the black powder, the remaining reaction mixture was centrifuged, the supernatant was removed, and the remaining solid was sonicated in Milli-Q water (15 mL) for 5 minutes then heated in a capped vial with stirring at 65 °C for 4 hours. The same procedure was repeated once more, with the final heating step duration of 15 hours. The powder was once again centrifuged, followed by removal of the supernatant, and then it was sonicated in CH_3OH (15 mL) for 5 minutes, then heated in the capped vial in CH_3OH at 65 °C for 5 hours. The CH_3OH wash procedure was also repeated one more time, then the powder was centrifuged, the supernatant was removed, and the black solid was dried under vacuum for 15 hours.

Determination of the 2-and-4e$^-$ ORR TOFs. The background-subtracted ring current (**Figure 2-14**) was taken for each potential probed during potentiostatic measurements (t = 0-120s, 121-240s, 241-360s, 361-480s, 481-600s) then divided by 1000 to calculate current passed in A = $C \cdot s^{-1}$ ($I = Q/t$). That current was divided by 0.2 to account for the 20% ring collection efficiency, then divided by Faraday's constant (96,485.3365 $C \cdot mol^{-1}$) and multiplied by Avogadro's number ($6.022 \cdot 10^{23}$ electrons$\cdot mol^{-1}$) to determine the number of electrons transferred to O_2 when reducing O_2 to H_2O_2 (2-electron ORR) per second. By ICP-MS the electrode was calculated to have an average of $1.1015 \cdot 10^{16}$ Ni sites deposited (See **Table 2-2** for standard deviation). By AAS, the electrode was calculated to have an average of $1.26199 \cdot 10^{16}$ Ni sites deposited (see **Table 2-3** for standard deviation). The number of electrons transferred per second was divided by the number of nickel sites as determined by AAS and ICP-MS, respectively, then multiplied those values by 3 to convert the 2e$^-$ ORR TOF to electrons$\cdot [Ni_3(HITP)_2]^{-1} \cdot sec^{-1}$ according to the two nickel

quantification methods (i.e. AAS and ICP-MS) (see **Tables 2-4** and **2-6**). In the main text, the TOF is expressed as a range defined by the values calculated using the two employed Ni quantification methods.

To determine the TOF for $4e^-$ ORR, the background and collection efficiency-corrected ring current was subtracted from the disk current (A) (**Figure 2-14**) to obtain the current passed during $4e^-$ ORR. The current (A) was divided by Faraday's constant then by number of nickel sites and multiplied by 3 to calculate the TOF (electrons·$[Ni_3(HITP)_2]^{-1}$·sec^{-1}) during $4e^-$ ORR according to the two employed Ni quantification methods (see **Tables 2-5** and **2-7**). In the main text, the TOF is expressed as a range defined by the values calculated using the two employed Ni quantification methods.

Rotating disk and rotating ring disk electrode (RRDE) investigations. Experiments were conducted in a two-compartment cell with a glass frit separating the auxiliary electrode from the working electrode; electrolyte = 0.10 M KOH; auxiliary electrode = Pt mesh; reference electrode = Hg/HgO (1.00 M KOH), working electrode = blank glassy carbon button (5 mm diameter) or glassy carbon button modified with $Ni_3(HITP)_2$ film and inserted in a polyarylether-ether ketone (PEEK) RRDE tip with a platinum ring; rotation rate = 2,000 rpm; scan speed = 5 $mV \cdot s^{-1}$; atmosphere = N_2 or O_2 sparged for 10 minutes through a fritted sparge tube before data collection, with continuous sparging during data collection. All voltammograms were collected by scanning cathodically from E = 0 V versus open circuit potential (OCP) to −0.300 V versus Hg/HgO (0.567 V versus RHE). The electrolyte solvent window was established by cycling a blank glassy carbon button under N_2 atmosphere. ORR activity of the unmodified glassy carbon was observed by cycling the unmodified glassy carbon electrode under O_2 from E = 0 V versus OCP to E = 0.400 V versus RHE. These controls preceded data collection of $Ni_3(HITP)_2$ modified glassy carbon under N_2 and O_2 atm. When relevant, a potential of E = 1.23 V vs RHE was applied to the Pt ring disk for oxidation of the ORR products. A 20% collection efficiency was applied for quantification of the ORR products using the current measured at the Pt ring disk.

Potentiostatic steady-state durability test. While rotating at 2,000 rpm, CV of the $Ni_3(HITP)_2$-modified glassy carbon electrode was taken at 5 $mV \cdot s^{-1}$ from E = 0 V vs OCP to E = −0.3 V versus Hg/HgO (E = 0.567 V vs RHE) under sparging O_2 atmosphere to measure the ORR activity. In this experiment, a titanium plate auxiliary electrode was used. O_2 sparged throughout the entirety of the experiment. The potential was held at E = 0.767 V vs RHE for 8 hours with O_2 sparging continuously. The current response was monitored with data points collected every 60 s. After the potentiostatic stability test was completed, CV was taken again under O_2 atmosphere at 5 $mV \cdot s^{-1}$ from E = 0 V vs OCP to E = −0.3 V versus Hg/HgO to compare the mass transport of the used material to that of the material before the stability test.

Koutecky-Levich data collection and determination of activation-controlled Tafel slope. CV (5 $mV \cdot s^{-1}$) under N_2 atmosphere was conducted from 0 V versus OCP to −0.3 V versus Hg/HgO (ORR potential range for $Ni_3(HITP)_2$). CV (5 $mV \cdot s^{-1}$) under O_2 atmosphere was conducted from 0 V versus OCP to −0.3 V versus Hg/HgO (ORR potential range for $Ni_3(HITP)_2$). Galvanostatic measurements were conducted with I = −1, −10, and −100 μA to identify the reliable potential range for potentiostatic measurements. Potentiostatic measurements were conducted from −20 mV to −200 mV versus Hg/HgO in increments of 20 mV. Each potential was held for 1 minute. This was conducted 5 times, with altering rotation speeds to extrapolate diffusion coefficient. The electrode was rotated at 2,000, 625, 816, 550, and 1,189 rpm respectively. This allowed for elimination of mass transport limitations when analyzing Tafel behavior *via* generation of the activation-controlled Tafel plot. CV (5 $mV \cdot s^{-1}$) under O_2 atmosphere was conducted from 0 V versus OCP to −0.3 V versus Hg/HgO (ORR potential range for $Ni_3(HITP)_2$). Chronoamperometry at E = −0.2 V versus Hg/HgO was run for 8 minutes under N_2 sparging atmosphere to eliminate O_2. CV (5 mV/s) under N_2 atmosphere was conducted from 0 V versus OCP to −0.3 V versus

Hg/HgO (ORR potential range for $Ni_3(HITP)_2$) to recheck double layer capacitance as indicator of potential catalyst decomposition. Ohmic drop was measured at I = −0.1 mA for iR correction.

ORR proton order study. Potential was measured over 25 minutes at a constant current $I = -5$ μA while varying the pH from 12.89 to 11.54 in the 0.10 M KOH electrolyte titrated with 1.0 M $HClO_4$.

Chapter 3

Mechanistic Evidence for Ligand-Centered Oxygen Reduction with the Conductive MOF Ni_3(hexaiminotriphenylene)$_2$

Portions of this chapter previously appeared in Miner, E. M.; Gul, S.; Ricke, N.D.; Pastor, E.; Yano, J.; Yachandra, V.K.; Van Voorhis , T.; Dincă, M. *ACS Catal.*, **2017**, *7*, 7726–7731 and are reproduced here with permission from the American Chemical Society.

3.1 Introduction

Understanding catalytic kinetics and thermodynamics to construct a reasonable reaction mechanism is central for both elucidating the behavior of a given catalyst and gaining predictive power over structure-function relationships. This predictive power aids in efficiently optimizing catalyst performance by systematically tuning the structural and electronic properties of the catalyst. One class of materials that could benefit from mechanism-guided optimization is non-platinum group metal (non-PGM) electrocatalysts for the O_2 reduction reaction (ORR) to water ($4e^-$ reduction) and / or hydrogen peroxide ($2e^-$ reduction). Such catalysts typically include abundant transition metals and / or heteroatoms such as N, O, and S doped into a carbonaceous matrix.[55,58,123,134–136] Although quite active and stable during ORR, previously reported non-PGM catalysts often consist of amorphous carbon mechanically blended with transition metal macrocycles or other metal and main group heteroatomic sources. These relatively poorly defined materials do not lend themselves to facile mechanistic studies; the inhomogeneous dispersion and irregular orientation of the dopants throughout the carbon matrix engenders structural ambiguity that makes identification, experimental probing, and computational modeling of active sites difficult.

Conversely, highly ordered metal-organic frameworks (MOFs) containing well-defined, spatially isolated active sites present an attractive platform for experimental and computational correlation between the chemical and electronic structure of a given catalyst and the electrocatalytic activity and mechanism, a feat that is traditionally restricted to homogeneous molecular systems. The previous chapter described that the electrically conductive MOF $Ni_3(HITP)_2$ (HITP = 2,3,6,7,10,11-hexaiminotriphenylene) (**Figure 3-1**) functions as an active ORR electrocatalyst stable in alkaline medium.[137] The activity of $Ni_3(HITP)_2$ compared well with those of the most active non-PGM electrocatalysts,[55,58,123,134–136] with an ORR onset potential ($j = -50\ \mu A \cdot cm^{-2}$) of 0.82 V versus RHE. Unlike other non-PGM catalysts, $Ni_3(HITP)_2$ presents a well-defined structure and thus the opportunity to determine whether the ORR activity is associated with the organic building blocks or the metal ions. These results could have implications for understanding the

wider class of non-PGM catalysts, whose mechanism for ORR activity remains the subject of numerous studies.

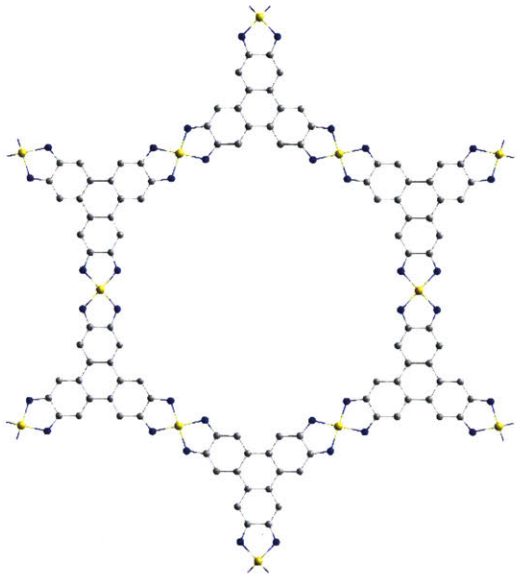

Figure 3-1. $Ni_3(HITP)_2$ structure. Ni, N, and C atoms are shown in yellow, blue, and gray, respectively. H atoms are omitted for clarity.

Here is presented experimental and computational evidence for a ligand-based active site in $Ni_3(HITP)_2$. The data showed no evidence for Ni involvement in the catalytic cycle, but suggested important consequences for changing the electronic structure of the ligand. Establishment of precise structure-function relationships in this material introduces the possibility for tuning the structure with atomic precision such that catalytic ORR activity, selectivity, and stability can be maximized.

3.2 Results and Discussion

Having previously shown that $Ni_3(HITP)_2$ reduces O_2 electrocatalytically in strongly basic medium (0.1 M KOH), the utility was explored over the wider aqueous pH range. It was found that the material was competent for ORR catalysis under all alkaline conditions (pH 8 and above), but not in acidic medium. Indeed, cyclic voltammograms (CVs) of $Ni_3(HITP)_2$ above pH 8 showed catalytic waves with no loss in

current density over 20 cycles, whereas catalytic current decreased with every cycle in acidic media (**Figure 3-2**).

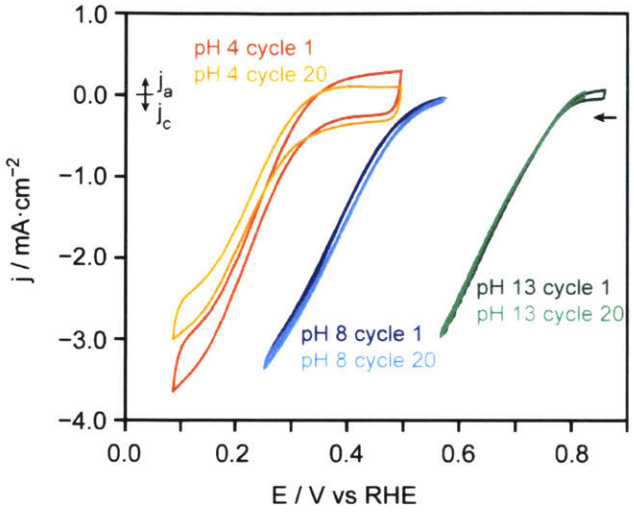

Figure 3-2. Cyclic voltammograms of $Ni_3(HITP)_2$ under O_2 atmosphere in pH 13, pH 8, and pH 4. Potentials are referenced versus RHE.

To derive a kinetic rate law for ORR with $Ni_3(HITP)_2$, we sought to determine the reaction order in $[O_2]$, $[H^+]$, and the number of electrons transferred prior to or during the rate limiting step. The reaction order in $[O_2]$ was measured at varying potentials as well as varying concentrations of O_2. At pH 13, in the potential range of 0.667 V to 0.787 V versus RHE, O_2 reduction exhibited an $[O_2]$ order of 0.78-0.88, nearing first order (**Figure 3-3a, Table 3-1**) At pH 8, in the potential range of 0.320 V to 0.520 V vs RHE, O_2 reduction is also first order in $[O_2]$ (**Figure 3-3b, Table 3-2**). To identify the number of electrons involved in the rate law, potentiostatic data was collected under O_2 atmosphere on a rotating disk electrode at varying rotation speeds (**Figure 3-4**), which allowed determination of the activation-controlled Tafel slopes. The Tafel slopes were nearly identical at pH 13 and pH 8, -128 mV·dec^{-1} and -124 mV·dec^{-1} (**Figure 3-5**), respectively, and were close to -118 mV·dec^{-1}, the value expected for an irreversible 1e$^-$ transfer in the rate-limiting step.[20] The linear Tafel slopes and consistent first order with respect to $[O_2]$ over

the activation-controlled ORR potential range suggested that the kinetic rate law does not change over the probed potential range.

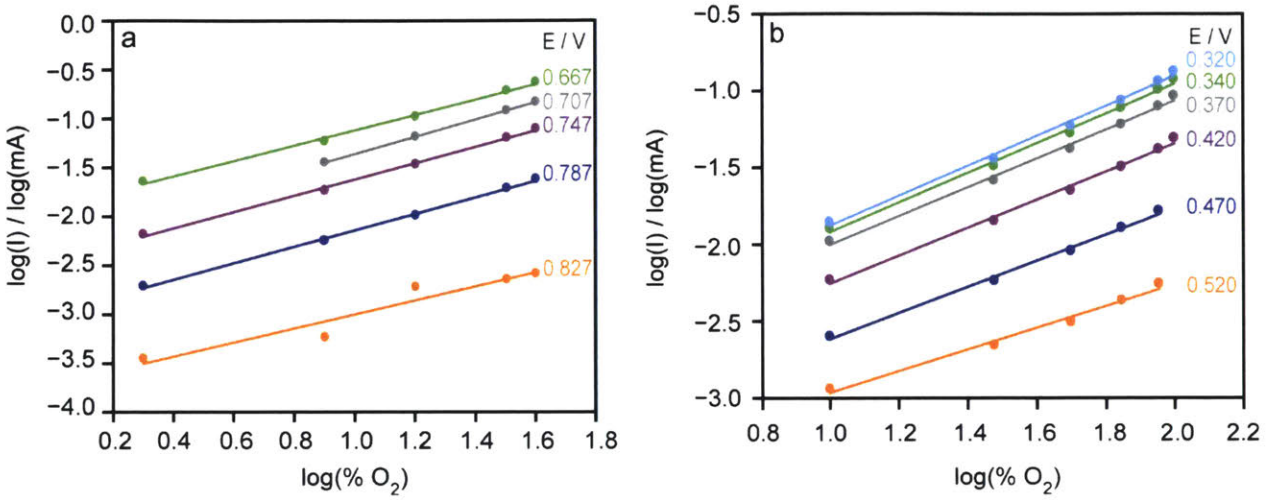

Figure 3-3. Potentiostatic [O_2] order for ORR with $Ni_3(HITP)_2$ **a)** in pH 13 and **b)** in pH 8 electrolyte. Potentials are referenced versus RHE.

Table 3-1. Corresponding slopes of the [O_2] order plots collected in pH 13, from **Figure 3-3a**.

E (V) vs RHE	Slope
0.827	0.72
0.787	0.84
0.747	0.83
0.707	0.88
0.667	0.78

To establish whether the $1e^-$ transfer step is coupled to proton transfer, galvanostatic [H^+] order data was collected while titrating the alkaline electrolyte from pH 13.0 to pH 9.5 and passing a cathodic current of 10 μA in the presence of O_2. These conditions evidenced a sub-Nernstian δE/δpH relationship of $-22\ mV \cdot dec^{-1}$, corresponding to a fractional order of $[H^+]^{1/6}$. This low fractional order implied that there were no proton-coupled electron transfer (PCET) steps prior to or in the rate-limiting step. Although

Table 3-2. Corresponding slopes of the [O_2] order plots collected in pH 8, from **Figure 3-3b**.

E (V) vs RHE	Slope
0.520	0.71
0.470	0.85
0.420	0.91
0.370	0.94
0.340	0.96
0.320	0.97

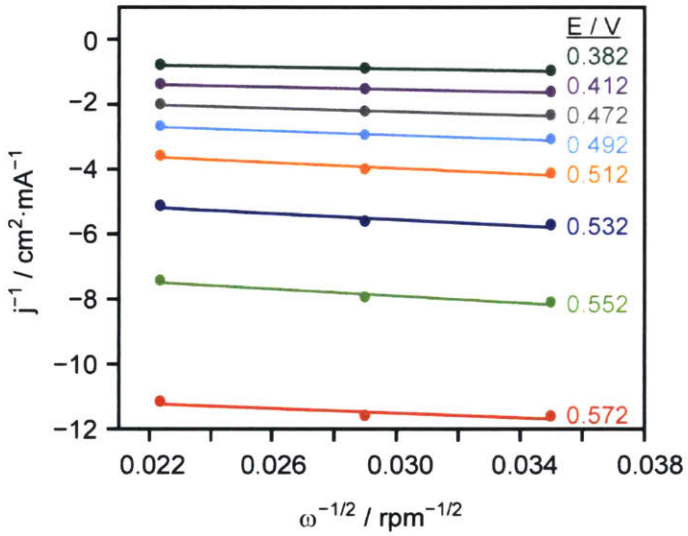

Figure 3-4. Koutecky-Levich plots for ORR with $Ni_3(HITP)_2$ in pH 8. Refer to Chapter 2 for the Koutecky-Levich plots for ORR on $Ni_3(HITP)_2$ in pH 13.

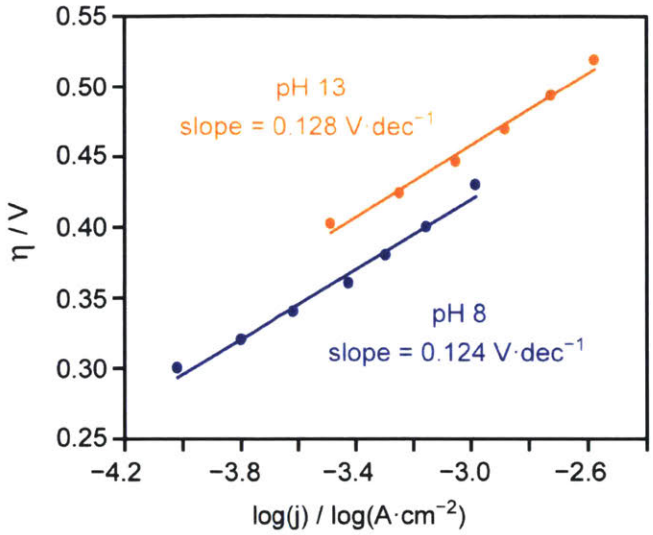

Figure 3-5. Tafel plots for ORR on $Ni_3(HITP)_2$ in pH 13 versus pH 8 electrolyte.

intriguing, a sub-Nernstian order in a given reactant is not unprecedented,[138–140] and can be associated with experimental conditions deviating from the ideal standards employed in electrokinetic derivations or from competing reaction kinetics, for instance. Notwithstanding, the fractional order in $[H^+]$ observed here was not caused by extraneous factors such as uncompensated Ohmic losses caused by ionic strength differences in the electrolyte: titrating towards acidic or towards basic pH values produced similar data under both O_2 and N_2 atmosphere (**Figure 3-6**).

Another potential source of the fractional $[H^+]$ order is the variation of electrical conductivity of the catalyst with pH, which would lead to different apparent current density as a function of pH at a fixed potential. However, the electrical conductivity of $Ni_3(HITP)_2$ films grown onto interdigitated electrodes decreased with decreasing pH, a trend opposite to what would be expected if the conductivity had any effect on the kinetic rate law (**Figure 3-7**). That is, rather than a decrease in electrical resistance of the MOF, signifying an increase in conductance at lower pH which may have explained the ORR potential dependence on pH, as pH was lowered to 8.5 an increase in resistance was observed. Although some hysteresis was

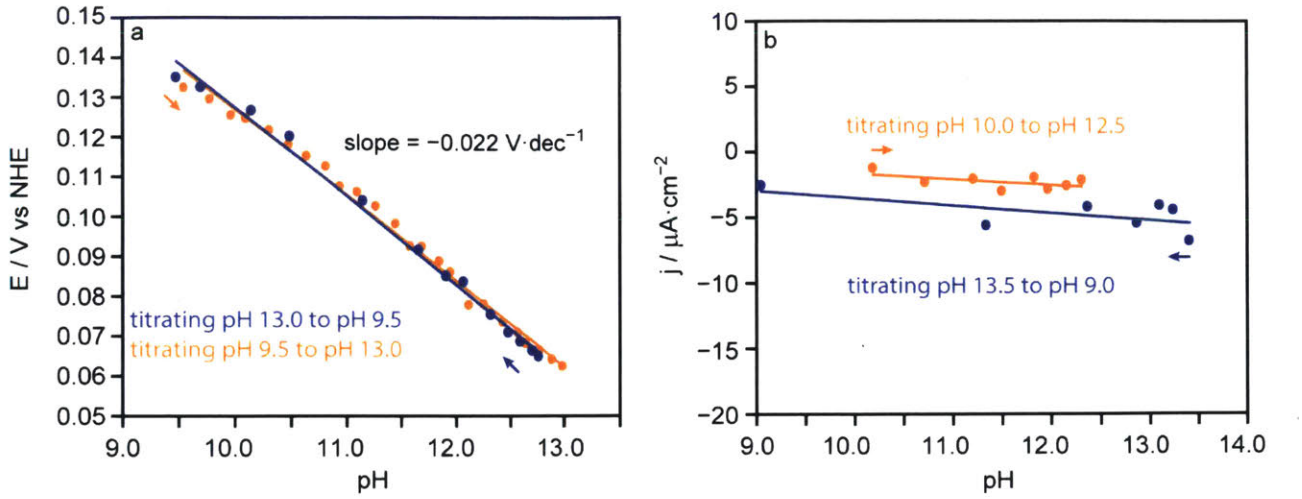

Figure 3-6. **a)** Dependence of ORR onset potential on pH, with acid and base titrant to show reversibility of the ORR potential dependence on pH, and **b)** Potentiostatic study of current passed by $Ni_3(HITP)_2$ in varying pH environments under N_2 atmosphere.

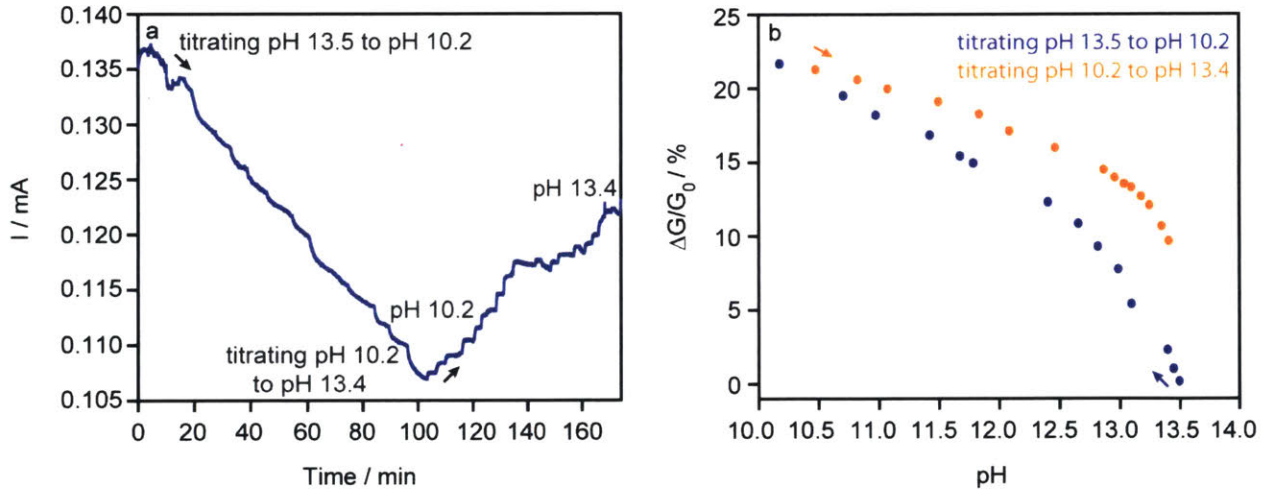

Figure 3-7. Dependence of $Ni_3(HITP)_2$ resistance on pH, **a)** full recording of current passed when E = 50 mV during acid and base titrations; **b)** change in current as a function of pH with acid titrant (blue) and base titrant (orange).

present when titrating the electrolyte back with base, approximately 63% of the conductance was recovered as the more basic pH was restored, indicating that the process resulting in lower electrical conductance in the MOF was, to some extent, reversible. The hysteresis observed in the current passed as a function of pH during the acid versus base titration may be due to acid-prompted partial decomposition of the catalyst *via* protonation of the imine nitrogen atoms, resulting in dissociation of the ligand from the Ni^{2+} centers.

Altogether, the data above points to the following empirical rate law (**Equation 3-1**):

$$j = k_0[O_2][H^+]^{1/6}e^{\alpha EF/RT} \qquad \textbf{Eq. 3-1}$$

where j is the measured steady state current density, k_0 is a potential-independent rate constant, E is the applied potential, α is the experimental transfer coefficient for the reaction (here, approximated as 0.5),[20,21] F is Faraday's constant, R is the gas constant, and T is the absolute temperature. The first order in $[O_2]$, partial order in $[H^+]$, and $1e^-$ transfer in the rate-limiting step pointed to O_2 binding to the catalyst as the rate-limiting step, with formation of superoxide. To identify the specific site for O_2 activation in the catalyst, films of $Ni_3(HITP)_2$ grown on indium-tin-oxide (ITO)-coated polyethylene terephthalate (PET) were subjected to in-situ investigation by X-ray absorption spectroscopy (XAS) at the Ni K-edge, in collaboration with S. Gul and E. Pastor. Potentiostatic ORR experiments on the $Ni_3(HITP)_2$ films evidenced no shift in the Ni K-edge in the X-ray absorption near-edge spectroscopic (XANES) region (**Figure 3-8a**). Additionally, the rising edge energy (8343.7 eV, measured at the half-height of the absorption edge) was close to that of a standard Ni(II) complex, nickel(II) phthalocyanine (8344.1 eV). If e^- transfer occurred before the rate-limiting step, this data would indicate that Ni remains in the +2 oxidation state throughout catalysis. R-space extended X-ray absorption fine structure (EXAFS) spectra of $Ni_3(HITP)_2$ before and during ORR indicated no significant change in the coordination environment or nearest neighbor distances with respect to the Ni atoms (**Figure 3-8b**). EXAFS spectra both before and during catalysis yielded similar

best fit parameters giving identical Ni-N bond distances of 1.84 Å (**Table 3-3**), consistent with square-planar divalent Ni atoms.[141]

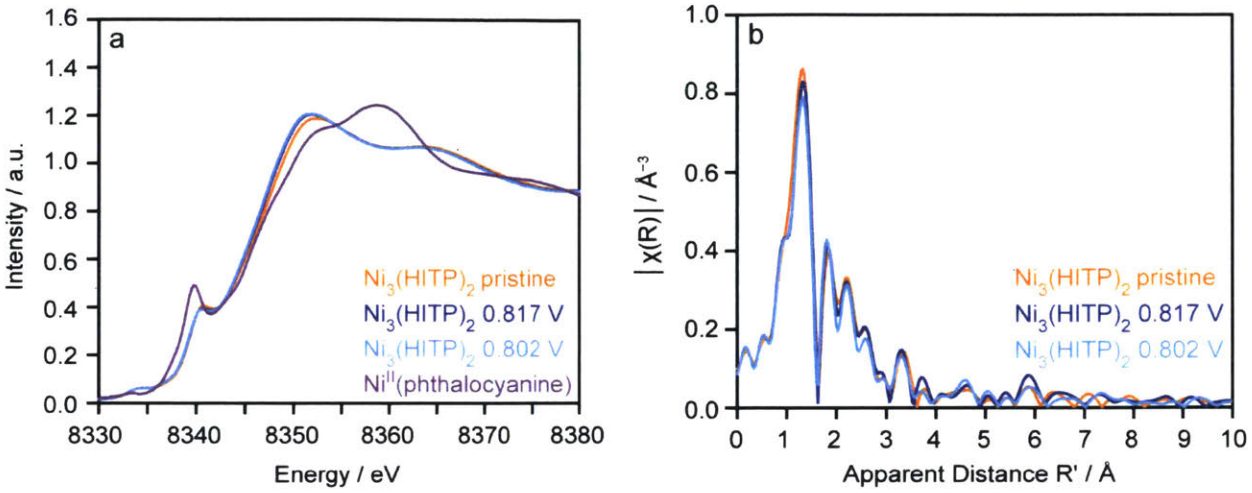

Figure 3-8. a) XANES spectrum of $Ni_3(HITP)_2$ before versus during ORR in pH 13 along with that of Ni(II) phthalocyanine; **b)** Fourier Transforms of k^2-weighted Ni K-edge EXAFS data of as-prepared $Ni_3(HITP)_2$ and under ORR conditions.

The data above suggest that *O_2 binding and activation in $Ni_3(HITP)_2$ do not occur on Ni, but on the ligand*. To determine which of the ligand atoms present the most favorable binding site for O_2, N. Ricke employed density functional theory (DFT) calculations.[142,143] Specifically, a neutral fragment consisting of a central $HITP^{3-}$ ligand bound to three Ni atoms and terminated with *o*-diiminobenzosemiquinonate ligands (**Figure 3-9a**) was considered. Using an isodesmic reaction scheme[144] with comparison to phthalimide (pK_a 8.30),[145] the pK_a of the MOF fragment was determined to be 25, thus confirming that all NH groups did not dissociate under experimental conditions. To identify the most likely active site for catalysis, we considered specific sites where O_2 would most readily bind: the Ni atom, the imine N atoms, or one of the three unique C atoms. The calculations indicated that chemical binding of O_2 to the Ni center had an uphill free energy of 1.4 eV, and no energy minimum was found for binding O_2 to

Table 3-3. Best fit parameters for Ni K-edge EXAFS curve fitting[a]

Sample	Path	R (Å)	N	σ^2 (10^{-3} Å^2)	R-factor (%)	ΔE_0 (eV)
As-prepared	Ni-N	1.84±0.01	4	3.25±1.59	0.81	−3.21±1.78
	Ni-C	2.71±0.01	4	3.45±2.56		
	Ni-N-C	2.95±0.01	8	3.00±0.20		
	Ni-N[b]	3.59±0.07	2	7.05±4.59		
	Ni-Ni[b]	3.81±0.05	2	9.09±6.43		
ORR @ 0.817 V	Ni-N	1.84±0.01	4	3.03±1.93	1.15	−2.84±2.22
	Ni-C	2.71±0.01	4	3.36±2.79		
	Ni-N-C	2.95±0.01	8	3.00±0.20		
	Ni-N[b]	3.60±0.10	2	7.05±4.59		
	Ni-Ni[b]	3.81±0.06	2	8.55±6.43		

[a]Fitting for the pristine sample and the sample during ORR was performed over the k-range $2.55 \leq k(Å^{-1}) \geq 11.60$ ($1.0 \leq R'(Å) \geq 3.6$. For the EXAFS curve measured during electroreduction of $Ni_3(HITP)_2$ at 0.817 V versus RHE, the data was fit for the k-range $2.55 \leq k(Å^{-1}) \geq 11.60$ ($1.0 \leq R'(Å) \geq 3.0$.

[b]Atoms from neighboring layers

a nitrogen atom, which together pointed to a carbon-based active site. Of the three unique C atoms, the optimal binding site was calculated to be the β-C relative to the imine group, as shown in **Figure 3-9b**. Although the binding energy of O_2 to this C in the absence of electron transfer was found to be uphill by 1.1 eV, no minimum was found for the remaining two distinct C sites, which were therefore unfavorable for O_2 binding. The potential for this β-C to serve as an O_2 binding site was further supported by Mulliken charge population analysis.[146] Whereas all other atoms had Mulliken populations of close to zero, the β-C was found to have a Mulliken population of −1.01 **(Figure 3-10, Table 3-4)**. This larger population indicated a likely site for reactivity, as charge localization can point to the easiest location for breaking

aromaticity. Importantly, the orientation of the C-bound O_2 with respect to the NH group of the HITP ligand raised the possibility of a stabilizing hydrogen bonding interaction between the distal O atom and the imine proton, which indeed were found to lie 1.98 Å apart.

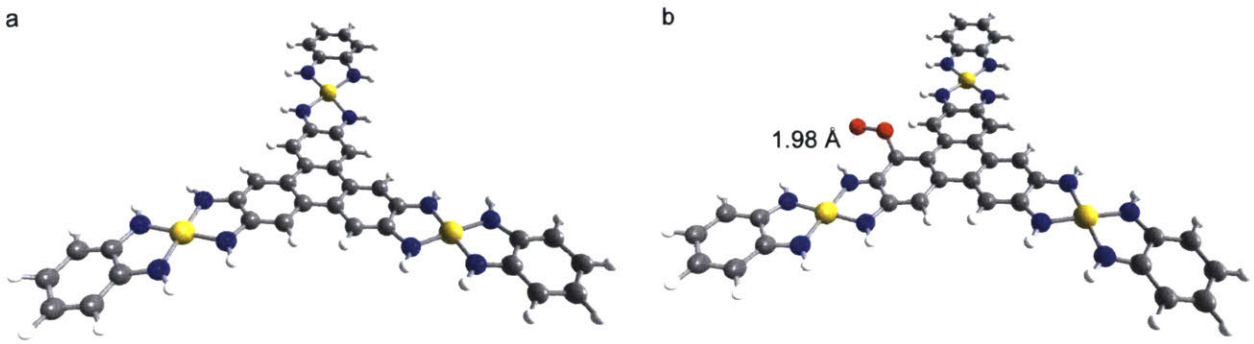

Figure 3-9. a) Model fragment of $Ni_3(HITP)_2$; **b)** Calculated binding site of O_2 onto the $Ni_3(HITP)_2$ fragment. C, H, N, Ni, and O atoms shown in gray, white, blue, yellow, and red, respectively.

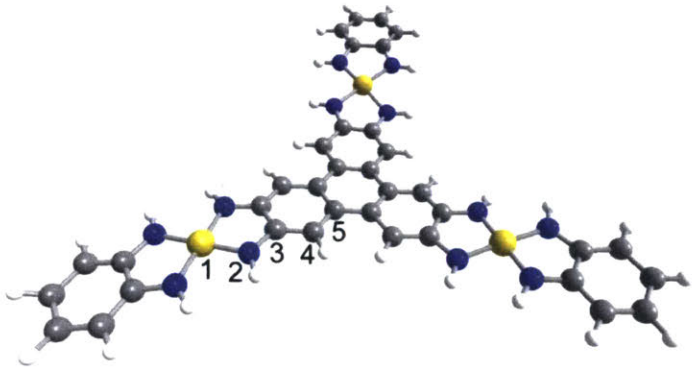

Figure 3-10. $Ni_3(HITP)_2$ model fragment with the relevant atoms (1-5) analyzed by Mulliken charge population analysis.

Table 3-4. Mulliken populations for the atoms numbered in **Figure 3-10** above, before versus after electrochemical O_2 binding.

Atom #	Population before O_2	Population after O_2
1	0.34	0.33
2	−0.78	−0.81
3	0.47	0.26
4	−1.01	−0.73
5	0.65	0.82

Given that the thermodynamic barrier for O_2 binding to the optimal carbon site was still higher than would be expected given the observed catalytic activity, the possibility of electron transfer accompanying O_2 binding was investigated. Indeed, binding of O_2 to the $Ni_3(HITP)_2$ fragment in concert with a $1e^-$ transfer to O_2 to form superoxide was found to be endergonic by only 0.1 eV in the absence of an applied potential (**Figure 3-11, Table 3-5**). Notably, the barrier for electrochemical binding of O_2 to the Ni sites was found

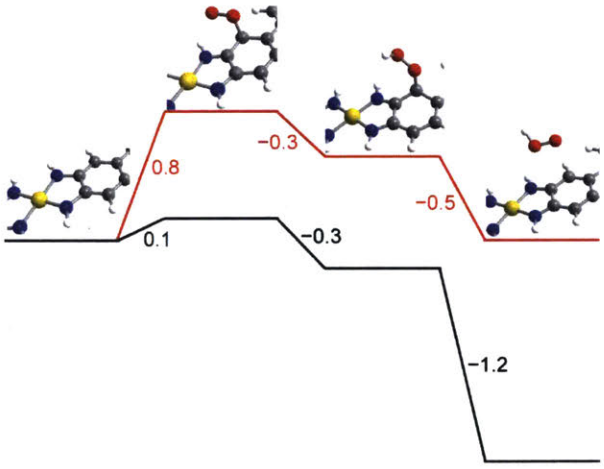

Figure 3-11. The free energy (eV) of each intermediate in the $2e^-$ ORR catalytic cycle with $Ni_3(HITP)_2$. The lower states (black) show the energetics at open circuit potential, whereas the upper states (red) show the free energy of each state with 0.69 V versus RHE applied potential such that the production of HO_2^- is thermodynamically reversible.

Table 3-5. Calculated thermodynamic parameters for ORR with the $Ni_3(HITP)_2$ model fragment and the molecular analogue $Ni(ISQ)_2$. These values were used to calculate the difference in free energy for possible catalytic paths of the $Ni_3(HITP)_2$ cluster. A scaling constant of 0.9512 was applied to the vibrational enthalpy and zero-point energy values listed here to account for the anharmonicity of vibrational molecular modes.

Cluster State in Catalytic Cycle	**Vacuum Energy, 0 K (Hartree)**	**Solvation Energy ($kCal \cdot mol^{-1}$)**	**Vibrational Enthalpy ($kCal \cdot mol^{-1}$)**	**Entropy ($Cal \cdot mol^{-1}$)**	**ZPE ($Cal \cdot mol^{-1}$)**
$Ni_3(HITP)_2$	−6571.6944	−42.68	410.29	235.59	387.23
$Ni_3(HITP)_2$–O_2 (C_β–O_2)	−6721.9619	−68.46	415.23	235.44	391.78
$Ni_3(HITP)_2$–O_2^- (C_β–O_2^-)	−6722.0685	−96.99	398.47	224.32	376.38
$Ni_3(HITP)_2$–O_2H	−6722.6269	−46.88	407.09	225.99	384.80
$Ni_3(HITP)_2$–O_2^- (Ni–O_2^-)	−6722.0495	−94.17	398.34	236.16	374.98
$Ni(ISQ)_2$	−2191.7560	−14.58	142.50	104.95	136.86
$Ni(ISQ)_2$–O_2 (C_β–O_2)	−2342.0040	−46.51	153.76	125.65	145.80
$Ni(ISQ)_2$-O_2^- (C_β–O_2^-)	−2342.1184	−70.83	146.03	118.50	138.81

to be considerably higher, at 0.6 eV. The barrier for electrochemical binding of O_2 onto the β-C was not prohibitive for O_2 binding and was consistent with the experimental observation of first order $[O_2]$ dependence as well as a Tafel slope of approximately −118 $mV \cdot dec^{-1}$.[20] In agreement with rate-limiting superoxide formation, subsequent protonation of superoxide was calculated to be exergonic by 0.3 eV. Lastly, the calculations indicated that transfer of a second electron to break the oxygen-catalyst bond and

release H_2O^- was favorable by 1.2 eV. Although Ni serving as an O_2 binding site here was unlikely, the spin density plot of the MOF model fragment showed that electrochemical binding of O_2 broke the spin symmetry, with excess spin distributed across both the metal and ligand (**Figure 3-12**). Thus, the Ni sites did not directly participate in O_2 reactivity, but they did contribute to the electronic structure of the ORR-active species.

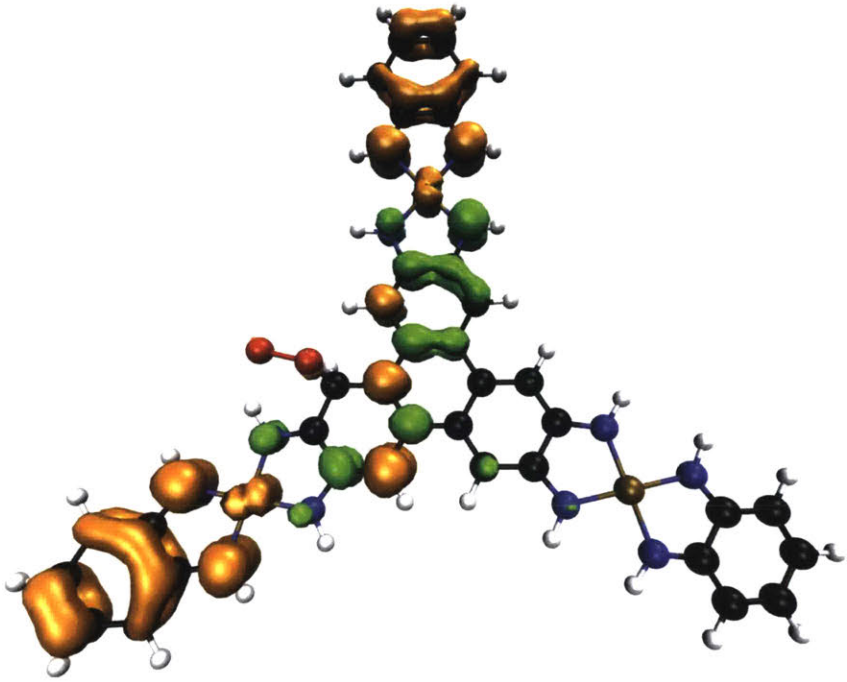

Figure 3-12. Excess spin density plot of the $Ni_3(HITP)_2$–O_2^- cluster (isovalue = 0.018). This cluster has an overall spin of 0.5, and features regions with both excess positive spin distributed across the ligand and metal (orange), and negative spin distributed across the ligand (green).

To obtain a more comprehensive picture of the full catalytic mechanism, potential sources of the fractional order in $[H^+]$ were further investigated. The earlier discussion on this subject notwithstanding, a plausible explanation for the partial proton order is that the absolute rate of the rate-limiting step – here, formation of MOF-bound superoxide – is only marginally slower than a subsequent proton-dependent non-

rate-limiting step.[21] Such a scenario would be consistent with a pH-dependent electron transfer from $Ni_3(HITP)_2$ to superoxide. To probe this hypothesis, we investigated the CV signature of the catalyst under pure N_2 as a function of pH. As shown in **Figure 3-13**, the oxidation potentials of $Ni_3(HITP)_2$ were indeed pH- dependent, indicating that changing the oxidation state of $Ni_3(HITP)_2$ was a PCET process. More

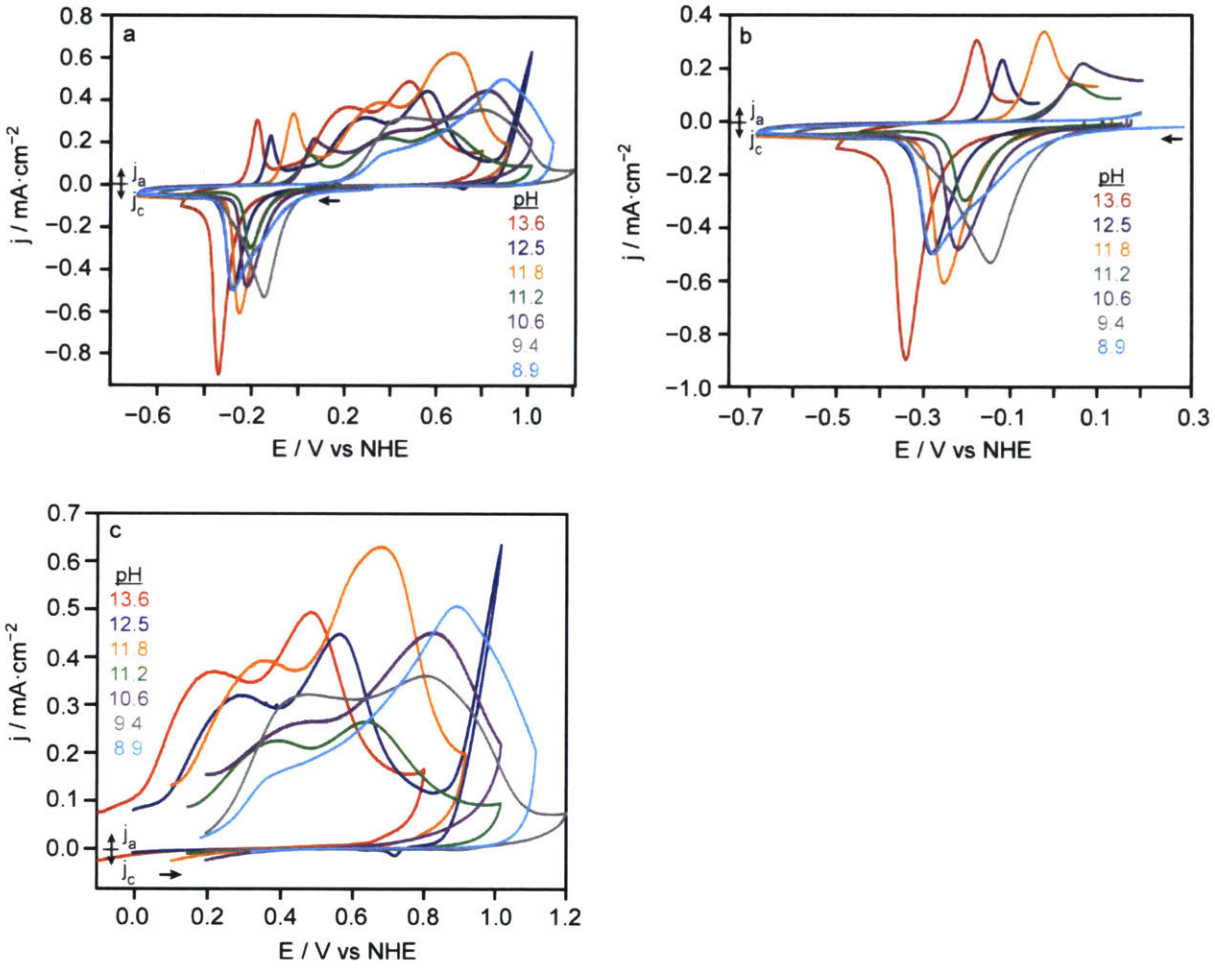

Figure 3-13. pH-dependent redox activity of $Ni_3(HITP)_2$ under N_2 atmosphere, showing **a)** the full voltammogram, then magnifying **b)** the quasi-reversible redox event, and **c)** the first and second irreversible oxidation events.

specifically, as the pH decreased, the oxidation potentials of $Ni_3(HITP)_2$ shifted more positively with a $\delta E_{redox}/\delta pH$ slope of 90-120 $mV \cdot dec^{-1}$ (**Figure 3-14**), as expected for a $2H^+$-$1e^-$ coupled transfer.[147] This Nernstian dependence of the MOF oxidation potentials on pH supported the hypothesis that the second (i.e. the non-rate-limiting) electron transfer step was associated with proton transfer and therefore was likely responsible for the fractional $[H^+]$ order during ORR. Similar pH-dependent redox activity was reported in a nitrogen-doped graphitic carbon ORR catalyst.[138]

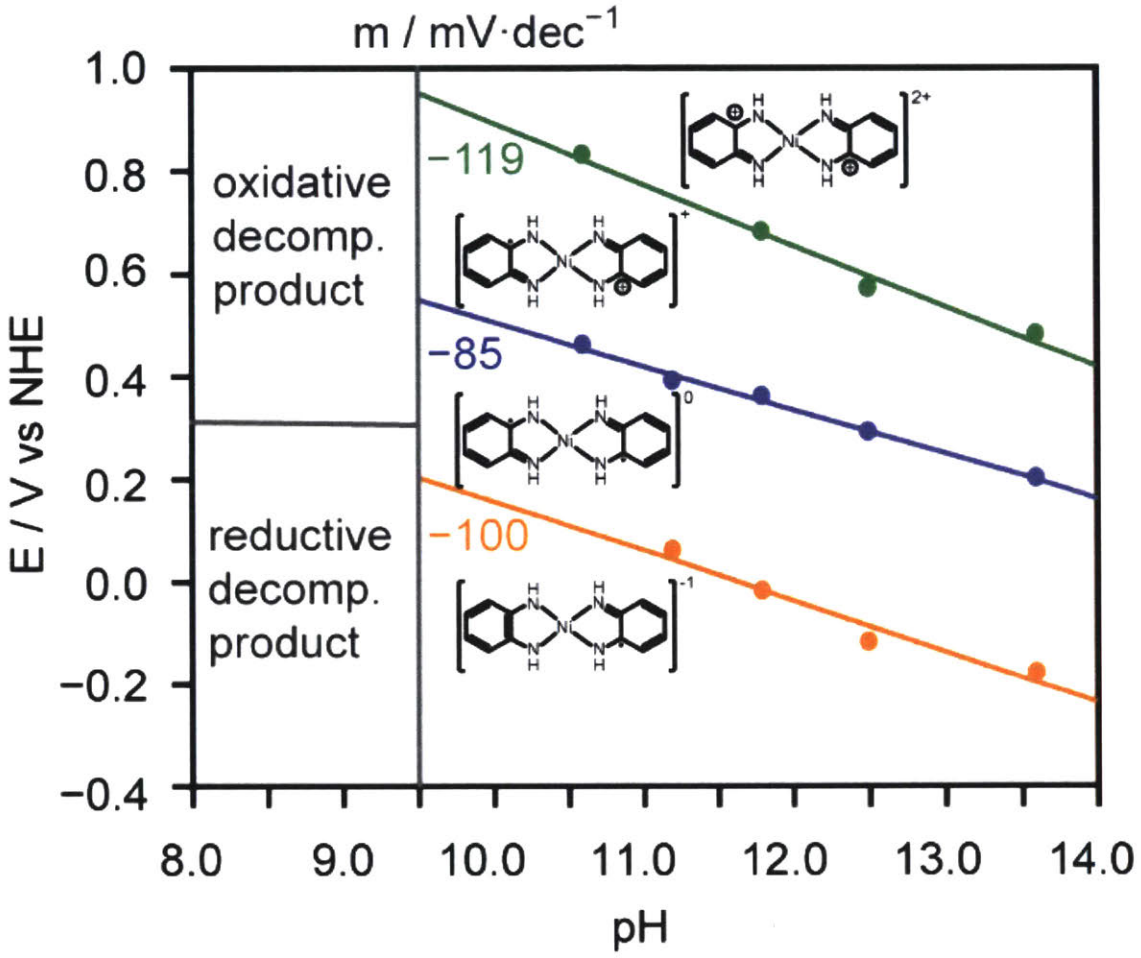

Figure 3-14. Pourbaix diagram of the oxidation states of $Ni_3(HITP)_2$ accessible at various potentials / pH environments.

With the discussed experimental and computational data in hand, the following mechanism for the $2e^-$ reduction of O_2 on $Ni_3(HITP)_2$ emerged (**Scheme 3-1**):

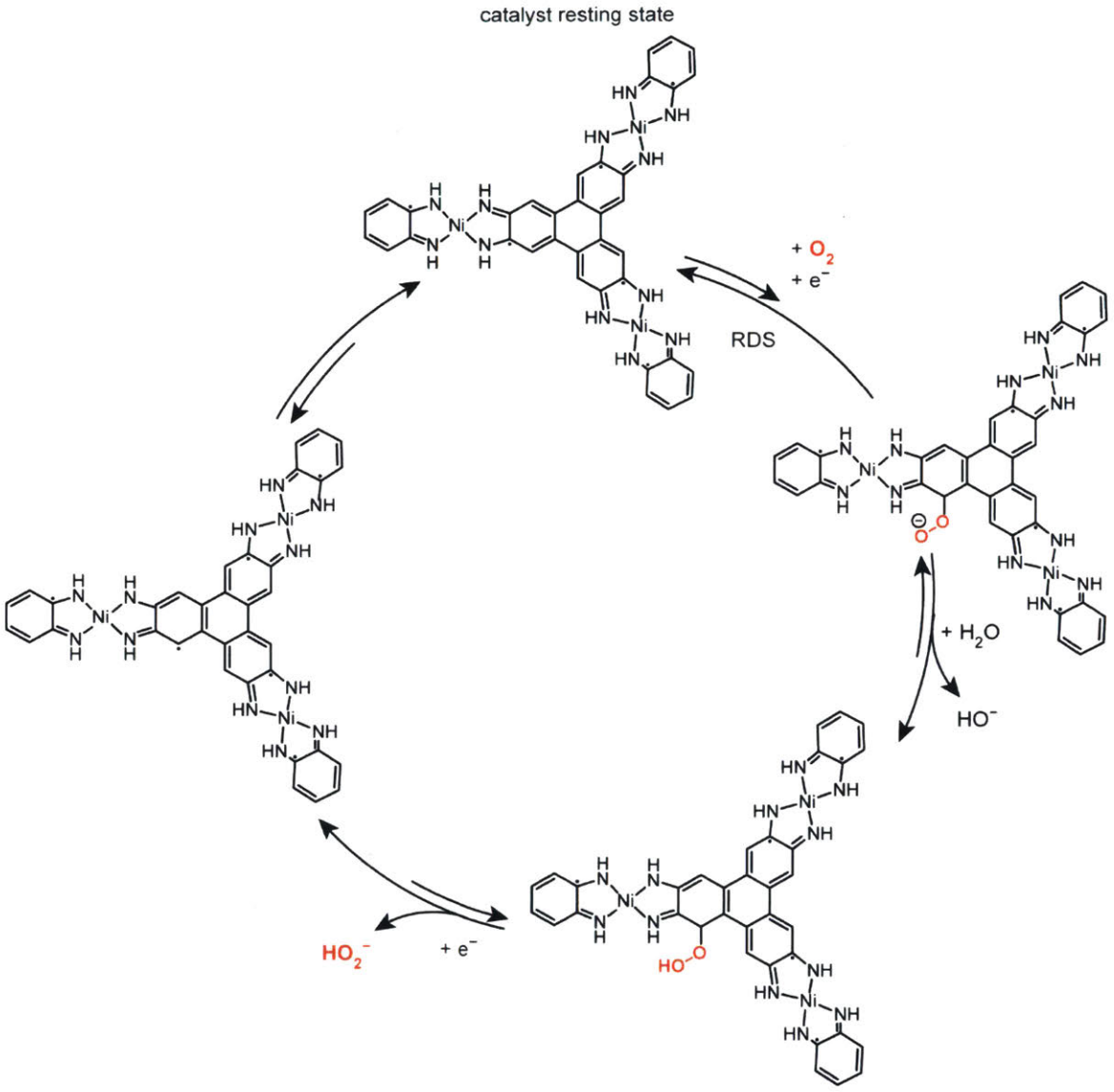

Scheme 3-1. Proposed mechanism for $2e^-$ O_2 electroreduction with $Ni_3(HITP)_2$.

I. Rate-limiting electron transfer and binding of O_2 to the β-C with respect to the ligand imine to form the superoxide adduct

II. Protonation of bound O_2^- by water to form a hydroperoxide

III. Electron transfer to the hydroperoxide and desorption of HO_2^-

IV. Regeneration of the catalyst resting state

This proposed mechanism was consistent with our experimental data and the computational studies, but it did not address whether the highly delocalized frontier orbitals of $Ni_3(HITP)_2$ were necessary for catalysis or whether a smaller fragment of this material would be sufficient for competent catalysis experimentally. To investigate the possibility of a small-molecule mimic of $Ni_3(HITP)_2$ acting as a competent ORR catalyst, we focused on the well-known molecular complex $Ni(ISQ)_2$ (ISQ = *o*-diiminobenzosemiquinonate, **Figure 3-15**).[148–155] Importantly, under conditions mimicking those employed for $Ni_3(HITP)_2$, $Ni(ISQ)_2$ showed no ORR activity (**Figure 3-16**).

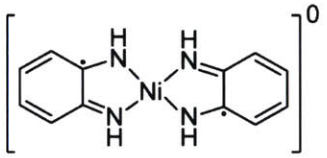

Figure 3-15. Structure of $Ni(ISQ)_2$.

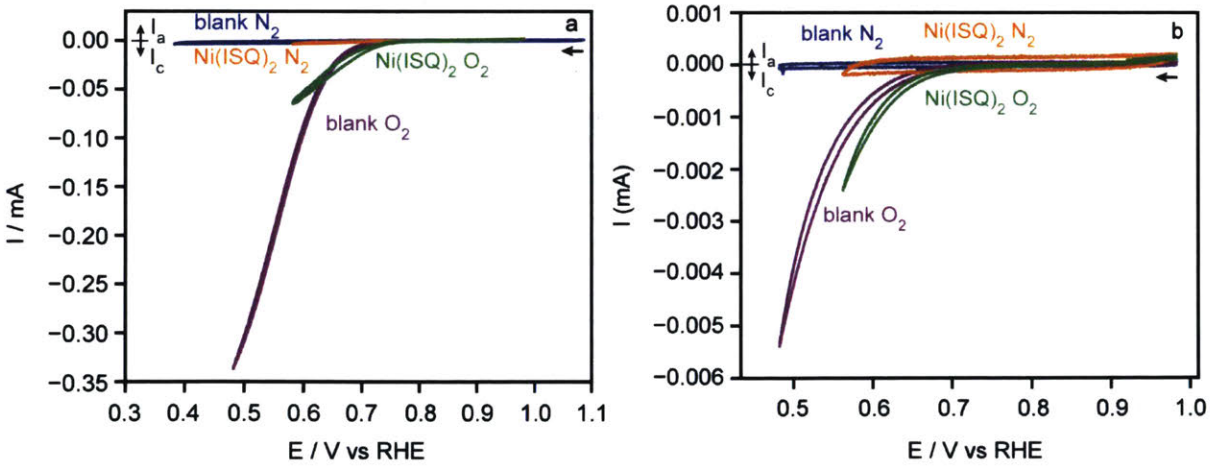

Figure 3-16. Cyclic voltammogram of O_2 electroreduction on the molecular species $Ni(ISQ)_2$ dropcast on **a)** glassy carbon, and **b)** ITO, in pH 13 electrolyte.

Density functional theory (DFT) provided insight into the dramatic difference in catalytic activity between the MOF and the molecular complex (**Figure 3-17**). Specifically, whereas O_2 binding and electron

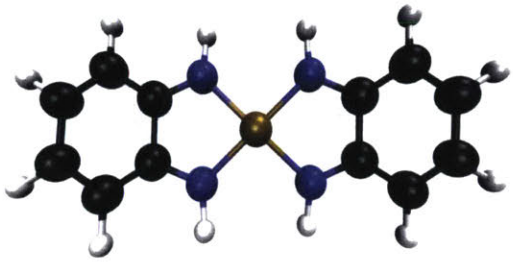

Figure 3-17. Optimized structure of $Ni(ISQ)_2$ by DFT. C, H, N, and Ni atoms shown in black, gray, blue, and gold, respectively.

transfer to the MOF was endergonic by only 0.1 eV (see above), calculations suggest that the formation of the superoxide complex with $Ni(ISQ)_2$ was endergonic by 0.7 eV at pH 13. Although in line with the experimental observation that the molecular complex was not a good ORR catalyst, this difference was surprisingly large and highlighted the importance of having a delocalized valence band in the MOF. Indeed, representations of the highest occupied molecular orbitals for $Ni(ISQ)_2$ and the more extended $Ni_3(HITP)_2$ model system described earlier showed significant redistribution of the π electron density in $Ni(ISQ)_2$, but very little disruption of the π system in $Ni_3(HITP)_2$ (**Figure 3-18**). In other words, the MOF is able to accommodate the key superoxide complex without significant disruption of its electronic structure, only by virtue of its extended covalent lattice. Thus, even though the metal itself does not play a significant role in ORR catalysis, the conductivity and electron delocalization in the MOF is essential for catalysis.

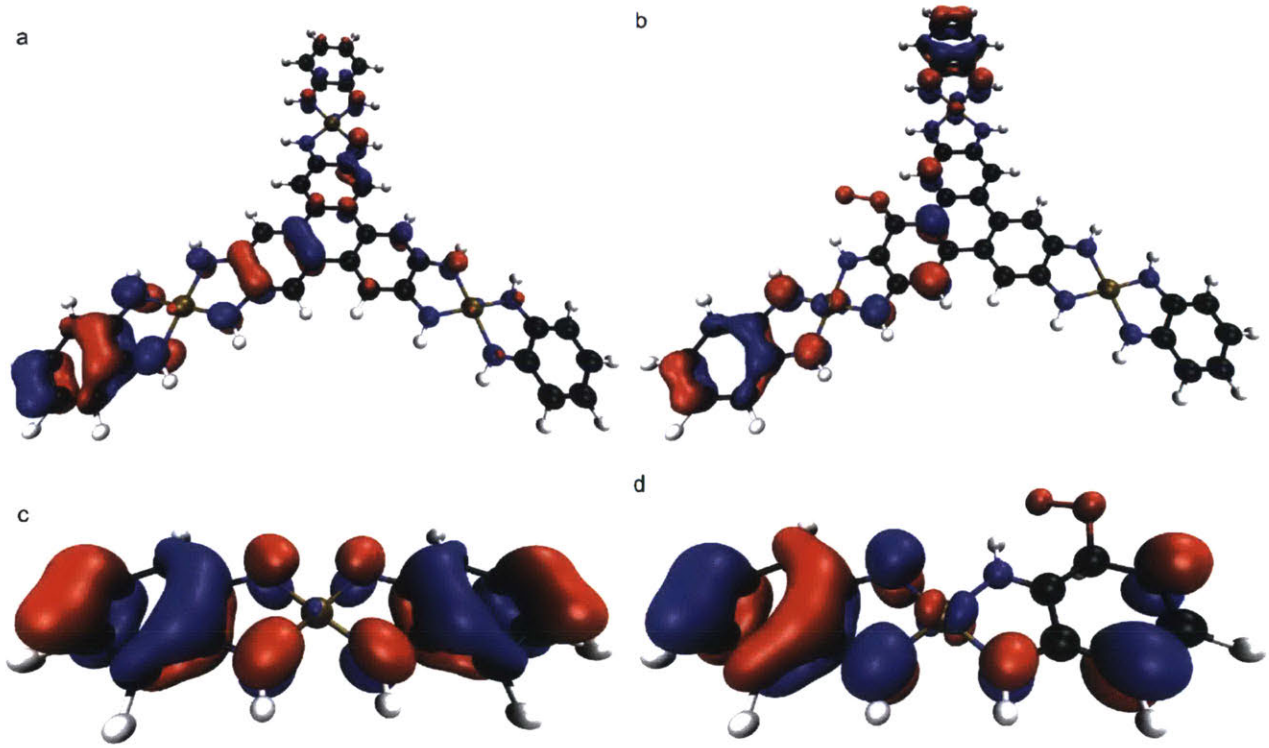

Figure 3-18. Calculated highest occupied molecular orbitals (HOMOs) for **a)** representative $Ni_3(HITP)_2$ fragment $Ni_3(HITP)(ISQ)_3$ without superoxide; **b)** representative $Ni_3(HITP)_2$ fragment $Ni_3(HITP)(ISQ)_3$ with bound superoxide; **c)** $Ni(ISQ)_2$ without superoxide; **d)** $Ni(ISQ)_2$ with bound superoxide.

3.3 Conclusions and outlook

Electrochemical and spectroscopic techniques supported by computational evidence revealed the that active site for catalytic O_2 reduction on $Ni_3(HITP)_2$, an electrically conductive MOF, was not metal-based, as proposed for many transition metal macrocycles, but rather ligand-based. The highly ordered MOF structure and well-defined active sites have enabled precise correlation of the structure and electronic structure of the catalyst with the ORR activity and mechanism, including the identification of a partial proton order related to the pH dependence of the MOF oxidation potentials. This comprehensive model for O_2 binding thermodynamics, electrokinetics, and detailed mechanism of ORR on $Ni_3(HITP)_2$ should enable

catalyst design in other conductive MOF systems. Most importantly, these studies showed that electron delocalization is critical for accessing key intermediates that become energetically prohibitive for molecular systems bearing only structural resemblance to the MOFs.

3.4 Methods

General comments. KOH (99.99% trace metals) and NaCl (99.99% trace metals) were purchased from Sigma-Aldrich. The aqueous electrolytes were made from Milli-Q water (18 MΩ). Oxygen gas was purchased from Airgas (99.8% purity). Reference and glassy carbon working electrodes were purchased from CH Instruments. Indium tin oxide (ITO) working electrodes were purchased from Delta Technologies, Ltd. Gold interdigitated electrodes on a corundum substrate was purchased from BVT Technologies (CC1.W1). Pt gauze (100 mesh, 99.9% metal basis) and wires (ϕ = 0.404 mm, annealed, 99.9% metal basis, and ϕ = 0.5 mm dia., hard, 99.95% metal basis) comprising the auxiliary electrode were purchased from Alfa Aesar.

Electrochemical measurements. The Pt auxiliary electrode was cleaned by submersion in concentrated HCl followed by sonication for 5min, washing with Milli-Q water, and drying under a stream of air before each experiment. Glassy carbon working electrodes were cleaned by submersion in concentrated HCl followed by sonication for 5min, washing with Milli-Q water, and drying under a stream of air. The glassy carbon working electrodes were then sequentially polished with 1, 0.3 and 0.05 μm diameter alumina powder from BASI. Unless otherwise noted, all electrochemical experiments were executed with a Bio-Logic SP200 potentiostat / galvanostat in a custom 2-compartment electrochemical cell. Rotating disk electrode studies were conducted with a Bio-Logic SP200 potentiostat / galvanostat and a Pine Research Instrumentation Modulated Speed Rotator. Unless otherwise specified, internal resistance of the electrolyte was measured with the Bio-Logic SP200 potentiostat / galvanostat by passing −100 μA current, and iR drop correction was applied. Generally, the resistance of 0.10 M KOH was measured to be ~20 Ω. Prior to

data collection under a given atmosphere (N_2 or O_2), the electrolyte was sparged for 20 minutes with that gas and sparged continuously during data collection. For the pH 13 (0.1 M KOH) electrolyte, a Hg/HgO reference electrode (1.0 M KOH) was used and for the pH 8 electrolyte (0.1 M NaCl), a Ag/AgCl electrode was used (1.0 M NaCl). Unless otherwise noted, cyclic voltammetry data was collected while rotating the working electrode at 2,000 r.p.m. and cycling at 5 $mV \cdot s^{-1}$.

Synthesis of the $Ni_3(HITP)_2$ film on glassy carbon electrode. 2,3,6,7,10,11-hexaaminotriphenylene hexahydrochloric acid (HATP•6HCl) salt (10.4 mg) was dissolved in Milli-Q water (6 mL) and heated to 65°C with stirring in a 20 mL capped glass vial (Vial A). In a second glass reaction vial (Vial B), nickel(II) chloride hexahydrate (4.6 mg) was dissolved in Milli-Q water (4 mL) and to this was added concentrated aqueous ammonium hydroxide (0.4 mL, 25% aqueous solution). The heated HATP solution in Vial A was added to the $NiCl_2/NH_4OH$ solution (Vial B) and two alumina micropolished glassy carbon electrodes (5 mm diameter) were placed in the reaction so that the polished faces of the GC buttons were parallel to the bottom of the reaction vial. Each button was inserted into an NMR tube cap so that only the polished face of the glassy carbon was exposed for modification. The vial was capped and the reaction was heated without stirring at 65 °C for 15 hours. The next day, the reaction afforded a translucent film on the glassy carbon electrode buttons. Additionally, a translucent black film was visible on the reaction vial walls and a black flaky solid had settled at the bottom of the reaction vial. The electrode film and the reaction mixture solid were purified separately.

The electrode was removed from the reaction mixture and heated in Milli-Q water (20 mL) at 65 °C for 4 hours in a capped vial, rinsed with Milli-Q water, then heated again in water 65 °C for 15 hours in a capped vial. The electrode was rinsed with CH_3OH and then heated in fresh CH_3OH in a capped vial at 65 °C for 5 hours. The CH_3OH was removed and the electrode was heated at 65 °C for 15 hours in fresh

CH_3OH. The next day after drying under dynamic vacuum, a black translucent film coating the polished side of the glassy carbon button was visible. The electrode button was stored under dynamic vacuum.

For purification of the black powder, the remaining reaction mixture was centrifuged, the supernatant was removed, and the remaining solid was sonicated in Milli-Q water (15 mL) for 5 minutes then heated in a capped vial with stirring at 65 °C for 4 hours. The same procedure was repeated once more, with the final heating step duration of 15 hours. The powder was once again centrifuged, followed by removal of the supernatant, and then it was sonicated in CH_3OH (15 mL) for 5 minutes, then heated in the capped vial in CH_3OH at 65 °C for 5 hours. The CH_3OH wash procedure was also repeated one more time, then the powder was centrifuged, the supernatant was removed, and the black solid was dried under vacuum for 15 hours.

Determination of the $Ni_3(HITP)_2$-mediated ORR order in $[O_2]$ in pH 13 electrolyte. The electrolyte was sparged with N_2 for 20 minutes and background CV of the $Ni_3(HITP)_2$ film on the glassy carbon working electrode was taken from 0 V versus OCP to −0.3 V versus Hg/HgO. The electrolyte was then sparged with O_2 for 10 minutes then CV under O_2 was taken from 0 V versus OCP to −0.3 V vs Hg/HgO. The $[O_2]$ order data was collected by holding the potential at E = −0.04 V, −0.08 V, −0.12 V, −0.16 V, and −0.2 V versus Hg/HgO for two minutes at each potential, going from 5% O_2 / 95% N_2 to 100% O_2 / 0% N_2 electrolyte atmosphere at each potential value, with sparging the new atmosphere for 5 minutes before data collection. For each potential, a log(I) versus log(partial pressure O_2) plot was made to extrapolate the order in O_2 and observe the dependence of the order on the potential.

Determination of the $Ni_3(HITP)_2$-mediated ORR order in $[O_2]$ in pH 8 electrolyte. The electrolyte was sparged with N_2 for 20 minutes and background CV of the $Ni_3(HITP)_2$ film on the glassy carbon working electrode was taken from 0 V versus OCP to −0.35 V versus Ag/AgCl. The electrolyte was then sparged

with O_2 for 10 minutes then CV under O_2 was taken from 0 V versus OCP to −0.35 V vs Ag/AgCl. The [O_2] order data was collected by holding the potential at E = −0.152 V, −0.202 V, −0.252 V, −0.302 V, −0.332 V, and −0.352 V versus Ag/AgCl for two minutes at each potential, going from 10% O_2 / 90% N_2 to 100% O_2 / 0% N_2 electrolyte atmosphere at each potential value, with sparging the new atmosphere for 5 minutes before data collection. For each potential, a log(I) versus log(partial pressure O_2) plot was made to extrapolate the order in O_2 and observe the dependence of the order on the potential.

Koutecky-Levich and Tafel studies in pH 8. Collection of the Kouteky-Levich and Tafel data in pH 13 was previously described in the Methods section of Chapter 2. CV in pH 8 electrolyte (0.1 M NaCl) (5 $mV \cdot s^{-1}$) under N_2 atmosphere then under O_2 atmosphere was conducted from 0 V versus OCP to −0.4 V versus Ag/AgCl (ORR potential range for $Ni_3(HITP)_2$) with the unmodified glassy carbon electrode then the $Ni_3(HITP)_2$-modified glassy carbon electrode. Potentiostatic measurements were conducted from −100 to −290 mV versus Ag/AgCl in increments of 20 mV under O_2 atmosphere. Each potential was held for 2 minutes. This was conducted five times, with altering rotation speeds to extrapolate the diffusion coefficient. The electrode was rotated at 2,000, 625, 816, 550 and 1,189 r.p.m., respectively. This allowed for elimination of mass transport limitations when analyzing Tafel behavior *via* generation of the activation-controlled Tafel plot.

ORR [H^+] order study. Potential was measured at a constant current I = −10 μA while varying the pH from 13.5 to 9.5 in the 0.10 M KOH electrolyte titrated with 1.0 M $HClO_4$ in the presence of O_2. Each potential required to pass −10 μA at a given pH was allowed to reach steady state before more titrant was added. Once pH 9.5 was reached, the electrolyte was titrated back up to pH 13 with 1.0 M KOH while repeating the aforementioned procedure for collecting [H^+] order data to test the reversibility of the data.

As a control, a freshly modified electrode was used and −0.35 V versus Ag/AgCl was applied under N_2 atmosphere while the electrolyte was titrated in the pH range mentioned above.

Probing the effect of the electrical resistance of $Ni_3(HITP)_2$ in varying pH environments. Synthesis and purification of Ni3(HITP)2 film on the interdigitated electrode. 2,3,6,7,10,11-hexaaminotriphenylene·6HCl (HATP) salt (10 mg) was dissolved in deionized water (4 mL) and heated to 65 °C in a 20 mL capped scintillation vial (Vial A). In a second glass reaction vial (Vial B), nickel(II) chloride hexahydrate (10 mg) was dissolved in deionized water (4 mL). The heated HATP solution in Vial A was added to the $NiCl_2$ (Vial B) and to this was added concentrated aqueous ammonium hydroxide (0.60 mL). The reaction was heated without stirring at 65°C for 2 hours. At the beginning of the reaction, one gold interdigitated electrode was taped with Kapton tape so that the leads were covered, and was submerged in the reaction vial so the film could grow onto the electrode. In addition to the film that grew on the electrode, a black flaky solid had settled at the bottom of the reaction vial. For purification, the electrode was heated in deionized water for 30 minutes at 60 °C then methanol for 30 minutes at 60 °C, then dried under dynamic vacuum and stored under N_2 for 12 hours before use.

Chemiresistive measurement. The device was wired up to a breadboard and flipped upside down so that the top of the electrode (the $Ni_3(HITP)_2$-modified portion) could be submerged into 0.1 M KOH electrolyte that had been sparged with N_2 for 30 minutes prior to data collection, then sparged constantly during data collection. The cell was sealed at the top with Parafilm, and holes were cut for the sparge tube, pH meter, and interdigitated electrode to be submerged in the electrolyte. A constant potential of 50 mV was applied, and the current was measured as a function of time. Current was measured for 2 minutes, then 1.0 M $HClO_4$ was titrated into the electrolyte to lower the pH. Current was measured again for 2 min or until steady state was achieved, and then more acid was added. This was repeated until the electrolyte reached pH 8.5. 1.0 M

KOH was then used to titrate the electrolyte back up to pH 12.9, still monitoring the current. Change in current ($\Delta G/G_0$) versus time was plotted.

Probing the pH-dependent redox potentials of $Ni_3(HITP)_2$. Cyclic voltammetry (CV) was run with an unmodified glassy carbon electrode from E = −1.1 V to E = 0.7 V versus SCE, then the first $Ni_3(HITP)_2$-modified electrode was used in pH 13.6, and CV was run scanning cathodically first from E = −1.1 V to E = 0.7 V versus SCE for two cycles (electrode 1). The electrolyte was then titrated to pH 12.5, an unused $Ni_3(HITP)_2$-modified working electrode (electrode 2) was installed, and the procedure was repeated. The electrolyte was then titrated to pH 11.8, and the same procedure for electrode 1 was used on the new electrode 3. The electrolyte was then titrated to pH 10.6, and the same procedure for electrode 1 was used on the new electrode 4. The electrolyte was then titrated to pH 11.2, and the same procedure for electrode 1 was used on the new electrode 5. The electrolyte was then titrated to pH 9.4, and the same procedure for electrode 1 was used on the new electrode 6. The electrolyte was then titrated to pH 8.9, and the same procedure for electrode 1 was used on the new electrode 7. The potentials associated with the peak currents passed in the three MOF oxidation events were plotted versus pH.

X-ray absorption spectroscopy of $Ni_3(HITP)_2$.

Synthesis of $Ni_3(HITP)_2$ film on the ITO-coated polyethylene terephthalate (PET) electrode. 2,3,6,7,10,11-hexaaminotriphenylene·6HCl (HATP) salt (10 mg) was dissolved in deionized water (4 mL) and heated to 65 °C in a 20 mL capped scintillation vial (Vial A). In a second glass reaction vial (Vial B), nickel(II) chloride hexahydrate (10 mg) was dissolved in deionized water (4 mL). The heated HATP solution in Vial A was added to the $NiCl_2$ (Vial B) and to this was added concentrated aqueous ammonium hydroxide (0.60 mL). The reaction was heated without stirring at 65°C for 2 h. At the beginning of the reaction, two ITO-coated PET electrodes (1 x 2 cm) were submerged in the reaction vial so the film could

grow onto the electrodes. In addition to the film that grew on the electrode, a black flaky solid had settled at the bottom of the reaction vial. For purification, the electrode was heated in deionized water for 30 minutes at 60 °C then methanol for 30 minutes at 60 °C, then dried under dynamic vacuum and packed under argon for shipment to the Stanford Synchrotron Radiation Lightsource.

In-situ X-ray absorption spectroscopy during ORR and electroreduction of the MOF. X-ray absorption spectroscopy (XAS) measurements on the Ni K-edge were performed at the Stanford Synchrotron Radiation Lightsource (SSRL) on beamline 9-3 with an electron energy of 3.0 GeV and an average ring current of 500 mA. The radiation was monochromatized using a cryogenically cooled Si (220) double-crystal monochromator which was detuned to 50% of the maximum flux at the Ni K-edge to eliminate higher harmonics. The incident and transmitted X-ray intensities were monitored by N_2-filled ion chambers (I_0, in front of the sample and I_1 behind the sample). Absorption spectra were recorded in transmission mode (using ion chamber I_1) for powder samples which were diluted with boron nitride (1% w/w) and packed in 0.5 mm aluminum sample holders using Kapton tape windows on both sides. The edge energy was calibrated with the Ni foil (placed between I_1 and I_2 ion chambers) spectrum by setting the first peak of the first derivative at 8333.0 eV. For the in-situ ORR experiment, the XAS data was recorded in fluorescence mode using a 100-element Ge monolithic solid-state detector (Canberra), and energy calibration was done by monitoring a glitch in the I_0 intensity.

The in-situ spectroscopic experiment was performed using a two-compartment glass cell as reported previously.[156] In this setup, a porous frit separated the two compartments and the compartment housing the working electrode has featured a hole with a diameter of 0.8 cm. A $Ni_3(HITP)_2$-coated ITO / PET substrate, as described above, was glued onto this hole with the catalyst film facing towards inside of the compartment (exposed to the electrolyte) and the X-rays probing through the unmodified side of the working electrode (facing the outside hutch). Electrochemistry was done using a Pt gauze counter electrode

and a Ag/AgCl reference electrode. The two compartments of the cell were filled with 0.1 M aqueous KOH and O_2 gas was constantly bubbled through the working compartment.

SamView (SixPack software, http://www.sams-xrays.com/sixpack) was used for XAS data reduction. Pre-edge and post-edge backgrounds were removed from the absorption spectra using Athena software (Demeter version 0.9.25),[157] and the resulting spectra were normalized with respect to the edge height. Background removal in *k*-space was done using a five-domain cubic spline. The extracted *k*-space data, $k^2\chi(k)$, was then Fourier transformed (FT) into *r*-space using a *k*-space window of 2.55–11.60 $Å^{-1}$. Artemis (Demeter software version 0.9.25) was used for fitting the EXAFS data in R-space where *ab initio* calculated phases and amplitudes were determined using program FEFF6 and used in the EXAFS equation

$$\chi(k) = S_0^2 \sum_j \frac{N_j}{kR_j^2} f_{eff_j}(\pi, k, R_j) e^{-2\sigma_j^2 k^2} e^{-2R_j/\lambda_j(k)} sin[2kR_j + \phi_{ij}(k)]$$

where N_j represents the coordination number of neighboring atoms in shell j at a distance R_j from the central atom(s). The $f_{eff_j}(\pi, k, R_j)$ term is the calculated amplitude function and the Debye-Waller term $e^{-2\sigma_j^2 k^2}$ denotes the amplitude damping due to thermal and static disorder in absorber-backscatterer distances. Losses due to inelastic scattering are defined by the mean free path term $e^{-2R_j/\lambda_j(k)}$, where $\lambda_j(k)$ is the electron mean free path. The sinusoidal term $\sin[2kR_j + \varphi_{ij}(k)]$ reflects the EXAFS oscillations where $\varphi_{ij}(k)$ is the *ab initio* phase function. The S_0^2 term is the amplitude reduction factor due to shake-up / shake-off processes occurring at the absorbing atom and is determined empirically. During the EXAFS fitting process, variable parameters included the bond distance (R_j) and mean square displacement of the bond distance (σ_j^2). In addition to the structural parameters, a non-structural parameter E_0 (the energy which represents the zero value of the photoelectron wave vector k) was also varied but restricted to a common value for each path in a given fit. The value for S_0^2 was determined from the fit to the data of nickel(II) phthalocyanine, and was fixed (0.80) during the fits. Some multiple scattering paths were also included in the fits to improve the fit quality.

It is important to note that the abscissa in **Figure 3-8b** represents the apparent distance (R') which is shorter than the real distance by ~0.5 Å due to the phase shift. The extracted best fit parameters are listed in **Table 3-3**. For the as-prepared sample as well as for the sample during ORR, to fit the EXAFS data between R' 1.65 and 2.0, a Ni–O path (from the $Ni(OH)_2$ phase) had to be included but the contribution accounted for only ~5% of Ni sites. There was not much contribution from the second shell Ni–Ni path of the hydroxide phase. This suggested that small molecular-sized $Ni(OH)_2$ particles may have been trapped in the $Ni_3(HITP)_2$ pores. The theoretical EXAFS functions were calculated using the $Ni_3(C_{18}H_{12}N_6)_2$ crystal structure information reported previously[158] as a slipped parallel model with an interlayer distance of 3.33 Å. In the best fit, distances of the nearest N and Ni from the neighboring layers were found to be at slightly longer distances (by ~0.2 Å) than the calculated phase in which the neighboring layers are displaced by $1/16^{th}$ in both the *a* and *b*-axis. This suggested a slightly greater displacement of the layers in the *ab*-plane than was featured in the calculated structure. Longer distances for both N and Ni suggested that the MOF layers were slightly more displaced along the *b*-axis than the *a*-axis. A relatively larger uncertainty in the bond distances and σ^2 values (**Table 3-3**) for neighboring layer N and Ni reflected a comparatively less ordered structure along the *c*-axis.

Cyclic voltammetry of $Ni(ISQ)_2$.

Synthesis of $Ni(ISQ)_2$.[149] A solution of 0.33 g of nickel chloride hexahydrate in 1.0 mL of water and 1.0 mL of concentrated aqueous ammonia was added to a solution of 0.2 g of *o*-phenylenediamine in 200 mL of warm (65 °C) water. This mixture was stirred in an open beaker for 24 hours. A deep blue / black precipitate formed and was collected by centrifugation (green supernatant), the solids were washed with water while stirring at 65 °C for 30 minutes, the suspension was centrifuged again, then the solids were washed with acetone while stirring at 23 °C, the suspension was centrifuged again, and the solids were

dried under dynamic vacuum. The material was stored under N_2 for 12 hours before use. Successful synthesis of the target material was confirmed with ^{1}HNMR in DMSO-d6, IR, and non-aqueous CV.

Deposition of $Ni(ISQ)_2$ onto the working electrodes. 2 mg of $Ni(ISQ)_2$ was suspended in 0.2 mL of acetone, sonicated for 20 minutes, then 2 x 5 μL of the suspension were dropcast onto both glassy carbon and ITO. CV was run in 0.1 M KOH with an SCE reference electrode and Pt counter electrode under both N_2 and O_2 atmosphere to assess the inherent ORR activity of $Ni(ISQ)_2$ compared to blank ITO and glassy carbon. To prevent the material from falling off of the working electrodes, neither were rotated. ORR activity of $Ni(ISQ)_2$ was tested on ITO in addition to glassy carbon to assess whether the activity observed on glassy carbon was simply the background ORR activity of the unmodified glassy carbon (ITO has considerably less ORR activity than glassy carbon).

Computational details. The B3LYP functional[159,160] and basis set 6-31+g(d),[161–164] with implicit solvation model IEF-PCM[165,166] were employed for the computational investigations. Density functional theory was utilized with the software package Q-Chem.[167] The free energy of each step in the O_2 reduction reaction was calculated using an established protocol that initially calculates the free energy of formation for each reactant and product.[168] Experimental atomization energies for the reference compounds at 0 K were utilized[169] along with DFT to calculate the energy of forming $Ni(ISQ)_2$ and $Ni_3(HITP)_2$ fragments from atoms at 0 K to obtain each atomization energy. Harmonic frequency analysis of the molecules in DFT to calculate the entropy and enthalpy of heating the compounds to 298 K, and implicit solvent for the free energy of solvation, were used to calculate the free energy of formation for each species. The molecular orbitals and spin density plots were generated using Visual Molecular Dynamics (VMD)[170] with an isovalue of 0.035 for the generated isosurfaces.

Chapter 4

Modular O_2 Electroreduction Activity in Triphenylene-Based Metal-Organic Frameworks

Portions of this chapter previously appeared in Miner, E. M.; Wang, L.; Dincă, M. *Chem. Sci.*, **2018**, 9, 6286-6291 and are reproduced here with permission from the Royal Society of Chemistry.

4.1 Introduction

Control over the architectural and electronic properties of heterogeneous catalysts poses a major obstacle in the targeted design of active, stable, and economically sustainable materials for producing fuels.[171] Metal-organic frameworks (MOFs) are compelling choices for electrocatalytic applications as their high surface area and tunable porosity and ligand structure affords densely packed active sites and tailor-made microenvironments for controllable reaction conditions within the pores. Despite the high potential for MOF-based electrocatalysts, synthesis of these materials often involves chelation of hard metal ions to hard N or O atoms in redox-inactive ligands. Typical compositions thus offer no low energy charge transport pathways or charge carriers, rendering these materials electrically insulating.[73] Excitingly, the emergence of intrinsically conducting or semiconducting metal-organic species[73,172–178] has made accessible the use of such materials as tunable, high surface area electrocatalysts for energy conversion reactions such as H_2 evolution,[179,180] O_2 evolution,[180,181] CO_2 reduction,[177] O_2 reduction,[137,182] and others.[183] The high level of atomic definition in these materials offers an opportunity to gain insight into the operative catalytic mechanisms and establish structure-function behavior. In particular, mechanistic studies of $Ni_3(HITP)_2$ (HITP = 2,3,6,7,10,11-hexaiminotriphenylene) revealed that the O_2 reduction reaction (ORR) proceeds on a ligand-based active site, and suggested that the metal identity and electron delocalization throughout the framework could have important implications for the electronic structure which in turn should govern electrocatalytic activity.[184] Herein, the role of the metal identity, chelating atom, and π-stacking in a suite of triphenylene-based conductive MOFs in influencing the ORR activity and mechanism is probed, with the goal of identifying the key players in this class for MOFs for dictating electrocatalytic behavior.

4.2 Results and discussion

To this end, several analogues featuring a hexa-substituted triphenylene core were synthesized. As shown in **Figure 4-1**, chelation of a divalent first-row transition metal with either the hexaamino or

hexahydroxytriphenylene (HHTP) ligand in the presence of base and air affords one of two phases. The three analogues of the hexagonal crystal system, $Ni_3(HITP)_2$, $Cu_3(HITP)_2$, and $Cu_3(HHTP)_2$ (referred to as the hexagonal MOFs), featured a 2D honeycomb lattice stacked in a slipped parallel configuration along the *c* axis (**Figure 4-1a and c**).[172,173,176] The two analogues of the trigonal crystal system, $Co_3(HHTP)_2$ and $Ni_3(HHTP)_2$ (referred to as the trigonal MOFs), featured alternating layers of the honeycomb lattice and

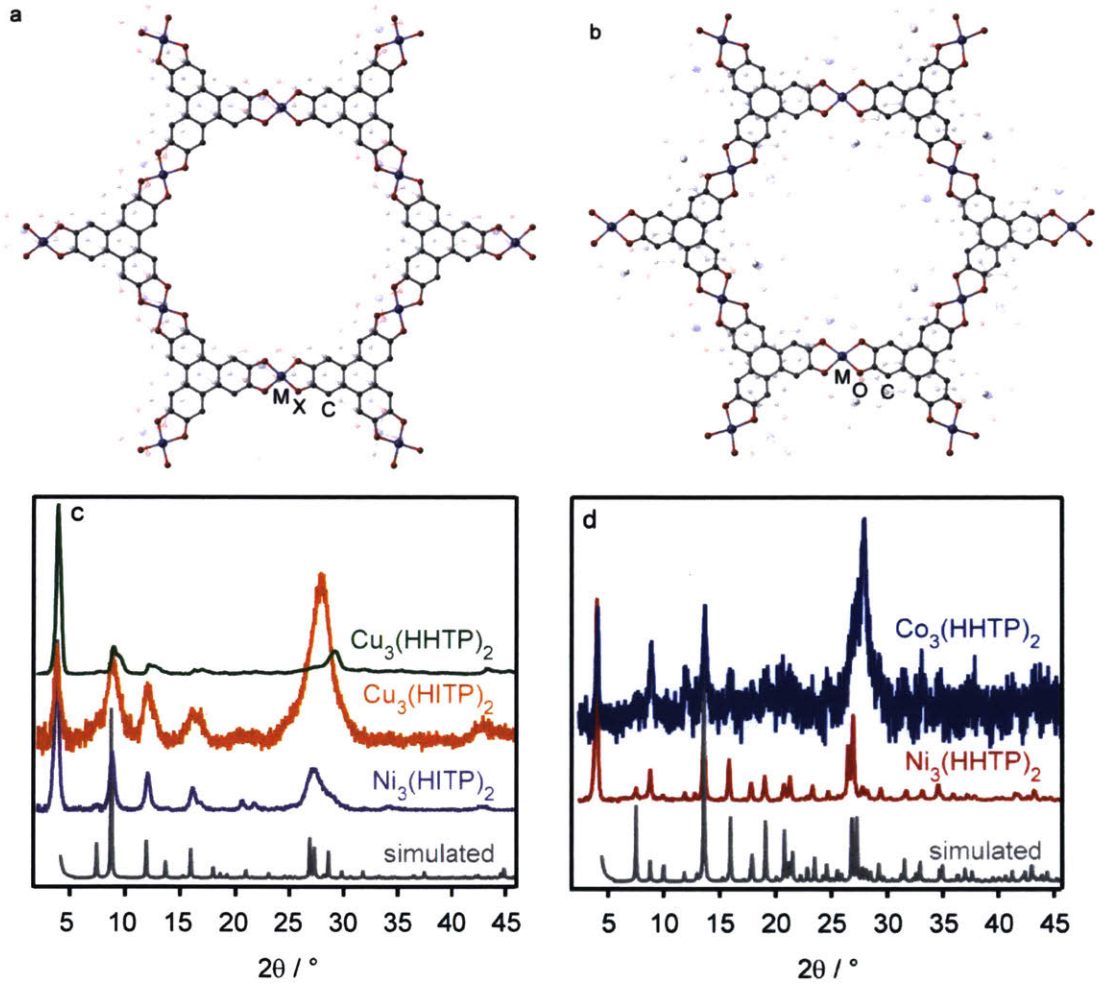

Figure 4-1. a) Hexagonal and **b)** trigonal phases of the triphenylene MOFs, and corresponding powder X-ray diffraction patterns (**c** and **d** for hexagonal and trigonal diffraction patterns, respectively). M = Co, Ni, or Cu; X = NH or O. H atoms are omitted for clarity.

trinuclear $M_3(HHTP)(H_2O)_{12}$ clusters that were rotated 60° with respect to the honeycomb lattice (**Figure 4-1b and d**).[176] Isolation of the hexagonal MOFs as well as the trigonal MOFs was confirmed with powder X-ray diffraction (**Figure 4-1c and d**).

The ORR activity of the MOF powders deposited on glassy carbon electrodes was probed in pH 13 and 8. The reductive current shown in **Figure 4-2** was observed for all analogues only under O_2, confirming that the current indeed stems from O_2 reduction (**Figure 4-3**). The cyclic voltammograms under O_2 atmosphere shown in **Figure 4-2** revealed that the hexagonal MOF $Cu_3(HITP)_2$ exhibited the highest initial ORR activity in both pH environments. However, the instability of this analogue to O_2 under experimental conditions resulted in a rapid loss of activity after the first CV cycle (**Figure 4-4**). This instability prevented collection of reliable data for ORR with $Cu_3(HITP)_2$, as the catalyst activity continuously declined during prolonged data collection. The other hexagonal MOFs, $Ni_3(HITP)_2$ and $Cu_3(HHTP)_2$, reduced O_2 with

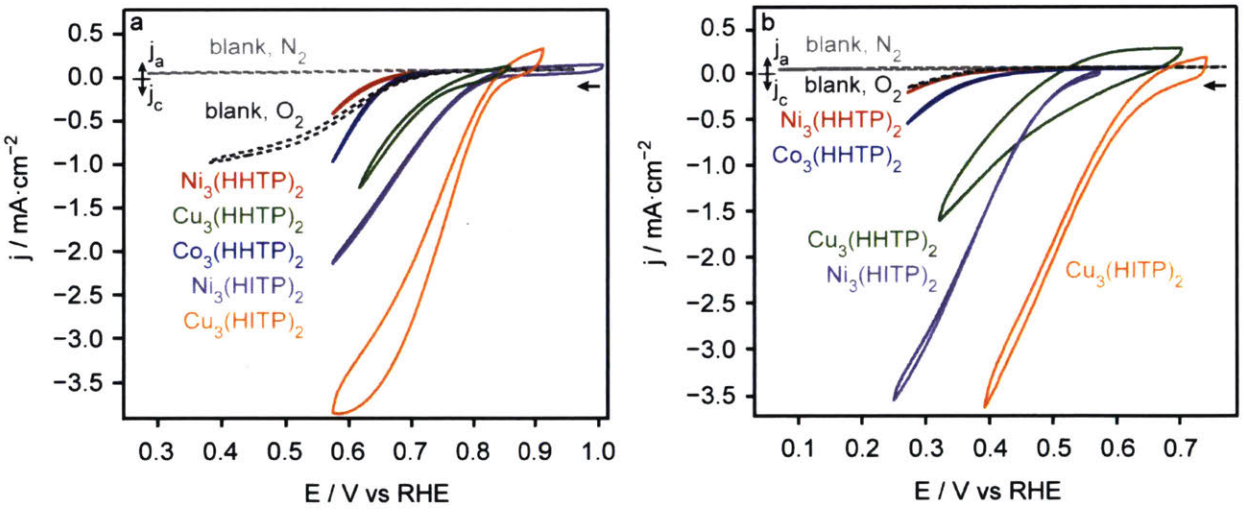

Figure 4-2. Cyclic voltammograms of O_2 electroreduction with the triphenylene MOFs in **a)** pH 13 and **b)** pH 8 electrolyte. "Blank" indicates the background current from the unmodified glassy carbon electrode cycled under O_2 and N_2 atmosphere.

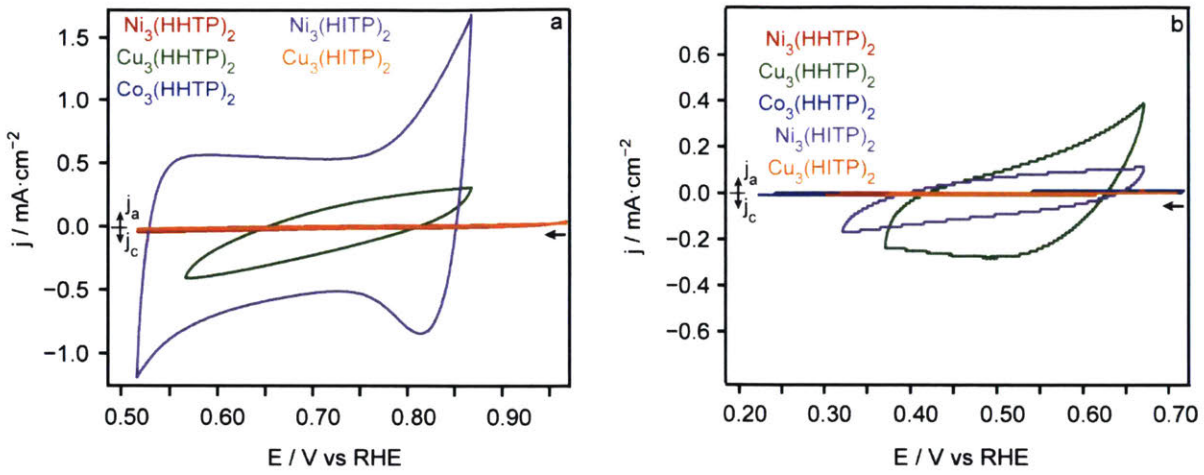

Figure 4-3. Cyclic voltammograms of the triphenylene MOFs under N_2 in **a)** pH 13 and **b)** pH 8.

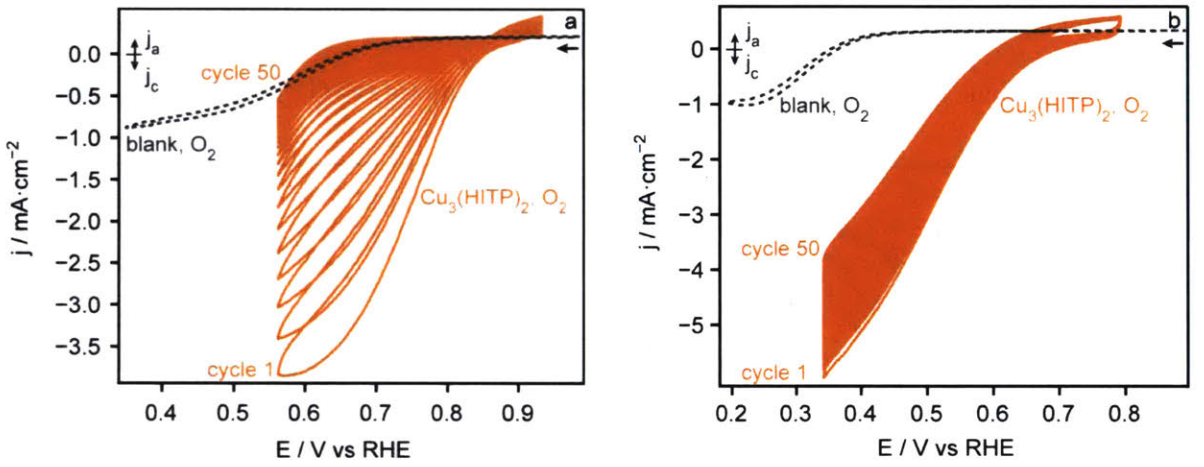

Figure 4-4. Cyclic voltammograms of $Cu_3(HITP)_2$ under O_2 in **a)** pH 13 and **b)** pH 8, showing the loss of activity due to instability of the catalyst. "Blank" indicates the background current from the unmodified glassy carbon electrode.

lower overpotential and higher current density than the trigonal MOFs. Although the trigonal MOFs $Co_3(HHTP)_2$ and $Ni_3(HHTP)_2$ seemed to contribute no catalytic activity beyond the glassy carbon background current, depositing these analogues on the more inert indium tin oxide showed nominal ORR

activity (**Figure 4-5**). This substrate-independent activity confirmed that kinetic data collected for these analogues on glassy carbon rotating disk electrodes represents the ORR kinetics of the MOFs rather than simply the blank electrodes. Potentiostatic reduction of O_2 over 8 hours in pH 13 revealed that the HHTP-based MOFs deactivated more quickly in base than did $Ni_3(HITP)_2$ (**Table 4-1**). This is likely due to

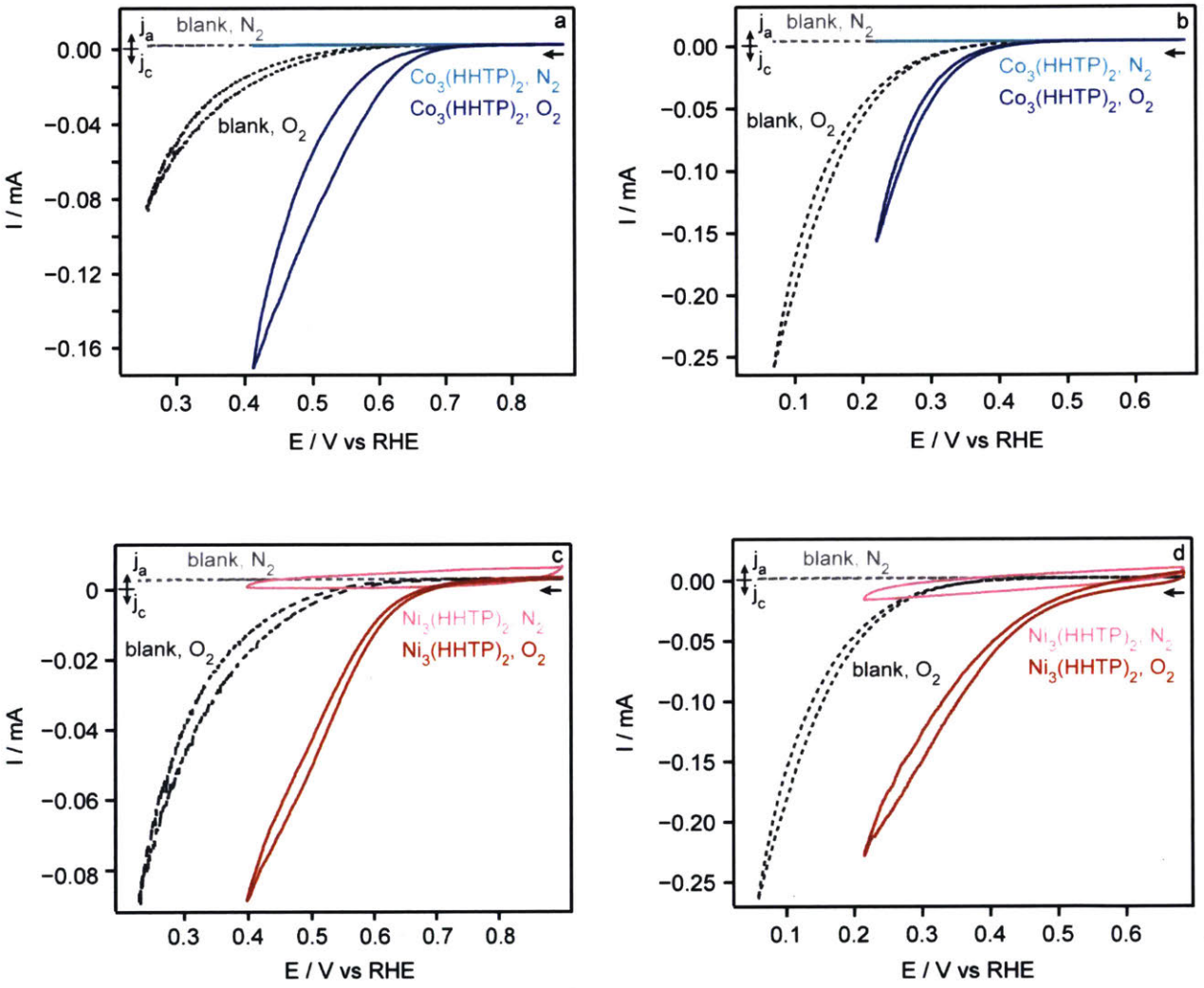

Figure 4-5. Cyclic voltammograms of $Co_3(HHTP)_2$ deposited on indium tin oxide (blank) in **a)** pH 13 and **b)** pH 8, and of $Ni_3(HHTP)_2$ in **c)** pH 13 and **d)** pH 8 under N_2 (lighter colors) and O_2 (darker colors).

Table 4-1. % current retained during potentiostatic ORR in pH 13 after 8 hours.

MOF	% current retained after 8 hours ORR
$Ni_3(HITP)_2$	88[137]
$Cu_3(HITP)_2$	6
$Co_3(HHTP)_2$	62
$Ni_3(HHTP)_2$	58
$Cu_3(HHTP)_2$	73

thermodynamic differences arising from better energetic and / or spatial overlap between the HITP ligand and Ni orbitals than the HHTP ligand and metal orbitals. The resulting longer metal-ligand bond distances in the HHTP MOFs could enable more facile decomposition of these analogues compared to that which features Ni-N coordination.[176,185–187]

To determine the product distribution of ORR with the triphenylene MOFs and how this may change as a function of increasing driving force, potentiostatic rotating ring disk electrode (RRDE) studies were conducted over the ORR potential window (**Figure 4-6**). Dividing the anodic current passed at the Pt ring from back-oxidizing the $2e^-$ reduction product by the total cathodic current passed at the MOF-modified disk from both the $2e^-$ and $4e^-$ reduction products (hydrogen peroxide and water, respectively) gave the potential-dependent faradaic efficiency plots shown in **Figure 4-7**. Unsurprisingly,[188] all MOFs exhibited potential-dependent faradaic efficiency, with the $4e^-$ reduction product favored when more than ~300 mV of overpotential is applied, and with the $2e^-$ reduction product favored at lower overpotentials.

The kinetic rate laws for ORR with the hexagonal and trigonal MOFs were obtained by probing the order in $[O_2]$, $[H^+]$, and electrons. Koutecky-Levich data collected in pH 8 and 13 (**Figure 4-8**) was used to generate activation-controlled Tafel plots (**Figure 4-9**) with slopes of 110-170 $mV \cdot dec^{-1}$ (**Table 4-2**). A slope of 118 $mV \cdot dec^{-1}$ is indicative of rate-limiting electron transfer,[21] and relevant for all analogues here.

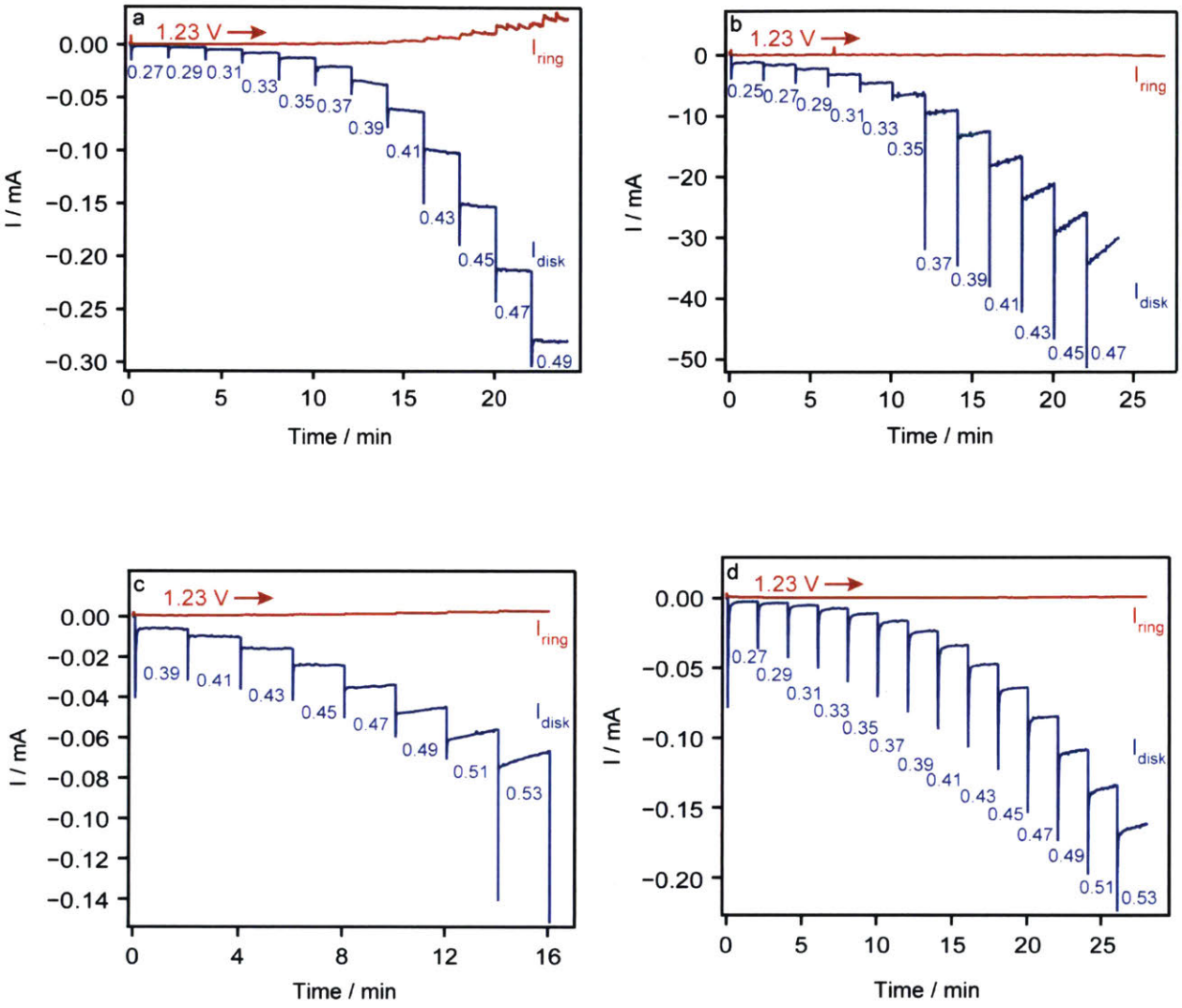

Figure 4-6. RRDE data for ORR with a) $Ni_3(HITP)_2$, b) $Co_3(HHTP)_2$, c) $Ni_3(HHTP)_2$, and d) $Cu_3(HHTP)_2$ in pH 8. Red indicates the ring current and blue indicates the disk current. Ring held at a constant potential of 1.23 V vs RHE. Disk potentials are listed as ORR overpotentials (η, V).

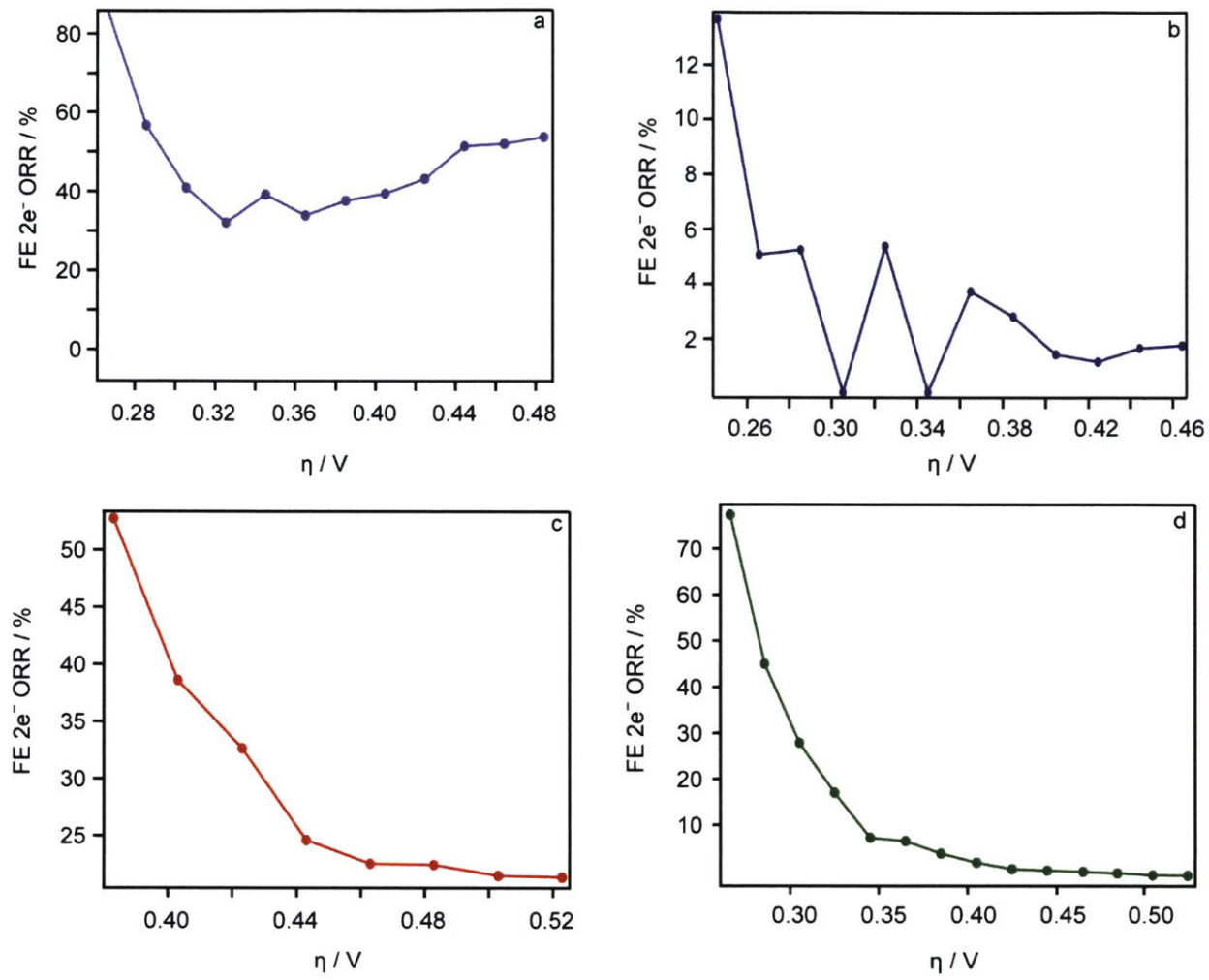

Figure 4-7. Faradaic efficiency (FE) for $2e^-$ ORR as a function of ORR overpotential with **a)** $Ni_3(HITP)_2$, **b)** $Co_3(HHTP)_2$, **c)** $Ni_3(HHTP)_2$, and **d)** $Cu_3(HHTP)_2$ in pH 8.

One notable exception is the Tafel data collected for $Co_3(HHTP)_2$ in pH 13, which featured a Tafel slope of 81 $mV \cdot dec^{-1}$. This slope could indicate that in pH 13, ORR with $Co_3(HHTP)_2$ did not proceed with rate-limiting electron transfer, but rather perhaps with rate-limiting O_2 chemisorption.[12] This pH-dependent electrokinetic behavior was consistent with the behavior Co-macrocycles active for ORR catalysis.[189] The Tafel data not only gave insight into whether rate-limiting electron transfer is relevant, but also provided

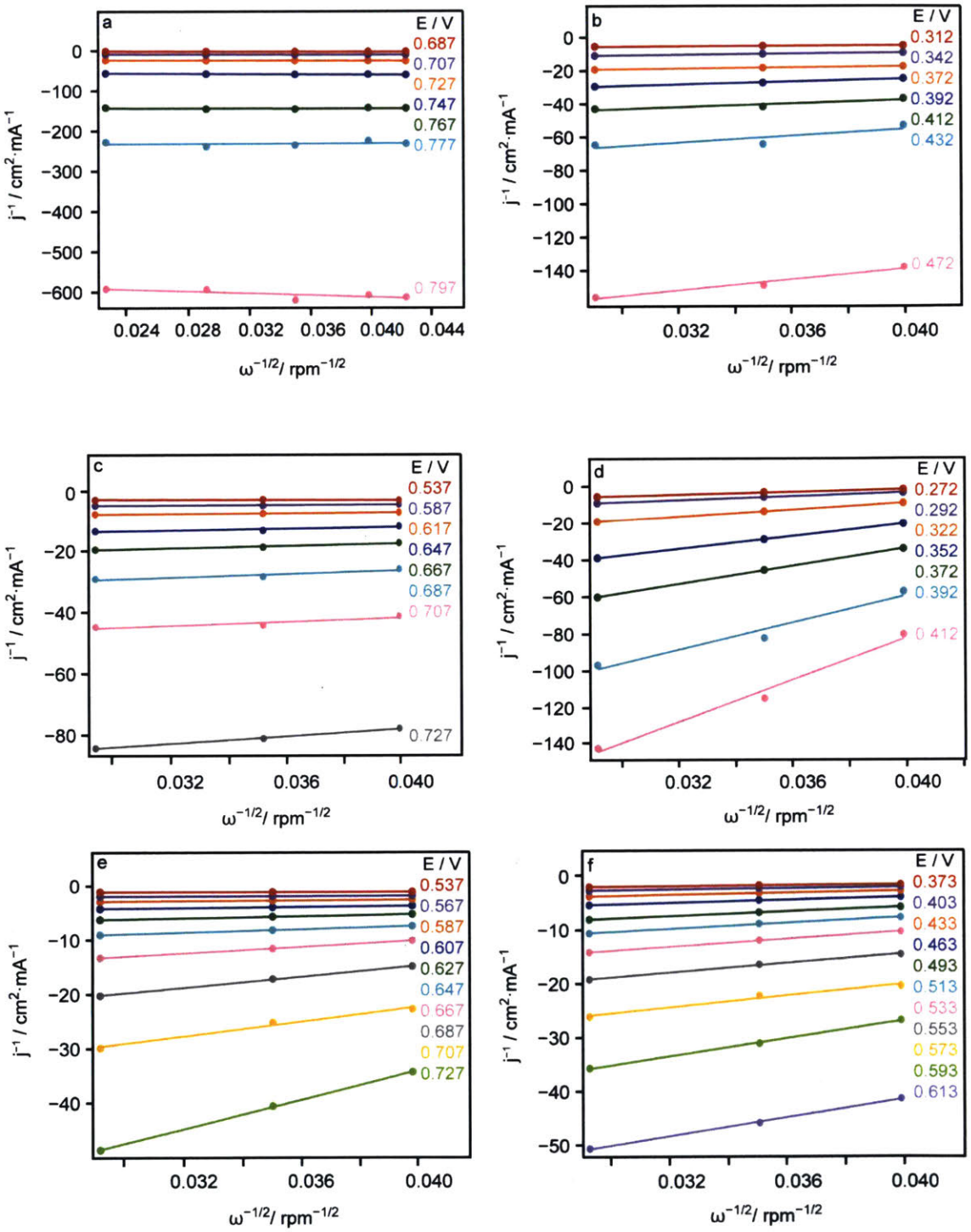

Figure 4-8. Koutecky-Levich plots (E vs RHE) used to generate the activation-controlled Tafel plots in **Figure 4-9**. $Co_3(HHTP)_2$ in pH 13 and 8 is shown in **a** and **b** respectively, $Ni_3(HHTP)_2$ in pH 13 and 8 is shown in **c** and **d** respectively, and $Cu_3(HHTP)_2$ in pH 13 and 8 is shown in **e** and **f**, respectively.

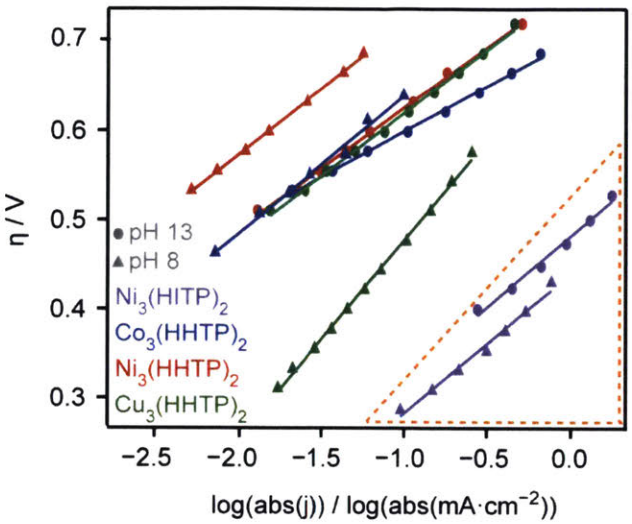

Figure 4-9. Tafel plots from ORR with the triphenylene MOFs at pH 13 (circles) and 8 (triangles). η represents the ORR overpotential and j represents the current density at a given overpotential. Orange dashed section indicates best catalyst performance (high current density passed with low overpotential).

Table 4-2. Tafel slopes corresponding to the Tafel plots in **Figure 4-9**.

MOF	pH	Tafel slope ($V \cdot dec^{-1}$)
$Ni_3(HITP)_2$	8	0.124
$Cu_3(HHTP)_2$	8	0.170
$Ni_3(HHTP)_2$	8	0.120
$Co_3(HHTP)_2$	8	0.120
$Ni_3(HITP)_2$	13	0.128
$Cu_3(HHTP)_2$	13	0.110
$Ni_3(HHTP)_2$	13	0.110
$Co_3(HHTP)_2$	13	0.081

relative rate constants as a means to directly compare catalytic activity (**Table 4-3**). The placement of the Tafel slopes from $Ni_3(HITP)_2$ in the lower right quadrant of the Tafel plot (**Figure 4-9**, dashed triangle) reflected the fast electrokinetics of this analogue at both pH 8 and 13, i.e. $Ni_3(HITP)_2$ passed a high cathodic current density (log(j)) with low overpotential (η).[12,21]

Table 4-3. Exchange current density values (j_0) as metrics for comparing ORR electrokinetics of the various MOF catalysts. Higher exchange current density is indicative of faster electrokinetics.

pH	MOF	Tafel equation	log(abs(j_0))	j_0 / mA·cm^{-2}
13	$Ni_3(HITP)_2$	y = 0.128x + 0.458	−3.5781	$2.64 \cdot 10^{-4}$
13	$Co_3(HHTP)_2$	y = 0.081x + 0.664	−8.1975	$6.35 \cdot 10^{-9}$
13	$Ni_3(HHTP)_2$	y = 0.107x + 0.714	−6.6729	$2.12 \cdot 10^{-7}$
13	$Cu_3(HHTP)_2$	y = 0.112x + 0.732	−6.5357	$2.91 \cdot 10^{-7}$
8	$Ni_3(HITP)_2$	y = 0.124x + 0.420	−3.3871	$4.10 \cdot 10^{-4}$
8	$Co_3(HHTP)_2$	y = 0.122x + 0.741	−6.0738	$8.44 \cdot 10^{-7}$
8	$Ni_3(HHTP)_2$	y = 0.117x + 0.810	−6.9231	$1.19 \cdot 10^{-7}$
8	$Cu_3(HHTP)_2$	y = 0.176x + 0.648	−3.6818	$2.08 \cdot 10^{-4}$

Potentiostatic data collected with varying overpotential and varying concentrations of O_2 in the electrolyte showed that for all analogues, more cathodic current (I) could be passed with increasing $[O_2]$ in pH 8 (**Figure 4-10**). This linear increase in log(I) versus log($[O_2]$) with slopes of ~1 (**Table 4-4**) over the ORR potential window indicated that all analogues followed first-order kinetics in $[O_2]$. It is noted that although the $\delta\log(I)/\delta\log(\%O_2)$ slope reflecting the ORR order in $[O_2]$ with $Cu_3(HITP)_2$ was reported here as 0.47-0.53, this may be quantitatively inaccurate due to the instability of this analogue to O_2. This data was included to reflect that ORR with $Cu_3(HITP)_2$, as with all other analogues reported here, exhibited a non-zero order in $[O_2]$. Experimental and computational data previously reported for ORR with $Ni_3(HITP)_2$

suggested rate-limiting O_2 binding concomitant with e^- transfer to $Ni_3(HITP)_2$ to form the superoxide adduct was likely.[137,184] The similar $[O_2]$ order and Tafel data of the triphenylene MOF analogues (with the exception of ORR with $Co_3(HHTP)_2$ in pH 13) supported the assertion that all other triphenylene MOFs reported here also exhibited rate-limiting electron transfer-O_2 binding to the catalyst during ORR.

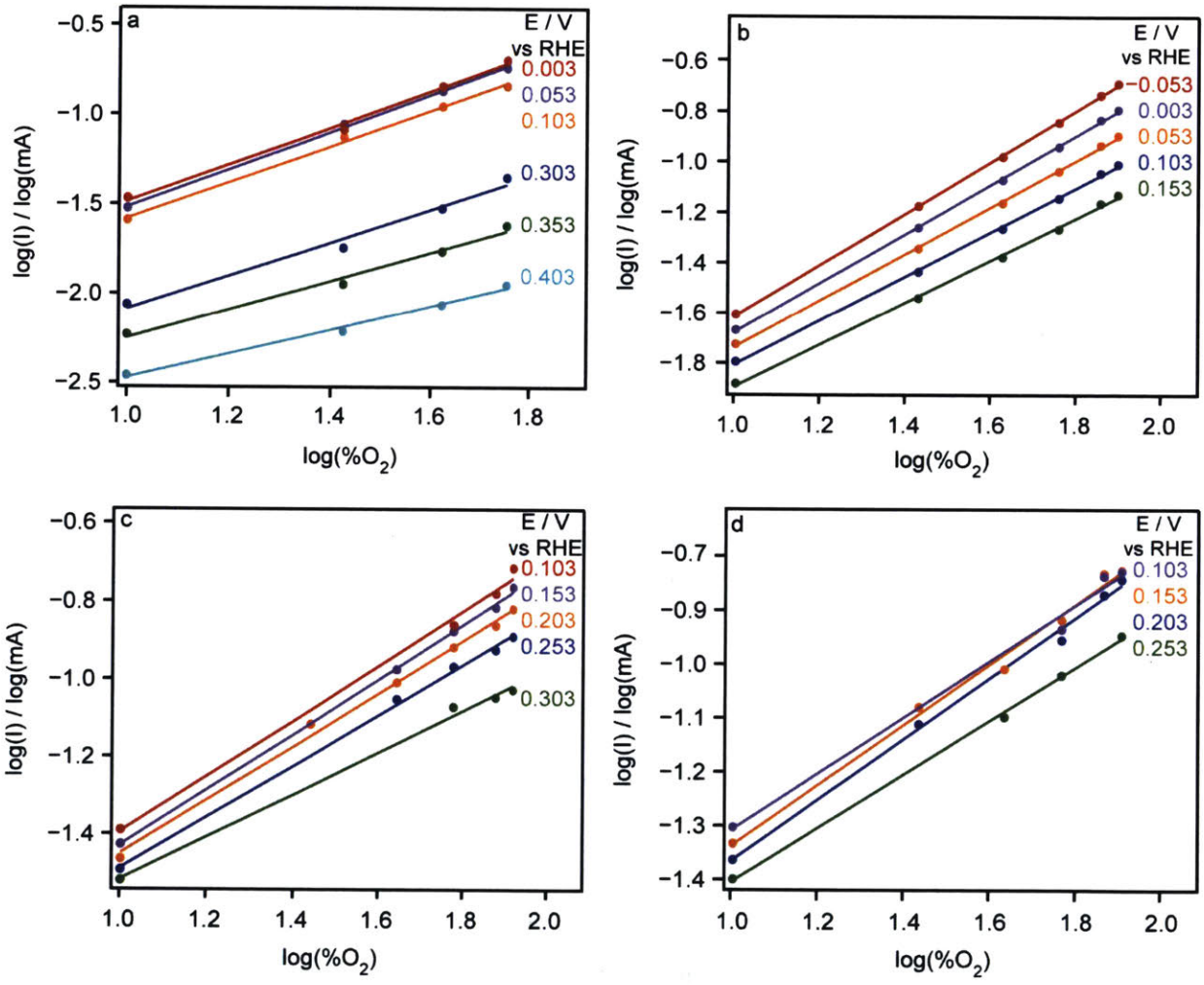

Figure 4-10. Potentiostatic $[O_2]$ order data for **a)** $Co_3(HHTP)_2$, **b)** $Ni_3(HHTP)_2$, **c)** $Cu_3(HHTP)_2$, and **d)** $Cu_3(HITP)_2$ in pH 8. Refer to Chapter 3 for the ORR $[O_2]$ order data for $Ni_3(HITP)_2$.

Given that the Tafel data from all analogues pointed to ORR proceeding with rate-limiting electron transfer, and considering the protonated nature of the ORR products, we investigated the possibility of

proton-coupled electron transfer (PCET) occurring in our systems. Galvanostatic data from each analogue was collected under O_2 while titrating the electrolyte from pH 13.5 to pH 8 (**Figure 4-11**). As shown in **Table 4-5**, all hexagonal MOFs exhibited a non-zero dependence of the ORR overpotential with $[H^+]$, whereas the trigonal MOFs featured $\delta E/\delta pH$ slopes of nearly zero. The independence of ORR overpotential on $[H^+]$ during ORR with the trigonal MOFs suggested that no electron transfer during ORR with those analogues was proton-coupled.[147] In contrast, all hexagonal MOFs exhibited a non-zero order in $[H^+]$. As

Table 4-4a. Corresponding slopes of the variable potential $[O_2]$ order plots collected in pH 8 for $Co_3(HHTP)_2$ (**Figure 4-10a**).

E / V vs RHE	Slope
0.403	0.60
0.353	0.72
0.303	0.84
0.103	0.91
0.053	0.94
0.003	0.93

Table 4-4b. Corresponding slopes of the variable potential $[O_2]$ order plots collected in pH 8 for $Ni_3(HHTP)_2$ (**Figure 4-10b**).

E / V vs RHE	Slope
0.153	0.80
0.103	0.84
0.053	0.88
0.003	0.93
-0.053	0.97

Table 4-4c. Corresponding slopes of the variable potential [O_2] order plots collected in pH 8 for $Cu_3(HHTP)_2$ (**Figure 4-10c**).

E / V vs RHE	Slope
0.303	0.52
0.253	0.62
0.203	0.65
0.153	0.68
0.103	0.68

Table 4-4d. Corresponding slopes of the variable potential [O_2] order plots collected in pH 8 for $Cu_3(HITP)_2$ (**Figure 4-10d**).

E / V vs RHE	Slope
0.253	0.47
0.203	0.53
0.153	0.53
0.103	0.49

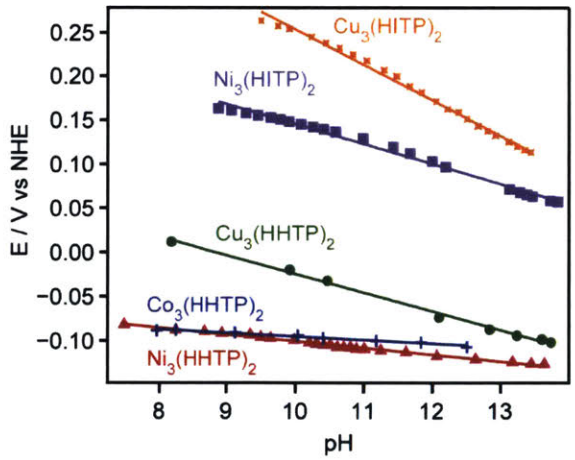

Figure 4-11. Dependence of ORR onset potential on pH for the triphenylene MOFs. Purple squares, orange X symbols, blue cross symbols, red triangles, and green circles correspond to $Ni_3(HITP)_2$, $Cu_3(HITP)_2$, $Co_3(HHTP)_2$, $Ni_3(HHTP)_2$, and $Cu_3(HHTP)_2$ respectively.

seen with $Ni_3(HITP)_2$,[184] the $\delta E/\delta pH$ slopes for all hexagonal MOFs were ~20 $mV \cdot dec^{-1}$, revealing a fractional $[H^+]$ dependence that ruled out rate-limiting PCET.[147] Although the $\delta E/\delta pH$ slope reflecting the ORR order in $[H^+]$ with $Cu_3(HITP)_2$ is reported here as 0.039 $V \cdot dec^{-1}$, this may be quantitatively inaccurate due to the instability of this analogue to O_2 under experimental conditions. This data was included to reflect that ORR with $Cu_3(HITP)_2$, as with the other hexagonal analogues, exhibits a non-zero order in $[H^+]$.

Table 4-5. Slopes corresponding to the ORR $[H^+]$ order data in **Figure 4-11**.

MOF	Phase	$\delta E/\delta pH$ ($V \cdot dec^{-1}$)
$Ni_3(HITP)_2$	Hexagonal	0.022
$Cu_3(HITP)_2$	Hexagonal	0.039
$Cu_3(HHTP)_2$	Hexagonal	0.020
$Ni_3(HHTP)_2$	Trigonal	0.007
$Co_3(HHTP)_2$	Trigonal	0.004

To explore the relationship between electron transfer and available proton concentration, cyclic voltammetry was run on the various MOFs under an inert atmosphere in varying pH environments. As previously observed with $Ni_3(HITP)_2$,[184] the hexagonal analogues $Cu_3(HHTP)_2$ and $Cu_3(HITP)_2$ underwent oxidation events that exhibited Nernstian pH dependence, i.e. were proton-coupled (**Figure 4-12 and 4-13**).[147] As with $Ni_3(HITP)_2$, the fractional $[H^+]$ order observed in ORR with the hexagonal analogues likely stemmed from PCET in the MOF-hydroperoxide adduct. If the rate of this second, proton-coupled electron transfer to O_2 was only marginally faster than the rate-limiting first electron transfer to O_2, some fractional $[H^+]$ may experimentally manifest. Fractional order in $[H^+]$ during ORR has also been observed in ORR with nitrogen-doped graphitic carbon[190] and precious metal catalysts.[139,140]

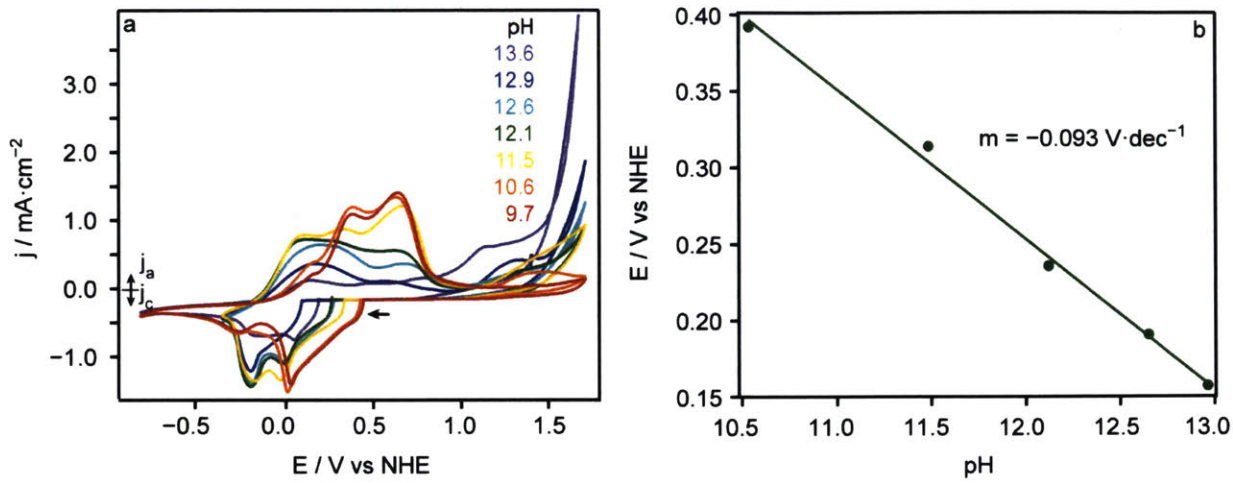

Figure 4-12. a) pH-dependent redox activity of $Cu_3(HHTP)_2$ under N_2 atmosphere, and **b)** plot of the peak oxidation potential 1 of $Cu_3(HHTP)_2$ as a function of pH.

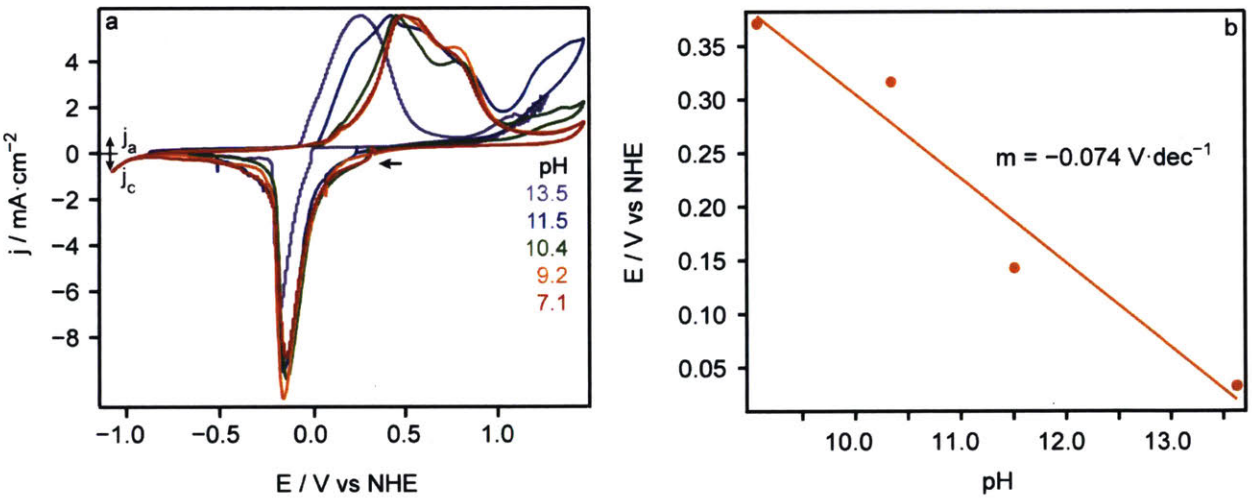

Figure 4-13. a) pH-dependent redox activity of $Cu_3(HITP)_2$ under N_2 atmosphere, and **b)** plot of the peak oxidation potential 1 of $Cu_3(HITP)_2$ as a function of pH.

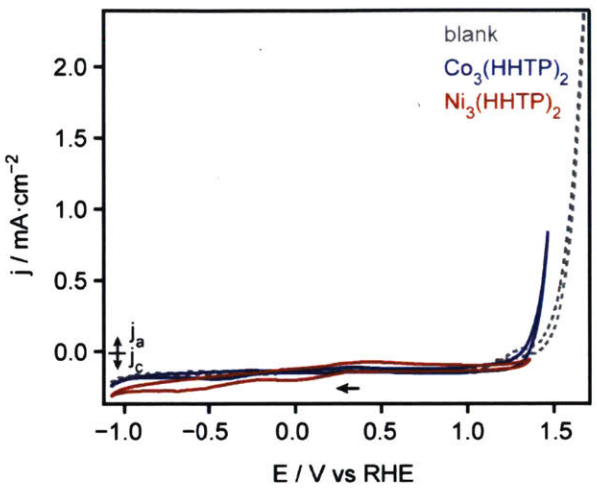

Figure 4-14. Cyclic voltammograms of the trigonal, redox-inactive MOFs $Co_3(HHTP)_2$ and $Ni_3(HHTP)_2$ under N_2, on a glassy carbon electrode (blank) in 0.1 M NaCl.

Considering that the non-zero ORR order in $[H^+]$ with the hexagonal MOFs was attributed to PCET in these redox-active analogues, the independence of ORR potential on pH observed in the trigonal MOFs was consistent with the lack of any faradaic events observed in the cyclic voltammograms of these analogues (**Figure 4-14**). This observation highlighted that although both the hexagonal and trigonal MOFs featured a honeycomb lattice that could enable electron delocalization in the *ab* plane, the disruption of the π-stacking in the *c* direction of the trigonal MOFs greatly altered the electrochemical properties of this phase. These phase-dependent differences in electrochemical properties were further underscored by the electrical conductivity (σ) and electroactive surface area (ESA) values (**Table 4-6**). The catalytically active hexagonal MOFs exhibited conductivity values upwards of 60 $S \cdot cm^{-1}$, whereas the conductivity values of the trigonal MOFs were up to five orders of magnitude lower. Similarly, deriving the ESAs from double layer capacitance measurements[191] revealed an order of magnitude higher ESAs in the hexagonal MOFs than in the trigonal MOFs. An ESA value for $Cu_3(HITP)_2$ could not be obtained due to its instability during prolonged measurements. Lower electrical conductivity and lower electroactive surface area values in the

trigonal MOFs may indicate that the inferior catalytic activity was a result of slower electron transfer kinetics and a lower density of electroactive catalytic sites. The redox inactivity of the trigonal MOFs also

Table 4-6. Electrical conductivity (σ) and electroactive surface area (ESA) values for the triphenylene MOFs.

MOF	σ ($S \cdot cm^{-1}$)	ESA ($F \cdot m^{-2}$)
$Ni_3(HITP)_2$	$6 \cdot 10^{1}$ [172,192]	$7.7 \cdot 10^{-7}$ [b]
$Cu_3(HITP)_2$	$2 \cdot 10^{-1}$ [173]	N/A[§]
$Cu_3(HHTP)_2$	$2 \cdot 10^{-1}$ [176,a]	$1.6 \cdot 10^{-6}$ [b]
$Ni_3(HHTP)_2$	$6 \cdot 10^{-3}$ [b]	$1.0 \cdot 10^{-7}$ [b]
$Co_3(HHTP)_2$	$2 \cdot 10^{-3}$ [b]	$1.0 \cdot 10^{-7}$ [b]

[a]Single crystal data

[b]This work

pointed to unfavorable electron transfer, and was consistent with the low activity for ORR. The experimental data indicated that concomitant electron transfer and O_2 binding to the trigonal MOFs was still relevant. However, in order to obtain the O_2 reduction products and achieve catalyst turnover, at least one more electron must be transferred to the bound hydroperoxide, and the reduced product can then dissociate from the catalyst. If the second electron transfer to O_2 is expected to occur by PCET from the MOF, but the MOF is redox-inactive in the ORR potential window (as seen in the trigonal analogues), significantly more driving force will be needed to reduce the hydroperoxide and achieve product formation and catalyst turnover (**Scheme 4-1**).[193] This greater necessary driving force was evident in the ORR cyclic voltammograms and Tafel data from the trigonal phases; much higher overpotential was required to achieve reductive current with the trigonal MOFs in the presence of O_2 relative to the hexagonal MOFs. As such,

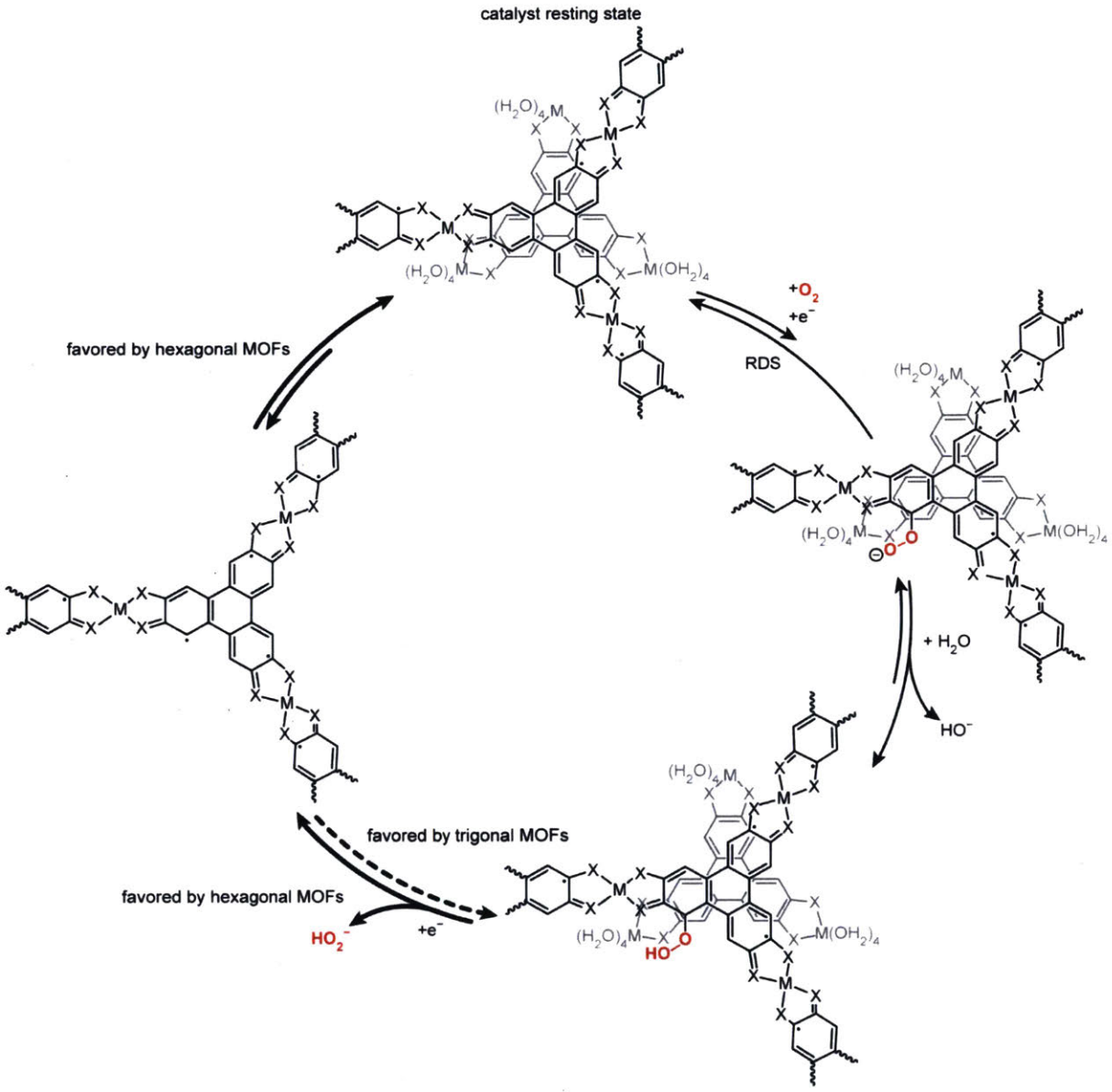

Scheme 4-1. Proposed mechanisms for $2e^-$ ORR with the hexagonal and trigonal MOFs. The black complex represents a fragment from the honeycomb lattice present in both phases. The gray complex indicates the $M_3(HHTP)(H_2O)_{12}$ cluster present in the trigonal MOFs. The bold solid versus dashed arrows indicate where the two mechanisms are thought to diverge, due to the redox inactivity of the trinuclear MOFs that hinders reduction of the hydroperoxide adduct.

the trigonal analogues never achieve the current density observed with the redox-active, hexagonal MOFs. Conversely, the high electrical conductivity and redox activity in the hexagonal MOFs enabled facile electron transfer to O_2 and subsequent catalyst turnover, which contributed the high ORR activity observed in this phase.

4.3 Conclusions and outlook

These results demonstrated that materials made from identical ligands and bearing structural similarities exhibited vastly different electron transfer properties under electrochemical bias. This led to distinct electrocatalytic responses in the oxygen reduction reaction, with the nearly eclipsed hexagonal phases exhibiting excellent activity that contrast with the virtual inactivity of the trigonal phases containing molecular species. We attributed the lack of catalytic activity in the latter to the high overpotential required for oxidizing a purported hydroperoxide intermediate. Knowledge of how the physical structures of conductive MOFs influence the electronic properties provides a foundation for predicting the broader utility of each analogue, and tailoring the phases to unique applications such as faradaic and capacitive energy storage, chemiresistive sensing, and electrochemical catalysis of other transformations.

4.4 Methods

General comments. KOH (99.99% trace metals), NaCl (99.99% trace metals), and $HClO_4$ (99.99% trace metals) were purchased from Sigma-Aldrich. The aqueous electrolytes were made from Milli-Q water (18 MΩ). Oxygen gas was purchased from Airgas (99.8% purity). Reference electrodes were purchased from CH Instruments. Indium tin oxide (ITO) working electrodes were purchased from Delta Technologies, Ltd. Pt gauze (100 mesh, 99.9% metal basis) and wires (ϕ = 0.404 mm, annealed, 99.9% metal basis, and ϕ =

0.5 mm dia., hard, 99.95% metal basis) comprising the auxiliary electrode were purchased from Alfa Aesar. Rotating disk electrode and Pt rotating ring disk electrode assemblies (1 mm width Pt) with glassy carbon working electrode inserts (5 mm diameter) were purchased from Pine Research Instrumentation. 2,3,6,7,10,11-hexahydroxytriphenylene (HHTP, 95%) was purchased from Acros Organics and recrystallized from ethanol before use. 5 wt% Nafion 117 solution in isopropanol was purchased from Sigma Aldrich. 2 mm and 8 mm slits were used during the powder X-ray diffraction data collection, with a scan rate of 0.02 degrees·second^{-1} and a dwell time of 0.2 seconds·step^{-1}.

Electrochemical measurements. The Pt auxiliary electrode was cleaned by submersion in concentrated HCl followed by sonication for 5min, washing with Milli-Q water, and drying under a stream of air before each experiment. Glassy carbon working electrodes were cleaned by submersion in concentrated HCl followed by sonication for 5min, washing with Milli-Q water, and drying under a stream of air. The glassy carbon working electrodes were then sequentially polished with 1, 0.3 and 0.05 μm diameter alumina powder from BASI. Unless otherwise noted, all electrochemical experiments were executed with a Bio-Logic SP200 potentiostat / galvanostat in a custom 2-compartment electrochemical cell. Rotating disk electrode studies were conducted with a Bio-Logic VMP3 potentiostat / galvanostat and a Pine Research Instrumentation Modulated Speed Rotator. Unless otherwise specified, internal resistance of the electrolyte was measured with the Bio-Logic SP200 potentiostat / galvanostat by passing −100 μA current, and iR drop correction was applied. Generally, the resistance of the electrolyte was measured to be ~20 Ω. Prior to data collection under a given atmosphere (N_2 or O_2), the electrolyte was sparged for 20 minutes with that gas and sparged continuously during data collection. For the pH 13 (0.1 M KOH) electrolyte, a Hg/HgO reference electrode (1.0 M KOH) was used and for the pH 8 electrolyte (0.1 M NaCl), a Ag/AgCl electrode was used (1.0 M NaCl). Unless otherwise noted, cyclic voltammetry data was collected while rotating the working electrode at 2,000 r.p.m. and cycling at 5 mV·s^{-1}.

Synthesis of the HITP MOFs. The 2,3,6,7,10,11-hexaaminotriphenylene (HATP) ligand and $Ni_3(HITP)_2$ was synthesized as described previously.[172] $Cu_3(HITP)_2$ was synthesized as described previously.[173]

Synthesis of the HHTP MOFs. Co, Ni, and $Cu_3(HHTP)_2$ were synthesized as reported previously.[176]

Deposition of the MOFs onto the electrodes. Catalyst inks were prepared by dispersing 2 mg of the catalyst in a volume of 1:1 Millipore water:isopropyl alcohol (190 μL) with 10 μL of 5 wt% Nafion. The ink solution was then sonicated for 25 minutes to get a uniform suspension. 2 x 5 μL of the catalyst ink was deposited on the polished or otherwise cleaned electrodes and dried under vacuum before use.

Determination of the MOF-mediated ORR order in [O_2]. The electrolyte was sparged with O_2 for 20 minutes then CV under O_2 was taken from 0 V versus OCP to −0.4 V vs Ag/AgCl. The [O_2] order data was collected by holding the potential at from the ORR onset potential to approximately −0.4 V vs Ag/AgCl for two minutes at each potential (refer to **Figure 4-9** for the exact potentials for each analogue), going from 10% O_2 / 90% N_2 to 100% O_2 / 0% N_2 electrolyte atmosphere at each potential value, with sparging the new atmosphere for 20 minutes before data collection. For each potential, a log(I) versus log(partial pressure O_2) plot was made to extrapolate the order in O_2 and observe the dependence of the order on the potential.

Koutecky-Levich and Tafel studies. Collection of the Kouteky-Levich and Tafel data in pH 13 was previously described in the Methods section of Chapter 2. CV in pH 8 electrolyte (0.1 M NaCl) (5 $mV \cdot s^{-1}$) under N_2 atmosphere then under O_2 atmosphere was conducted from 0 V versus OCP to −0.4 V versus Ag/AgCl (ORR potential range) with the unmodified glassy carbon electrode then the MOF-modified

glassy carbon electrode. Potentiostatic measurements were conducted from the ORR onset potential to the potential at which diffusion limitations prevented steady current (refer to **Figure 4-7** for exact potentials for each analogue) in increments of 20 mV under O_2 atmosphere. Each potential was held for 2 minutes. This was conducted three times, with altering rotation speeds to extrapolate the diffusion coefficient. The electrode was rotated at 625, 816, and 1,189 r.p.m., respectively. This allowed for elimination of mass transport limitations when analyzing Tafel behavior *via* generation of the activation-controlled Tafel plot.

ORR [H^+] order study. Potential versus Ag/AgCl was measured at a constant current I = −10 μA while varying the pH from 13.5 to 8.0 in the 0.10 M KOH electrolyte titrated with 1.0 M $HClO_4$ in the presence of O_2 while rotating at 2,000 r.p.m. Each potential required to pass −10 μA at a given pH was allowed to reach steady state before more titrant was added. Potential versus pH was plotted and the slope was divided by the Tafel slope to obtain the ORR order in [H^+].

Probing the pH-dependent redox potentials of the MOFs. Cyclic voltammetry (CV) was run with an unmodified glassy carbon electrode from E = −1.1 V to E = 0.7 V versus SCE, then the first MOF-modified electrode was used in pH 13.6, and CV was run scanning cathodically first from E = −1.1 V to E = 0.7 V versus SCE for two cycles (electrode 1). The electrolyte was then titrated to a lower pH (refer to **Figures 4-11** and **4-12** for the exact pH environments studied for each analogue) an unused MOF-modified working electrode (electrode 2) was installed, and the procedure was repeated. The electrolyte was then titrated to yet a lower pH, and the same procedure for electrode 1 was used on the new electrode 3. This procedure was repeated with a minimum of 5 electrodes (at least 5 pH values) for each redox-active analogue. The potentials associated with the peak currents passed in the MOF oxidation events were plotted versus pH. Since $Co_3(HHTP)_2$ and $Ni_3(HHTP)_2$ showed no redox activity, CV was only collected in pH 8.

Stability testing MOFs in pH 13 electrolyte. CV was conducted under O_2 with the MOF-modified glassy carbon electrode for 50 cycles from 0.1 V to -0.3 V versus Hg/HgO to monitor loss in ORR activity with progressing cycles. For potentiostatic durability tests, 1 CV cycle was collected for each sample to determine the activation-controlled ORR potential window. The potential was then held within that potential window for 8 hours and the percent current retained during ORR in the activation-controlled region was calculated.

Faradaic efficiency for $2e^-$ ORR with MOFs. The potential on the MOF-modified disk was held from 0.67 V to 0.38 V vs RHE in pH 8, with more cathodic potentials applied every two minutes in increments of 20 mV under an O_2 atmosphere while rotating at 2,000 r.p.m. Simultaneously, the Pt ring potential was held at 0.53 V vs SCE (1.23 V vs RHE), sufficient to re-oxidize H_2O_2 on the Pt surface but not H_2O. Once the cathodic current from the disk and the anodic current from the ring was collected, the faradaic efficiency (FE) for $2e^-$ ORR was calculated using the following equation:

$$FE_{H_2O_2} = \frac{I_{ring}}{0.18 \cdot I_{disk}} \cdot 100$$

where I_{ring} = the average Pt ring current taken from the last 10 seconds at a given potential, I_{disk} = the average MOF-modified disk current taken from the last 10 seconds at a given potential, and 0.18 = the collection efficiency of the Pt ring, which had been calibrated with potassium ferro / ferricyanide.

Electroactive surface area (ESA) measurements. In 0.1 M NaCl, cyclic voltammograms of the MOF were collected under N_2 in the non-faradaic potential range of 0 V to 0.05 V vs SCE at scan rates (v) of 10, 8, 6, 4, and 2 $mV \cdot s^{-1}$, respectively. Capacitive current (I) at 0.025 V vs SCE was plotted versus v,

giving a slope that represented the double layer capacitance in Farads. This was divided by the geometric surface area of the electrode to approximate the electroactive surface area ($F \cdot m^{-2}$).

Pressed pellet conductivity. Conductivity measurements were executed using a home-built press previously described.[194] MOF powder was pressed between two stainless steel rods (2 mm diameter) inside of a glass capillary. Pellet resistance was measured with a multimeter.

Part II

◊

Ionically Conductive Cu-Azolate MOFs as Solid-State Electrolytes for Metal and Metal-Ion Batteries

Chapter 5

Metal- and Covalent-Organic Frameworks (MOFs and COFs) as Solid-State Electrolytes for Metal and Metal-Ion Batteries

5.1 Introduction

Society's long-standing energy demands have fueled for centuries the quest for power-dense, portable, and economically viable energy carriers. Since the birth of the first rechargeable battery in 1860,[195] emerging battery technologies have provided both answers to these demands as well as additional obstacles. One ubiquitous energy storage device, the metal or metal-ion battery, offers quintessential examples of both. The strongly reducing nature of Group 1 and 2 metal ions qualifies these elements as viable energy-dense anode materials: standard reduction potentials several volts below that of the standard hydrogen electrode (SHE) allow a thermodynamically favorable oxidation of these metals to readily release electrons that shuttle through an external circuit, generating the electric current that serves as the power supply during battery discharge. Integration of energy-dense materials into devices allows power sources to be compact and portable, by maximizing energy output per unit mass of material. Further, the reversibility of these oxidation events makes possible extensive battery cycling, thus providing a rechargeable power source. Indeed, current Li-ion batteries boast an energy density of 265 $Wh \cdot kg^{-1}$, with the potential of a 20% improvement, and are operable for over 1,000 charge-discharge cycles.[196]

Although the chemical properties of metal-ion batteries offer impressive performance and exciting possibilities, harnessing the power of such reactive workhorses in a controlled manner comes with its own challenges. In Li-ion batteries, formation of Li dendrites during charging can puncture the battery membrane separating the anode from the cathode, causing a leakage of flammable electrolyte if the electrolyte is liquid, or causing a short-circuit should the dendrites reach the cathode. Another limitation of Li-ion batteries stems from the first charging cycle, which causes the formation of a stable reduction product known as the solid-electrolyte interphase (SEI) layer at the anode due to the fact that the anode and cathode lithiate at potentials outside the stability window of common liquid electrolytes. Formation of the SEI layer diminishes the cathode capacity, thus necessitating a larger amount of cathode material to be incorporated into the battery relative to the anode mass. This additional material lowers the battery's energy density.

Another downfall of the charge-discharge process in Li-ion batteries is that a poorly formed SEI will limit battery cycle life due to continuous reactivity of the electrolyte at the anode and irreversible loss of Li^+ ions.[196]

From an economic standpoint, the increasingly widespread adoption of rechargeable batteries also highlights the difference in cost and geopolitical availability between Li metal and more abundant metals such as Na, Mg, K, Ca, or Al. These heavier metals are indeed the focus of intense research in the context of electrical energy storage, but present their own challenges. Na, an attractive candidate due to its high abundance, relatively small ionic radius, high specific capacity, and low reduction potential (2.71 V vs SHE), has shown more problematic reactivity with organic liquid electrolytes compared to Li and presents the same dendrite formation challenges as Li batteries.[197,198] Mg, another viable candidate, is 5 orders of magnitude more abundant than Li, does not form dendrites during charging, and offers almost double the volumetric capacity of Li (3,833 $mAh \cdot mL^{-1}$ versus 2,062 $mAh \cdot mL^{-1}$ for Mg/Mg^{2+} versus Li/Li^+, respectively). However, the most common commercial electrolytes used in Li-ion batteries are not appropriate choice for Mg-ion batteries because the SEI layer formed in the latter is completely insulating for Mg^{2+}, an obvious problem for battery cyclability.[196] Owing to its higher atomic weight, which inherently leads to lower energy density, K has received comparatively less attention than Li and Na as a battery material. However, its abundance and lower cost may offset this handicap, especially considering that K also does not alloy with Al, a popular and cheap current collector that otherwise needs further processing when used in Li-ion batteries. Additionally, the weaker Lewis acidity of K^+ ions relative to Li^+ and Na^+ ions accounts for lower desolvation energy and enhanced transport kinetics across the electrolyte/electrode interface, which ultimately increases ionic conductivity.[199] Lastly, Ca^{2+} features a small ionic radius and a stable divalent oxidation state that would afford higher energy density. It has high natural abundance, and a standard reduction potential close to that of Li^+ which would allow a high potential window for electrolytes. However, one significant obstacle preventing development of Ca batteries with organic liquid

electrolytes is that diffusion of Ca^{2+} ions through the SEI layer prevents re-plating of Ca on the anode during charging.[200] Even further enhancement of capacity can be achieved by taking advantage of trivalent ions such as Al^{3+}, which features quadruple the volumetric capacity of Li^{+} (8046 $mAh \cdot cm^{-3}$). Although this is a promising feature for energy storage advancement, challenges with Al-ion battery systems containing liquid electrolytes stem from the formation of passive oxide films on the electrode surface and / or from anode corrosion.[201]

Efforts have also been made to improve metal and metal-ion battery performance by further optimizing cell components beyond the metal anodes, and in particular the electrolyte. The impedance of all metal-ion batteries is likely elevated due to mobile species besides the active metal ions (e.g. charge-balancing anions, solvent molecules, etc.) during cycling.[196] Pursuing various formulations of anode and cathode materials,[202–205] developing new supporting electrolytes, and new solvent or solvent mixtures[206–208] have all been explored as potential solutions to these challenges. The focus of this review is to present an argument for solid-state, rather than liquid, electrolytes in such batteries and to discuss the potential utility of crystallographically-ordered, metal- and covalent-organic frameworks (MOFs and COFs), as solid-state electrolytes. The review specifically covers reported MOFs and COFs as solid-state electrolytes, distills metrics for vetting solid electrolyte candidates, and considers future directions for this field.

5.2 Motivation for and evolution of solid-state battery electrolytes

Motivation for a solid-state electrolyte is several-fold. Firstly, solid-state electrolytes would eliminate the hazard of housing a flammable liquid material inside of the battery, enhancing safety. Secondly, a solid-state electrolyte may allow for immobilization of charge-balancing anions, which would allow maximization of the cation transference number. Thirdly, many liquid electrolytes are not stable in the required potential window imposed by the battery electrodes. Solid electrolytes should aim to address all of these challenges. In addition to minimizing the formation of reactive byproducts, a more stable electrolyte may prevent the formation of an SEI layer, consequently improving the energy density of the

cell by eliminating the need for excess sacrificial cathode material. Elimination of the SEI layer would also increase the viability of Mg and Ca-ion batteries, the development of which is currently limited by the inability of these ions to travel through the SEI layer during charging. Finally, for metal anode batteries, liquid electrolytes provide no morphological control over anodic plating of the metal during battery charging; a solid electrolyte with sufficient mechanical strength may encourage uniform plating, thereby preventing dendrite formation.

Several classes of materials have been evaluated as potential solid electrolytes for metal or metal-ion batteries, including polymers and composites thereof,[209] inorganic solids[209] and as will be discussed further, MOFs and COFs. Polymer electrolytes can offer enhanced potential stability windows and cation transference numbers compared to liquid electrolytes, due to the immobilized anionic hopping sites along the polymer backbone. However, polymers are ineffective at preventing dendrite growth and typically exhibit ambient temperature conductivity values that are too low for commercial applications (10^{-8}-10^{-5} $S \cdot cm^{-1}$).[196,197] Additives such as ceramics or ionic liquids have been doped into polymer matrices to enhance ion mobility, creating more conductive polymer composites. Dopants can increase the electrolyte conductivity by 2-3 orders of magnitude, but optimization of the polymer / dopant blend and obtaining mechanistic understanding of the transport pathways in such hybrids is not trivial.[210] Additionally, dopants in the polymer matrix often compromise the electrode-electrolyte interface, and these dopants can exhibit lower electrochemical or chemical stability and form themselves a resistive layer at the electrode.[197] In terms of ionic conductivity and mechanical robustness, inorganic solid electrolytes are among the most promising solid electrolytes thus far. Li_3OX-based antiperovskites ($X = Cl^-$, Br^-) exhibit Li^+ activation energies of 0.18-0.26 eV and conductivities of up to $2 \cdot 10^{-3}$ $S \cdot cm^{-1}$ at 25 °C, exceeding the conductivities of polymer electrolytes.[211] However, preparation of Li_3OX antiperovskites involves thermal treatment that inadvertently removes charge-balancing lithium, resulting in decreased charge carrier density. Additionally, challenges exist regarding yield and phase purity for these materials that contribute to poor interfacial

contact between the electrode and electrolyte. This, combined with formation of insulating SEI layers, increases battery resistance.[212] Antiperovskites have also been shown to conduct Na^+ ions, albeit with modest conductivities of ca.10^{-5} $S \cdot cm^{-1}$ at 160 °C and activation energies of 0.6-0.8 eV.[213] Much higher conductivities are observed in *closo*-borate salts ACB_9H_{10} (A = Li^+ or Na^+), which boast conductivities of 0.03 $S \cdot cm^{-1}$ at temperatures above an ordered-disordered phase transition temperature. Noteworthy activation energies of 0.29 eV (Li^+) and 0.20 eV (Na^+) and potential stability windows of ~5 V were measured. A logistical barrier with these *closo*-borate materials is that the phase transition is reversible, and thus the material must be kept above 127 °C (Li^+) and 107 °C (Na^+) in order to maintain the conductive properties.[214] Another archetypal Na^+ electrolyte that has garnered attention is the Na Superionic Conductor (NASICON), $Na_{1+x}Zr_2Si_xP_{3-x}O_{12}$ ($0 \leq x \leq 3$).[215] As its name suggests, phase-pure NASICON exhibits high Na^+ conductivities on the order of 10^{-3} $S \cdot cm^{-1}$ at 25 °C, the same order of magnitude conductivity as β-alumina Na^+ electrolytes.[215] However, this electrolyte exhibits instability to molten sodium salts, limiting battery applications. Additionally, ionically insulating ZrO_2 impurities lower conductivity values. When contemplating other metals for energy storage applications, Mg^{2+} conduction presents exciting opportunities as well as unique challenges due to its highly polarizing nature. Mg^{2+} ion solid electrolytes include $Mg(BH_4)_2$ and $MgZr_4(PO_4)_6$, which feature relatively modest conductivities of 10^{-9} to 10^{-7} $S \cdot cm^{-1}$, respectively, even at > 100 °C. Notably, the best Mg^{2+} ion solid conductor is in fact a MOF, Mg_2(dobpdc), impregnated with $Mg(OPhCF_3)_2$ ($^-OPhCF_3$ = 4-trifluoromethylphenolate) and $Mg(TFSI)_2$ ($TFSI^-$ = bis(trifluoromethanesulfonyl)imide).[216] This material features a Mg^{2+} conductivity of 10^{-4} $S \cdot cm^{-1}$ at 25 °C and will be discussed in greater detail below.

Demonstrating the highest Mg^{2+} ion conductivity among solids notwithstanding, MOFs and COFs possess an arsenal of additional properties that identify them as attractive candidates for solid-state electrolytes[217–221] (**Figure 5-1**). Firstly, the high surface area of MOFs and COFs, which is commonly thousands of $m^2 \cdot g^{-1}$,[222] enables a high density of metal cations and hopping sites, contributing to a

maximized power density in a compact device. The long-range order and well-defined ion conductivity pathways in MOFs and COFs provides affords efficient ion shuttling while reducing much of the diffusion limitations associated with nonporous solids, especially for highly polarized species. The crystallographic definition offers homogeneously dispersed hopping sites while eliminating impedance stemming from electrolyte reorganization, as seen with liquid and polymer electrolytes.[207,210] The electronic structure of MOFs and COFs is also beneficial in that their composition rarely offers a high density of mobile electrons or holes, with most materials in this class being excellent electrical insulators.[73] This insulating character is an essential property of the electrolyte, so as to separate the anode and cathode and prevent short circuiting. Porous solid-state electrolytes can also aid in optimizing cation transference numbers; liquid electrolytes often exhibit transference numbers of < 0.4 because both the cations and anions are mobile.[223,224] Conversely, anions can be coordinated to or integrated directly into the MOF/COF structure and are therefore immobilized during battery charging and discharging, enhancing battery efficiency. Not only can such materials be used to immobilize anions, but they can also trap byproducts that may be generated during battery cycling that otherwise decrease battery lifetime upon contact with the electrodes.[225] Further, because pores can host liquid electrolytes without leakage, porous solids offer the dielectric benefits of liquid electrolytes without the safety concerns of the latter. Finally, synthetic tunability of MOFs and COFs is a powerful feature: the ability to alter the pore size, polarity, material density, metal (in the case of MOFs) and anion identity, as well as the coordination environment enables the design of a host of electrolytes

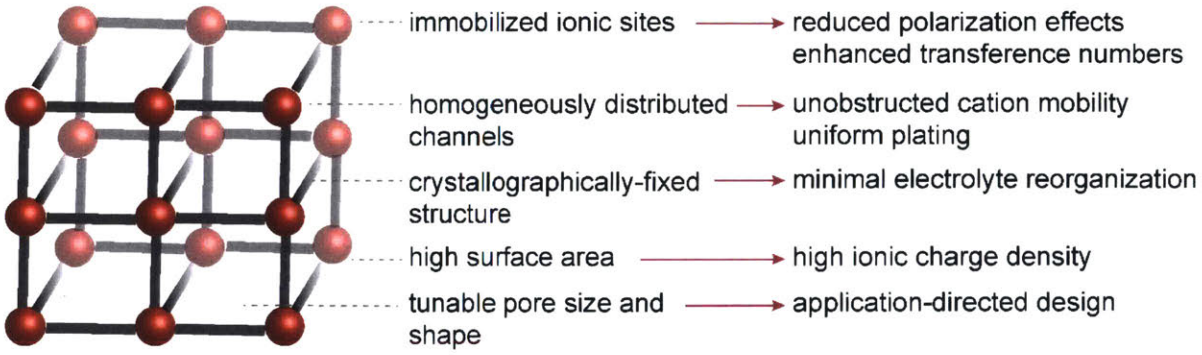

Figure 5-1. Attractive features of MOFs and COFs as solid-state electrolytes.

featuring a wide range of properties that can meet a variety of device-specific criteria. Although beyond the scope of this review, it should be noted that the tunability of MOFs and COFs in terms of their pK_a and water stability makes them effective proton conductive electrolytes for proton exchange membranes.[226–229] Indeed, most studies of ion conduction in these materials have focused on proton conduction, but emerging in the past decade have been pioneering investigations of Groups 1 and 2 metal ion conduction. Whereas proton conductivity often relies on the installation of acidic functional groups within the framework, conduction of metal ions has different requirements, as will be discussed below.

5.3 Metal-ion conduction in MOF / COF composites

The utility of MOFs/COFs as solid electrolytes is highlighted both by their intrinsic properties and by their role in composites with polymers and ionic liquids (ILs). As part of composites, the ordered, crystalline nature of these materials aids in controlling polymer and IL aggregation by housing the polymers or ILs within the pores, while still retaining the ionically conductive and non-flammable properties of the polymers and ILs themselves. In polymer composites, materials such as polyethylene oxide (PEO) or polyethylene glycol (PEG) are commonly incorporated into the evacuated MOF/COF pores by stirring the latter in organic solutions of Li-containing polymers or by a solvent-free, hot press method. Access to an arsenal of composite formulation techniques allows for tailoring the electrolyte preparation procedure to accommodate limitations of a given host, e.g. mechanical instability, incompatibility to certain solvents, etc. Such polymer composites exhibit ionic conductivity values between 10^{-6} and 10^{-4} $S \cdot cm^{-1}$,[230–235] higher by up to two orders of magnitude compared to polymer-Li salt composites alone.[233] Co-formulation of MOFs and COFs with polymers has been thoroughly reviewed previously.[217] Although entrapping the polymers within the host pores can prevent polymer crystallization and aggregation, which in turn enhances conductivity, this approach to electrolyte development did introduce several challenges. Filling the pores with a guest material significantly decreases surface area, which in turn contributes to higher diffusion

limitations for ion migration, effectively nullifying one of the inherent advantages of porous materials as solid electrolytes. Additionally, the reported alkali metal transference numbers for these electrolytes are never higher than 0.55, and can be as low as 0.34, offering little to no improvement over liquid electrolytes.[231,232,234,235] These modest transference numbers indicate that although encaging the polymers within the MOFs or COFs does enhance conductivity, this approach fails to immobilize charge-balancing anions and other mobile species. Finally, the challenge with predicting the ultimate properties of the composites, or understanding their interfacial structure, makes rational design of such electrolytes difficult.

Incorporation of ILs into MOFs and COFs pores has also produced composites with some notable properties as solid electrolytes. Isolating ILs within confined micropores is particularly desirable because it can change the phase transition temperature of certain ILs that otherwise solidify and are therefore not usable at ambient temperature.[236] The four primary strategies for impregnating MOFs and COFs with ILs are: soaking the material in an IL with or without a co-solvent, allowing the IL to anchor to coordinatively unsaturated sites within the porous host; the "ship in a bottle" method wherein precursors for the IL are introduced inside of the MOF/COF such that the final IL assembles within the pores; capillary action-promoted diffusion of the IL into the pores;[236,237] and one-pot assembly of the IL composite.[238,239] An appropriate method may be chosen based on the presence or absence of coordinatively unsaturated sites in the MOF/COF, the sizes of the aperture openings, and the molecular sizes of the ILs themselves.

An early example of a MOF-IL composite as a solid electrolyte was reported by Fujie, Kitagawa, and coworkers,[240] who physically blended Zn(2-methylimidazole)$_2$ (ZIF-8) with EMI-TFSI (1-ethyl-3-methylimidazolium trifluoromethanesulfonimide) / LiTFSI to obtain an electrolyte. A low activation energy of 0.16 eV and an ionic conductivity of 10^{-5} S·cm^{-1} at 25 °C was reported for this composite, which nevertheless was lower than that of the MOF-IL combination alone, measured in the absence of the Li salt. Blending EMI-TFSI/Li-TFSI with $Zr_6O_4(OH)_4(H_2TCPP)_3$ (MOF-525, H_2TCPP = tetracarboxyphenylporphyrin) gave an electrolyte with a conductivity of 10^{-4} S·cm^{-1} and a Li^+ transference

number of 0.36.[241] Although still only in the same range as liquid electrolytes, the transference number for the MOF-IL composite was a marked improvement upon the transference number measured for EMI-TFSI / LiTFSI itself, and was attributed to confinement of the EMI^+ and $TFSI^-$ ions within the MOF pores. These early studies of MOF/ILs composites highlighted certain potential benefits of confining the ILs to micropores, but also revealed unexpected results such as diminished conductivity upon addition of Li^+. A similar trend was observed in a composite of $ZnO_4(BDC)_3$ (MOF-5, BDC^{2-} = 1,4-benzenedicarboxylate) with AMImTFSI (1-allyl-3-methylimidazolium TFSI).[238] Doping this composite with increasing amounts of LiTFSI afforded electrolytes with gel-like consistencies with good ionic conductivities of 10^{-3}-10^{-2} $S \cdot cm^{-1}$ at 51 °C, which showed inverse dependence with the amount of Li^+. Although the authors attributed this unexpected observation to a change to a more tortuous Li^+ conduction pathway in the more highly loaded samples, experiments to substantiate such mechanistic implications are difficult and often not pursued in the MOF/COF literature thus far. Regardless, these rather complex composites exhibit impressively low activation energies of < 0.1 eV and working potential windows greater than 5.2 V, warranting additional future studies.

One word of caution is that both the anion and the cation in an IL have non-zero mobilities within the framework, and both can contribute to overall ionic conductivity, such that the metal cations are not the only charged mobile species within these electrolytes.[242] Measuring the Li^+ transference numbers of the composites is an important step in identifying the Li^+ contribution to the conductivity. Additionally, as with polymer composite electrolytes discussed above, understanding the interfacial interaction between the MOF/COF and the IL is difficult, making the discovery of new IL-based composites squarely an empirical challenge with little hope of rational design.[239]

5.4 Metal-ion conduction in MOFs and COFs

Coordinating anions to open metal or other cationic sites. The structural and compositional tunability of MOFs and COFs is one of the attributes that encourages their exploration as neat solid

electrolytes. Although the ability of these materials to intercalate ions has resulted in numerous works detailing their use as battery electrode materials,[218,221,243–246] employing them as solid-state electrolytes has emerged only recently. One of the pioneering studies in this context was published in 2011 by Wiers, Long, and coworkers.[247] This study reported soaking $Zn_4O(BTB)_2$ (MOF-177, BTB^{3-} = 1,3,5-benzenetribenzoate), $H_3[(Cu_4Cl)_3(BTTri)]_8$ (Cu-BTTri, $BTTri^{3-}$ = 1,3,5-tris(1*H*-1,2,3-triazol-5-yl)benzene), and $Mg_2(dobdc)$ ($dobdc^{4-}$ = 5-dioxido-1,4-benzene-dicarboxylate) in 1:1 ethylene carbonate:diethyl carbonate solutions of $LiBF_4$ and conducting electrical impedance spectroscopy (EIS) on the pressed pellet samples. The Li^+-doped MOFs yielded ionic conductivities ranging from 10^{-9} to 10^{-6} $S \cdot cm^{-1}$, with the most promising host being $Mg_2(dobdc)$. Although an intriguing early result, the ionic conductivity of $1.8 \cdot 10^{-6}$ $S \cdot cm^{-1}$ observed in $Mg_2(dobdc)$ was still at least two orders of magnitude lower than the technological benchmark for battery applications.[207] Taking advantage of the coordinatively unsaturated Mg^{2+} sites in this framework, the authors added Li^{i}OPr and showed that coordination of $^{-i}$OPr to these sites immobilized the anions and allowed the cations to move more freely, further increasing the conductivity by a factor of 10. The optimized electrolyte, $Mg_2(dobdc) \cdot 0.35Li^iOPr \cdot 0.25LiBF_4 \cdot EC \cdot DEC$ (EC = ethylene carbonate, DEC = diethyl carbonate) (**Figure 5-2**) exhibited a conductivity of $3.1 \cdot 10^{-4}$ $S \cdot cm^{-1}$ and an activation energy of 0.15 eV, meeting superionic conductor qualifications.[248] The need for $LiBF_4$ in this optimized formulation was justified by implicating it in inter-particle conductivity, with EC and DEC solvating the Li^+ ions in the pores and improving inter-particle contacts.

The Long Group later expanded upon the notion of immobilizing charge-balancing anions on open metal sites in MOFs in order to maximize exclusively Li^+ mobility. The framework UiO-66 ($Zr_6O_4(OH)_4(BDC)_6$) can undergo thermal dehydration to afford coordinatively-unsaturated Zr^{4+} sites[249,250] (**Figure 5-3a**). Ameloot, Long, and coworkers capitalized on this feature by soaking the dehydrated UiO-66 in a tetrahydrofuran solution of Li-O^{t}Bu, consequently saturating the Zr^{4+} coordination sphere with alkoxide anions and incorporating charge-balancing Li^+ cations.[251] The resulting Li^+ ionic conductivity was

reported to be $1.8 \cdot 10^{-5}$ $S \cdot cm^{-1}$, one order of magnitude lower than the reported $Mg_2(dobdc) \cdot 0.35Li^iOPr \cdot 0.25LiBF_4 \cdot EC \cdot DEC$[247] but still competitive with solid polymer electrolytes.[208,252] Further, the bulky aliphatic groups on the alkoxide shield the negative charge of the anion, thus weakening the interaction between the anion and the Li^+ cations and enabling a low Li^+ activation energy of 0.18 eV. Unfortunately, a symmetric Li cell with this electrolyte could only be cycled 3 times before shorting due to Li dendrite formation. It may be possible that altering the pore shapes / channel orientations may allow better control over the uniformity of Li plating, which could aid in decreasing dendrite formation. If dendrites formed along grain boundaries, forming larger host crystals and thus decreasing grain boundary density, or adding a polymeric binder to mitigate the effects of grain boundaries, may also help eliminate dendrite formation.

In addition to Li^+ conduction, another promising application of porous material-based electrolytes is conduction of more charge-dense Mg^{2+} ions. One consideration when designing materials for Mg^{2+} conduction is the larger size of Mg^{2+} ions compared to that of Li^+, particularly when solvated, which necessitates larger pore size to allow Mg^{2+} transport. Aubrey, Long, and coworkers explored both $Mg_2(dobdc)$ (structure shown in **Figure 5-2**) and its expanded analogue $Mg_2(dobpdc)$ ($dobpdc^{4-}$ = 4,4′-dioxidobiphenyl-3,3′-dicarboxylate) as Mg^{2+} ion conductors.[216] In line with the expanded pore size of $Mg_2(dobpdc)$ compared to that of $Mg_2(dobdc)$ (diameter = 21 Å versus 13 Å), $Mg_2(dobpdc)$ could accommodate more than three times the mole equivalents of free Mg^{2+} ions than the $Mg_2(dobdc)$ host and more than two times the mole equivalents of the dielectric triglyme, which was added to all samples. This is accompanied by a more than 100-fold increase in conductivity, with conductivity values of $\sim 10^{-4}$ $S \cdot cm^{-1}$ observed in $Mg_2(dobpdc)$-$Mg(TFSI)_2$ and $\sim 10^{-6}$ $S \cdot cm^{-1}$ observed in $Mg_2(dobdc)$-$Mg(TFSI)_2$. Champion

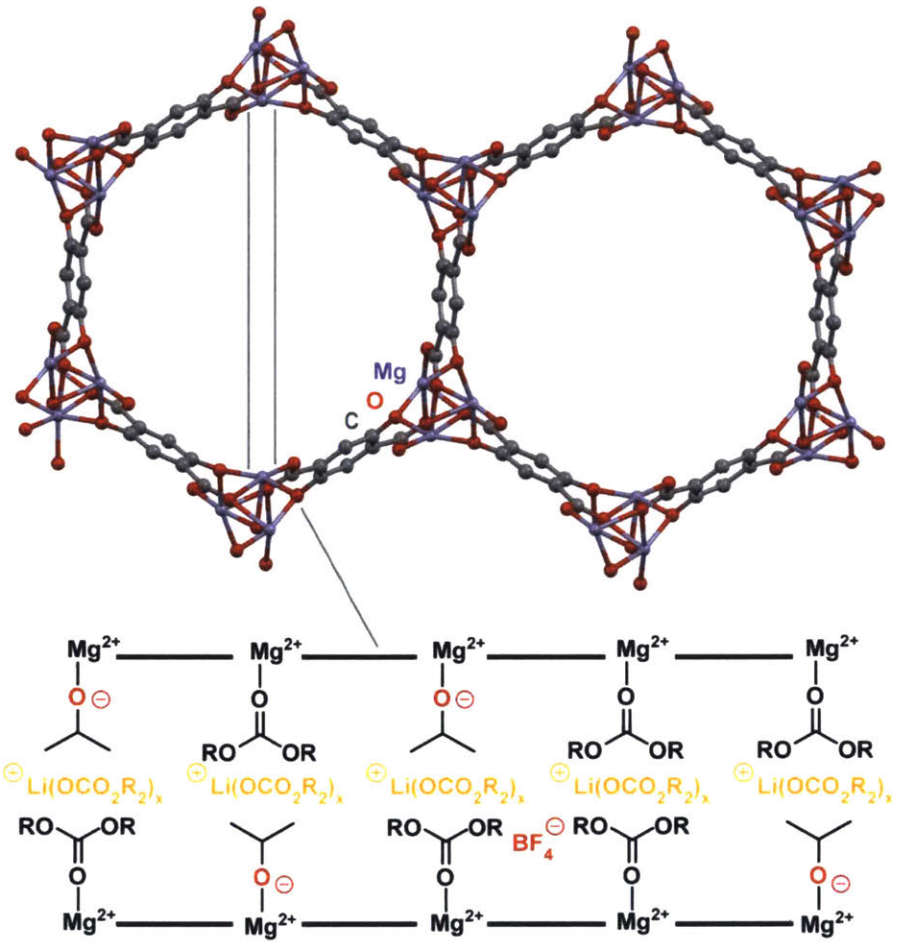

Figure 5-2. A portion of the structure of $Mg_2(dobdc)\cdot 0.35Li^iOPr\cdot 0.25LiBF_4\cdot EC\cdot DEC$. The cross-sectional view depicts the envisioned migration path for Li^+ ions through the electrolyte. H atoms are omitted for clarity.

devices made from soaking the MOFs in $Mg(TFSI)_2$ and $Mg(OPhCF_3)_2$ afforded conductivities of 10^{-4} $S\cdot cm^{-1}$ with $Mg_2(dobdc)$ and slightly higher with $Mg_2(dobpdc)$. These conductivity values are higher than those reported for any solid Mg^{2+} electrolytes and, combined with low activation energies of 0.11-0.19 eV, render the materials relevant for commercial applications. Studies of the stability of these materials to prolonged cycling and to Mg metal or other electrode materials would be useful for exploring the potential of these MOFs in a battery assembly.

The ability to coordinate a variety of anions to open metal sites in MOFs and impart conductivity of various cations introduces the opportunity to establish material-specific trends in performance. For example, Park, Tulchinsky, and Dincă reported an anionic Cu^{II}-azolate MOF, $(CH_3)_2NH_2[Cu_2Cl_3BTDD]\cdot(DMF)_4(H_2O)_{4.5}$ (MIT-20, H_2BTDD = bis(1H-1,2,3-triazolo[4,5-*b*],[4′,5′-*i*])dibenzo-[1,4]dioxin) that featured charge-balancing dimethylammonium cations (**Figure 5-3b**).[253] Presence of free dimethylammonium cations in the parent structure suggested that the MOF could accommodate and potentially conduct metal cations. Removal of residual DMF and water molecules, as well as one equivalent of dimethylammonium chloride afforded a neutral framework, Cu_2Cl_2BTDD. The thermodynamic favoring of the anionic framework during synthesis allowed a quantitative yield of the anionic MIT-20 charge-balanced by free Group 1 and 2 metal cations when soaking in the respective metal salts. Because this quantitative transformation of MIT-20 affords isostructural materials regardless of the nature of the anion, soaking the MOF in LiCl, LiBr, and $LiBF_4$ salts with addition of the dielectric propylene carbonate (PC) enabled the exploration of the effect of anion identity on electrolyte performance. Gratifyingly, an increasing softness of the anion correlated well with increasing Li^+ conductivity (10^{-5} S·cm^{-1} to 10^{-4} S·cm^{-1}) and decreasing activation energy (0.32 to 0.16 eV). A Li^+ transference number of 0.66 was measured for MIT-20-LiCl, confirming that the primary contributor to the conductivity was mobile Li^+. MIT-20 also exhibited good Na^+ and Mg^{2+} conductivity ($\sigma_{Na} = 1.8\cdot10^{-5}$ S·cm^{-1} and $\sigma_{Mg} = 8.8\cdot10^{-7}$ S·cm^{-1}) and activation energies of 0.39 eV and 0.37 eV upon soaking in solutions of NaSCN and $MgBr_2$, respectively. The ability to install both different anions and different cations within the MIT-20 structure highlights the versatility of this material as a solid electrolyte. This material also exemplifies the generalization that MOFs and COFs which have isostructural phases that are isolable in multiple states of formal charge could be promising candidates for ionically conductive solid electrolytes.

Another example of capitalizing on the modularity of MOFs to establish structure-function relationships was Shen, Dunn, and coworkers' exploration of the MIL-100 and UiO series of MOFs as

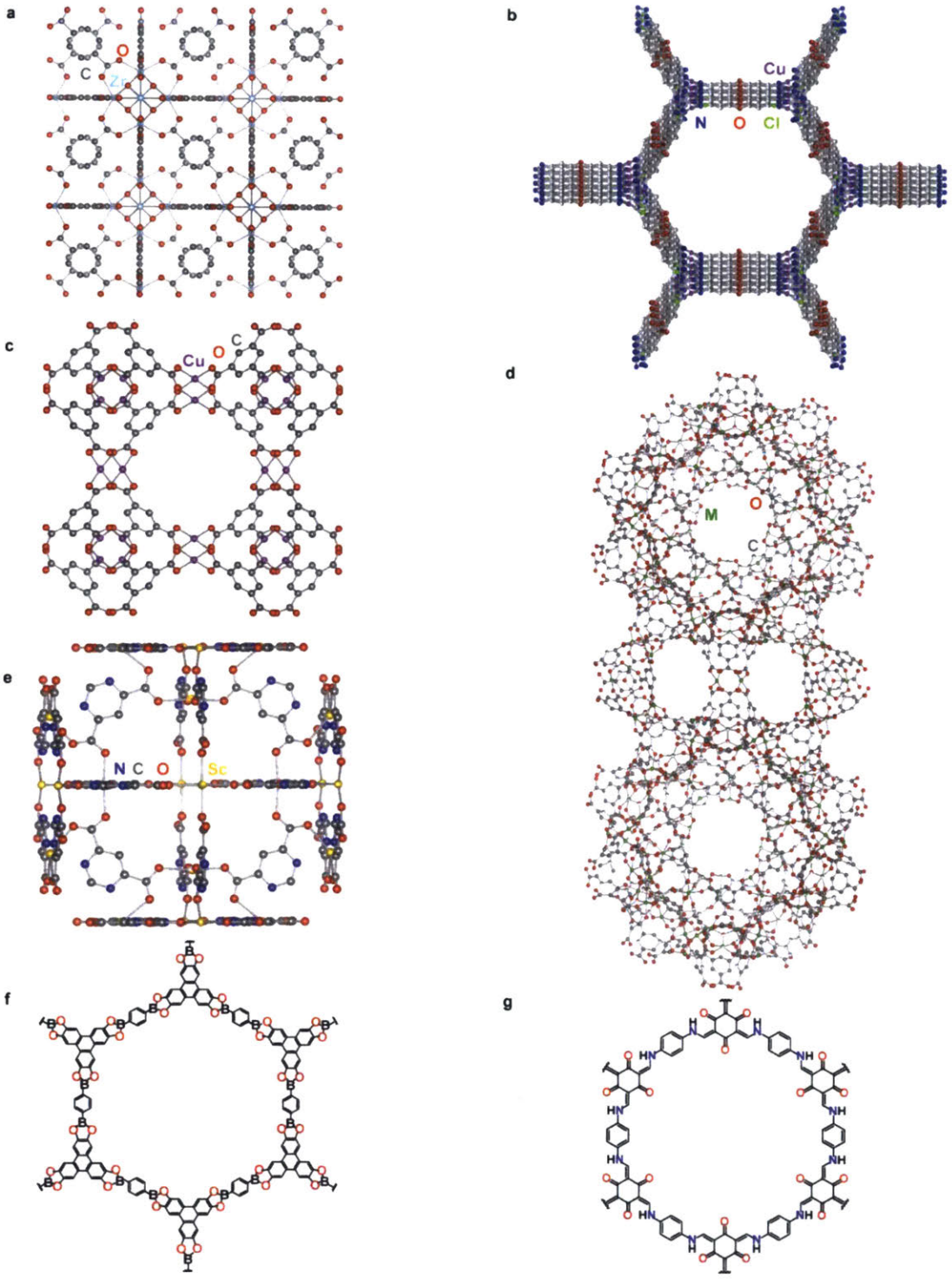

Figure 5-3. Structures of MOFs and COFs that have served as pioneers in the porous solid electrolyte field: **a)** UiO-66 (isomorphic with UiO-67), **b)** MIT-20, **c)** HKUST-1, **d)** MIL-100 (M = Cr^{3+} Fe^{3+}, or Al^{3+}), **e)** $[ScX(\mu_4\text{-pmdc})_2(H_2O)_2]\cdot 5H_2O$, **f)** COF-5, and **g)** TpPa-1. H_2O molecules and H atoms are omitted.

tunable solid electrolytes.[254] A proof-of-principle was demonstrated by targeting the installation of ClO_4^- ions from a PC solution of $LiClO_4$ onto the coordinatively unsaturated Cu^{2+} sites of activated $Cu_3(BTC)_2$ (HKUST-1, BTC^{3-} = benzene-1,3,5-tricarboxylate) (**Figure 5-3c**), allowing Li^+ ions to move freely upon polarization for a Li^+ conductivity of $3.8 \cdot 10^{-4}$ $S \cdot cm^{-1}$ and an activation energy of 0.18 eV. A similar PC-$LiClO_4$ treatment of materials in the activated MIL-100 series ($M_3O(BTC)_2OH$, M = Cr^{3+} Fe^{3+}, or Al^{3+}) (**Figure 5-3d**) produced solids whose conductivity ranged from 10^{-3} $S \cdot cm^{-1}$ to 10^{-2} $S \cdot cm^{-1}$. The highest ionic conductivity of the MIL-100 MOFs, observed with MIL-100-Al^{3+}, was consistent with the assertion that the increased Lewis acidity of Al^{3+} compared to Fe^{3+} and Cr^{3+} led to decreased ion pairing strength between the ClO_4^- and the Li^+, thus enhancing Li^+ mobility. The effect of MOF pore size on ionic conductivity was also explored using activated UiO-66 and the larger-pore $Zr_6O_4(OH)_4(BPDC)_6$ (UiO-67, $BPDC^{2-}$ = biphenyl-4,4′-dicarboxylate). Soaking these MOFs in PC solutions of $LiClO_4$ gave Li^+ conductivities of $1.8 \cdot 10^{-4}$ $S \cdot cm^{-1}$ and $6.5 \cdot 10^{-4}$ $S \cdot cm^{-1}$ for UiO-66 and UiO-67, respectively. The higher Li^+ conductivity observed in UiO-67 was attributed to the larger pore size being able to accommodate a higher extent of solvation around the Li^+ ions, which enhances mobility. This trend was consistent with that observed in Mg_2(dobdc) versus its expanded analogue Mg_2(dobpdc), as discussed earlier. Lower activation energy was measured in UiO-67 versus UiO-66 as well (E_a = 0.12 eV versus 0.21 eV for UiO-67 versus UiO-66, respectively).

In addition to coordinating anions to open metal sites as cation hopping sites within MOFs, anions have also been incorporated into positively charged MOF/COF structures simply through weaker Coulombic interactions. Recently, Chen and coworkers reported a cationic COF comprised of alternatively linked triaminoguanidinium and 1,3,5-triformylphloroglucinol ligands which was proposed to feature π–π stacking, forming channels from the aligned pores.[255] Stirring the COF in an aqueous solution of LiTFSI replaced the parent chloride ions with $TFSI^-$ ions. One equivalent of $TFSI^-$ was charge-balancing the triaminoguanidinium within the framework and one equivalent was charge-balancing Li^+ ions which

remained in the electrolyte matrix. This electrolyte exhibited a conductivity of $5.74 \cdot 10^{-5}$ $S \cdot cm^{-1}$ at 30 °C and an activation energy of 0.34 eV. The Li^+ transference number of 0.61 was consistent with at least a portion of the $TFSI^-$ ions being immobilized through interaction with the cationic triaminoguanidinium groups. Additionally, a respectable operating potential window of 3.8 V was measured. Studies suggested that the $TFSI^-$ ion existed within the framework both as a "free" anion stabilized within the COF channel through Coulombic interactions, and as an ion pair. The ion-paired $TFSI^-$ likely decreases the Li^+ transference number, given that the equivalent of $TFSI^-$ present within the framework to charge-balance the Li^+ is likely not coordinated to the COF. Although this example showcases post-synthetic alteration of the anion identity that is not feasible in borate-based COFs (see below), the challenge with utilizing a cationic COF rather than a coordinatively-unsaturated charge-neutral MOF is that addition of alkali metal salts such as LiTFSI introduces equivalents of monoanions both to charge-balance the cationic framework and to ion-pair with the metal cations. Such electrolytes still possess an advantageously high density of anionic hopping sites and the safety features of solid electrolytes, but obtaining higher metal cation transference numbers will likely be a challenge due to the large percentage of mobile anions. An interesting extension upon this work could involve soaking the COF in a polylithium salt.[256–260] This could yield the COF with equal equivalents of the polyanion immobilized within the channels, triaminoguanidinium groups within the framework itself, and mobile Li^+. One consideration with this approach would be careful selection of the anion, particularly in terms of size; Chen et. al. reported diminished π–π stacking within the COF upon replacing the Cl^- ions with larger $TFSI^-$ ions. This partial collapse of the stacked structure may obstruct metal transport pathways within the framework.

Incorporating anions directly into the structure. An alternative to introducing stoichiometric equivalents of anions concomitant with mobile cations is to target inherently negative frameworks, where the negative charges are built into the MOF/COF building blocks themselves. In 2015, Van Humbeck, Long, and coworkers reported crosslinked tetraarylborate moieties that form a negatively charged porous

polymer wherein the anionic borates serve as immobile Li^+ hopping sites.[261] This approach was inspired by early reports of linear polymers containing ionic groups such as anionic perfluoroalkyl carboxylates[262] or cationic diallyldimethylammonium units[263] within the polymer structure. Such polymers were also used as solid electrolytes with the goal of achieving single-ion conductivity, and exhibited mobile ion transference numbers nearing unity. The observed conductivities for such polymers fell in the 10^{-6} to 10^{-5} $S \cdot cm^{-1}$ range, possibly due to undesirably large distances between the hopping sites along the polymer backbone. In contrast, the material designed by Van Humbeck, Long, et al. features an interpenetrated network that provides a high density of ion hopping sites. Measurements gave a Li^+ conductivity of $3.6 \cdot 10^{-5}$ $S \cdot cm^{-1}$, which increased further by one order of magnitude upon perfluorination of the aryl groups in the tetraarylborate network ($\sigma_{Li} = 2.7 \cdot 10^{-4}$ $S \cdot cm^{-1}$). Installation of electron-withdrawing fluorine atoms on the aryl rings was thought to weaken the borate-Li^+ interaction and thus encourage Li^+ mobility through the electrolyte. As expected, immobilization of the anions within the framework afforded strong single-ion conducting character with a high Li^+ transference number ($t_{Li} = 0.9$). Interestingly, altering synthetic conditions afforded a permanently porous fluorinated tetraarylborate material (BET surface area = 480 $m^2 \cdot g^{-1}$) that exhibited ten-fold lower conductivity than its dense-phase congener. Although this difference in conductivity between the porous and dense phase is consistent with the need for closely packed hopping sites, the activation energies of the two phases were identical, 0.25 eV. The phase-independent activation energy data may point to dominating surface conduction pathways as proposed by the authors. However, the distinct differences in conductivity as a function of phase density and the fact that the identities of the hopping sites do remain constant in both phases highlights the importance of hopping site density on ionic conductivity. Most tellingly, it emphasizes that three-dimensionally connected pores become detrimental to ion transport beyond a certain diameter.

Another example of anionic borates being featured in ionically conductive MOFs and COFs was a spiroborate-based COF synthesized by base-promoted transesterification of diols and trimethylborate using

LiOH as the base. The latter served the roles of both deprotonating the diol during the transesterification and providing the Li^+ ions for the electrolyte,[264] thus allowing a one-pot synthesis of a Li^+-loaded solid electrolyte (**Figure 5-4**). Incorporating the spiroborate structure into the COF was motivated by previous reports of Li borate salts used as Li^+ electrolytes.[265] The spiroborate COF / polyvinylidine fluoride (PVDF) formulation exhibited a Li^+ conductivity of $3.05 \cdot 10^{-5}$ $S \cdot cm^{-1}$ and an activation energy of 0.24 eV. In addition to favorable conductivity and activation energy values, a high Li^+ transference number of 0.8 was measured. Finally, a respectable potential window of ca. 4.5 V was reported, further highlighting the utility of solid-state electrolytes over liquid electrolytes that decompose at lower potentials. The formation of inherently negatively charged frameworks provides a host matrix with a homogeneous distribution of cation hopping sites that contributes nothing to increasing the anion transference number. It provides a promising blueprint for very efficient cation conductors, but has only rarely been used thus far.

One instance where this strategy proved effective with MOFs involved the substitution of trivalent Sc^{3+} ions in $[ScX(\mu_4\text{-pmdc})_2(H_2O)_2] \cdot 5H_2O$ ($pmdc^{2-}$ = pyrimidine-4,6-dicarboxylate; X = Li^+ or Na^+) (**Figure 5-3e**) by divalent Cd^{2+} or Mn^{2+}.[266] Low conductivity in the parent samples presumably stems from the alkali metal cations being affixed in the framework, thus hindering their mobility. As such, aliovalent substitution of Sc^{3+} with Cd^{2+} or Mn^{2+} was pursued with the goal of installing additional free alkali metal cations for charge balance. Indeed, free Li^+ and Na^+ ions compensated for the charge imbalance created by this aliovalent substitution. However, these ions still contributed low Li^+ and Na^+ conductivity values (10^{-7} to 10^{-6} $S \cdot cm^{-1}$ for the Cd^{2+} and Mn^{2+}-doped MOFs). The authors reported enhanced Li^+ and Na^+ conductivity values from simply soaking the parent Sc^{3+}-MOFs in solutions of $LiBF_4$ or $NaPF_6$. The resulting electrolytes exhibited ionic conductivities of 10^{-5} $S \cdot cm^{-1}$ (Na^+) and 10^{-4} $S \cdot cm^{-1}$ (Li^+). Even though the soaking procedure afforded enhanced conductivity, this treatment also caused cracking of the crystals, while peak broadening in the ^1H and ^7Li NMR spectra revealed increased structural heterogeneity. Together, these observations complicate the direct correlation between conductivity and the mobile charge density

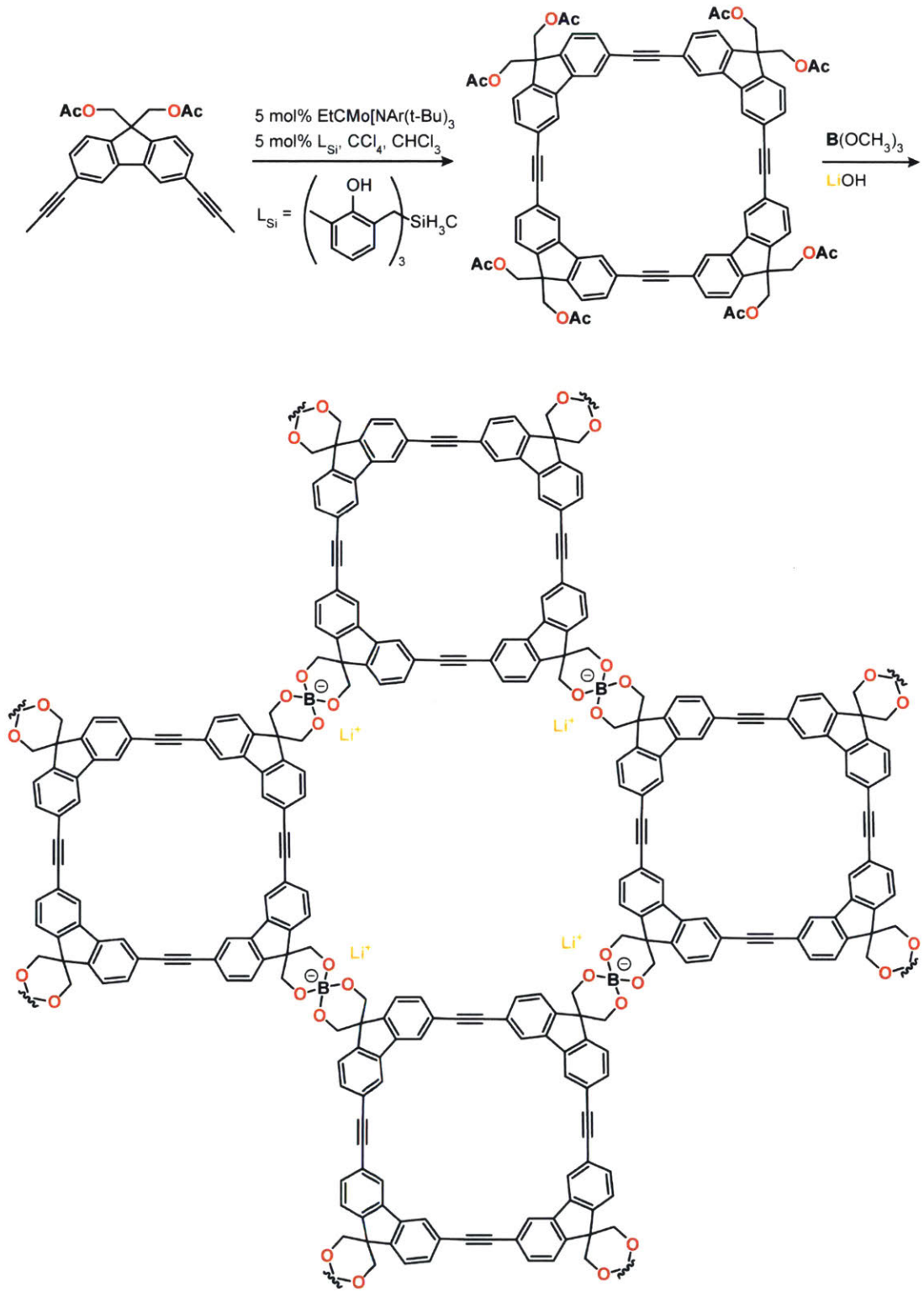

Figure 5-4. Spiroborate COF featuring anionic sites integrated into structure, and charge-balancing Li^+ ions provided by the base during synthesis.

and prevent detailed studies probing potentially new conduction mechanisms in the metal-exchanged samples. Such information could have been useful in explaining the large discrepancy in activation energies for the Li samples versus the Na samples (0.25 eV versus 0.64 eV, respectively). Despite the low conductivity observed in the aliovalently doped samples described above, the idea that aliovalent substitution can increase the mobile cation density in a MOF is potentially quite general and could in principle be applied to MOFs made from tri- or higher-valent metal ions, with cation substitution in general established as a versatile synthetic technique in this class.[267]

Neutral host frameworks. Although neutral host frameworks that do not easily accommodate anions may not seem like ideal candidates for solid electrolytes, some notable examples that highlight the importance of processing porous solid electrolytes do use such hosts. For instance, uniaxial pressure applied to $C_9H_4BO_2$ (COF-5) (**Figure 5-3f**) and TpPa-1 (Tp = triformylphloroglucinol, Pa = paraphenylenediamine) (**Figure 5-3g**) promoted preferred orientation of platelet crystallites, thereby forcing alignments of the COF pores and the formation of long-range channels for more efficient ion transport.[268] Soaking these materials in solutions of $LiClO_4$ followed by evaporation and uniaxial pressing afforded solid electrolytes with conductivities of $2.6 \cdot 10^{-4}$ $S \cdot cm^{-1}$ and $1.5 \cdot 10^{-4}$ $S \cdot cm^{-1}$ for COF-5 and TpPa-1, respectively. Although ^7Li NMR experiments confirmed the highly mobile nature of Li^+, the mobility of the charge-balancing ClO_4^- anions which can also contribute to the conductivity, was not measured. As before, obtaining the Li^+ transference numbers for these COFs would be critical for assessing the Li^+ contribution to the total ionic conductivity.

Recently, the notion of forming true hybrids between porous materials and polymers for ion conduction has been pursued in the form of the "polyelectrolyte" COFs such as TPB-DMTP-COF (TPB = 1,3,5-tri(4-aminophenyl)benzene, DMTP = 2,5-dimethoxyterephthalaldehyde) and TPB-BMTP-COF (BMTP = 2,5-bis((2-methoxyethoxy)methoxy)terephthalaldehyde).[269] Condensation of TPB with either DMTP or BMTP resulted in porous, stacked 2D COFs with either methoxy groups (TPB-DMTP-COF) or

oligo(ethylene oxide) chains (TPB-BMTP-COF) branching off of the phenyl rings and lining the pore walls. This approach aimed to combine the ion transport benefits of polymer electrolytes with the mechanical and thermal stability of MOF/COF electrolytes. Soaking these porous, crystalline structures in solutions of $LiClO_4$ afforded materials with conductivities of 10^{-7} $S \cdot cm^{-1}$ (TPB-DMTP-COF) and 10^{-6} $S \cdot cm^{-1}$ (TPB-BMTP-COF) at 40 °C, both improvements upon that of the PEO-Li^+ complex, which has a Li^+ conductivity of 10^{-8} $S \cdot cm^{-1}$ at 40 °C. It should be noted that both materials exhibit high activation energies for ionic transport, 0.96 eV for TPB-DMTP-COF and 0.87 eV for TPB-BMTP-COF, which suggests that improvements are likely for a class of materials that allows for considerable combinatorial potential. Once again, more systematic improvements would be facilitated by ^7Li NMR studies and measurements of the Li^+ transference numbers to parse out the mobility of free Li^+ ions versus ion-paired $LiClO_4$. The approach of implementing polymeric building blocks that have proven ion conductivity into crystallographically well-defined and mechanically and thermally robust COF structures is intriguing. Further structural characterization of these analogues after incorporation of Li salts would aid in determining whether the COF structure is retained in the final electrolyte matrix.

5.5 Scouting criteria: What makes a MOF / COF ionically conductive?

The several examples discussed herein were chosen to showcase the multiple approaches available for achieving ionic conductivity in MOFs and COFs. When evaluating these porous materials as potential candidates for ion conduction, the following considerations may prove useful:

- Does the MOF feature metal sites with coordination environments that include removable solvent molecules, or other anion docking sites?
- Are anions incorporated into the MOF/COF structure, e.g. as part of the building blocks or by Coulombic forces?
- Is the material isolable in multiple states of formal charge? Is isolation of these states reversible?
- Is the MOF/COF electrically insulating?

- Is there a high density of hopping sites within the structure?
- What are the sizes of metal ions that could be accommodated within the pores?
- Would the mobile metal ions be solvated in the pores? How many equivalents of solvated metal ions can the structure accommodate?

When testing MOFs and COFs for ion conduction, the following criteria can serve as reference benchmarks for evaluating performance:

- Ionic conductivity $\geq 10^{-4}$ S·cm^{-1}, ideally when T ~ 25 °C[248]
- Electrical conductivity $\leq 10^{-10}$ S·cm^{-1}, to avoid cell shorting[207]
- Activation energy ≤ 0.4 eV[248]
- Working potential window of ≥ 4 V for commercial applications[270]
- Transference number of ≥ 0.5, to avoid polarization effects[253]
- Structurally stable to the desired mobile metal salts, dielectric additives, and the electrode materials
- No or nominal increase in resistance during cycling

5.6 Conclusions / Future directions

The continuously growing energy demand is being addressed with innovative, sustainable technology and metal and metal-ion batteries remain leaders for electrical energy storage in terms of combined energy density, portability, longevity, and cost. Continued optimization of these devices requires enhanced safety and even greater operating efficiency, both of which can be greatly improved by an optimized solid-state electrolyte. MOFs and COFs have gained attention as promising candidates for solid-state electrolyte technology due to their crystallographic definition which contributes immobilized and homogeneously distributed ion hopping paths, enhanced thermal and mechanical stability, and a morphology that in principle could prevent hazardous dendrite formation. The high surface area of these materials allows an abundance of cation hopping sites, which aids in minimizing battery resistance. Reports detailing installation of hopping sites into MOFs and COFs both by coordinating anions to cationic sites

within the frameworks and by installing anionic sites directly as components of the frameworks highlight the versatility of this class of materials for battery electrolyte applications. Several examples have shown great promise in this arena by exhibiting ionic conductivities of 10^{-6} to 10^{-4} $S \cdot cm^{-1}$ under ambient conditions, activation energies of 0.1-0.4 eV, cation transference numbers of 0.6-0.9, and potential windows exceeding 4.0 V.

Looking forward, exploring the effect of MOF/COF crystal size on conductivity could aid in elucidating whether ion mobility is an inter- or intra-crystal phenomenon. Such studies could also aid in optimizing conductivity versus dendrite formation, which may occur along grain boundaries. Further, many of the reported MOFs and COFs have shown promising properties when combined with monolithium salts. Expansion of these studies could involve use of a polylithium salt, to achieve higher Li^+ loading. Another underexplored area is the utilization of inherently anionic materials balanced by potentially mobile cations residing in the pores. This may encourage homogeneous distribution of the charge balancing metal ions throughout the host matrix while minimizing incorporation of mobile, exogenous species that are typically introduced using more iterative electrolyte preparation methods. Additionally, hybridizing porous materials with traditional polymer electrolytes may allow for retention of the ionically conductive properties of the polymers while adding benefits associated with porous solid electrolytes, e.g. minimized electrolyte reorganization, maximized hopping site density, and potentially no dendrite growth. Finally, targeting good ion conductors for K^+, Ca^{2+}, or Al^{3+} transport in the MOF/COF context could prove fruitful given that these larger/higher-valent ions might require larger pores than typically available with denser materials. Employing MOFs and COFs as solid electrolytes for K-ion, Ca-ion, or Al-ion batteries would combine the benefits of porous material-based electrolytes with the advantages of using energy-dense, earth-abundant ions. The wealth of metal and ligand combinations that may engender a host of pore shapes, sizes, and local electronic environments that may accommodate any number of metal ions lays an expansive foundation for a bright future of MOF/COF-based solid electrolytes.

Chapter 6

Multi-Valent Ionic Conductivity in a Cu-Azolate Metal-Organic Framework

6.1 Introduction

Since the emergence of the first rechargeable galvanic cell in 1860,[195] rechargeable batteries have become an enabling technology for a range of critical processes in modern life. Although old in a sense, rechargeable battery technologies represent an important field of modern research, spurred by the scale and variety of applications stemming from an inevitable transition to renewable and clean energy technologies. Among the various possible technologies, metal and metal-ion batteries are particularly versatile in serving a range of applications especially in consumer electronics, where they offer a combination of high volumetric capacity and ~1000-cycle lifetime that is well suited for such devices.[196] However, despite significant advances there is much room for improvement in efficiency, lifetime, and safety of metal and metal-ion batteries. All these could be improved by transitioning from liquid electrolytes, the current industry standard, to solid ion conductors. Liquid electrolytes exhibit relatively narrow potential stability windows, cation transference numbers of < 0.4 that lead to lifetime-limiting polarization effects, and little control over the uniformity of Li plating during charging.[196] Non-uniform plating can cause dendrite formation, which may result in piercing the battery separator and leakage of the flammable organic liquid electrolyte, or if contact is made with the other electrode, circuit shorting. Efforts to address these challenges have included development of solid-state electrolytes.[197,210–214,271–279] Although solid electrolytes exhibit higher potential stability windows, higher transference numbers, and are safer by virtue of their reduced flammability and increased mechanical stability, they can suffer from low conductivity and poor interfacial contact between the electrodes and the electrolyte.[196,197,212,213,271] An ideal system would combine the lower transport and interfacial resistance of liquid electrolytes with the safety and enhanced stability features of solid electrolytes.

One class of materials that may provide clues to addressing these challenges is metal-organic frameworks (MOFs). The high surface area of MOFs offers the ability to install a high density of charged species in a small geometric volume. This allows for closely packed cation hopping sites, which could

minimize activation energy for ion transport and increase ion conductivity. Additionally, the ordered porosity of MOFs could aid in controlling the uniformity of cation plating at the anode during charging, thus preventing dendrite formation. Many MOFs present metal sites whose coordination spheres are initially occupied by solvent molecules. Removing the solvent molecules exposes coordinatively unsaturated cationic sites onto which anions can be docked. The coordinated anions require charge-balancing cations that become the only mobile charge carriers, thus maximizing cation transference numbers. Finally, altering the lability and / or valency of the metal centers, changing pore polarity by ligand functionalization, and enlarging the pore diameter by extending the ligand length offer multiple tunable variables for systematic optimization of electrolyte performance. Indeed, several MOFs have been explored as solid-state electrolytes, and have featured many of the benefits listed above.[216,247,251,253,254,266] Although promising, many of these MOFs require additional salt content in excess of what would be expected based on the number of available anion binding sites. This necessarily implies that not only cations, but also anions will be mobile, which in turn reduces the cation transference numbers. Additionally, activation energies in such materials are sometimes higher than is desired, as ion pairing between anions and cations is still strong. Some of the reported MOF-based electrolytes have also shown poor stability to electrochemical cycling, eliminating their viability for rechargeable batteries. To expand upon current MOF electrolytes, we took advantage of a Cu-azolate material, $Cu_4(ttpm)_2$ (H_4ttpm = tetrakis(4-tetrazolylphenyl)methane)[280] that presents multiple anion binding sites, which lead to high mobile Li^+, Mg^{2+}, and Al^{3+} density. The ability to reconstitute this MOF in various types of metal salts allowed for modulation of the ion pairing strength, as evidenced by conductivity and activation energy values that change as a function of anion identity.

6.2 Results and discussion

The anionic parent material, $Cu[(Cu_4Cl)(ttpm)_2]_2 \cdot CuCl_2$, and the neutral framework, $Cu_4(ttpm)_2 \cdot 0.6CuCl_2$, were synthesized according to a reported procedure.[280] It was previously shown that

Cu_4(tetrazole)$_8$ secondary building units (SBUs) in the original material feature 5 possible halide binding sites, a portion of which can be made available by Soxhlet extraction with methanol (**Scheme 6-1**).[280] Importantly, some of these sites bear bridging halides. This opens the possibility of reducing the ion pairing

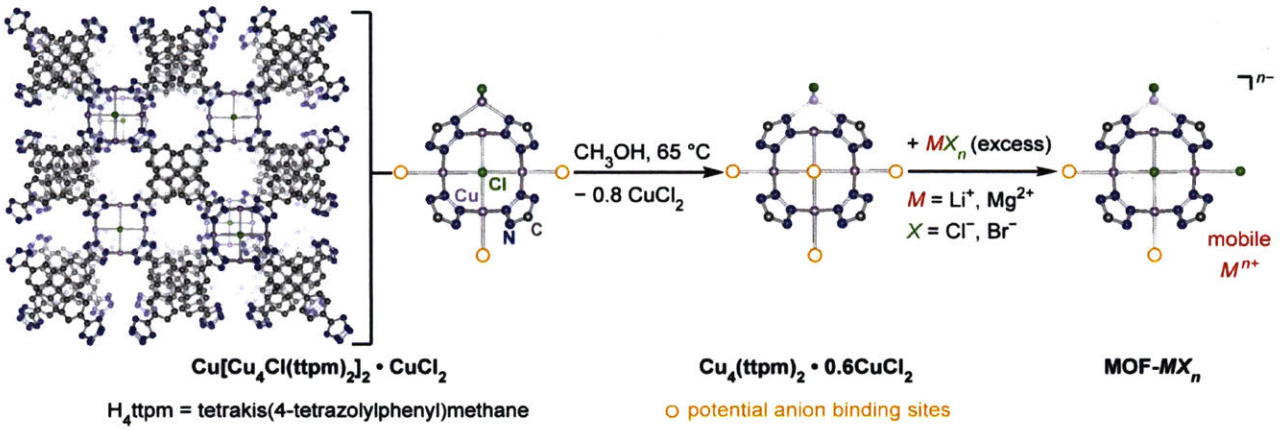

Scheme 6-1. Synthesis of $Cu[(Cu_4Cl)(ttpm)_2]_2 \cdot CuCl_2$, $Cu_4(ttpm)_2 \cdot 0.6CuCl_2$, and the target MOF-$MX_n$, where $M = Li^+$ or Mg^{2+}; $X = Cl^-$, Br^-, or I^-; and $n = 1$ or 2.

between mobile cations and bridging halides because electron density on the latter would be screened by multiple Cu^{2+} ions. Reconstitution of $Cu_4(ttpm)_2 \cdot 0.6CuCl_2$ in saturated THF solutions of various Group 1 and 2 metal halide salts afforded anionic structures balanced with alkali and alkaline earth metal cations (**Scheme 6-1**). The resulting materials were washed with propylene carbonate (PC), a commonly used dielectric that solvates the metal cations and can improve inter-particle conductivity.[216,253] Inductively-coupled plasma-mass spectrometry (ICP-MS) and quantitative ^1H NMR spectroscopy of digested samples (**Figures 6-1 to 6-6**) provided the Group 1 and 2 metal content, and propylene carbonate content, respectively, for the final electrolyte formulations (**Table 6-1**).

That the coordination mode of the halides can be defined within the crystallographic parameters of the MOF as opposed to random dispersion of the salts within the electrolyte matrix was evidenced by powder X-ray diffraction (PXRD) and scanning electron microscopy-energy dispersive X-ray spectroscopy

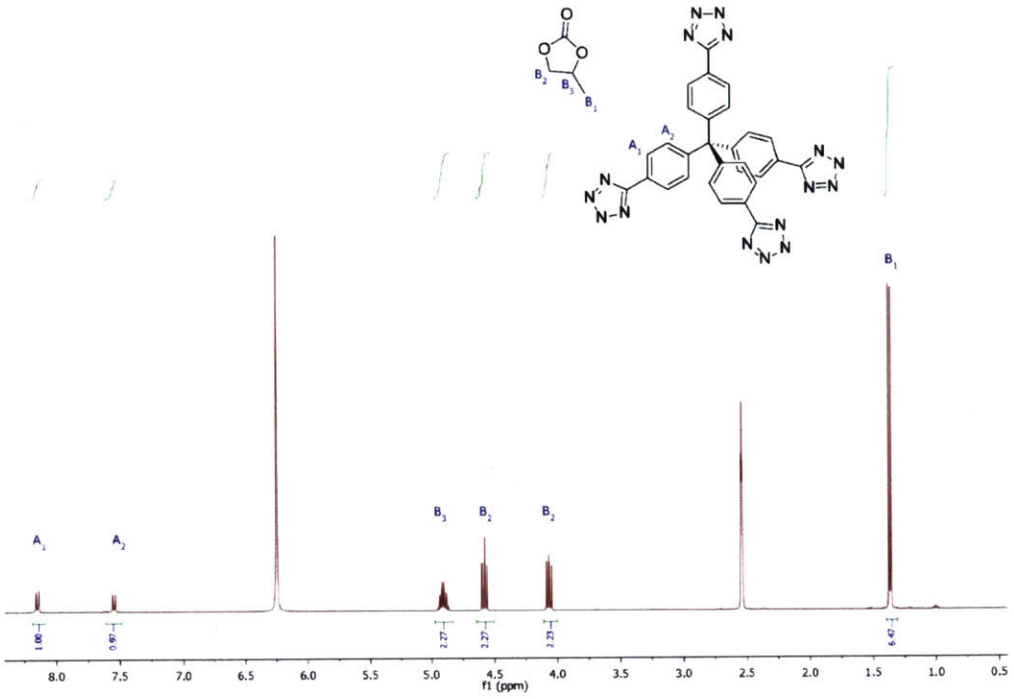

Figure 6-1. ^{1}H NMR spectrum of digested MOF-LiCl.

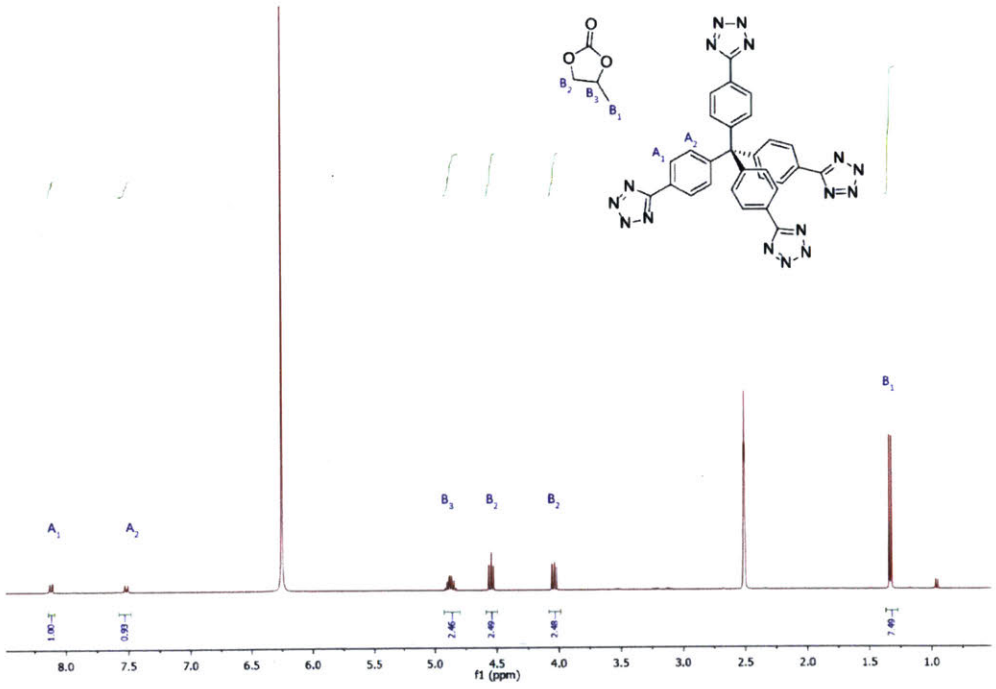

Figure 6-2. ^{1}H NMR spectrum of digested MOF-LiBr.

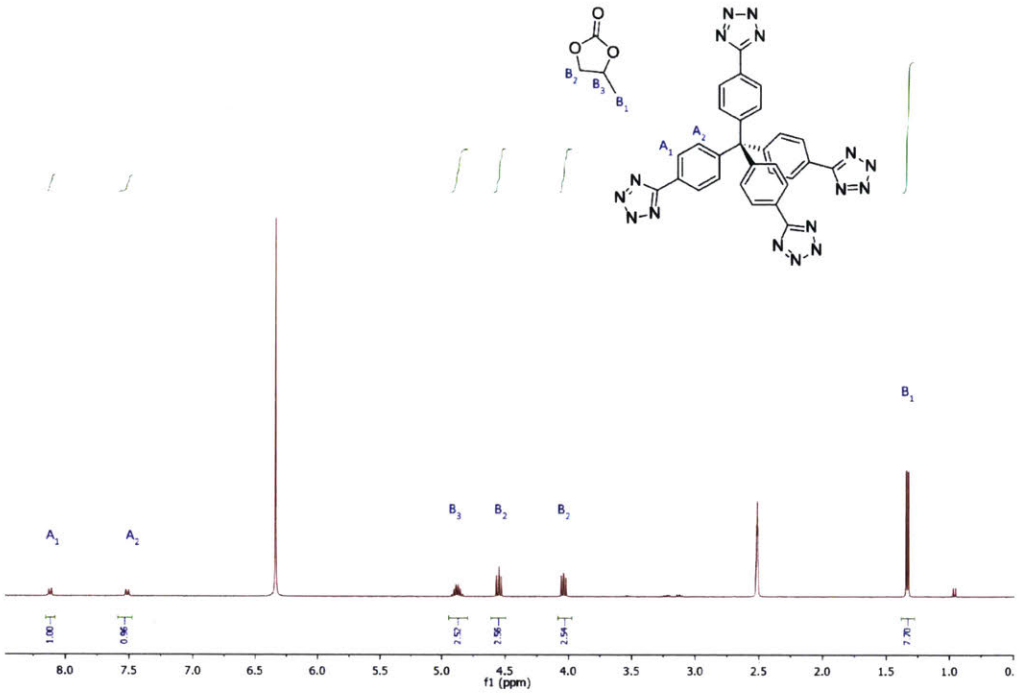

Figure 6-3. ^{1}H NMR spectrum of digested MOF-LiI.

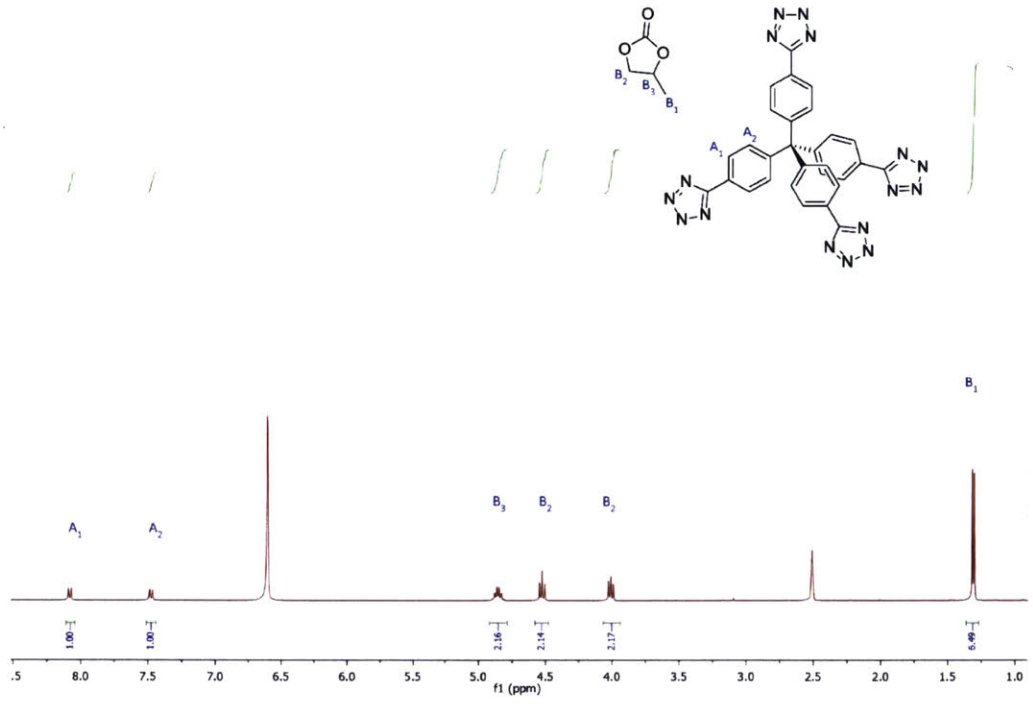

Figure 6-4. ^{1}H NMR spectrum of digested MOF-$MgCl_2$.

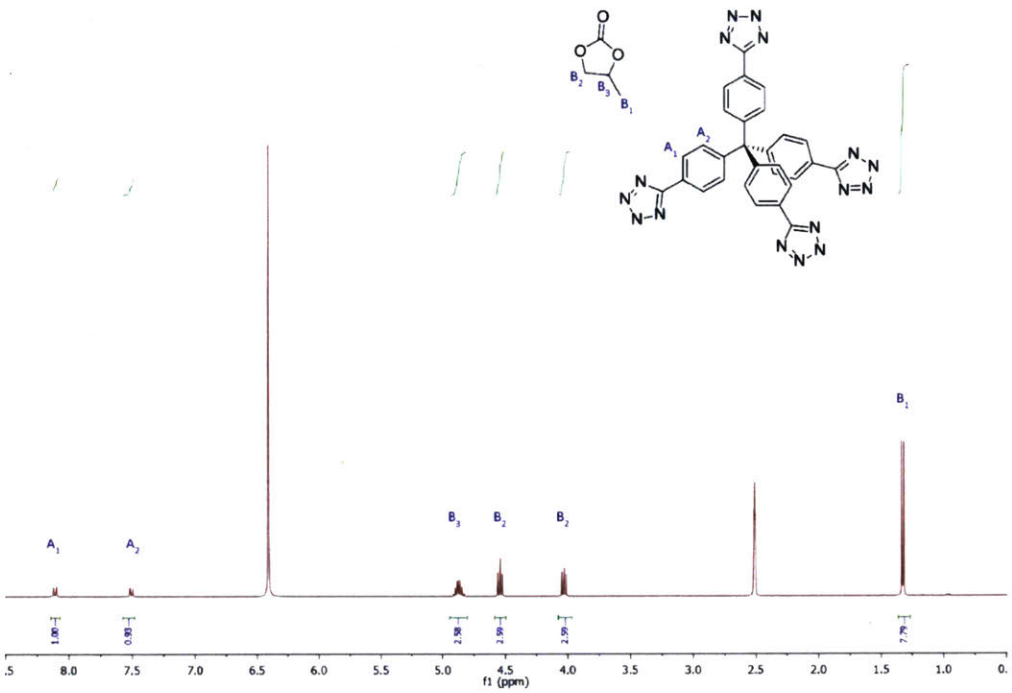

Figure 6-5. ^{1}H NMR spectrum of digested MOF-$MgBr_2$.

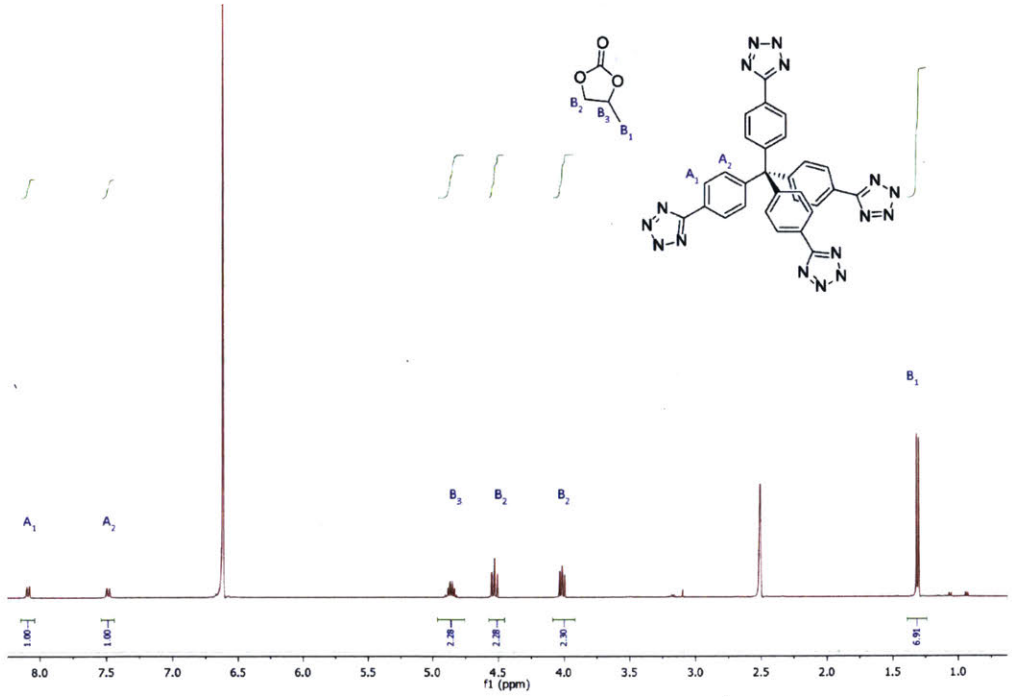

Figure 6-6. ^{1}H NMR spectrum of digested MOF-MgI_2.

Table 6-1. Formulas of MOF-MX_n, including metal ratios as determined by ICP-MS and propylene carbonate (PC) content from ^{1}H NMR spectroscopy.

Sample name	Cu	M (M = Li^+, Mg^{2+})	X (X = Cl^-, Br^-, I^-)	Formula
MOF-LiCl	2.5	1.0	1.0	$Cu_4(ttpm)_2(CuCl_2)_{0.6}(LiCl)_{1.8}\cdot 19PC$
MOF-LiBr	2.4	1.0	1.0	$Cu_4(ttpm)_2(CuCl_2)_{0.6}(LiBr)_{1.8}\cdot 20PC$
MOF-LiI	4.5	1.0	1.0	$Cu_4(ttpm)_2(CuCl_2)_{0.6}(LiI)_{1.0}\cdot 20PC$
MOF-$MgCl_2$	6.1	1.0	2.0	$Cu_4(ttpm)_2(CuCl_2)_{0.6}(MgCl_2)_{0.8}\cdot 17PC$
MOF-$MgBr_2$	6.4	1.0	2.0	$Cu_4(ttpm)_2(CuCl_2)_{0.6}(MgBr_2)_{0.7}\cdot 21PC$
MOF-MgI_2	7	1.0	2.0	$Cu_4(ttpm)_2(CuCl_2)_{0.6}(MgI_2)_{0.7}\cdot 15PC$

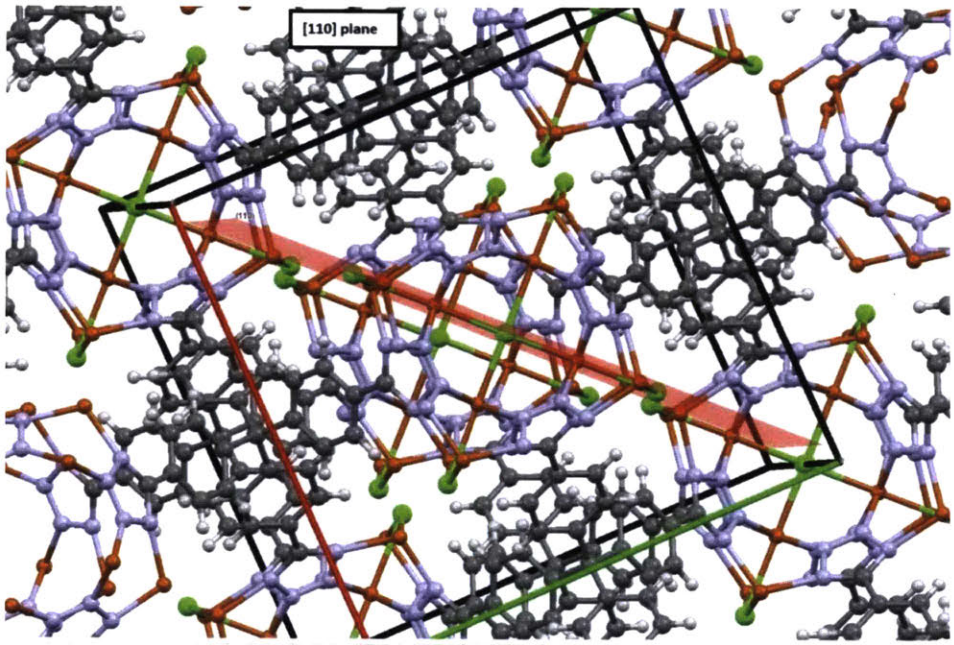

Figure 6-7. [110] reflection of $Cu[(Cu_4Cl)(ttpm)_2]_2\cdot CuCl_2$ (red plane), showcasing the contribution of the electron density of the halides within this plane.

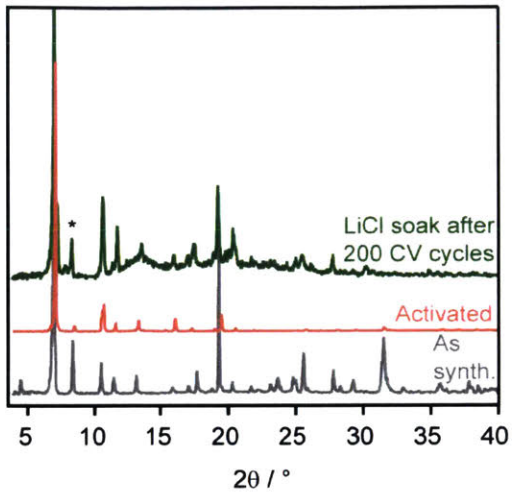

Figure 6-8. Representative PXRD pattern showcasing the disappearance and reemergence of the [110] reflection at 8° 2θ (largely contributed by the halide electron density), as well as stability of the MOF to electrochemical cycling. See **Figure 6-9** for PXRD patterns of the other analogues.

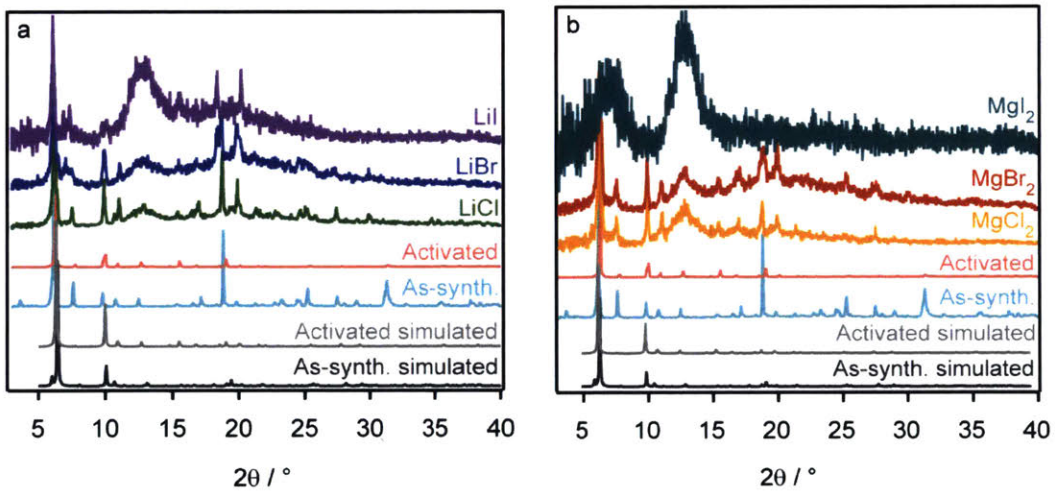

Figure 6-9. PXRD patterns of **a)** MOF-Li*X* and **b)** MOF-MgX_2 after variable-temperature EIS measurements. 'As-synth.' represents $Cu[(Cu_4Cl)(ttpm)_2]_2 \cdot CuCl_2$ and 'activated' represents $Cu_4(ttpm)_2 \cdot 0.6CuCl_2$.

(SEM-EDS). Soxhlet extracting the anionic $Cu[(Cu_4Cl)(ttpm)_2]_2 \cdot CuCl_2$ resulted in almost total disappearance of the PXRD peak at ~8° 2θ, which represents the [110] reflection to which the electron density of both bridging and axial chlorides is a major contributor (**Figure 6-7**). PXRD patterns of the MOF-MX_n samples showed a reemergence of this reflection, consistent with immobilized halides having a crystallographically distinct coordination mode within the Cu_4-lined cluster (**Figure 6-8, Figure 6-9**). PXRD confirmed that the MOF retains its structure both during the synthetic manipulation with chloride and bromide salts, and during at least 200 cyclic voltammetry (CV) cycles of these respective electrolytes. However, treating the MOF with LiI or MgI_2 resulted in major reduction of crystallinity with the former and total destruction of the MOF structure with the latter (**Figure 6-9**). This is not unexpected, as I^- is readily oxidized by Cu^{2+} and CuI_2 itself is unstable to disproportionation.[281–284]

The reactivity of the MOF-MI_n samples was further supported by the abundance of faradaic events observed in the MOF-LiI CV (**Figure 6-10**). This decomposition prevented collection of reproducible MOF-MgI_2 data. In addition to the PXRD patterns supporting crystallographically defined reincorporation of the anions into the MOF during the electrolyte soak procedure, SEM-EDS showed homogeneous

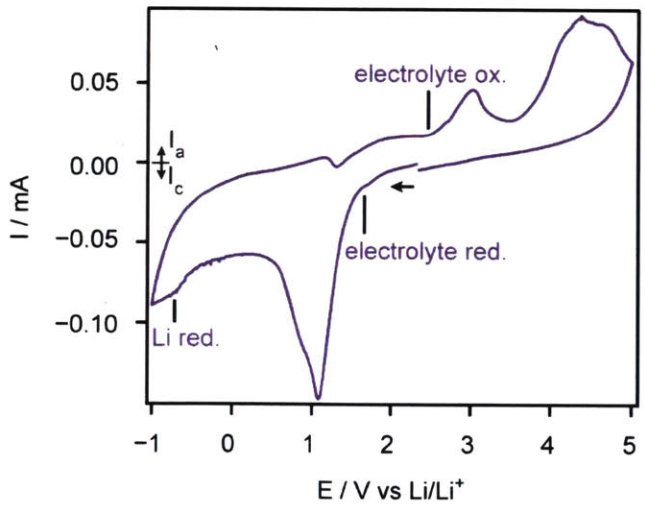

Figure 6-10. Cyclic voltammogram of MOF-LiI.

distribution of the halides throughout the MOF-LiCl electrolyte. The homogeneity of chloride as well as copper distribution in the spectra confirmed that no amorphous MX_n phase had aggregated within the electrolyte matrix. Further, reduction of the crystallite size by two orders of magnitude during the electrolyte soak procedure was consistent with the MX_n salts penetrating the crystals themselves rather than residing in grain boundaries or other more kinetically accessible locations (**Figure 6-11**).

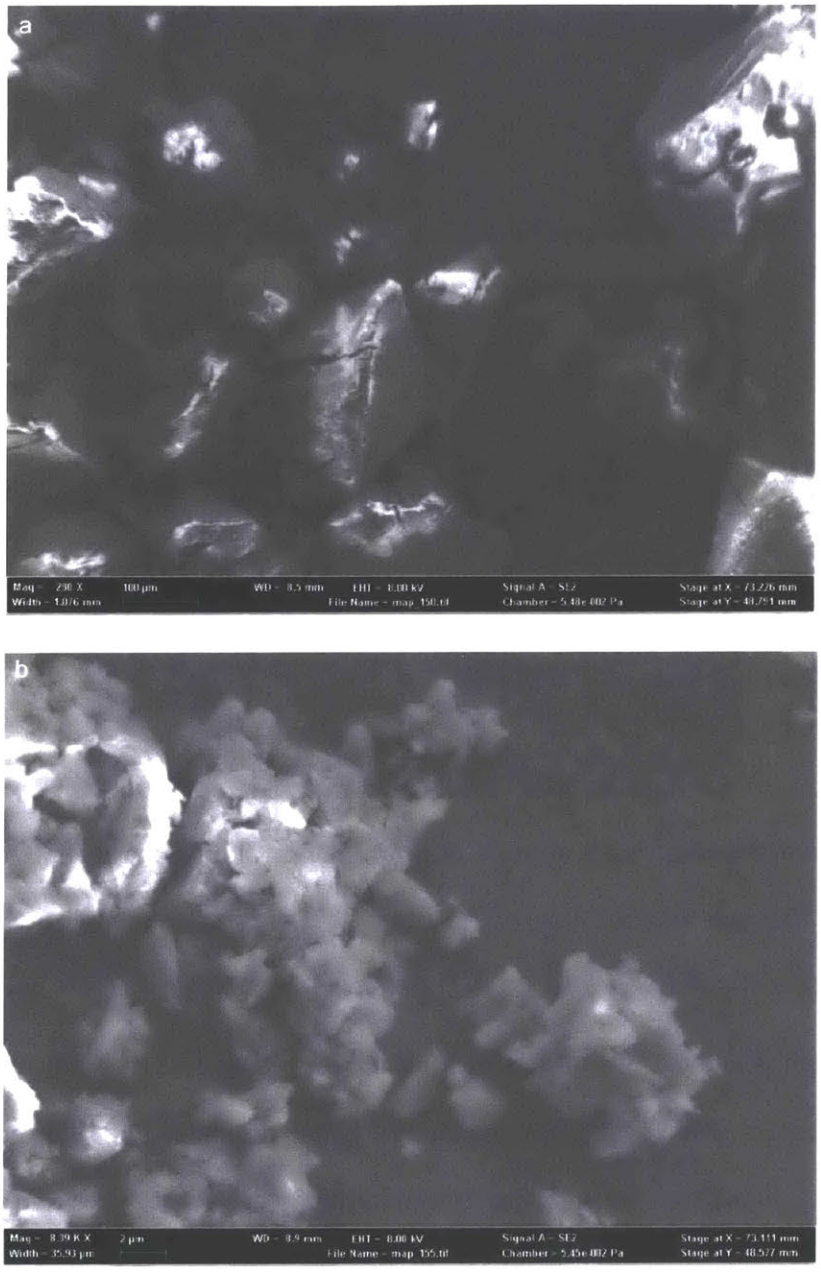

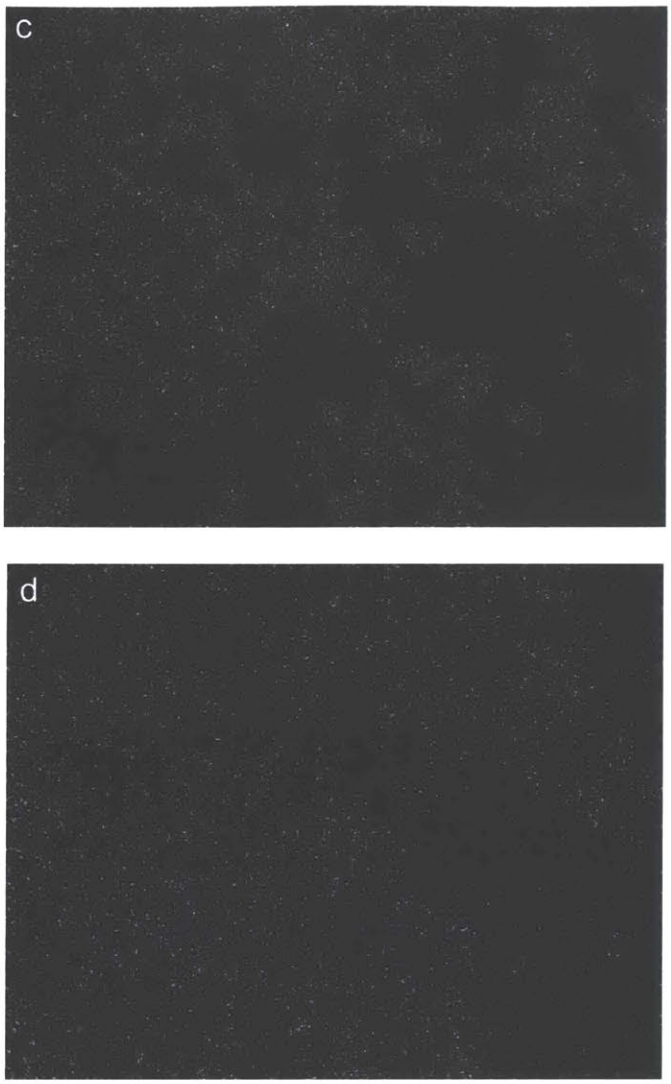

Figure 6-11. SEM images of **a)** $Cu_4(ttpm)_2 \cdot 0.6CuCl_2$, **b)** MOF-LiCl. EDS maps of MOF-LiCl are shown in **c** and **d** (Cu and Cl, respectively).

Stoichiometric reincorporation of structurally significant anions into a MOF has only been reported, to our knowledge, for one other MOF.[253] Immobilization of stoichiometric amounts of cation hopping sites within a material presents a promising template in the development of tunable solid electrolytes.

To ensure that the parent $Cu_4(ttpm)_2 \cdot 0.6CuCl_2$ was sufficiently electrically insulating for preventing short circuiting, −50 to 50 V was applied to a pressed pellet and the resulting current was measured. The generated I-V curve yielded an electrical conductivity of $5.08 \cdot 10^{-12}$ $S \cdot cm^{-1}$, identifying $Cu_4(ttpm)_2 \cdot 0.6CuCl_2$ as an electrical insulator and a suitable electrolyte material (**Figure 6-12**).[207] Additionally, confirmation that the free $CuCl_2$ would not convolute the ionic conductivity data was obtained

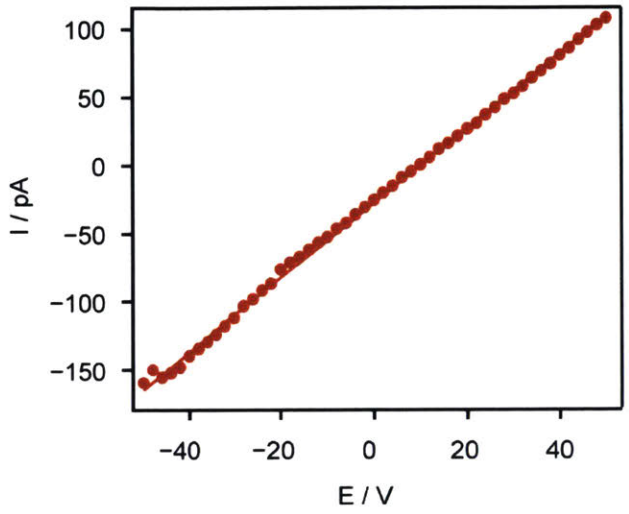

Figure 6-12. I-V curve used to calculate the electrical conductivity of $Cu_4(ttpm)_2 \cdot 0.6CuCl_2$.

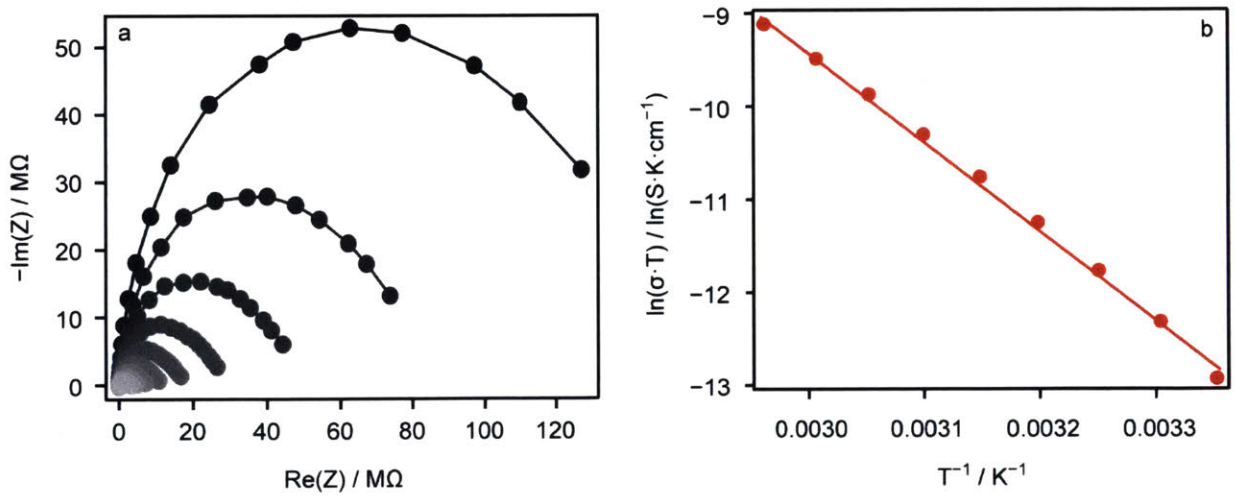

Figure 6-13. a) Variable-temperature electrochemical impedance spectra (lighter color signifies higher temperature) of $Cu_4(ttpm)_2 \cdot 0.6CuCl_2$ and **b)** the resulting Arrhenius plot.

by calculating the activation energy of the parent MOF. Variable-temperature electrochemical impedance spectroscopic (EIS) measurements revealed $Cu_4(ttpm)_2 \cdot 0.6CuCl_2$ to have a high activation energy of 0.85 eV (**Figure 6-13**).

The MOF-MX_n powders were loaded into a test cell and individually measured for conductivity. Fitting the resulting EIS spectra to the circuit shown in the Methods section gave Li^+ conductivities ranging from $2.4 \cdot 10^{-5}$ S·cm^{-1} (MOF-LiCl) to $1.1 \cdot 10^{-4}$ (MOF-LiI) at 25° C for the MOF-LiX samples (**Figure 6-14, Table 6-2**). Excitingly, this data highlighted the ability to systematically tune the conductivity by

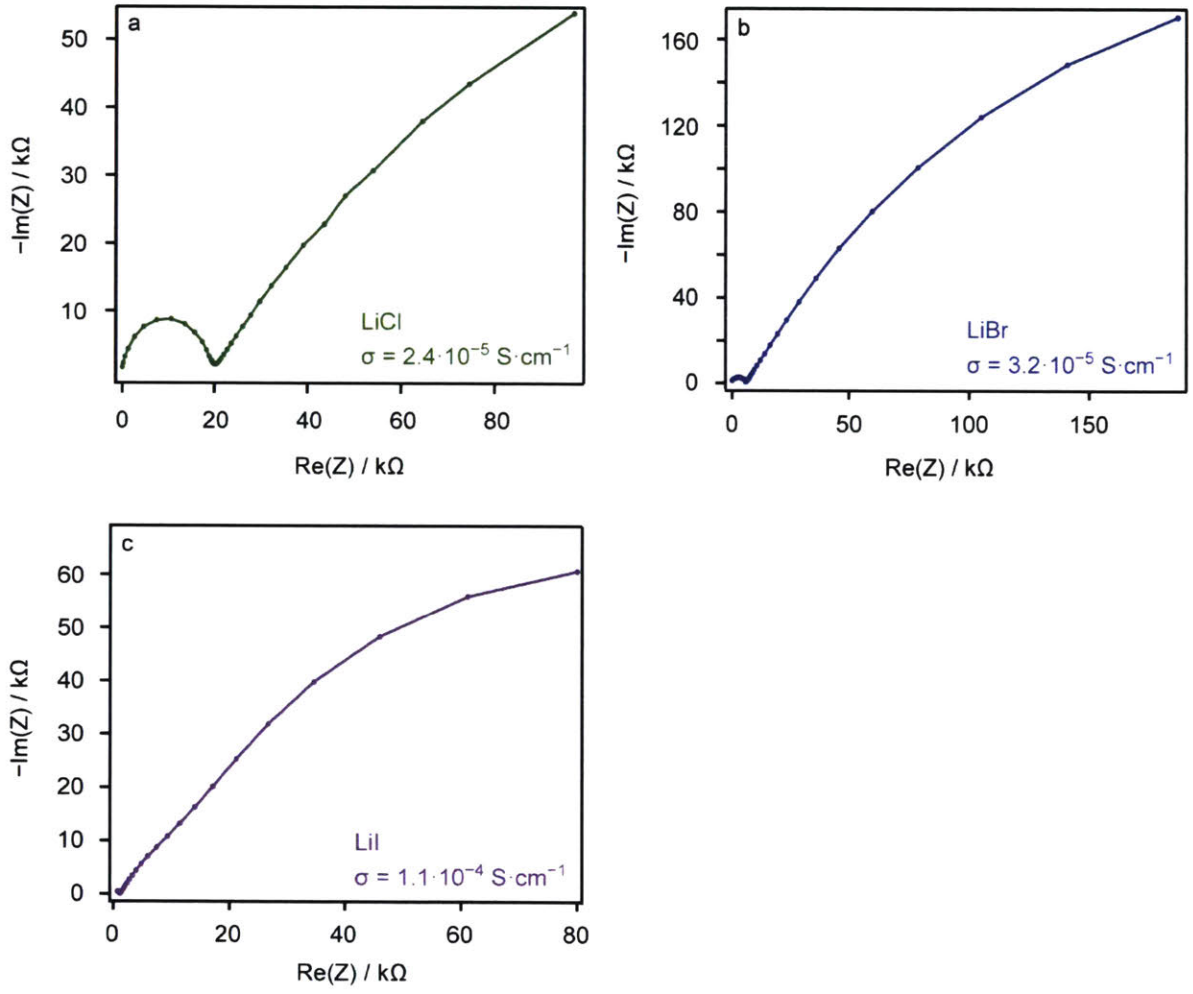

Figure 6-14. Electrochemical impedance spectra of MOF-LiCl (green, **a**), MOF-LiBr (blue, **b**), and MOF-LiI (purple, **c**), and corresponding conductivity values, collected at 25 °C.

Table 6-2. Conductivity, activation energy, and Li^+ transference number values of MOF-Li*X*.

Electrolyte	σ (S·cm^{-1})	E_a (eV)	Li^+ transference #
MOF-LiCl	$2.4 \cdot 10^{-5}$	0.34	0.69
MOF-LiBr	$3.2 \cdot 10^{-5}$	0.30	0.42
MOF-LiI	$1.1 \cdot 10^{-4}$	0.24	0.34

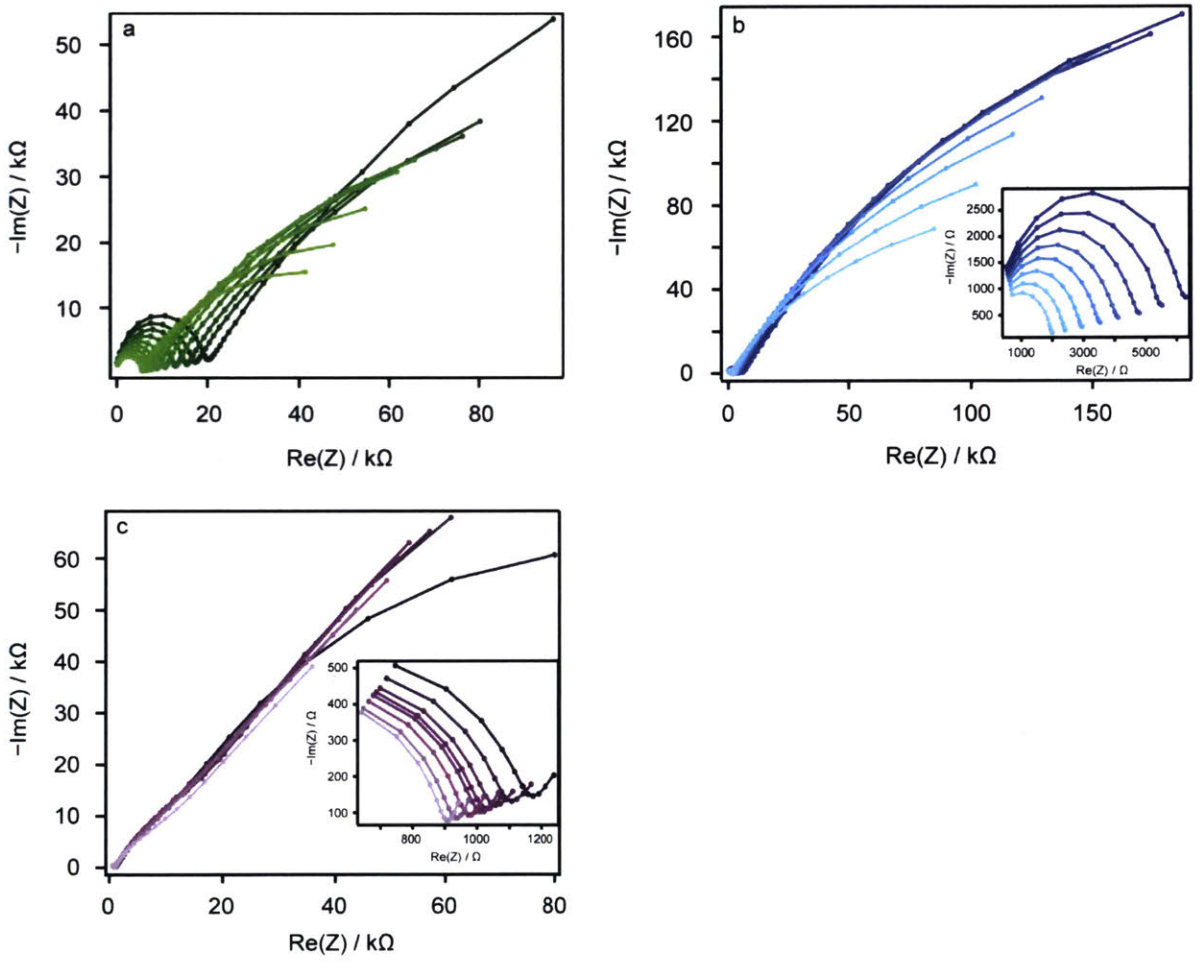

Figure 6-15. Variable-temperature electrochemical impedance spectra (lighter color signifies higher temperature) of **a)** MOF-LiCl, **b)** MOF-LiBr, and **c)** MOF-LiI.

modulating the softness of the anion, in turn altering the ionic strength of the Li-halide interaction. Additional utility of this modular structure was showcased in the activation energies. Variable-temperature EIS (**Figure 6-15**) and construction of the corresponding Arrhenius plots gave activation energies which also varied as a function of anion softness (E_a = 0.34 eV to 0.24 eV for MOF-LiCl and MOF-LiI, respectively) (**Table 6-2**). These low activation energies of < 0.4 eV are on-par with those of superionic conductors and are of commercial significance.[248] To evaluate the immobility of the halide ions within the MOF upon battery polarization, Li^+ transference numbers were calculated for MOF-Li*X* (**Figures 6-16 to 6-18**). MOF-LiCl yielded a high Li^+ transference number of 0.69, indicating that almost 70% of the current passed resulted from mobile Li^+ ions as opposed to other mobile, charged species.[223] This transference number is competitive with many solid electrolytes and a marked improvement upon liquid electrolytes, which typically exhibit Li^+ transference numbers of 0.3-0.4.[223,224] In those cases, the current is dominated by other mobile ions which can migrate to the electrodes and cause polarization effects that decrease battery lifetime. Ironically, the modularity of the anion identity here produces both quantifiable improvements in terms of conductivity and activation energy of the electrolytes, as well as challenges following these same trends. Transference numbers of the MOF-LiBr and MOF-LiI samples were calculated to be 0.42 and 0.34,

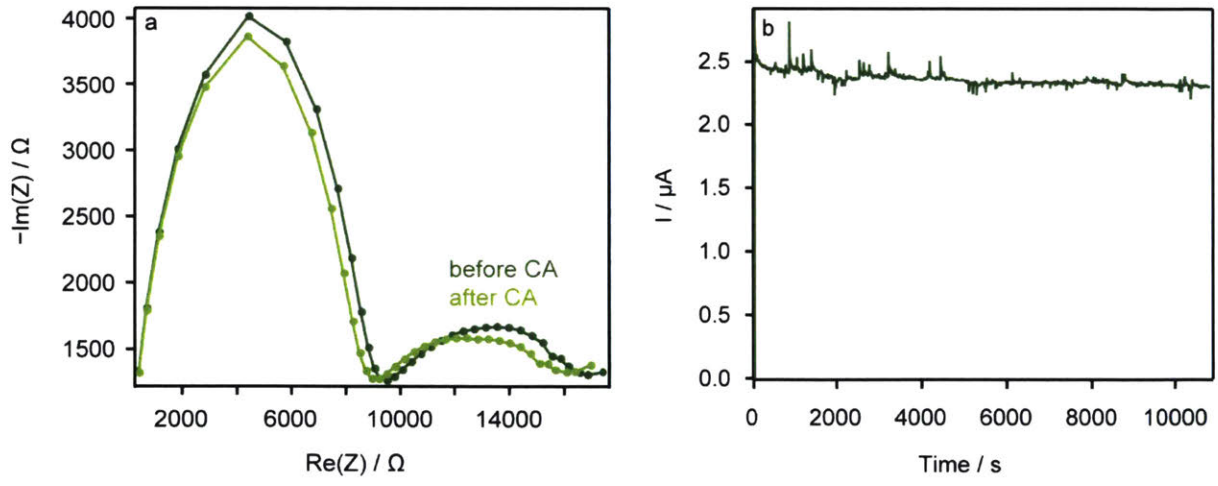

Figure 6-16. a) Electrochemical impedance spectra and **b)** potentiostatic measurement used to calculate the Li^+ transference number of MOF-LiCl.

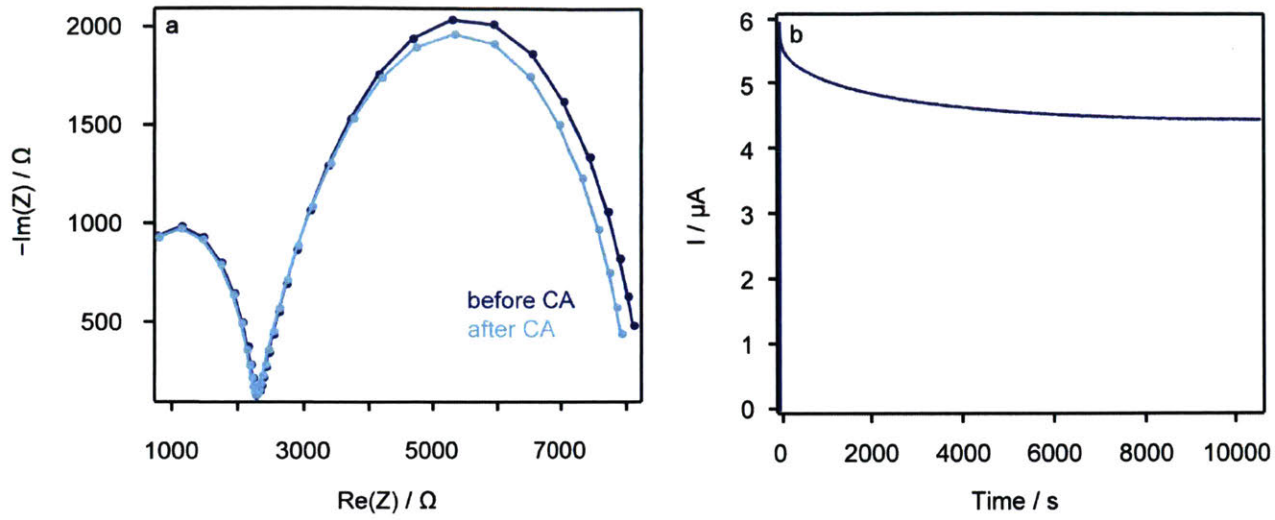

Figure 6-17. a) Electrochemical impedance spectra and **b)** potentiostatic measurement used to calculate the Li^+ transference number of MOF-LiBr.

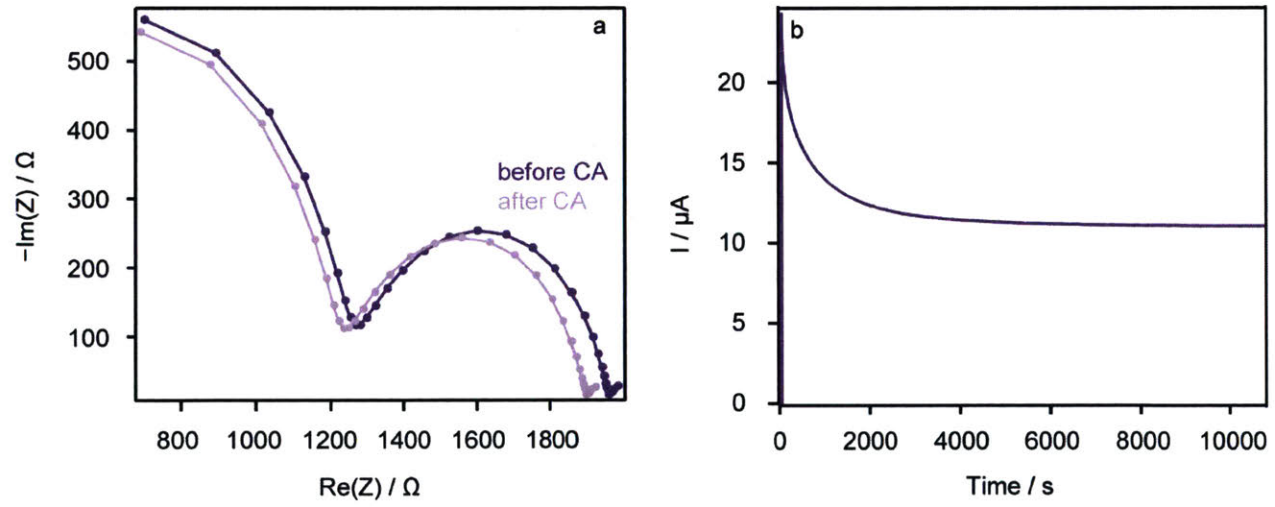

Figure 6-18. a) Electrochemical impedance spectra and **b)** potentiostatic measurement used to calculate the Li^+ transference number of MOF-LiI.

respectively (**Table 6-2**). This is likely due to the fact that in addition to ion pairing strength between the Li^+ and the anions decreasing with increasing anion softness, the Coulombic forces immobilizing the anions close to the Cu^{2+} centers also weaken with increasing anion softness.[285] Thus, upon application of electrochemical bias, a higher percentage of Br^- and I^- ions migrate to the opposite electrode compared to Cl^- ions. One possible solution could involve utilizing anions of enhanced steric bulk so that their mobility is more limited compared to those of monoatomic anions. A caveat with this approach may be that significantly increasing the anion size could result in lower loading of the desired metal salt, due to pore volume constraints within the MOF.

To further analyze the durability of the MOF-Li*X* electrolytes, electrochemical cycling experiments were conducted. Over 200 cycles, MOF-LiCl and MOF-LiBr retained reversible stripping and plating of Li, with only slight increase in overpotential (**Figure 6-19**). Additionally, the crystallinity of the structures was retained during extended electrochemical measurements (**Figure 6-9**). Interestingly, MOF-LiCl showed an increase in anodic current between cycles 1 and 30, after which time the current then decreased with progressing cycles. This may be due to slower kinetics observed in MOF-LiCl, consistent with the lower conductivity compared to that of MOF-LiBr. MOF-LiBr passed the maximum faradaic current during the first cycle, and current decreased over the subsequent cycles. As expected, the instability of MOF-LiI was highlighted during these cycling measurements. All faradaic current was lost over 78 cycles. In addition to reversible Li/Li^+ cycling, the electrolyte potential windows were evaluated as another metric for electrolyte robustness. MOF-LiCl exhibited a potential window of 4.5 V, suitable for battery applications.[286] MOF-LiBr featured a slightly narrower potential window of 3.5 V, likely due to partial oxidation of Br^- (**Figure 6-20**). Both MOF-LiCl and MOF-LiBr possessed potential windows wider than those of many non-aqueous liquid electrolytes, which are commonly limited to ~3 V.[287] As mentioned previously, MOF-LiI contained a multitude of faradaic events, likely from reactivity of I^- with Cu^{2+}. Despite the incompatibility

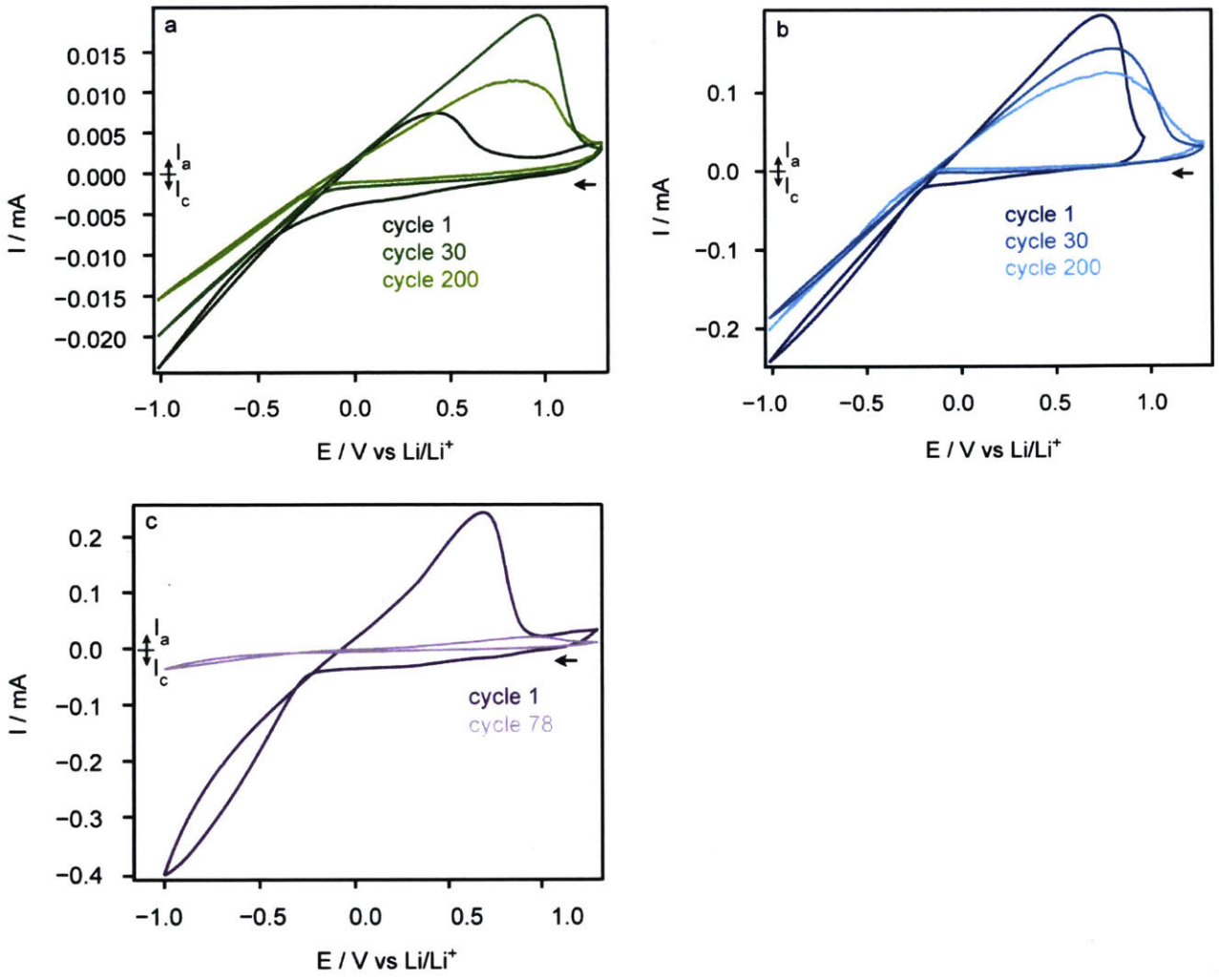

Figure 6-19. Cyclic voltammograms of **a)** MOF-LiCl, **b)** MOF-LiBr, and **c)** MOF-LiI showing the reversibility of Li stripping and plating during cycling.

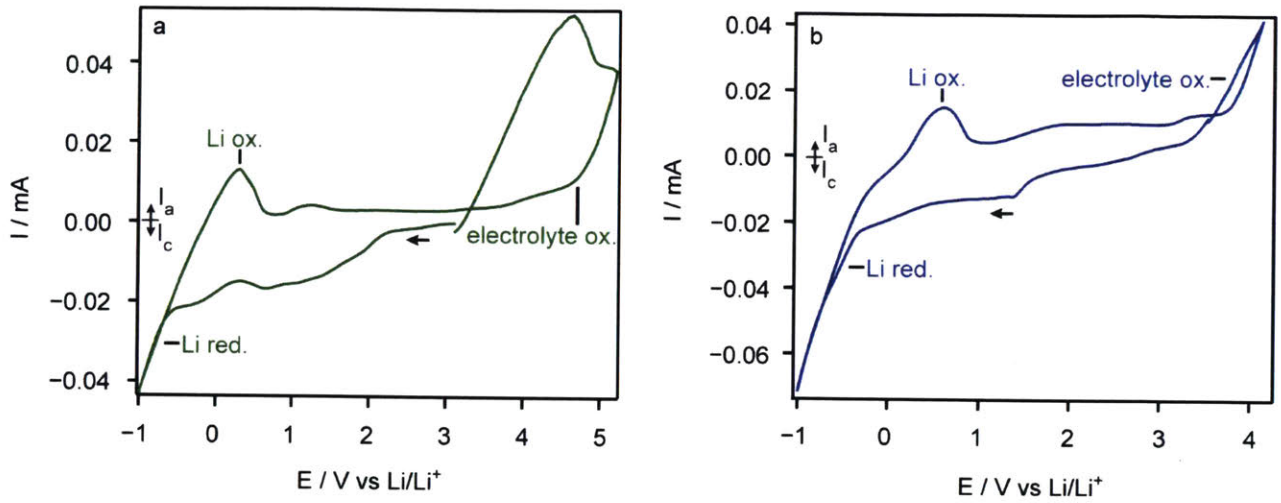

Figure 6-20. Electrolyte potential windows of **a)** MOF-LiCl and **b)** MOF-LiBr. See **Figure 6-10** for the corresponding MOF-LiI voltammogram.

of I^- with the cupric framework, $Cu_4(ttpm)_2 \cdot 0.6CuCl_2$ proved to be a versatile host capable of modular Li^+ electrolyte performance.

Although the high volumetric capacity and reversible redox activity intrinsic to lithium identifies Li and Li-ion batteries as attractive energy sources, safety, performance, and abundance (consequently, cost) obstacles that cannot be overcome with cell optimization has encouraged exploration of other metals for battery applications. Mg^{2+}, although less reducing than Li^+, has almost double the volumetric capacity of Li^+, due to its divalent charge and still relatively small ionic radius.[196] Additionally, Mg^{2+} is not plagued by the dendrite formation issues faced by Li^+, and Mg is 5 orders of magnitude more abundant than Li.[196] As such, we sought to explore the potential of $Cu_4(ttpm)_2 \cdot 0.6CuCl_2$ as a Mg^{2+} conductive solid electrolyte. EIS of MOF-$MgCl_2$ and MOF-$MgBr_2$ collected at 25 °C revealed the same modular trend as observed in the MOF-Li*X* analogues, in that ionic conductivity increased with increased anion softness (**Figure 6-21**). Specifically, MOF-$MgCl_2$ exhibited an ionic conductivity of $1.2 \cdot 10^{-5}$ $S \cdot cm^{-1}$ and MOF-$MgBr_2$ exhibited

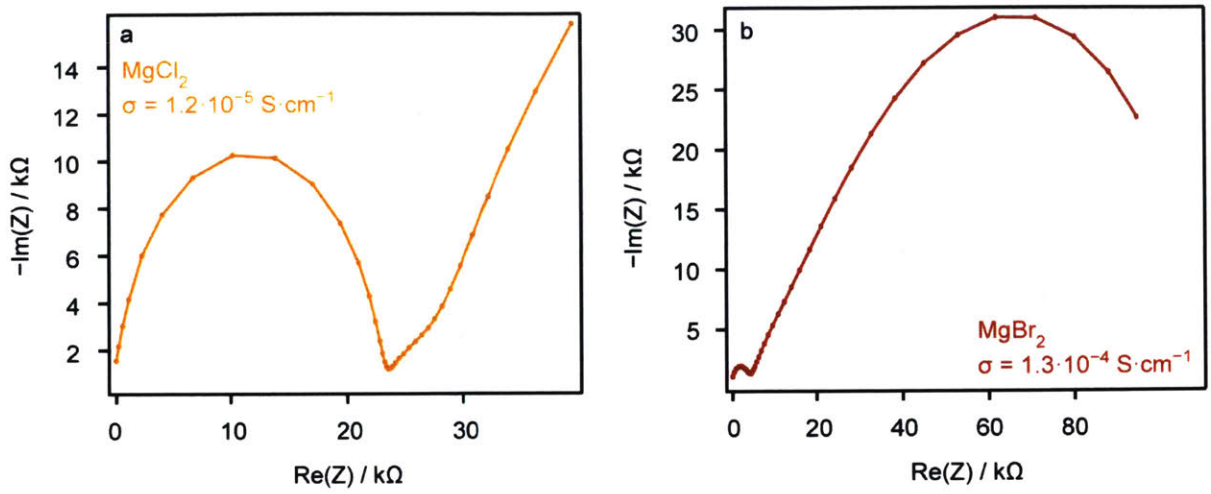

Figure 6-21. Electrochemical impedance spectra of MOF-$MgCl_2$ (orange, **a**) and MOF-$MgBr_2$ (red, **b**), and corresponding conductivity values, collected at 25 °C.

an ionic conductivity of $1.3 \cdot 10^{-4}$ S·cm^{-1}. Impressively, the conductivity measured for MOF-$MgBr_2$ shares the spotlight of the highest reported Mg^{2+} conductivity in a solid electrolyte to date, along with another MOF.[216] Activation energies calculated from the Arrhenius data were in-line with the previously observed trend; the activation energies for MOF-$MgCl_2$ and MOF-$MgBr_2$ were 0.32 and 0.24 eV, respectively (**Figure 6-22**, **Table 6-3**, **Figure 6-23**). This data serves as an exciting foundation for further exploring the potential of $Cu_4(ttpm)_2 \cdot 0.6CuCl_2$ as a solid electrolyte for Mg^{2+} ion battery applications.

The ability to further enhance volumetric capacity[201] was explored by insertion of Al^{3+} from $AlCl_3$. The resulting electrolyte, MOF-$AlCl_3$ ($Cu_4(ttpm)_2(CuCl_2)_{0.6}(AlCl_3)_{0.5} \cdot 20PC$) (**Figure 6-24**), gave an average conductivity value of $8.1 \cdot 10^{-6}$ S·cm^{-1} at 25 °C and an activation energy of 0.32 eV (**Figure 6-25**). As with the other chloride samples, crystallinity was retained during electrochemical measurements (**Figure 6-26**). Although the measured conductivity values fell several orders of magnitude below previously reported solid and liquid Al-conductive electrolytes,[201,288] this study highlights the potential for MOFs to

serve as a class of tunable Al-ion battery electrolytes, and expands the utility of $Cu_4(ttpm)_2 \cdot 0.6CuCl_2$ to conducting even higher-valent ions.

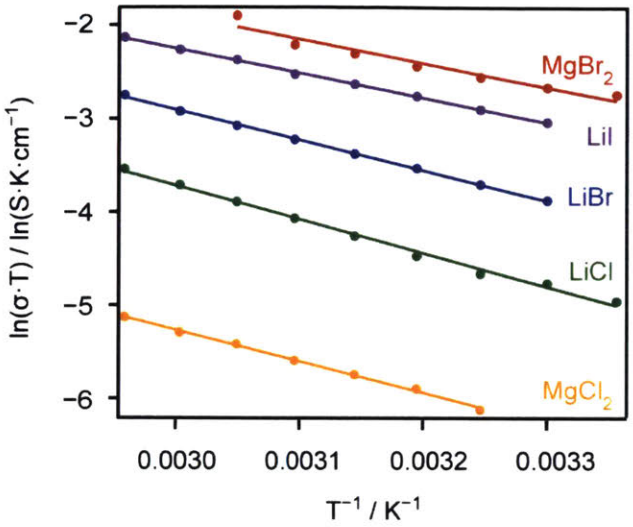

Figure 6-22. Arrhenius plots for the respective MOF-MX_n electrolytes, used to calculate the activation energy values. MOF-$MgBr_2$ shows the highest conductivity out of all analogues tested, and is among the most conductive solid Mg^{2+} electrolytes reported.

Table 6-3. Conductivity and activation energy values of MOF-MgX_2.

Electrolyte	**σ (S·cm^{-1})**	**E_a (eV)**
MOF-$MgCl_2$	$1.2 \cdot 10^{-5}$	0.32
MOF-$MgBr_2$	$1.3 \cdot 10^{-4}$	0.24

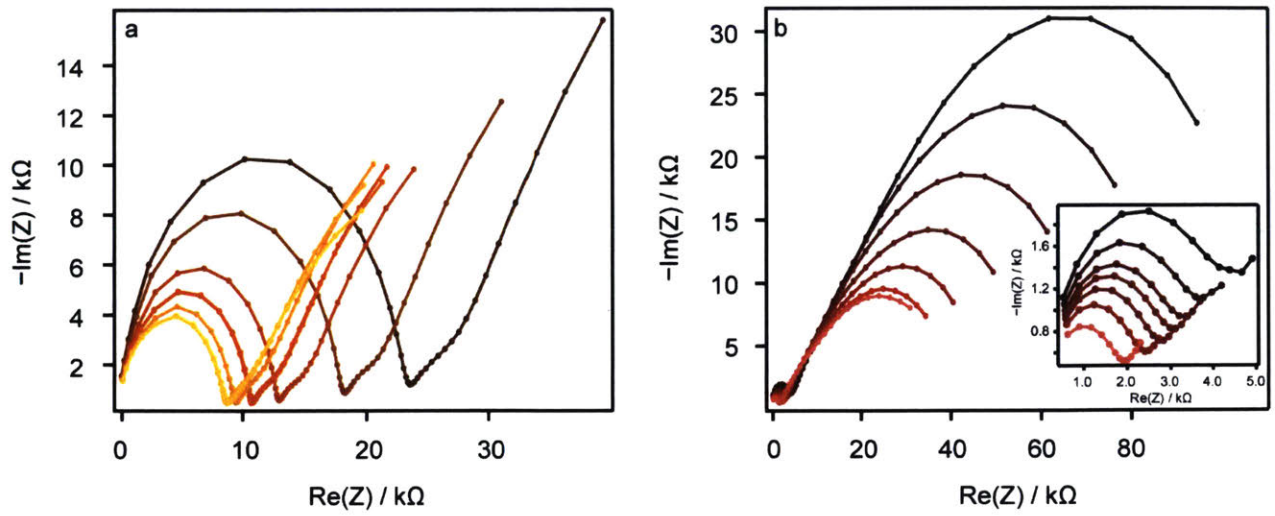

Figure 6-23. Variable-temperature electrochemical impedance spectra (lighter color signifies higher temperature) of **a)** MOF-$MgCl_2$, **b)** MOF-$MgBr_2$.

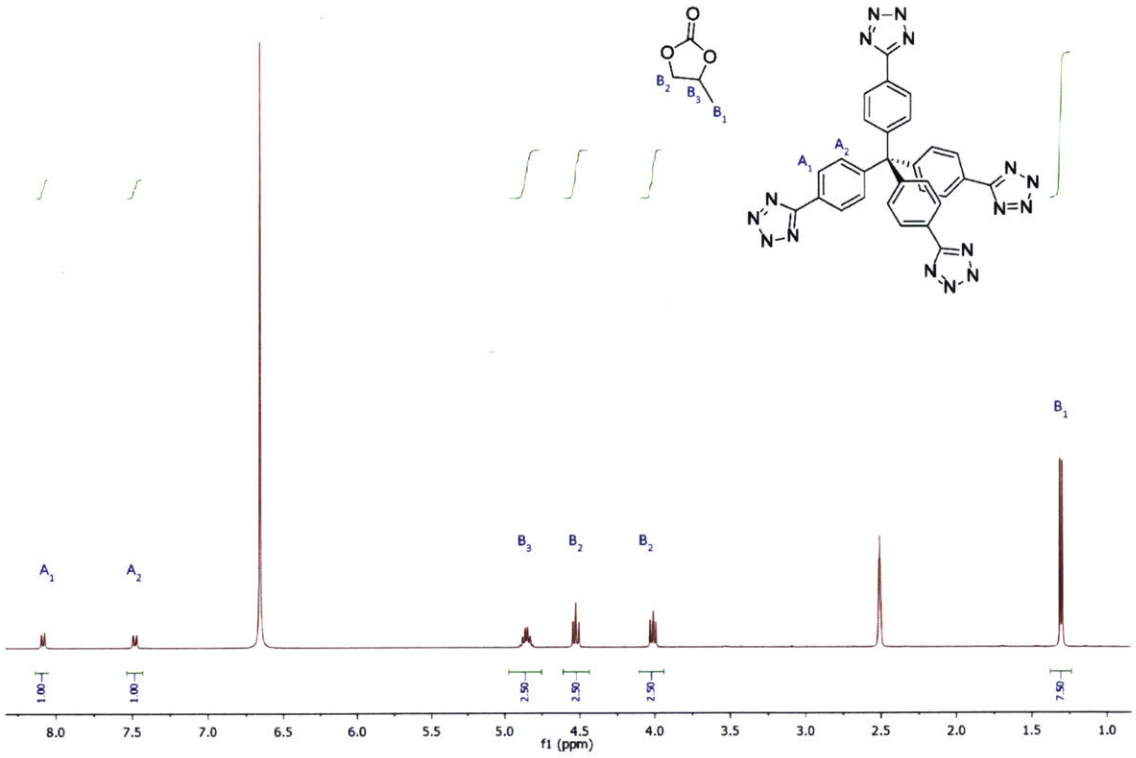

Figure 6-24. ^{1}HNMR spectrum of digested MOF-$AlCl_3$.

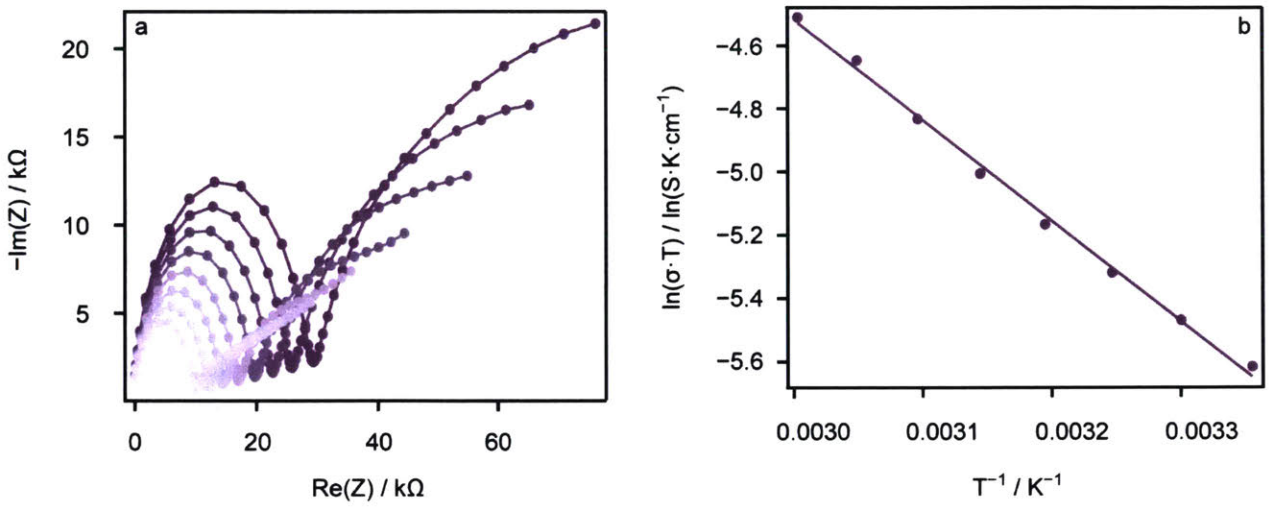

Figure 6-25. a) Variable-temperature electrochemical impedance spectra (lighter color signifies higher temperature) of MOF-$AlCl_3$ and **b)** the resulting Arrhenius plot.

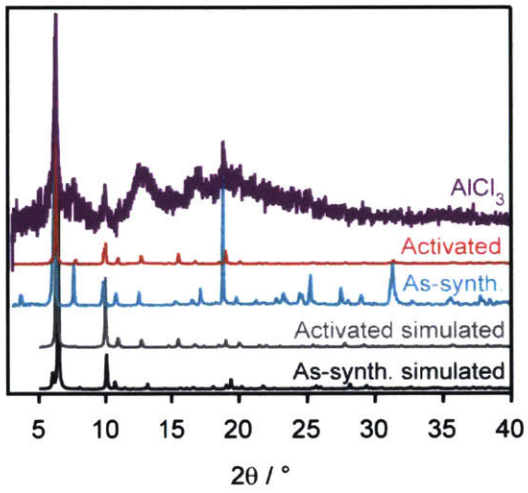

Figure 6-26. PXRD patterns of MOF-$AlCl_3$ after variable-temperature EIS measurements. 'As-synth.' represents $Cu[(Cu_4Cl)(ttpm)_2]_2 \cdot CuCl_2$ and 'activated' represents $Cu_4(ttpm)_2 \cdot 0.6CuCl_2$.

6.3 Conclusions and outlook

Here is shown a Cu-azolate MOF that features an abundance of open metal sites, into which stoichiometric amounts of coordinating halides and charge-balancing mobile metal ions can be loaded. The high surface area of the MOF results in a high density of Li^+, Mg^{2+}, and Al^{3+} guests and immobilized halides, contributing ionic conductivities between 10^{-6}-10^{-4} $S \cdot cm^{-1}$, and activation energies between 0.24-0.34 eV. The ability to expose within the MOF a multitude of open coordination sites enables reincorporation of various anions, the identities of which dictate the ion pairing strength with the mobile metal cations, allowing tunable electrolyte performance. The potential for a bridging coordination mode with the anion may aid in further reduction of ion pairing strength between mobile cations and immobilized anions due to electron density on the anion being shielded by multiple Cu^{2+} sites. This MOF is one of the first in a promising class of frameworks that introduces the opportunity to control the identity, geometry, and distribution of the cation hopping sites offering a versatile template for application-directed design of solid electrolytes.

6.4 Methods

General comments. $CuCl_2 \cdot 2H_2O$ (≥ 99%, Alfa Aesar), tetraphenylmethane (96%, Alfa Aesar), triethylamine hydrochloride (TEA·HCl, 98%, ChemCruz), NaN_3 (99%, Alfa Aesar), LiCl (≥ 99%, anhydrous, Acros Organics), Br_2 (≥ 99.5%, Fisher Chemical), LiBr (≥ 99%, anhydrous, Sigma-Aldrich), LiI (≥ 99%, anhydrous, Alfa Aesar), $MgCl_2$ (≥ 99%, anhydrous, Alfa Aesar), $MgBr_2$ (98%, anhydrous, Strem), MgI_2 (≥ 99.9%, anhydrous, Alfa Aesar), N,N-dimethylformamide (DMF, 99.9%, Omnisolv), methanol (MeOH, ACS grade, VWR Analytical), hydrochloric acid (HCl 36.5-38%, ACS grade, VWR-Analytical), and anhydrous propylene carbonate (PC, 99.7 %, Sigma-Aldrich) were obtained from commercial sources and used as received. Dry tetrahydrofuran (THF), DMF, toluene, and MeOH were obtained by degassing with a vigorous flow of Ar for 45 min and then passing the solvent through two

alumina columns in a Glass Contour Solvent System. The solvents were further degassed by three cycles of freeze-pump-thaw. All solvents except for MeOH were stored over 4 Å molecular sieves.

Synthesis of tetrakis(4-tetrazolylphenyl)methane (H_4ttpm), the parent MOF Cu[(Cu_4Cl)(ttpm)$_2$]$_2$·$CuCl_2$, and the activated MOF Cu_4(ttpm)$_2$·0.6$CuCl_2$. Syntheses of the aforementioned ligand and MOFs were conducted according to a literature procedure.[280] Synthesis of the desired frameworks were confirmed with powder X-ray diffraction and elemental analysis.

Synthesis of MOF-Li*X* (*X* = Cl^-, Br^-, I^-). In an N_2 glove box, Cu_4(ttpm)$_2$·0.6$CuCl_2$ (60 mg, 0.039 mmol) was suspended in saturated Li*X* / THF solutions (0.078 mmol (2 equivalents), 0.197 mmol (5 equivalents), and 0.393 mmol (10 equivalents) of LiCl, LiBr, and LiI in 5 mL THF, respectively). The suspension was stirred in the glove box for 4 days, during which time the large, dark green crystals transformed to pale green (or, in the case of LiI, pale purple) crystallites. The solids were collected by vacuum filtration, washed on the filter with THF (5 mL) and propylene carbonate (5 mL), and dried to afford a free-flowing powder.

Synthesis of MOF-MgX_2 (X = Cl^-, Br^-). In an N_2 glove box, Cu_4(ttpm)$_2$·0.6$CuCl_2$ (60 mg, 0.039 mmol) was suspended in saturated MgX_2 / THF solutions (0.107 mmol (2.7 equivalents) or 0.197 mmol (5 equivalents) of $MgCl_2$ or $MgBr_2$ in 5 mL THF, respectively). The suspension was stirred in the glove box for 4 days, during which time the large, dark green crystals transformed to pale green crystallites. The solids were collected by vacuum filtration, washed on the filter with THF (5 mL) and propylene carbonate (5 mL), and dried to afford a free-flowing powder.

Synthesis of MOF-MgI_2. In an N_2 glove box, Cu_4(ttpm)$_2$·0.6$CuCl_2$ (60 mg, 0.039 mmol) was suspended in a saturated MgI_2 solutions in diethyl ether (solubility issues were encountered during the THF soak) (1.07

mmol, 27 equivalents). The suspension was stirred in the glove box for 4 days, during which time the large, dark green crystals transformed to dark purple-brown crystallites. The solids were collected by vacuum filtration, washed on the filter with diethyl ether (5 mL) and propylene carbonate (5 mL), and dried to afford a free-flowing brown powder.

Synthesis of MOF-$AlCl_3$. In an N_2 glove box, $Cu_4(ttpm)_2 \cdot 0.6CuCl_2$ (60 mg, 0.039 mmol) was suspended in 5 mL of saturated $AlCl_3$ / THF solution (0.197 mmol, 5 equivalents). The suspension was stirred in the glove box for 4 days, during which time the large, dark green crystals transformed to pale green crystallites. The solids were collected by vacuum filtration, washed on the filter with THF (5 mL) and propylene carbonate (5 mL), and dried to afford a free-flowing powder.

Physical measurements. Powder X-ray diffraction (PXRD) patterns were recorded on Bruker D8 Discover diffractometer using Nickel-filtered Cu-Kα radiation (λ = 1.5418 Å) with accelerating voltage and current of 40 kV and 40 mA, respectively. Samples for PXRD were prepared by placing a thin layer of the appropriate material on a zero-background silicon crystal plate and sealed under inert atmosphere with an X-ray transparent cap (Bruker). ^1H NMR spectra were recorded on a Bruker AVANCE-400 MHz NMR spectrometer with a Magnex Scientific superconducting magnet. Elemental analysis was performed by Robertson Microlit Laboratories, Ledgewood NJ. Copper, lithium, and magnesium analyses were conducted with inductively coupled plasma mass spectrometry (ICP-MS) on an Agilent 7900 at the MIT Center for Environmental Health Sciences (MIT CEHS). Standards were prepared from analytical standard solutions purchased from ULTRA Scientific (Mg and Cu) and Ricca Chemicals (Li). Scanning electron microscopy-energy dispersive spectroscopy (SEM-EDS) was conducted with an Ultra 55 using SmartSEM SEM software and EDAX Genesis EDS software at the Harvard Center for Nanoscale Systems. The samples were mounted on carbon fiber tape and coated with 5 nm of carbon before being transferred into

the chamber. Prior to EDS data collection, the instrument was calibrated with Cu tape (0.93 keV). The images were acquired at a working distance of 8.6 mm and an electron beam energy of 8.00 kV.

Electrical conductivity measurements of $Cu_4(ttpm)_2 \cdot 0.6CuCl_2$. A home-built in situ press[289] was used to make a 2-contact-probe device from pressed pellets in a N_2-filled glovebox. An electrometer (Keithley Instruments model 6517B) was connected to the home-built in situ press through triax cables (Keithley Instruments model 237-ALG-2) and a banana cable (Keithley Instruments model 8607). The current-voltage (I-V) measurements were performed at room temperature in a N_2 atmosphere by sweeping the voltage from −50 V to 50 V. The area of the pellet determined by the inner diameter of the glass tube (Ace glass) was 0.0338 cm^2.

Electrochemical impedance spectroscopy. The powder pellet was prepared in an EQ-STC split-able test cell (MTI Corporation) by pressing powder between stainless steel blocking electrodes of 5 mm diameter under dry N_2 atmosphere. Pressure was applied by tightening the spring tension adjustment nut on the upper split. The thicknesses of the pellets typically ranged from 0.4 mm to 0.7 mm. The alternating current (AC) impedance analysis was performed using a two-probe method with a Bio-Logic SP200 potentiostat/galvanostat over the frequency range 1 MHz–1 Hz, with an input voltage amplitude of 100 mV. The pellet was maintained at the target temperature by an Espec BTL-433 chamber. Data was recorded every 5 °C between 25 °C to 65 °C with heating-cooling-heating-cooling. Each temperature was held for 3 h to reach thermal equilibrium. After each cycle, the temperature as maintained for 30 min before moving on to the subsequent cycle. The resistance was obtained by fitting the Nyquist plot to the model circuit shown in **Figure 6-27**, using the EC-Lab software.

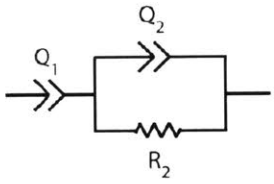

Figure 6-27. The equivalent circuit used for fitting impedance spectra. R_2 is a resistor and Q_1 and Q_2 are constant phase elements which are imperfect capacitors.

The ionic conductivity was calculated using **Equation 6-1**:

$$\sigma = \frac{L}{AR} \qquad \textbf{Eq. 6-1}$$

where σ is ionic conductivity, L is the pellet thickness, A is the pellet area and R is the resistance obtained from the measurement. The activation energy was calculated with the Nernst-Einstein relation

$$\sigma = \frac{\sigma_0}{T}\exp(-\frac{E_a}{kT}) \qquad \textbf{Eq. 6-2}$$

where σ_0 is a pre-exponential factor, T is the temperature, E_a is the activation energy and k is the Boltzmann constant.[248]

Electrochemical measurements of transference numbers. The transference numbers were measured following a previously reported method.[290] The powder pellet was prepared in a EQ-STC split-able test cell (MTI corporation) by pressing powder between Li foil (0.75 mm, Alfa Aesar) of 5 mm diameter under dry Ar atmosphere. Pressure was applied by tightening the spring tension adjustment nut on the upper split. The direct current (DC) polarization measurement was performed on cells Li | MOF-LiX | Li (where X = Cl^-, Br^-, I^-,) using a Bio-Logic SP200 potentiostat/galvanostat with an applied potential of 50 mV at 25 °C. The current response was measured as a function of time for 3 h. The AC impedance measurement was conducted over the frequency range 1 MHz – 1 Hz, with an input voltage amplitude of 100 mV.

$$t_{Li^+} = \frac{I^S(\Delta V - I^0R^0)}{I^0(\Delta V - I^SR^S)} \qquad \textbf{Eq. 6-3}$$

The transference number determined from **Equation 6-3** where I^s is the steady-state current, I^0 is the initial current, ΔV is the applied potential, and R^0 and R^s are the initial and steady-state resistances of the passivating layers, respectively. R^0 and R^s could be determined from the AC impedance measurement immediately before and after the DC polarization measurement. The resistance was obtained by fitting the Nyquist plot to the model circuit in **Figure 6-28** using EC-Lab software.

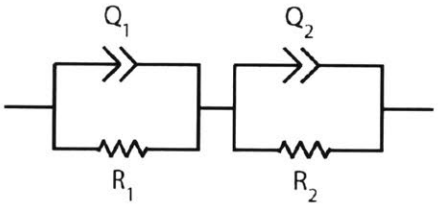

Figure 6-28. The equivalent circuit used for fitting impedance spectra. R_1 and R_2 are resistors and Q_1 and Q_2 are constant phase elements which are imperfect capacitors.

Galvanostatic cycling measurements. Cycling measurements were performed on the same symmetrical cell setup used for transference number measurements. Galvanostatic cycling for symmetrical cells Li | MOF-Li*X* | Li (where X = Cl^-, Br^-, I^-) were performed using a Bio-Logic SP200 potentiostat/galvanostat at a current density of ± 50 $\mu A \cdot cm^{-2}$, passing each current density for 3 hours each.

Li redox cycling studies. The powder pellet was prepared in a EQ-STC split-able test cell (MTI corporation) by pressing powder between Li foil (0.75 mm, Alfa Aesar) of 5 mm diameter, and a stainless steel mesh working electrode (Alfa Aesar) under dry Ar atmosphere. The Li-electrolyte interface was allowed to equilibrate at open circuit at room temperature for 24 h. Cyclic voltammetry (CV) was run at 25 °C, and an IR drop determination (single point impedance) was conducted before the measurement. The sweep rate of 5 $mV \cdot s^{-1}$ was constant. The cell was cycled from −1.0 V to 1.0 V vs Li/Li^+ for 200 cycles to

test the reversibility of Li deposition and stripping. All data was collected using a Bio-Logic SP200 potentiostat/galvanostat and the software package EC-Lab.

Electrolyte potential window measurements. The powder pellet was prepared in a EQ-STC split-able test cell (MTI corporation) by pressing powder between Li foil (0.75 mm, Alfa Aesar) of 5 mm diameter, and a stainless steel mesh working electrode (Alfa Aesar) under dry Ar atmosphere. The Li-electrolyte interface was allowed to equilibrate at open circuit at room temperature for 24h. Cyclic voltammetry (CV) was run at 25 °C, and an IR drop determination (single point impedance) was conducted before the measurement. The sweep rate of 5 $mV \cdot s^{-1}$ was constant. The cell was cycled from −1.0 V to 5.0 V vs Li/Li^+, the range in which a sharp onset of anodic current was observed. This anodic current signified the electrolyte potential window.

Bibliography

(1) Turner, J. A. *Science* **2004**, *305*, 972–974.

(2) Chu, S.; Majumdar, A. *Nature* **2012**, *488*, 294–303.

(3) Grove, W. R. *London Edinburgh Philos. Mag. J. Sci.* **1842**, *21*, 417–420.

(4) Mahato, N.; Banerjee, A.; Gupta, A.; Omar, S.; Balani, K. *Prog. Mater. Sci.* **2015**, *72*, 141–337.

(5) Kraytsberg, A.; Ein-Eli, Y. *Energy & Fuels* **2014**, *28*, 7303–7330.

(6) Sharaf, O. Z.; Orhan, M. F. *Renew. Sustain. Energy Rev.* **2014**, *32*, 810–853.

(7) Gewirth, A. A.; Varnell, J. A.; DiAscro, A. M. *Chem. Rev.* **2018**, 118, 2313-2339.

(8) Wang, W.; Xu, X.; Zhou, W.; Shao, Z. *Adv. Sci.* **2017**, *4*, 1600371-1600392.

(9) Shao, M.; Chang, Q.; Dodelet, J.; Chenitz, R. *Chem. Rev.* **2016**, *116*, 3594–3657.

(10) Falkowski, J. M.; Concannon, N. M.; Yan, B.; Surendranath, Y. *J. Am. Chem. Soc.* **2015**, *137*, 7978–7981.

(11) Baschuk, J. J.; Li, X. *Int. J. Energy Res.* **2001**, *25*, 695–713.

(12) Song, C.; Zhang, J. Electrocatalytic Oxygen Reduction Reaction. In *PEM Fuel Cell Electrocatalysts and Catalyst Layers*; Zhang, J., Ed.; Springer: London, 2008, 89–134.

(13) Sawyer, D. *Oxygen Chemistry*; Oxford University Press, Inc.: New York, NY, 1991.

(14) Chatterjee, S.; Sengupta, K.; Samanta, S.; Das, P. K.; Dey, A. *Inorg. Chem.* **2013**, *52*, 9897–9907.

(15) Thorum, M. S.; Anderson, C. A.; Hatch, J. J.; Campbell, A. S.; Marshall, N. M.; Zimmerman, S. C.; Lu, Y.; Gewirth, A. A. *J. Phys. Chem. Lett.* **2010**, *1*, 2251–2254.

(16) Ramaswamy, N.; Mukerjee, S. *Adv. Phys. Chem.* **2012**, *2012*, 1–17.

(17) Ramaswamy, N.; Mukerjee, S. *J. Phys. Chem. C* **2011**, *115*, 18015–18026.

(18) Jackson, M. N.; Surendranath, Y. *J. Am. Chem. Soc.* **2016**, *138*, 3228–3234.

(19) Jin, H.; Guo, C.; Liu, X.; Liu, J.; Vasileff, A.; Jiao, Y.; Zheng, Y.; Qiao, S. *Chem. Rev.* **2018**, *118*, 6337–6408.

(20) Gileadi, E. *Physical Electrochemistry*; Wiley-VCH Verlag GmbH & Co. KGaA: Weinheim, 2011.

(21) Gileadi, E. *Electrode Kinetics for Chemists, Chemical Engineers, and Materials Scientists*; Wiley, John & Sons, Incorporated: New York, NY, 1993.

(22) Singh, K.; Razmjooei, F.; Yu, J. *J. Mater. Chem. A* **2017**, *5*, 20095–20119.

(23) Guo, S.; Li, D.; Zhu, H.; Zhang, S.; Markovic, N. M.; Stamenkovic, V. R.; Sun, S. *Angew. Chemie Int. Ed.* **2013**, *52*, 3465–3468.

(24) Kakade, B. A.; Wang, H.; Tamaki, T.; Ohashi, H.; Yamaguchi, T. *RSC Adv.* **2013**, *3*, 10487-10496.

(25) Kariuki, N. N.; Khudhayer, W. J.; Karabacak, T.; Myers, D. J. *ACS Catal.* **2013**, *3*, 3123–3132.

(26) Wu, J.; Zhang, J.; Peng, Z.; Yang, S.; Wagner, F. T.; Yang, H. *J. Am. Chem. Soc.* **2010**, *132*, 4984–4985.

(27) Huang, X.; Zhao, Z.; Cao, L.; Chen, Y.; Zhu, E.; Lin, Z.; Li, M.; Yan, A.; Zettl, A.; Wang, Y. M.; Duan, X.; Mueller, T.; Huang, Y. *Science* **2015**, *348*, 1230–1234.

(28) Zheng, Y.; Jiao, Y.; Jaroniec, M.; Jin, Y.; Qiao, S. Z. *Small* **2012**, *8*, 3550–3566.

(29) Singh, S. K.; Takeyasu, K.; Nakamura, J. *Adv. Mater.* **2018**, 1804297-1804314.

(30) Yang, L.; Jiang, S.; Zhao, Y.; Zhu, L.; Chen, S.; Wang, X.; Wu, Q.; Ma, J.; Ma, Y.; Hu, Z. *Angew. Chemie Int. Ed.* **2011**, *50*, 7132–7135.

(31) Sheng, Z.; Gao, H.; Bao, W.; Wang, F.; Xia, X. *J. Mater. Chem.* **2012**, *22*, 390–395.

(32) Fukushima, T.; Drisdell, W.; Yano, J.; Surendranath, Y. *J. Am. Chem. Soc.* **2015**, *137*, 10926–10929.

(33) Ricke, N. D.; Murray, A. T.; Shepherd, J. J.; Welborn, M. G.; Fukushima, T.; Van Voorhis, T.; Surendranath, Y. *ACS Catal.* **2017**, *7*, 7680–7687.

(34) Yuan, X.; Ding, X.; Wang, C.; Ma, Z. *Energy Environ. Sci.* **2013**, *6*, 1105-1124.

(35) Khomenko, V. G.; Barsukov, V. Z.; Katashinskii, A. S. *Electrochim. Acta* **2005**, *50*, 1675–1683.

(36) Baresel, V. D.; Sarholz, W.; Scharner, P.; Schmitz, J. *Berichte der Bunsen-Gesellschaft* **1974**, *78*, 608–611.

(37) Trapp, V.; Christensen, P.; Hamnett, A. *J. Chem. Soc. Faraday Trans.* **1996**, *92*, 4311-4319.

(38) Behret, H.; Binder, H.; Sandstede, G. *Electrochim. Acta* **1975**, *20*, 111–117.

(39) Gao, M.; Jiang, J.; Yu, S. *Small* **2012**, *8*, 13–27.

(40) Gao, M.; Xu, Y.; Jiang, J.; Yu, S. *Chem. Soc. Rev.* **2013**, *42*, 2986-3017.

(41) Hamdani, M.; Singh, R. N.; Chartier, P. *Int. J. Electrochem. Sci.* **2010**, *5*, 556–577.

(42) King, W. J.; Tseung, A. C. C. *Electrochim. Acta* **1974**, *19*, 485–491.

(43) Singh, R. N.; Koenig, J.; Poillerat, G.; Chartier, P. T *J. Electroanal. Chem. Interfacial Electrochem.* **1991**, *314*, 241–257.

(44) Cheng, F.; Shen, J.; Peng, B.; Pan, Y.; Tao, Z.; Chen, J. *Nat. Chem.* **2011**, *3*, 79–84.

(45) Lukaszewicz, J. P.; Imaizumi, S.; Yuasa, M.; Shimanoe, K.; Yamazoe, N. *J. Mater. Sci.* **2006**, *41*, 6215–6220.

(46) Zhu, L.; Susac, D.; Teo, M.; Wong, K.; Wong, P.; Parsons, R.; Bizzotto, D.; Mitchell, K.; Campbell, S. *J. Catal.* **2008**, *258*, 235–242.

(47) Susac, D.; Zhu, L.; Teo, M.; Sode, A.; Wong, K. C.; Wong, P. C.; Parsons, R. R.; Bizzotto, D.; Mitchell, K. A. R.; Campbell, S. A. *J. Phys. Chem. C* **2007**, *111*, 18715–18723.

(48) Vante, N. A.; Tributsch, H. *Nature* **1986**, *323*, 431–432.

(49) Yan, B.; Concannon, N. M.; Milshtein, J. D.; Brushett, F. R.; Surendranath, Y. *Angew. Chemie Int. Ed.* **2017**, *56*, 7496–7499.

(50) Yan, B.; Krishnamurthy, D.; Hendon, C. H.; Deshpande, S.; Surendranath, Y.; Viswanathan, V. *Joule* **2017**, *1*, 600–612.

(51) Jasinski, R. *J. Electrochem. Soc.* **1965**, *112*, 526–528.

(52) Jahnke, H.; Schönborn, M.; Zimmermann, G. Organic Dyestuffs as Catalysts for Fuel Cells. In

Physical and Chemical Applications of Dyestuffs; Springer-Verlag: Berlin/Heidelberg; 1976, 133–181.

(53) Tang, H.; Yin, H.; Wang, J.; Yang, N.; Wang, D.; Tang, Z. *Angew. Chemie Int. Ed.* **2013**, *52*, 5585–5589.

(54) *Physical and Chemical Applications of Dyestuffs*; Schafer, P.F; Gerischer, H.; Willig, F.; Meier, H.; Jahnke, H.; Schonborn, M.; Zimmermann, G., Ed.; Springer, 1976.

(55) Masa, J.; Xia, W.; Muhler, M.; Schuhmann, W. *Angew. Chemie Int. Ed.* **2015**, *54*, 10102–10120.

(56) Chen, Z.; Higgins, D.; Yu, A.; Zhang, L.; Zhang, J. *Energy Environ. Sci.* **2011**, *4*, 3167–3192.

(57) Fukuzumi, S.; Lee, Y.; Nam, W. *ChemCatChem* **2018**, *10*, 9–28.

(58) Wu, G.; Zelenay, P. *Acc. Chem. Res.* **2013**, *46*, 1878–1889.

(59) Liu, Y.; Yue, X.; Li, K.; Qiao, J.; Wilkinson, D. P.; Zhang, J. *Coord. Chem. Rev.* **2016**, *315*, 153–177.

(60) Griffith, J. S. *Proc. R. Soc. A Math. Phys. Eng. Sci.* **1956**, *235*, 23–36.

(61) Pauling, L. *Nature* **1964**, *203*, 182–183.

(62) Vaska, L. *Acc. Chem. Res.* **1976**, *9*, 175–183.

(63) Tatsumi, K.; Hoffmann, R. *J. Am. Chem. Soc.* **1981**, *103*, 3328–3341.

(64) Jones, R. D.; Summerville, D. A.; Basolo, F. *Chem. Rev.* **1979**, *79*, 139–179.

(65) Yeager, E. Electrocatalysis on Non-Metallic Surfaces. In *The National Bureau of Standards U.S. Special Publication 455*; **1976**; 203–316.

(66) Zagal, J. H. *Coord. Chem. Rev.* **1992**, *119*, 89–136.

(67) Zagal, J. H.; Griveau, S.; Silva, J. F.; Nyokong, T.; Bedioui, F. *Coord. Chem. Rev.* **2010**, *254*, 2755–2791.

(68) Wan, G.; Shigehara, K.; Tsuchida, E.; Anson, F. C. *J. Electroanal. Chem. Interfacial Electrochem.* **1984**, *179*, 239–250.

(69) *Comprehensive Treatise of Electrochemistry*; Conway, B. E., Bockris, J. O., Yeager, E., Khan, S. U. M., White, R. E., Eds.; Springer US: Boston, MA, 1983.

(70) Kozawa, A.; Zilionis, V. E.; Brodd, R. J. *J. Electrochem. Soc.* **1970**, *117*, 1470-1474.

(71) Zagal, J. *J. Electrochem. Soc.* **1980**, *127*, 1506-1517.

(72) Van Den Brink, F.; Visscher, W.; Barendrecht, E. *J. Electroanal. Chem. Interfacial Electrochem.* **1984**, *172*, 301–325.

(73) Sun, L.; Campbell, M. G.; Dincă, M. *Angew. Chemie Int. Ed.* **2016**, *55*, 3566–3579.

(74) Wang, H.; Zhu, Q.; Zou, R.; Xu, Q. *Chem* **2017**, *2*, 52–80.

(75) Strickland, K.; Miner, E.; Jia, Q.; Tylus, U.; Ramaswamy, N.; Liang, W.; Sougrati, M.; Jaouen, F.; Mukerjee, S. *Nat. Commun.* **2015**, *6*, 7343.

(76) Strickland, K.; Pavlicek, R.; Miner, E.; Jia, Q.; Zoller, I.; Ghoshal, S.; Liang, W.; Mukerjee, S. *ACS Catal.* **2018**, *8*, 3833–3843.

(77) Jahan, M.; Bao, Q.; Loh, K. P. *J. Am. Chem. Soc.* **2012**, *134*, 6707–6713.

(78) Jahan, M.; Liu, Z.; Loh, K. P. *Adv. Funct. Mater.* **2013**, *23*, 5363–5372.

(79) Jiang, M.; Li, L.; Zhu, D.; Zhang, H.; Zhao, X. *J. Mater. Chem. A* **2014**, *2*, 5323-5329.

(80) Wang, H.; Yin, F.; Chen, B.; Li, G. *J. Mater. Chem. A* **2015**, *3*, 16168–16176.

(81) Barkholtz, H.; Chong, L.; Kaiser, Z.; Xu, T.; Liu, D. *Catalysts* **2015**, *5*, 955–965.

(82) Zhang, D.; Chen, W.; Li, Z.; Chen, Y.; Zheng, L.; Gong, Y.; Li, Q.; Shen, R.; Han, Y.; Cheong, W.; Gu, L.; Li, Y. *Chem. Commun.* **2018**, *54*, 4274–4277.

(83) Yang, Z. K.; Lin, L.; Xu, A. *Small* **2016**, *12*, 5710–5719.

(84) Bhattacharyya, S.; Das, C.; Maji, T. K. *RSC Adv.* **2018**, *8*, 26728–26754.

(85) Liao, P.; Shen, J.; Zhang, J. *Coord. Chem. Rev.* **2017**, *373*, 22–48.

(86) Zhao, M.; Huang, Y.; Peng, Y.; Huang, Z.; Ma, Q.; Zhang, H. *Chem. Soc. Rev.* **2018**, *47*, 6267–6295.

(87) Xiao, P.; Xu, Y. *J. Mater. Chem. A* **2018**, Advance Article.

(88) Ko, M.; Mendecki, L.; Mirica, K. A. *Chem. Commun.* **2018**, *54*, 7873–7891.

(89) Mao, J.; Yang, L.; Yu, P.; Wei, X.; Mao, L. *Electrochem. Commun.* **2012**, *19*, 29–31.

(90) Usov, P. M.; Huffman, B.; Epley, C. C.; Kessinger, M. C.; Zhu, J.; Maza, W. A.; Morris, A. J. *ACS Appl. Mater. Interfaces* **2017**, *9*, 33539–33543.

(91) Lions, M.; Tommasino, J.; Chattot, R.; Abeykoon, B.; Guillou, N.; Devic, T.; Demessence, A.; Cardenas, L.; Maillard, F.; Fateeva, A. *Chem. Commun.* **2017**, *53*, 6496–6499.

(92) Mani, P.; Sheelam, A.; Das, S.; Wang, G.; Ramani, V. K.; Ramanujam, K.; Pati, S. K.; Mandal, S. *ACS Omega* **2018**, *3*, 3830–3834.

(93) Bard, Allen J.; Faulkner, L. R. *Electrochemical Methods*; John Wiley & Sons, Inc.: New York, NY, **1980**.

(94) Mao, J.; Yang, L.; Yu, P.; Wei, X.; Mao, L. *Electrochem. Commun.* **2012**, *19*, 29–31.

(95) Jahan, M.; Bao, Q.; Loh, K. P. *J. Am. Chem. Soc.* **2012**, *134*, 6707–6713.

(96) Jahan, M.; Liu, Z.; Loh, K. P. *Adv. Funct. Mater.* **2013**, *23*, 5363–5372.

(97) Clough, A. J.; Yoo, J. W.; Mecklenburg, M. H.; Marinescu, S. C. *J. Am. Chem. Soc.* **2015**, *137*, 118–121.

(98) Hinogami, R.; Yotsuhashi, S.; Deguchi, M.; Zenitani, Y.; Hashiba, H.; Yamada, Y. *ECS Electrochem. Lett.* **2012**, *1*, H17–H19.

(99) Lin, S.; Diercks, C. S.; Zhang, Y.-B.; Kornienko, N.; Nichols, E. M.; Zhao, Y.; Paris, A. R.; Kim, D.; Yang, P.; Yaghi, O. M.; Chang, C. *Science* **2015**, *349*, 1208–1213.

(100) Dong, R.; Pfeffermann, M.; Liang, H.; Zheng, Z.; Zhu, X.; Zhang, J.; Feng, X. *Angew. Chemie Int. Ed.* **2015**, *54*, 12058–12063.

(101) Zhang, P.; Hou, X.; Liu, L.; Mi, J.; Dong, M. *J. Phys. Chem. C* **2015**, 28028–28037.

(102) Sheberla, D.; Sun, L.; Blood-Forsythe, M. A.; Er, S.; Wade, C. R.; Brozek, C. K.; Aspuru-Guzik,

A.; Dincă, M. *J. Am. Chem. Soc.* **2014**, *136*, 8859–8862.

(103) Afsahi, F.; Kaliaguine, S. *J. Mater. Chem. A* **2014**, *2*, 12270–12279.

(104) Aijaz, A.; Fujiwara, N.; Xu, Q. *J. Am. Chem. Soc.* **2014**, *136*, 6790–6793.

(105) Kung, C.; Wang, T. C.; Mondloch, J. E.; Fairen-Jimenez, D.; Gardner, D. M.; Bury, W.; Klingsporn, J. M.; Barnes, J. C.; Van Duyne, R.; Stoddart, J. F.; Wasielewski, M. R.; Farha, O. K.; Hupp, J. T. *Chem. Mater.* **2013**, *25*, 5012–5017.

(106) Xia, W.; Zhu, J.; Guo, W.; An, L.; Xia, D.; Zou, R. *J. Mater. Chem. A* **2014**, *2*, 11606–11613.

(107) Wang, X.; Zhou, J.; Fu, H.; Li, W.; Fan, X.; Xin, G.; Zheng, J.; Li, X. *J. Mater. Chem. A* **2014**, *2*, 14064-14070.

(108) Zhang, G.; Li, C.; Liu, J.; Zhou, L.; Liu, R.; Han, X.; Huang, H.; Hu, H.; Liu, Y.; Kang, Z. *J. Mater. Chem. A* **2014**, *2*, 8184-8189.

(109) Zhang, L.; Su, Z.; Jiang, F.; Yang, L.; Qian, J.; Zhou, Y.; Li, W.; Hong, M. *Nanoscale* **2014**, *6*, 6590–6602.

(110) Zhao, D.; Shui, J.; Chen, C.; Chen, X.; Reprogle, B. M.; Wang, D.; Liu, D. *Chem. Sci.* **2012**, *3*, 3200-3205.

(111) Zhao, D.; Shui, J.-L.; Grabstanowicz, L. R.; Chen, C.; Commet, S. M.; Xu, T.; Lu, J.; Liu, D. *Adv. Mater.* **2014**, *26*, 1093–1097.

(112) Zhao, S.; Yin, H.; Du, L.; He, L.; Zhao, K.; Chang, L.; Yin, G.; Zhao, H.; Liu, S.; Tang, Z. *ACS Nano* **2014**, *8*, 12660–12668.

(113) Zhao, X.; Zhao, H.; Zhang, T.; Yan, X.; Yuan, Y.; Zhang, H.; Zhao, H.; Zhang, D.; Zhu, G.; Yao, X. *J. Mater. Chem. A* **2014**, *2* , 11666-11671.

(114) Zhu, D.; Li, L.; Cai, J.; Jiang, M.; Qi, J.; Zhao, X. *Carbon N. Y.* **2014**, *79*, 544–553.

(115) Li, J.; Chen, Y.; Tang, Y.; Li, S.; Dong, H.; Li, K.; Han, M.; Lan, Y.; Bao, J.; Dai, Z. *J. Mater. Chem. A* **2014**, *2*, 6316-6319.

(116) Li, Q.; Xu, P.; Gao, W.; Ma, S.; Zhang, G.; Cao, R.; Cho, J.; Wang, H.; Wu, G. *Adv. Mater.* **2014**, *26*, 1378–1386.

(117) Li, Q.; Pan, H.; Higgins, D.; Cao, R.; Zhang, G.; Lv, H.; Wu, K.; Cho, J.; Wu, G. *Small* **2015**, *11*, 1443-1452.

(118) Kong, A.; Mao, C.; Lin, Q.; Wei, X.; Bu, X.; Feng, P. *Dalt. Trans.* **2015**, *44*, 6748–6754.

(119) Ge, L.; Yang, Y.; Wang, L.; Zhou, W.; De Marco, R.; Chen, Z.; Zou, J.; Zhu, Z. *Carbon N. Y.* **2015**, *82*, 417–424.

(120) Palaniselvam, T.; Biswal, B. P.; Banerjee, R.; Kurungot, S. *Chemistry* **2013**, *19*, 9335–9342.

(121) Pandiaraj, S.; Aiyappa, H. B.; Banerjee, R.; Kurungot, S. *Chem. Commun.* **2014**, *50*, 3363–3366.

(122) Strickland, K.; Miner, E.; Jia, Q.; Tylus, U.; Ramaswamy, N.; Liang, W.; Sougrati, M.; Jaouen, F.; Mukerjee, S. *Nat. Commun.* **2015**, *6*, 7343–7351.

(123) Shi, H.; Shen, Y.; He, F.; Li, Y.; Liu, A.; Liu, S.; Zhang, Y. *J. Mater. Chem. A* **2014**, *2*, 15704–15716.

(124) Zhao, S.; Yin, H.; Du, L.; Yin, G.; Tang, Z.; Liu, S. *J. Mater. Chem. A* **2014**, *2*, 3719–3724.

(125) Alonso-Vante, N. *Chemphyschem* **2010**, *11*, 2732–2744.

(126) Serov, A.; Artyushkova, K.; Niangar, E.; Wang, C.; Dale, N.; Jaouen, F.; Sougrati, M.; Jia, Q.; Mukerjee, S.; Atanassov, P. *Nano Energy* **2015**, *16*, 293–300.

(127) Xie, Y.; Tang, C.; Hao, Z.; Lv, Y.; Yang, R.; Wei, X.; Deng, W.; Wang, A.; Yi, B.; Song, Y. *Faraday Discuss.* **2014**, *176*, 393–408.

(128) Lin, Q.; Bu, X.; Kong, A.; Mao, C.; Bu, F.; Feng, P. *Adv. Mater.* **2015**, *27*, 3431–3436.

(129) Wang, Y.; Kong, A.; Chen, X.; Lin, Q.; Feng, P. *ACS Catal.* **2015**, *5*, 3887–3893.

(130) Liu, Y.; Wu, Y.-Y.; Lv, G.-J.; Pu, T.; He, X.; Cui, L. *Electrochim. Acta* **2013**, *112*, 269–278.

(131) Grosvenor, A. P.; Biesinger, M. C.; Smart, R. S. C.; McIntyre, N. S. *Surf. Sci.* **2006**, *600*, 1771–1779.

(132) Biesinger, M. C.; Payne, B. P.; Lau, L. W. M.; Gerson, A.; Smart, R. S. C. *Surf. Interface Anal.* **2009**, *41*, 324–332.

(133) Blizanac, B. B.; Ross, P. N.; Markovic, N. M. *Electrochim. Acta* **2007**, *52*, 2264–2271.

(134) He, W.; Wang, Y.; Jiang, C.; Lu, L. *Chem. Soc. Rev.* **2016**, *45*, 2396–2409.

(135) Jia, Q.; Ramaswamy, N.; Tylus, U.; Strickland, K.; Li, J.; Serov, A.; Artyushkova, K.; Atanassov, P.; Anibal, J.; Gumeci, C.; Barton, S. C.; Sougrati, M.; Jaouen, F.; Halevi, B.; Mukerjee, S. *Nano Energy* **2016**, *29*, 65–82.

(136) Raj, C. R.; Samanta, A.; Noh, S. H.; Mondal, S.; Okajima, T.; Ohsaka, T. Emerging New *J. Mater. Chem. A* **2016**, *4*, 11156–11178.

(137) Miner, E. M.; Fukushima, T.; Sheberla, D.; Sun, L.; Surendranath, Y.; Dincă, M. *Nat. Commun.* **2016**, *7*, 10942-10949.

(138) Li, Q.; Noffke, B. W.; Wang, Y.; Menezes, B.; Peters, D. G.; Raghavachari, K.; Li, L. *J. Am. Chem. Soc.* **2014**, *136*, 3358–3361.

(139) Sepa, D.B.; Vojnovic, M.V.; Vracar, Lj. M. *Electrochim. Acta* **1987**, *32*, 129–134.

(140) Ramaswamy, N.; Mukerjee, S. *J. Phys. Chem. C* **2011**, *115*, 18015–18026.

(141) Robertson, J. M.; Woodward, I. *J. Chem. Soc.* **1937**, 219-230.

(142) Kohn, W.; Sham, L. J. *Phys. Rev.* **1965**, *140*, A1133–A1138.

(143) Hohenberg, P.; Kohn, W. *Phys. Rev.* **1964**, *136*, B864–B871.

(144) Sastre, S.; Casasnovas, R.; Muñoz, F.; Frau, J. *Theor. Chem. Acc.* **2013**, *132*, 1310-1318.

(145) Bell, R. P.; Higginson, W. C. E. *Proc. R. Soc. A Math. Phys. Eng. Sci.* **1949**, *197*, 141–159.

(146) Mulliken, R. S. *J. Chem. Phys.* **1955**, *23*, 1833–1840.

(147) Weinberg, D. R.; Gagliardi, C. J.; Hull, J. F.; Murphy, C. F.; Kent, C. A.; Westlake, B. C.; Paul, A.; Ess, D. H.; McCafferty, D. G.; Meyer, T. J. *Chem. Rev.* **2012**, *112*, 4016–4093.

(148) Feigl, F.; Fürth, M. *Monatshefte für Chemie* **1927**, *48*, 445–450.

(149) Balch, A. L.; Holm, R. H. *J. Am. Chem. Soc.* **1966**, *88*, 5201–5209.

(150) Stiefel, E. I.; Waters, J. H.; Billig, E.; Gray, H. B. *J. Am. Chem. Soc.* **1965**, *87*, 3016–3017.

(151) Marks, D. R.; Phillips, D. J.; Redfern, J. P. *J. Chem. Soc. A Inorganic, Phys. Theor.* **1967**, 1464-1469.

(152) Marks, D. R.; Phillips, D. J.; Redfern, J. P. *J. Chem. Soc. A Inorganic, Phys. Theor.* **1968**, 2013-2017.

(153) Bachler, V.; Olbrich, G.; Neese, F.; Wieghardt, K. *Inorg. Chem.* **2002**, *41*, 4179–4193.

(154) Herebian, D.; Bothe, E.; Neese, F.; Weyhermüller, T.; Wieghardt, K. *J. Am. Chem. Soc.* **2003**, *125*, 9116–9128.

(155) Das, A.; Han, Z.; Brennessel, W. W.; Holland, P. L.; Eisenberg, R. *ACS Catal.* **2015**, *5*, 1397–1406.

(156) Kanan, M. W.; Yano, J.; Surendranath, Y.; Dincă, M.; Yachandra, V. K.; Nocera, D. G. *J. Am. Chem. Soc.* **2010**, *132*, 13692–13701.

(157) Ravel, B.; Newville, M. *J. Synchrotron Radiat.* **2005**, *12*, 537–541.

(158) Sheberla, D.; Sun, L.; Blood-Forsythe, M. A.; Er, S.; Wade, C. R.; Brozek, C. K.; Aspuru-Guzik, A.; Dincă, M. *J. Am. Chem. Soc.* **2014**, *136*, 8859–8862.

(159) Becke, A. D. *J. Chem. Phys.* **1993**, *98*, 5648–5652.

(160) Lee, C.; Yang, W.; Parr, R. G. *Phys. Rev. B* **1988**, *37*, 785–789.

(161) Frisch, M. J.; Pople, J. A.; Binkley, J. S. *J. Chem. Phys.* **1984**, *80*, 3265–3269.

(162) Hehre, W. J.; Ditchfield, R.; Pople, J. A. *J. Chem. Phys.* **1972**, *56*, 2257–2261.

(163) Ditchfield, R.; Hehre, W. J.; Pople, J. A. *J. Chem. Phys.* **1971**, *54*, 724–728.

(164) Clark, T.; Chandrasekhar, J.; Spitznagel, G. W.; Schleyer, P. V. R. *J. Comput. Chem.* **1983**, *4*, 294–301.

(165) Cancès, E.; Mennucci, B.; Tomasi, J. *J. Chem. Phys.* **1997**, *107*, 3032–3041.

(166) Chipman, D. M. *J. Chem. Phys.* **2000**, *112*, 5558–5565.

(167) Shao, Y.; Gan, Z.; Epifanovsky, E.; Gilbert, A. T. B.; Wormit, M.; Kussmann, J.; Lange, A. W.; Behn, A.; Deng, J.; Feng, X.; Ghosh, D.; Goldey, M.; Horn, P. R.; Jacobson, L. D.; Kaliman, I.; Khaliullin, R. Z.; Kuś, T.; Landau, A.; Liu, J.; Proynov, E. I.; Rhee, Y. M.; Richard, R. M.; Rohrdanz, M. A.; Steele, R. P.; Sundstrom, E. J.; Woodcock, H. L.; Zimmerman, P. M.; Zuev, D.; Albrecht, B.; Alguire, E.; Austin, B.; Beran, G. J. O.; Bernard, Y. A.; Berquist, E.; Brandhorst, K.; Bravaya, K. B.; Brown, S. T.; Casanova, D.; Chang, C.-M.; Chen, Y.; Chien, S. H.; Closser, K. D.; Crittenden, D. L.; Diedenhofen, M.; DiStasio, R. A.; Do, H.; Dutoi, A. D.; Edgar, R. G.; Fatehi, S.; Fusti-Molnar, L.; Ghysels, A.; Golubeva-Zadorozhnaya, A.; Gomes, J.; Hanson-Heine, M. W. D.; Harbach, P. H. P.; Hauser, A. W.; Hohenstein, E. G.; Holden, Z. C.; Jagau, T.-C.; Ji, H.; Kaduk, B.; Khistyaev, K.; Kim, J.; Kim, J.; King, R. A.; Klunzinger, P.; Kosenkov, D.; Kowalczyk, T.; Krauter, C. M.; Lao, K. U.; Laurent, A. D.; Lawler, K. V.; Levchenko, S. V.; Lin, C. Y.; Liu, F.; Livshits, E.; Lochan, R. C.; Luenser, A.; Manohar, P.; Manzer, S. F.; Mao, S.-P.; Mardirossian, N.; Marenich, A. V.; Maurer, S. A.; Mayhall, N. J.; Neuscamman, E.; Oana, C. M.; Olivares-Amaya, R.; O'Neill, D. P.; Parkhill, J. A.; Perrine, T. M.; Peverati, R.; Prociuk, A.; Rehn, D. R.; Rosta, E.; Russ, N. J.; Sharada, S. M.; Sharma, S.; Small, D. W.; Sodt, A.; Stein, T.; Stück, D.; Su, Y.-C.; Thom, A. J. W.; Tsuchimochi, T.; Vanovschi, V.; Vogt, L.; Vydrov, O.; Wang, T.; Watson, M. A.; Wenzel, J.; White, A.; Williams, C. F.; Yang, J.; Yeganeh, S.; Yost, S. R.; You, Z.; Zhang, I. Y.; Zhang, X.; Zhao, Y.; Brooks, B. R.; Chan, G. K. L.; Chipman, D. M.; Cramer, C. J.; Goddard, W. A.; Gordon, M. S.; Hehre, W. J.; Klamt, A.; Schaefer, H. F.; Schmidt, M. W.; Sherrill, C. D.; Truhlar, D. G.; Warshel, A.; Xu, X.; Aspuru-Guzik, A.; Baer, R.; Bell, A. T.; Besley, N. A.; Chai, J.-D.; Dreuw, A.; Dunietz, B. D.; Furlani, T. R.; Gwaltney, S. R.; Hsu, C.-P.; Jung, Y.; Kong, J.; Lambrecht, D. S.; Liang, W.; Ochsenfeld, C.; Rassolov, V. A.; Slipchenko, L. V.; Subotnik, J. E.; Van Voorhis, T.; Herbert, J. M.; Krylov, A. I.; Gill, P. M. W.; Head-Gordon,

M. *Mol. Phys.* **2015**, *113*, 184–215.

(168) Mavros, M. G.; Tsuchimochi, T.; Kowalczyk, T.; McIsaac, A.; Wang, L.; Van Voorhis, T. *Inorg. Chem.* **2014**, *53*, 6386–6397.

(169) Chase, M. W. *NIST-JANAF Thermochemical Tables, 4th Edition*; American Institute of Physics: New York, NY, 1998.

(170) Humphrey, W.; Dalke, A.; Schulten, K. *J. Mol. Graph.* **1996**, *14*, 33–38.

(171) *Heterogeneous Catalysis for Today's Challenges*; Trewyn, B., Ed.; Green Chemistry Series; Royal Society of Chemistry: Cambridge, **2015**.

(172) Sheberla, D.; Sun, L.; Blood-Forsythe, M. A.; Er, S.; Wade, C. R.; Brozek, C. K.; Aspuru-Guzik, A.; Dincă, M. *J. Am. Chem. Soc.* **2014**, *136*, 8859–8862.

(173) Campbell, M. G.; Sheberla, D.; Liu, S. F.; Swager, T. M.; Dincă, M. *Angew. Chemie Int. Ed.* **2015**, *54*, 4349–4352.

(174) Campbell, M. G.; Liu, S. F.; Swager, T. M.; Dincă, M. *J. Am. Chem. Soc.* **2015**, *137*, 13780–13783.

(175) Dou, J.; Sun, L.; Ge, Y.; Li, W.; Hendon, C. H.; Li, J.; Gul, S.; Yano, J.; Stach, E. A.; Dincă, M. *J. Am. Chem. Soc.* **2017**, *139*, 13608–13611.

(176) Hmadeh, M.; Lu, Z.; Liu, Z.; Gándara, F.; Furukawa, H.; Wan, S.; Augustyn, V.; Chang, R.; Liao, L.; Zhou, F.; Perre, E.; Ozolins, V.; Suenaga, K.; Duan, X.; Dunn, B.; Yamamto, Y.; Terasaki, O.; Yaghi, O. M. *Chem. Mater.* **2012**, *24*, 3511–3513.

(177) Lin, S.; Diercks, C. S.; Zhang, Y.-B.; Kornienko, N.; Nichols, E. M.; Zhao, Y.; Paris, A. R.; Kim, D.; Yang, P.; Yaghi, O. M.; Chang, C. *Science* **2015**, *349*, 1208–1213.

(178) Clough, A. J.; Skelton, J. M.; Downes, C. A.; de la Rosa, A. A.; Yoo, J. W.; Walsh, A.; Melot, B. C.; Marinescu, S. C. *J. Am. Chem. Soc.* **2017**, *139*, 10863–10867.

(179) Clough, A. J.; Yoo, J. W.; Mecklenburg, M. H.; Marinescu, S. C. *J. Am. Chem. Soc.* **2015**, *137*,

118–121

(180) Downes, C. A.; Marinescu, S. C. *ChemSusChem* **2017**, *10*, 4374–4392.

(181) Jia, H.; Yao, Y.; Zhao, J.; Gao, Y.; Luo, Z.; Du, P. *J. Mater. Chem. A* **2018**, *6*, 1188–1195.

(182) Liu, X.; Hu, W.; Jiang, W.; Yang, Y.; Niu, S.; Sun, B.; Wu, J.; Hu, J. *ACS Appl. Mater. Interfaces* **2017**, *9*, 28473–28477.

(183) Liao, P.; Shen, J.; Zhang, J. *Coord. Chem. Rev.* **2018**, *373*, 22-48.

(184) Miner, E. M.; Gul, S.; Ricke, N. D.; Pastor, E.; Yano, J.; Yachandra, V. K.; Van Voorhis, T.; Dincă, M. *ACS Catal.* **2017**, *7*, 7726–7731.

(185) Brückner, C.; Caulder, D. L.; Raymond, K. N. *Inorg. Chem.* **1998**, *37*, 6759–6764.

(186) Hall, G. S.; Soderberg, R. H. *Inorg. Chem.* **1968**, *7*, 2300–2303.

(187) Liaw, D. S.; Peng, S. M.; Chern, S. S.; Sheu, S. C. *Acta Crystallogr. Sect. C Cryst. Struct. Commun.* **1986**, *42*, 402–404.

(188) Passard, G.; Ullman, A. M.; Brodsky, C. N.; Nocera, D. G. *J. Am. Chem. Soc.* **2016**, *138*, 2925–2928.

(189) Zagal, J. H.; Aguirre, M. J.; Páez, M. A. *J. Electroanal. Chem.* **1997**, *437*, 45–52.

(190) Li, Q.; Noffke, B. W.; Wang, Y.; Menezes, B.; Peters, D. G.; Raghavachari, K.; Li, L. *J. Am. Chem. Soc.* **2014**, *136*, 3358–3361.

(191) Wang, L.; Wu, Y.; Cao, R.; Ren, L.; Chen, M.; Feng, X.; Zhou, J.; Wang, B. *ACS Appl. Mater. Interfaces* **2016**, *8*, 16736–16743.

(192) Sun, L.; Liao, B.; Sheberla, D.; Kraemer, D.; Zhou, J.; Stach, E. A.; Zakharov, D.; Stavila, V.; Talin, A. A.; Ge, Y.; Allendorf, M.; Chen, G.; Leonard, F.; Dincă, M. *Joule* **2017**, *1*, 168–177.

(193) Costentin, C.; Savéant, J. *ACS Catal.* **2017**, *7*, 4876–4880.

(194) Wudl, F.; Bryce, M. R. *J. Chem. Educ.* **1990**, *67*, 717-718.

(195) Kurzweil, P. *J. Power Sources* **2010**, *195*, 4424–4434.

(196) Bucur, C. B. *Challenges of a Rechargeable Magnesium Battery*; SpringerBriefs in Energy; Springer International Publishing: Cham, 2018.

(197) Zhao, C.; Liu, L.; Qi, X.; Lu, Y.; Wu, F.; Zhao, J.; Yu, Y.; Hu, Y.; Chen, L. *Adv. Energy Mater.* **2018**, *8*, 1703012-1703032.

(198) Ren, W.; Zhu, Z.; An, Q.; Mai, L. *Small* **2017**, *13*, 1604181-1604212.

(199) Wu, X.; Leonard, D. P.; Ji, X. *Chem. Mater.* **2017**, *29*, 5031–5042.

(200) Wang, M.; Jiang, C.; Zhang, S.; Song, X.; Tang, Y.; Cheng, H. *Nat. Chem.* **2018**, *10*, 667–672.

(201) Zhang, Y.; Liu, S.; Ji, Y.; Ma, J.; Yu, H. *Adv. Mater.* **2018**, *30*, 1706310-1706333.

(202) *Handbook of Battery Materials*; Daniel, C., Besenhard, J. O., Eds.; Wiley-VCH Verlag GmbH & Co. KGaA: Weinheim, Germany, 2011.

(203) Zhang, J.; Xu, W.; Henderson, W. A. *Lithium Metal Anodes and Rechargeable Lithium Metal Batteries*; Springer Series in Materials Science; Springer International Publishing: Cham, 2017; Vol. 249.

(204) Li, W.; Song, B.; Manthiram, A. *Chem. Soc. Rev.* **2017**, *46*, 3006–3059.

(205) Whittingham, M. S. *Chem. Rev.* **2004**, *104*, 4271–4302.

(206) *Electrolytes for Lithium and Lithium-Ion Batteries*; Jow, T. R., Xu, K., Borodin, O., Ue, M., Eds.; Modern Aspects of Electrochemistry; Springer New York: New York, NY, 2014; Vol. 58.

(207) Goodenough, J. B.; Kim, Y. *Chem. Mater.* **2010**, *22*, 587–603.

(208) Xu, K. *Chem. Rev.* **2004**, *104*, 4303–4418.

(209) Sun, C.; Liu, J.; Gong, Y.; Wilkinson, D. P.; Zhang, J. *Nano Energy* **2017**, *33*, 363–386.

(210) Ngai, K. S.; Ramesh, S.; Ramesh, K.; Juan, J. C. *Ionics* **2016**, *22*, 1259–1279.

(211) Zhao, Y.; Daemen, L. L. *J. Am. Chem. Soc.* **2012**, *134*, 15042–15047.

(212) Li, S.; Zhu, J.; Wang, Y.; Howard, J. W.; Lü, X.; Li, Y.; Kumar, R. S.; Wang, L.; Daemen, L. L.; Zhao, Y. *Solid State Ionics* **2016**, *284*, 14–19.

(213) Wang, Y.; Wang, Q.; Liu, Z.; Zhou, Z.; Li, S.; Zhu, J.; Zou, R.; Wang, Y.; Lin, J.; Zhao, Y. *J. Power Sources* **2015**, *293*, 735–740.

(214) Tang, W. S.; Matsuo, M.; Wu, H.; Stavila, V.; Zhou, W.; Talin, A. A.; Soloninin, A. V.; Skoryunov, R. V.; Babanova, O. A.; Skripov, A. V.; Unemoto, A.; Orimo, S.; Udovic, T. J. *Adv. Energy Mater.* **2016**, *6*, 1502237-1502243.

(215) Hueso, K. B.; Armand, M.; Rojo, T. *Energy Environ. Sci.* **2013**, *6*, 734-749.

(216) Aubrey, M. L.; Ameloot, R.; Wiers, B. M.; Long, J. R. *Energy Environ. Sci.* **2014**, *7*, 667-671.

(217) Kitao, T.; Zhang, Y.; Kitagawa, S.; Wang, B.; Uemura, T. *Chem. Soc. Rev.* **2017**, *46*, 3108–3133.

(218) Wang, L.; Han, Y.; Feng, X.; Zhou, J.; Qi, P.; Wang, B. *Coord. Chem. Rev.* **2016**, *307*, 361–381.

(219) Yamada, T.; Otsubo, K.; Makiura, R.; Kitagawa, H. *Chem. Soc. Rev.* **2013**, *42*, 6655-6669.

(220) Ke, F.; Wu, Y.; Deng, H. *J. Solid State Chem.* **2015**, *223*, 109–121.

(221) Wu, H.; Lou, X. W. *Sci. Adv.* **2017**, *3*, eaap9252-eaap9266.

(222) Farha, O. K.; Eryazici, I.; Jeong, N. C.; Hauser, B. G.; Wilmer, C. E.; Sarjeant, A. A.; Snurr, R. Q.; Nguyen, S. T.; Yazaydın, A. Ö.; Hupp, J. T. *J. Am. Chem. Soc.* **2012**, *134*, 15016–15021.

(223) Zugmann, S.; Fleischmann, M.; Amereller, M.; Gschwind, R. M.; Wiemhöfer, H. D.; Gores, H. J. *Electrochim. Acta* **2011**, *56*, 3926–3933.

(224) Diederichsen, K. M.; McShane, E. J.; McCloskey, B. D. *ACS Energy Lett.* **2017**, *2*, 2563–2575.

(225) Wang, H.; Lustig, W. P.; Li, J. *Chem. Soc. Rev.* **2018**, *47*, 4729-4756.

(226) Kim, S.; Joarder, B.; Hurd, J. A.; Zhang, J.; Dawson, K. W.; Gelfand, B. S.; Wong, N. E.; Shimizu, G. K. H. *J. Am. Chem. Soc.* **2018**, *140*, 1077–1082.

(227) Karim, M. R.; Hatakeyama, K.; Koinuma, M.; Hayami, S. *J. Mater. Chem. A* **2017**, *5*, 7243–7256.

(228) Yamada, T.; Sadakiyo, M.; Shigematsu, A.; Kitagawa, H. *Bull. Chem. Soc. Jpn.* **2016**, *89*, 1–10.

(229) Meng, X.; Wang, H.; Song, S.; Zhang, H. *Chem. Soc. Rev.* **2017**, *46*, 464–480.

(230) Yuan, C.; Li, J.; Han, P.; Lai, Y.; Zhang, Z.; Liu, J. *J. Power Sources* **2013**, *240*, 653–658.

(231) Zhu, K.; Liu, Y.; Liu, J. *RSC Adv.* **2014**, *4*, 42278–42284.

(232) Gerbaldi, C.; Nair, J. R.; Kulandainathan, M. A.; Kumar, R. S.; Ferrara, C.; Mustarelli, P.; Stephan, A. M. *J. Mater. Chem. A* **2014**, *2*, 9948–9954.

(233) Angulakshmi, N.; Kumar, R. S.; Kulandainathan, M. A.; Stephan, A. M. *J. Phys. Chem. C* **2014**, *118*, 24240–24247.

(234) Senthil Kumar, R.; Raja, M.; Anbu Kulandainathan, M.; Manuel Stephan, A. *RSC Adv.* **2014**, *4*, 26171–26175.

(235) Suriyakumar, S.; Kanagaraj, M.; Angulakshmi, N.; Kathiresan, M.; Nahm, K. S.; Walkowiak, M.; Wasiński, K.; Półrolniczak, P.; Stephan, A. M. *RSC Adv.* **2016**, *6*, 97180–97186.

(236) Fujie, K.; Kitagawa, H. *Coord. Chem. Rev.* **2016**, *307*, 382–390.

(237) Wang, Z.; Wang, Z.; Yang, L.; Wang, H.; Song, Y.; Han, L.; Yang, K.; Hu, J.; Chen, H.; Pan, F. *Nano Energy* **2018**, *49*, 580–587.

(238) Singh, A.; Vedarajan, R.; Matsumi, N. *J. Electrochem. Soc.* **2017**, *164*, H5169–H5174.

(239) Luo, Q.; An, B.; Ji, M.; Zhang, J. *Mater. Chem. Front.* **2018**, *2*, 219–234.

(240) Fujie, K.; Ikeda, R.; Otsubo, K.; Yamada, T.; Kitagawa, H. *Chem. Mater.* **2015**, *27*, 7355–7361.

(241) Wang, Z.; Tan, R.; Wang, H.; Yang, L.; Hu, J.; Chen, H.; Pan, F. *Adv. Mater.* **2018**, *30*, 1704436-1704443.

(242) Fujie, K.; Otsubo, K.; Ikeda, R.; Yamada, T.; Kitagawa, H. *Chem. Sci.* **2015**, *6*, 4306–4310.

(243) Park, J.; Lee, M.; Feng, D.; Huang, Z.; Hinckley, A. C.; Yakovenko, A.; Zou, X.; Cui, Y.; Bao, Z. *J. Am. Chem. Soc.* **2018**, *140*, 10315-10323.

(244) Zhou, J.; Wang, B. *Chem. Soc. Rev.* **2017**, *46*, 6927–6945.

(245) Tang, H.; Zheng, M.; Hu, Q.; Chi, Y.; Xu, B.; Zhang, S.; Xue, H.; Pang, H. *J. Mater. Chem. A* **2018**, *6*, 13999–14024.

(246) Fu, X.; Yu, D.; Zhou, J.; Li, S.; Gao, X.; Han, Y.; Qi, P.; Feng, X.; Wang, B. *CrystEngComm*

2016, *18*, 4236–4258.

(247) Wiers, B. M.; Foo, M.; Balsara, N. P.; Long, J. R. *J. Am. Chem. Soc.* **2011**, *133*, 14522–14525.

(248) Linford, R. G.; Hackwood, S. *Chem. Rev.* **1981**, *81*, 327–364.

(249) Valenzano, L.; Civalleri, B.; Chavan, S.; Bordiga, S.; Nilsen, M. H.; Jakobsen, S.; Lillerud, K. P.; Lamberti, C. *Chem. Mater.* **2011**, *23*, 1700–1718.

(250) Chavan, S.; Vitillo, J. G.; Gianolio, D.; Zavorotynska, O.; Civalleri, B.; Jakobsen, S.; Nilsen, M. H.; Valenzano, L.; Lamberti, C.; Lillerud, K. P.; Bordiga, S. *Phys. Chem. Chem. Phys.* **2012**, *14*, 1614–1626.

(251) Ameloot, R.; Aubrey, M.; Wiers, B. M.; Gómora-Figueroa, A. P.; Patel, S. N.; Balsara, N. P.; Long, J. R. *Chem. Eur. J.* **2013**, *19*, 5533–5536.

(252) Quartarone, E.; Mustarelli, P. *Chem. Soc. Rev.* **2011**, *40*, 2525-2540.

(253) Park, S. S.; Tulchinsky, Y.; Dincă, M. *J. Am. Chem. Soc.* **2017**, *139*, 13260–13263.

(254) Shen, L.; Wu, H. Bin; Liu, F.; Brosmer, J. L.; Shen, G.; Wang, X.; Zink, J. I.; Xiao, Q.; Cai, M.; Wang, G.; Lu, Y.; Dunn, B. *Adv. Mater.* **2018**, *30*, 1707476-1707484.

(255) Chen, H.; Tu, H.; Hu, C.; Liu, Y.; Dong, D.; Sun, Y.; Dai, Y.; Wang, S.; Qian, H.; Lin, Z.; Chen, L. *J. Am. Chem. Soc.* **2018**, *140*, 896–899.

(256) Witt, O.; Mauser, H.; Friedl, T.; Wilhelm, D.; Clark, T. *J. Org. Chem.* **1998**, *63*, 959–967.

(257) Geiculescu, O.; Xie, Y.; Rajagopal, R.; Creager, S.; DesMarteau, D. *J. Fluor. Chem.* **2004**, *125*, 1179–1185.

(258) Geiculescu, O. *Solid State Ionics* **2002**, *148*, 173–183.

(259) Trzeciak, T.; Niedzicki, L.; Groszek, G.; Wieczorek, P.; Marcinek, M.; Wieczorek, W. *J. Power Sources* **2014**, *252*, 229–234.

(260) Nie, J.; Li, X.; Liu, D.; Luo, R.; Wang, L. *J. Fluor. Chem.* **2004**, *125*, 27–31.

(261) Van Humbeck, J. F.; Aubrey, M. L.; Alsbaiee, A.; Ameloot, R.; Coates, G. W.; Dichtel, W. R.;

Long, J. R. *Chem. Sci.* **2015**, *6*, 5499–5505.

(262) Bannister, D.; Davies, G.; Ward, I.; McIntyre, J. *Polymer* **1984**, *25*, 1291–1296.

(263) Hardy, L. C.; Shriver, D. F. *Macromolecules* **1984**, *17*, 975–977.

(264) Du, Y.; Yang, H.; Whiteley, J. M.; Wan, S.; Jin, Y.; Lee, S.; Zhang, W. *Angew. Chemie Int. Ed.* **2016**, *55*, 1737–1741.

(265) Moriya, M.; Kato, D.; Sakamoto, W.; Yogo, T. *Chem. Commun.* **2011**, *47*, 6311-6313.

(266) Cepeda, J.; Pérez-Yáñez, S.; Beobide, G.; Castillo, O.; Goikolea, E.; Aguesse, F.; Garrido, L.; Luque, A.; Wright, P. A. *Chem. Mater.* **2016**, *28*, 2519–2528.

(267) Brozek, C. K.; Dincă, M. *Chem. Soc. Rev.* **2014**, *43*, 5456–5467.

(268) Vazquez-Molina, D. A.; Mohammad-Pour, G. S.; Lee, C.; Logan, M. W.; Duan, X.; Harper, J. K.; Uribe-Romo, F. J. *J. Am. Chem. Soc.* **2016**, *138*, 9767–9770.

(269) Xu, Q.; Tao, S.; Jiang, Q.; Jiang, D. *J. Am. Chem. Soc.* **2018**, *140*, 7429–7432.

(270) Wang, L.; Chen, B.; Ma, J.; Cui, G.; Chen, L. *Chem. Soc. Rev.* **2018**, *47*, 6505-6602.

(271) Sun, C.; Liu, J.; Gong, Y.; Wilkinson, D. P.; Zhang, J. *Nano Energy* **2017**, *33*, 363–386.

(272) Ohta, N.; Takada, K.; Zhang, L.; Ma, R.; Osada, M.; Sasaki, T. *Adv. Mater.* **2006**, *18*, 2226–2229.

(273) Takada, K.; Ohta, N.; Zhang, L.; Fukuda, K.; Sakaguchi, I.; Ma, R.; Osada, M.; Sasaki, T. *Solid State Ionics* **2008**, *179*, 1333–1337.

(274) Sakuda, A.; Kitaura, H.; Hayashi, A.; Tadanaga, K.; Tatsumisago, M. *Electrochem. Solid-State Lett.* **2008**, *11*, A1-A3.

(275) Sakuda, A.; Kitaura, H.; Hayashi, A.; Tadanaga, K.; Tatsumisago, M. *J. Electrochem. Soc.* **2009**, *156*, A27-A32.

(276) Woo, J. H.; Trevey, J. E.; Cavanagh, A. S.; Choi, Y. S.; Kim, S. C.; George, S. M.; Oh, K. H.; Lee, S. *J. Electrochem. Soc.* **2012**, *159*, A1120–A1124.

(277) Hayashi, A.; Nishio, Y.; Kitaura, H.; Tatsumisago, M. *Electrochem. Commun.* **2008**, *10*, 1860–

1863.

(278) Kitaura, H.; Hayashi, A.; Ohtomo, T.; Hama, S.; Tatsumisago, M. *J. Mater. Chem.* **2011**, *21*, 118–124.

(279) Ohta, N.; Takada, K.; Sakaguchi, I.; Zhang, L.; Ma, R.; Fukuda, K.; Osada, M.; Sasaki, T. *Electrochem. Commun.* **2007**, *9*, 1486–1490.

(280) Dincă, M.; Dailly, A.; Long, J. R. *Chem. - A Eur. J.* **2008**, *14*, 10280–10285.

(281) Traube, I. *Deutsch. Chem. Ges.* **1884**, *17*, 1064.

(282) Kolthoff, I. M. *Recl. des Trav. Chim. des Pays-Bas.* **1926**, *45*, 153–161.

(283) Holleman, A. F.; Wiberg, E. *Inorganic Chemistry*; Academic Press: San Diego.

(284) Copper, Silver and Gold. In *Chemistry of the Elements*; Greenwood, N. N., Earnshaw, A., Eds.; Elsevier, 1997, 1173–1200.

(285) *CRC Handbook of Chemistry and Physics*, 81st ed.; Lide, D. R., Ed.; CRC Press: Boca Raton, 2000.

(286) Wang, L.; Chen, B.; Ma, J.; Cui, G.; Chen, L. *Chem. Soc. Rev.* **2018**, *47*, 6505–6602.

(287) Goodenough, J. B.; Park, K. *J. Am. Chem. Soc.* **2013**, *135*, 1167–1176.

(288) Schoetz, T.; de Leon, C. P.; Ueda, M.; Bund, A. *J. Electrochem. Soc.* **2017**, *164*, A3499–A3502.

(289) Sun, L.; Park, S. S.; Sheberla, D.; Dincă, *J. Am. Chem. Soc.* **2016**, *138*, 14772–14782.

(290) Evans, J.; Vincent, C. A.; Bruce, P. G. *Polymer* **1987**, *28*, 2324–2328.

Acknowledgements

There are many people to whom I am incredibly grateful for their role in my becoming the scientist and person I am today. First and foremost, I would like to thank my advisor, Professor Mircea Dincă, who has been a source of wisdom, encouragement, and ideas for experiments for me to try even after I have disposed of all of my samples. Truly Mircea, I have appreciated the independence you have allowed me on my projects, and for your helping me become a more thoughtful, thorough, and invested scientist. Finally, thank you for granting me the greatest group job of Puppy Walker.

To my thesis committee chair, Professor Yogesh (Yogi) Surendranath, I give my sincere thanks for bestowing upon me both electrochemistry knowledge throughout my entire Ph.D., as well as electrochemistry equipment in my first year when all our lab had in that vein was a shoebox with some protruding cables. Additionally, Yogi, I have appreciated your guidance and support regarding both my development as a scientist and my professional development, particularly during our annual meetings. To my third committee member, Professor Yang Shao-Horn, thank you for adding an engineer's perspective to my research. Exposure to a different approach to research has made me a more well-rounded problem solver.

To all Dincă Group members, past and present, thank you for making this experience more fun than that amount of time in lab should be. I have so enjoyed discussing science with all of you, seeing your ideas and projects develop, and escaping the lab on group trips or other outings. You are a special group and I will always cherish you, and have an especially fond place in my heart for the Physical Properties subgroup. Within that, I would like to acknowledge Lu Wang, our visiting student with whom I had the pleasure of collaborating. Lu, thank you for your sunny disposition and valuable contributions to the ORR project. I am also incredibly grateful to Dr. Minyuan (Miller) Li and Professor Michael Campbell for their roles in mentoring me at the start of graduate school. Additionally, I acknowledge Miller for bequeathing the Safety Officer duties to me, and thank Mike for letting me dogsit. At the risk of playing favorites, I would be

remiss if I did not specifically thank Amanda Stubbs for her comradery and friendship during graduate school. Amanda, you and Jessica Weber made every day at MIT brighter. Within the MIT staff, I would like to thank everyone in the Chemistry Education Office for making our department go 'round. I would also like to thank Christine Brooks and David D'Amore for all they do.

Eric, thank you for your support in and out of lab. Without you, I would not know how to generate a pivot table. To my parents, John and Sharon Miner, I give my biggest thanks for always encouraging me to pursue my goals, and supporting me during the peaks and valleys that accompany those pursuits. To my sisters, Abbey and Ellery Miner, thank you for being the best cheerleaders anyone could ask for, and for always making me laugh. Even from afar, I am thankful to always be so close with my family and loved ones. Despite geographical distance from family for the past nine years, I have been blessed with the Waltman family who has been physically by my side through college and graduate school. Frank, Kim, Timothy, Sarah, Patrick, Amanda, and crazy animals, thank you for including me in all of your adventures, and always making sure I have a home in New England.

Finally, I would like to warmly thank both the MIT and the Greater Boston communities. Boston has been my home through many events and times of growth during undergraduate and graduate school, and this dirty water will always be special to me. To everyone in and around Boston who has been in my life during this time, thank you for the lessons, laughs, and memories.